

MCGILL UNIVERSITY

DOCTORAL THESIS

Modeling and Simulation of Long-term Rotational Dynamics of Large Space Debris

Author:

Luc B. M. SAGNIÈRES

Supervisor:

Prof. Inna SHARF

*A thesis submitted to McGill University in partial fulfillment of the requirements
for the degree of Doctor of Philosophy in Mechanical Engineering*

in the

Department of Mechanical Engineering
Aerospace Mechatronics Laboratory



March 2019, Montreal, QC, Canada

© Luc Sagnières, 2019

*To each and every star,
whose light shines down and fills my dreams...*



Caroline Corbasson
"Dust to Dust"
Dust and spray on paper

Abstract

The increase in Earth-orbiting space debris has been the cause of significant debate over the last decade. Large space debris (>10 cm), mostly defunct satellites and upper stages, populate the near-Earth environment and represent a significant risk to current and future space missions. Active Debris Removal (ADR) has been proposed as a solution to this problem, where a removal spacecraft would be launched, would rendezvous with a target, capture and stabilize it, and finally remove it from orbit. However, precise knowledge of the target's rotational parameters ahead of time is key for the stabilization and capture of the debris, especially since current ADR techniques may be dangerous for debris spinning at high angular velocities. Many external torques affect the spin characteristics of uncontrolled debris and the long-term (order of years), cumulative effect of these have only recently started to be studied.

A novel comprehensive coupled orbit-attitude propagator, called the Debris Spin/Orbit Simulation Environment (D-SPOSE), for the analysis and prediction of the rotational motion of these large space debris is therefore developed in order to determine, to the highest degree of accuracy possible, the evolution of the rotational parameters of uncontrolled space objects over a time scale of years. This tool, created for space debris remediation purposes, would benefit the space debris community by being able to predict the future attitude state of ADR targets, long before mission launch. The developed propagator includes a widespread list of external gravitational and non-gravitational perturbations, including high-order gravitational accelerations, the gravity-gradient torque, third-body perturbations from the Sun and the Moon, aerodynamic drag and torque, direct, Earth-emitted, and reflected radiation pressure and torque, the eddy-current torque, and internal energy dissipation. The developed model is tested and validated against past observations of the evolution of the angular motion of uncontrolled space objects, namely several spherical geodetic satellites, for which an abundant amount of observations exist.

Another potentially significant source of disturbances for large space debris is the transfer of momentum from bombardment by small debris (down to the μm scale)

and micrometeoroids, the effect of which is a research area still in its infancy. The influence of hypervelocity impacts on the attitude and orbital motion of spacecraft is further investigated and incorporated into D-SPOSE. As collisions are completely random in the space environment, the spacecraft equations of motion will take the form of stochastic differential equations. Correspondingly, a stochastic framework to solve these equations in a Monte Carlo simulation for the distributions of the target's orbital and rotational parameters is outlined, making use of impact fluxes from the European Space Agency's Meteoroid and Space Debris Terrestrial Environment Reference model.

D-SPOSE is then applied to two different debris objects. First, the rotational motion of the inoperative European satellite and "most wanted" ADR target Envisat is investigated. Comparisons of simulation results to observations provide insights into the evolution of its complex attitude dynamics and reveal potential difficulties for an upcoming ADR mission. It is shown that as Envisat's rotation slows down, its relative spin stabilization effect will decrease, which will lead the gravity-gradient torque and other environmental torques to drive the satellite toward a larger tumbling motion. Second, the model is applied to another large inoperative satellite, TOPEX/Poseidon, for which a number of model parameters are missing. As well, differently from Envisat, observations of TOPEX/Poseidon have shown it to be rotating with an increasing angular rate. D-SPOSE is employed to investigate the spacecraft's rotational dynamics and in combination with observation results, to obtain estimates of the satellite's parameters, including its moments of inertia and magnetic properties, which are important for future prediction of its rotational motion.

Résumé

L'augmentation du nombre de débris spatiaux en orbite autour de la Terre a été à l'origine de nombreux débats au cours des dix dernières années. Les gros débris spatiaux (> 10 cm), principalement des satellites morts et des étages supérieurs, peuplent l'espace autour de la Terre et représentent un risque important pour les missions spatiales actuelles et futures. L'élimination active des débris (ADR) a été proposée comme solution à ce problème, dans le cadre de celle-ci un vaisseau spatial serait lancé, rencontrerait une cible, la capturerait, la stabiliserait, puis la retirerait de son orbite. Cependant, une connaissance précise des paramètres de rotation de la cible est essentielle pour la stabilisation et la capture du débris, d'autant plus que les techniques ADR actuelles peuvent être dangereuses pour des débris tournant à des vitesses angulaires élevées. De nombreux couples externes affectent les caractéristiques de rotation des débris incontrôlés, et leurs effets cumulatifs à long terme (d'un ordre de plusieurs années) n'ont que récemment commencé à être étudiés.

Un nouveau propagateur d'orbite et d'attitude, appelé D-SPOSE, dédié à l'analyse et la prévision du mouvement de rotation de ces gros débris spatiaux est donc mis en avant, afin de déterminer, au plus haut degré de précision possible, l'évolution des paramètres de rotation d'objets spatiaux incontrôlés sur une période de plusieurs années. Cet outil, créé à des fins d'assainissement des débris spatiaux et ayant un fonctionnement malléable, serait bénéfique pour la communauté car il permettrait de prédire l'état d'attitude futur des cibles ADR bien avant le lancement de la mission. Le propagateur développé comprend une liste étendue de perturbations externes gravitationnelles et non gravitationnelles, notamment les accélérations gravitationnelles d'ordre élevé, le couple à gradient de gravité, les perturbations dues au Soleil et à la Lune, la traînée et le couple aérodynamique, la pression et le couple de radiation directe, émise, et réfléchie par la Terre, le couple à courants de Foucault, et la dissipation d'énergie interne. Le modèle développé est testé et validé grâce aux observations passées de l'évolution du mouvement angulaire d'objets spatiaux incontrôlés, à savoir

plusieurs satellites géodésiques sphériques, pour lesquels il existe une quantité abondante d'observations.

Une autre source potentiellement importante de perturbations pour les gros débris spatiaux est le transfert de moment par bombardement de petits débris (allant jusqu'au micromètre) et de micrométéoroïdes. L'analyse de leurs effets est un domaine de recherche encore balbutiant. L'influence des impacts à hypervitesse sur l'attitude et le mouvement orbital des engins spatiaux est ensuite étudiée et intégrée à D-SPOSE. Puisque les collisions sont complètement aléatoires dans l'environnement spatial, les équations de mouvement des engins spatiaux prendront la forme d'équations différentielles stochastiques. Parallèlement, un cadre stochastique permettant de résoudre ces équations par simulation Monte Carlo pour la distribution des paramètres orbitaux et de rotation de la cible est décrit, en utilisant les flux d'impact du modèle de l'Agence spatiale européenne MASTER-2009.

D-SPOSE est ensuite appliqué à deux débris différents. En premier lieu, le mouvement de rotation du satellite européen et cible ADR "la plus recherchée", Envisat, est étudié. Les comparaisons des résultats de simulations avec les observations fournissent des informations sur l'évolution de sa dynamique d'attitude complexe et révèlent des difficultés potentielles pour une mission ADR future. Il est démontré que lorsque la rotation d'Envisat ralentit, son effet de stabilisation relative de spin diminuera, ce qui conduira le couple à gradient de gravité et d'autres couples environnementaux à entraîner le satellite vers un mouvement de basculement plus important. Deuxièmement, le modèle est appliqué à un autre satellite inopérant, TOPEX/Poseidon, pour lequel un certain nombre de paramètres sont manquants. De même, contrairement à Envisat, les observations de TOPEX/Poseidon ont montré que celui-ci était en rotation avec une vitesse angulaire croissante. D-SPOSE est utilisé pour étudier la dynamique de rotation de l'engin spatial et, en combinaison avec les résultats des observations, pour obtenir des estimations des paramètres du satellite, y compris ses moments d'inertie et ses propriétés magnétiques, qui sont importants pour la prévision future de son mouvement de rotation.

Acknowledgements

I have been looking forward to writing this section for a very long time. It is my chance to give credit where credit is due. The support of everyone mentioned here, in all the forms that it came in, was endless, and in no way could I ever return the favor or show the magnitude and extent of my true appreciation. I am indebted to you all, and for that, I am tremendously grateful.

First and foremost, I would like to thank Prof. Inna Sharf, not only for her indispensable advice and direction over the last four years, but also for the great trust she showed throughout my time under her wing, first accepting a non-engineer as a Ph.D. student, and then letting me go on my own adventures abroad. I feel like I have grown immensely as a researcher thanks to her, and I know I will substantially benefit from the skill set she has passed on for my many endeavours to come.

De plus, je souhaiterais remercier tout particulièrement Florent Deleflie et Carine Briand. Arrivant à Paris sans point d'ancrage professionnel, j'ai été accueilli très chaleureusement au sein du magnifique Observatoire de Paris. Ils n'ont pas eu peur de m'adopter et leur hospitalité fut essentielle pour la conclusion de ma thèse. La générosité de toutes les équipes de l'Observatoire de Paris et de l'Institut de Mécanique Céleste et de Calcul des Éphémérides (IMCCE) m'a énormément touchée.

My educational journey, however, goes back further. I have not forgotten the scientific foundation I received from my prior supervisors, Dr. Marina Galand and Prof. David Hanna, and my early instructors, especially M. Douthe, M. Rivet, Mme. Mauger, and Mme. Ferté-Prévot, among many others. They laid the groundwork for the contributions that came out of my doctoral work.

I would also like to acknowledge my Ph.D. Supervisory Committee as well as my internal and external examiners for their time and the many anonymous journal article reviewers for their feedback that improved the content of this work significantly.

Furthermore, for the many questions answered and the knowledge transferred, the coffee breaks shared and wild theories compared, the frisbees thrown and brilliance shown, the code debugged and beers chugged, I would like to express my infinite

gratitude to the friends and colleagues I have had the pleasure of encountering at the Aerospace Mechatronics Laboratory (AML), the Center for Intelligence Machines (CIM), and IMCCE, most notably Damien, Fiona, Josh, Gareth, Eitan, Eleonora, Mikkel, Ali, Kelsey, and Alexis. In addition, this list would not be complete without mentioning my previous friends and colleagues at McGill and Imperial, Spathetic and the Raccoons, that helped shape the passion I have today for what I do, and the old CIMF crowd, with whom I have had the most captivating discussions on every subject imaginable. An enormous thank you in particular to Ulysse, Johanna, Alex, Josh, and Ruth.

A very special shout-out is necessary to the various artists whose talent you will experience going throughout this document: Caroline, John, Pierre, Marion, Hetty, Philippe, and Éloy. These friends were kind enough to present me with delightful artwork that encompass my thesis topic beautifully.

Of course, the work detailed in this thesis would not have been possible without the financial and logistical support of the institutions I received help from: McGill University and its Faculty of Engineering and Department of Mechanical Engineering, the McGill Institute for Aerospace Engineering, CIM and AML, Hydro-Québec, the Natural Sciences and Engineering Research Council, Paris Observatory and IMCCE, Mitacs, the Fonds de Recherche du Québec Nature et Technologies, Compute Canada and Calcul Québec, and the Canadian Space Agency.

I would also like to thank the crew at the Humble Lion and Cuillier for their endless supply of liquid energy. These morning coffee runs were the rocket fuel required to propel my research forward. The smiles I came across every time I walked through their doors lighted up my days.

Cheesily, I hold in my heart the moral support and encouragements I have received from my family, in the various and unique ways they expressed them, very dearly. Maman, Papa, Louis, Fanny, Xavier, Amandine, Yves, Marigona, Bénédicte, Margaux, Paul, Marco, Luca, et tous les autres à venir, there are no better words I can find other than a simple merci. Thanks for having my back.

Finally, always there to raise me up when I am down, to keep me dreaming while keeping my feet on the ground, for simply being awesome, Alice, thank you for the happiness I have discovered through your unconditional joy of living and generosity.

Now onto the next adventure...

Claims Of Originality

The main contributions of this thesis are the following:

- The development of a comprehensive, publicly available, open-source¹, coupled orbit-attitude propagator.
 - This tool bridges a gap in the space debris community by enabling high-accuracy predictions of the evolution of the rotational dynamics of large space debris.
 - The tool's comprehensiveness enables a wide array of possible applications such as re-entry analyses, mission planning, sensitivity studies, and accurate orbital propagation studies for Space Situational Awareness.
 - The multiple external environmental models included provide the user with a highly flexible mode of operation.
 - It contains more complete analytical expressions than usually employed for the gravity-gradient torque, eddy-current torque, and aerodynamic torque.
- The derivation of a stochastic methodology to consider hypervelocity impacts in the equations of orbital and attitude motion of spacecraft.
 - The compound Poisson process is shown to adequately represent the momentum transfer from hypervelocity impacts.
 - A framework to solve the stochastic differential equations of motion in a Monte Carlo simulation is highlighted.
 - The influence of hypervelocity impacts on the attitude and orbital motion of satellites is examined for two debris objects.
- Obtaining insights into the rotational motion of two large space debris and potential Active Debris Removal targets by comparing simulation results to observations.

¹The software is available on the McGill Aerospace Mechatronics Laboratory GitHub: <https://github.com/McGill-AML/D-SPOSE>

- The attitude motion of the space debris of interest Envisat is shown to be highly complex, composed of a precession, nutation, and librarion, with characteristics evolving with time.
- A lack of agreement between observations is identified and recommendations are put forward for obtaining better estimates of its rotational state from observations.
- The rotational dynamics of the inoperative satellite TOPEX/Poseidon is analyzed and information about its unknown moments of inertia and magnetic properties are obtained.
- A detailed energy analysis shows that the spacecraft is spinning about its minor principal axis and that damping could eventually bring the satellite into a different rotational state.

The code used in the development of the tool, called the Debris SPin/Orbit Simulation Environment (D-SPOSE), was written by Luc Sagnières. Some of the orbital mechanics functions were reproduced from algorithms outlined in Vallado [1]. The SGP4 algorithm is obtained directly from C++ code written by David Vallado and available on the CelesTrak website² [1]. The fortran functions for DTM-2013 were provided by Sean Bruinsma [2]. The source codes for NRLMSISE-00³, HWM14⁴, and JB2008⁵ were taken from their respective websites [3, 4, 5]. The D-SPOSE code was reviewed and its compilation architecture improved by Damien Goblot. The Earth's albedo and infrared grids were provided by Ali Sammneh [6]. Satellite Laser Ranging data for LAGEOS-2 and TOPEX/Poseidon were provided by Daniel Kucharski [7]. The spin period and spin axis orientation information obtained from light curves for Ajisai and LAGEOS-2 were provided by Nikolay Koshkin and Toshimichi Otsubo, respectively [8, 9]. All of the tables and figures were generated by Luc Sagnières, using various software including MATLAB, Microsoft PowerPoint, and MASTER-2009. This thesis was compiled in LaTeX using Overleaf. The analysis of simulations was the fruit of discussions between Luc Sagnières and Inna Sharf. The final text is the result of suggestions and comments from Inna Sharf, Florent Delefie and multiple anonymous journal article reviewers.

²<https://www.celesttrak.com/software/vallado-sw.php>

³<https://ccmc.gsfc.nasa.gov/modelweb/atmos/nrlmsise00.html>

⁴<https://agupubs.onlinelibrary.wiley.com/doi/full/10.1002/2014EA000089>

⁵<https://sol.spacenvironment.net/jb2008/>

Guidance was also provided by Inna Sharf throughout the entire development of the work that came out of this thesis.

Furthermore, parts of this thesis have previously appeared in the following journal articles and conference papers:

- Sagnières, L. B. M. and I. Sharf (2018), Long-term rotational motion analysis and comparison to observations of the inoperative Envisat, *J. Guid. Control Dyn.*, 42, 364-376, doi:[10.2514/1.G003647](https://doi.org/10.2514/1.G003647).
- Sagnières, L. B. M., I. Sharf, and F. Deleflie, Validation of a novel coupled orbit-attitude propagator by comparison to SLR data and light curves, *69th International Astronautical Congress*, Abstract ID 46562, Bremmen, Germany, October 2018.
- Sagnières, L. B. M. and I. Sharf, **Uncertainty Characterization of Atmospheric Density Models for Orbit Prediction of Space Debris**, *7th European Conference on Space Debris*, ESA/ESOC, Darmstadt, Germany, April 2017.
- Sagnières, L. B. M. and I. Sharf, **Evolution of Spacecraft Orbital Motion due to Hypervelocity Impacts from Debris and Meteoroids**, *7th European Conference on Space Debris*, ESA/ESOC, Darmstadt, Germany, April 2017.
- Sagnières, L. B. M. and I. Sharf (2017), Stochastic modeling of hypervelocity impacts in attitude propagation of space debris, *Adv. Space Res.*, 59, 1128-1143, doi:[10.1016/j.asr.2016.11.030](https://doi.org/10.1016/j.asr.2016.11.030).
- Sagnières, L. B. M. and I. Sharf, Stochastic Modeling of Hypervelocity Impacts on Attitude Propagation of Space Debris, *26th AAS/AIAA Space Flight Mechanics Meeting*, AAS 16-462, Napa, CA, USA, February 2016.

Contents

Abstract	v
Résumé	vii
Acknowledgements	ix
Claims Of Originality	xi
Contents	xv
List of Figures	xix
List of Tables	xxi
Abbreviations	xxiii
Physical Constants	xxvii
Symbols	xxix
1 Introduction	3
1.1 Space Debris Environment	3
1.2 Mitigation and Remediation	6
1.2.1 International Guidelines	6
1.2.2 Active Debris Removal	7
1.3 Satellite Rotational Dynamics	9
1.3.1 Observing Inoperative Spacecraft	9
1.3.2 Modeling Efforts	10

1.4 Thesis Outline	12
2 D-SPOSE: Debris SPin/Orbit Simulation Environment	15
2.1 Spacecraft Dynamics	16
2.1.1 Reference Frames	16
Earth-Centered Inertial Frame	16
Earth-Centered Earth-Fixed Frame	16
Orbital Elements and the Earth-Centered Orbital Frame	19
Satellite-Centered Orbital Frame	21
Body-Fixed Frame	22
2.1.2 Orbit and Attitude Equations	22
2.2 Gravitational Perturbations	25
2.2.1 Earth's Gravitational Field	25
2.2.2 Gravity-Gradient Torque	25
2.2.3 Third-body Interactions	26
2.3 Non-Gravitational Perturbations	27
2.3.1 Aerodynamic Drag and Torque	27
2.3.2 Eddy-current Torque	29
2.3.3 Radiation Perturbations	30
Direct Solar Radiation	31
Earth's Albedo and Infrared Emissions	32
2.3.4 Internal Energy Dissipation	32
2.4 Propagator Inputs and Operating Modes	33
2.4.1 Input Files Format	33
2.4.2 Environmental Models	35
Geopotential Model	35
Solar System Ephemerides	35
Atmospheric Models	35
Geomagnetic Field	39
Earth's Radiation Budget	39
2.5 Validation	40
2.5.1 LAGEOS-2	41
2.5.2 LARES	45
2.5.3 Ajisai	47
2.6 Concluding Remarks	51

3 Stochastic Modeling of Hypervelocity Impacts	55
3.1 Particle Impacts	56
3.2 Collisions as a Compound Poisson Process	58
3.2.1 Stochastic Processes	58
3.2.2 ESA's MASTER-2009 Model	59
3.2.3 Converting Impact Fluxes to Probability Density Functions	62
3.3 Numerical Solution to Stochastic Differential Equations with Jumps	64
3.3.1 Implementing Collisions in Spacecraft Motion Equations	64
3.3.2 Solving the Stochastic Differential Equation	65
3.3.3 Generating Independent Collisions	67
Computing Random Linear Momentum	67
Computing Random Impact Location	69
3.4 Ejecta Momentum	70
3.5 Case Studies	72
3.5.1 Influence on Attitude	72
Envisat	73
High Area-to-Mass Ratio Objects	78
3.5.2 Influence on Orbit	80
Envisat	81
High Area-to-Mass Ratio Object	82
3.6 Concluding Remarks	83
4 The Envisat Enigma	87
4.1 Simulation Inputs	88
4.2 Propagation Results	91
4.3 Sensitivity Study on Input Parameters	96
4.4 Review of Observational Results	99
4.5 Propagation to 2025: Removal Mission Date	103
4.6 Recommendations	105
5 TOPEX/Poseidon in Minor-Axis Spin	109
5.1 Determining Inertia Properties from Observations	110
5.1.1 Gravitational Effects on Angular Momentum	110
5.1.2 Moments of Inertia Relationship	112
5.2 Investigation using D-SPOSE	116

5.2.1	Simulation Inputs	116
5.2.2	Propagation Results	117
5.3	Energy Analysis	120
5.3.1	Internal Energy Dissipation	120
5.3.2	Work-Energy Balance	122
5.4	Attitude Motion Predictions	124
5.5	Summary of Findings	126
6	Conclusion	131
6.1	Summary of Contributions	131
6.2	Recommendations for Future Research	133
A	Evaluating Gravitational Perturbations	135
B	Aerodynamic Torque Surface Integrals	139
B.1	Theory	139
B.2	First Integral	141
B.3	Second Integral	143
C	Magnetic Field Computation	147
D	Computing Ejecta Momentum	151
D.1	Ejecta Model by Rival and Mandeville (1999)	151
D.2	Computation of Ejecta Momentum	154
D.2.1	Momentum from Spall Products	155
D.2.2	Momentum from Cone Fragments	155
Mass distribution		155
Grazing Impacts		156
Oblique Impacts		159
E	Analytical Momentum Transfer from Hypervelocity Impacts	163
E.1	Hohmann Transfer from Hypervelocity Impacts	163
E.2	Hypothetical Spacecraft	164
E.3	Envisat	165
Bibliography		167

List of Figures

2.1	Earth-Centered Inertial Frame	17
2.2	Earth-Centered Earth-Fixed Frame	18
2.3	Earth-Centered Orbital Frame	20
2.4	Satellite-Centered Orbital Frame	21
2.5	Body-Fixed Frame	22
2.6	Globally-Averaged Atmospheric Density at 400 km for 2014	38
2.7	LAGEOS-2 Surface Geometry Model	42
2.8	Evolution of LAGEOS-2 Spin Parameters in Inertial Frame	44
2.9	Evolution of LAGEOS-2 Spin Axis in ECO Frame from Simulation	45
2.10	Evolution of LARES Spin Parameters in Inertial Frame	47
2.11	Evolution of LARES Spin Axis in ECO Frame from Simulation	48
2.12	Evolution of Ajisai Spin Parameters in Inertial Frame	49
2.13	Evolution of Ajisai Spin Axis in ECO Frame from Simulation	50
3.1	MASTER-2009 Impactor Mass Flux Distribution	61
3.2	MASTER-2009 Impact Velocity Flux Distribution	61
3.3	MASTER-2009 3D Impact Direction Flux Distribution	62
3.4	PDF for Time Between Collisions from MASTER-2009	63
3.5	Flowchart of the Algorithm for Attitude Propagation from Hypervelocity Impacts	73
3.6	Simplified Model of Envisat in Body Frame	75
3.7	Cumulative Distribution Function of Angular Momentum Magnitude Transfer for (a) Envisat and (b) a HAMR object	76
3.8	Evolution of PDF for Envisat's Rotational Kinetic Energy under Observed Initial Conditions: (a) with Momentum Enhancement and (b) without	76
3.9	Evolution of PDF for Envisat's Rotational Kinetic Energy for Random Initial Orientation: (a) with Momentum Enhancement and (b) Without .	78

3.10 Evolution of PDF for the HAMR Object's Rotational Kinetic Energy: (a) with Momentum Enhancement and (b) without	80
3.11 Flowchart of the Algorithm for Coupled Orbit-Attitude Propagation from Hypervelocity Impacts	81
3.12 SMA PDF Evolution for Envisat (a) with Momentum Enhancement and (b) without	82
3.13 SMA PDF Evolution for the HAMR Object	83
4.1 Tessellated Model of Envisat's Surface Geometry in the Body-Fixed Frame	90
4.2 Schematic of Angular Motions Experienced by Envisat	92
4.3 Examples of the Evolution of Envisat's Angular Motions for the Baseline Scenario	94
4.4 Evolution of Envisat's Angular Motion for the Four-Year Propagation . .	95
4.5 Evolution of Envisat's Angular Motions for Supplemental Simulations .	98
4.6 Reproduction of Envisat's Angular Velocity Estimates as a Function of Time from Observational Studies	100
4.7 Long-Term Evolution of Envisat's Angular Velocity as a Function of Time	104
5.1 ECO and the Orbital Coordinate System [7]	113
5.2 Observations of TOPEX/Poseidon a) Spin Period, b) Elevation, and c) Azimuth in the Orbital Coordinate System [7]	113
5.3 Observations of TOPEX/Poseidon Angular Velocity and Spin Axis Orientation in the ECO Frame	114
5.4 TOPEX/Poseidon Surface Geometry Model with Solar Panel Orientation at: a) 0° and b) 285°	117
5.5 D-SPOSE Results Under the Gravity-Gradient Torque vs. Observations .	118
5.6 Simulations Including Radiation Pressure and Varying I^*	119
5.7 D-SPOSE Results for $I_x < I_z$	119
5.8 Best Fit Simulations Varying I_z , M , and γ vs. Observations	120
5.9 Simulations with Internal Energy Dissipation	121
5.10 Evolution of the System Energy	124
5.11 Predictions of TOPEX/Poseidon's Spin Motion	125
5.12 Evolution of the Spin Axis Orientation in ECO Frame	126
D.1 Surface Reference Frame	152

List of Tables

2.1	List of Classical Orbital Elements	19
2.2	Two-Line Element Set Content	20
2.3	External Perturbations and Environmental Models	24
2.4	Parameters of the Spherical Geodetic Satellites	42
2.5	Initial Conditions for Spherical Geodetic Satellites	43
3.1	Ejecta Model Parameters	72
3.2	Envisat Simulation Results	77
3.3	HAMR Simulation Results	79
4.1	Influence of Initial Conditions and Perturbation Model Parameters . . .	97
4.2	Summary of Envisat Angular Motion Studies	99
5.1	Characteristics of Spin Axis Orientation Points where $\dot{\lambda} = 0$	115
5.2	Parameters of Best Fit Simulations	120

Abbreviations

ADR	Active Debris Removal
AIUB	Astronomical Institute University of Bern
ASI	Agenzia Spaziale Italiana
AU	Astronomical Unit
BGS	British Geological Survey
BLITS	Ball Lens In The Space
CCR	Corner Cube Reflector
CDF	Cumulative Distribution Function
CERES	Clouds and the Earth's Radiant Energy System
CHAMP	CHAllenging Minisatellite Payload
CLOUD	Population CLOUDs
CLS	Collecte Localisation Satellites
CNES	Centre National d'Études Spatiales
COLL	COLLision Fragments
COPUOS	Committee On the Peaceful Uses of Outer Space
COSPAR	Committee On SPAce Research
D-SPOSE	Debris SPin/Orbit Simulation Environment
DGC	Defence Geographic Centre
DTM	Drag Temperature Model
ECEF	Earth-Centered Eeart Fixed
ECI	Earth-Centered Inertial
ECMWF	European Centre for Medium-Range Weather Forecasts
ECO	Earth-Centered Orbital
EGM	Earth Gravitational Model
EJEC	EJECta Particles
ESA	European Space Agency
ESOC	European Space Operations Centre
ESTEC	European Space Research and TECnology Centre

EXPL	EXPLosion Fragments
GEO	Geosynchronous Equatorial Orbit
GMST	Greenwich Mean Sidereal Time
GOCE	Gravity Field and Steady-State Ocean Circulation Explorer
GRACE	Gravity Recovery And Climate Experiment
HAMR	High Area-to-Mass Ratio
HWM	Horizontal Wind Model
IADC	Inter-Agency Space Debris Coordination Committee
IAGA	International Association of Geomagnetism and Aeronomy
IDS	International DORIS Service
IGRF	International Geomagnetic Reference Field
ILRS	International Laser Ranging Service
ISAR	Inverse Synthetic Aperture Radar
ISS	International Space Station
OTA	In-Orbit Tumbling Analysis
JAXA	Japan Aerospace EXploration Agency
JB	Jacchia-Bowman
LAGEOS	LAser GEodynamic Satellite
LARASE	LAser RAnged Satellites Experiment
LARES	LAser RElativity Satellite
LASSOS	LArase Satellites Spin MOdel Solutions
LEO	Low-Earth Orbit
LMRO	Launch and Mission Related Objects
LOSSAM	LageOS Spin Axis Model
MASTER	Meteoroid And Space Debris Terrestrial Environment Reference
MLI	Multi-Layer Insulation
MSIS	Mass Spectrometer and Incoherent Scatter
MTBG	MeTeoroid BackGround
NAKD	Sodium (NA) - Potassium (K) Alloy Droplets
NASA	National Aeronautics and Space Administration
NCEI	National Centers for Environmental Information
NGA	National Geospatial-Intelligence Agency
NOAA	National Oceanic and Atmospheric Administration
NORAD	NORth American Aerospace Defense Command
NRL	Naval Research Laboratory

ORDEM	ORbital Debris Engineering Model
PAFL	PAint FLakes
PDF	Probability Density Function
PEDAS	Panel on Potentially Environmentally Detrimental Activities in Space
RA	Right Ascension
RKDP	Runge-Kutta Dormand-Prince
RRA	Retro Reflector Array
SCO	Satellite-Centered Orbital
SDE	Stochastic Differential Equation
SGP	Simplified General Perturbations
SLR	Satellite Laser Ranging
SMA	Semi-Major Axis
SRM	Solid Rocket Motor
SRMD	Solid Rocket Motor Dust
SRMS	Solid Rocket Motor Slag
SS	Supplemental Simulation
SSN	Space Surveillance Network
TEME	True Equator Mean Equinox
TIRA	Tracking and Imaging RAdar
TLE	Two-Line Element
UN	United Nations
WMM	World Magnetic Model
YORP	Yarkovsky-O'Keefe-Radzievskii-Paddack

Physical Constants

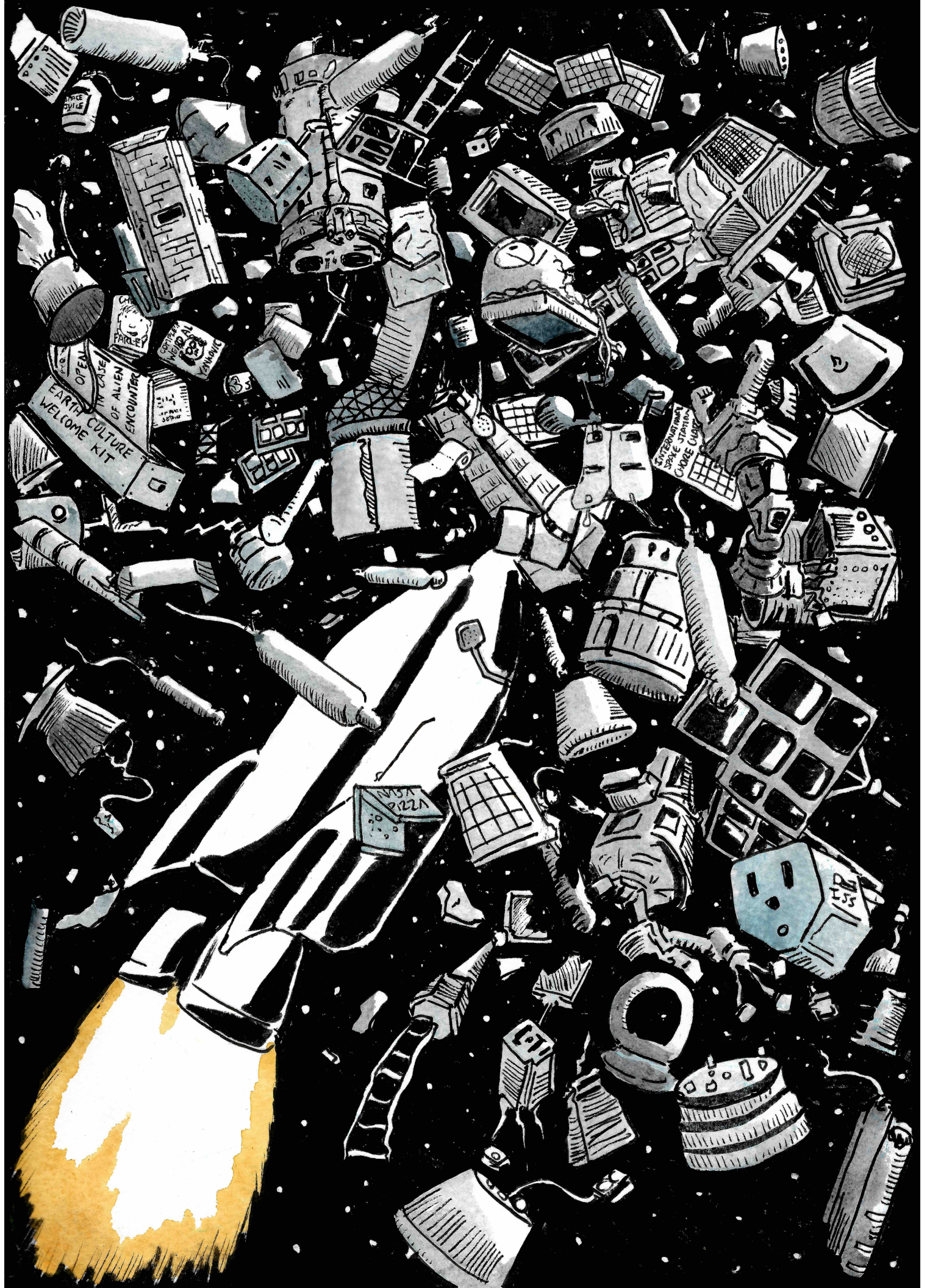
Astronomical Unit	$a_u = 1.495978707 \times 10^{11} \text{ m}$
Earth Angular Velocity	$\omega_E = 7.29211514670698 \times 10^{-5} \text{ rad s}^{-1}$
Earth Equatorial Radius	$R_E = 6378.1363 \text{ km}$
Earth Gravitational Parameter	$\mu = 3986004.418 \times 10^8 \text{ m}^3 \text{ s}^{-1}$
Earth Mean Reference Spherical Radius	$a_M = 6371.2 \text{ km}$
Moon Gravitational Parameter	$\mu_2 = 4902.799 \times 10^9 \text{ m}^3 \text{ s}^{-1}$
Solar Radiation Constant	$S_R = 1361 \text{ W m}^{-2}$
Speed of Light	$c = 2.99792458 \times 10^8 \text{ m s}^{-1}$
Sun Gravitational Parameter	$\mu_1 = 1.32712428 \times 10^{20} \text{ m}^3 \text{ s}^{-1}$

Symbols

A	surface area	m^2
a	semi-major axis	m
\mathbf{a}	acceleration	$\text{m}\cdot\text{s}^{-2}$
\mathbf{B}	magnetic field	T
$C_{l,m}$	spherical harmonic coefficient	
C_r	reflectivity coefficient	
c_D	drag coefficient	
\mathbf{C}	rotation matrix	
\mathbf{c}_p	center of pressure position	m
d	Earth surface element-satellite distance	m
e	eccentricity	
F	cumulative distribution function	
f	probability density function	
\mathbf{f}	force	N
g_n^m	Gauss coefficient	
h_n^m	Gauss coefficient	
\mathbf{h}	angular momentum	$\text{kg}\cdot\text{m}^2\cdot\text{s}^{-1}$
\mathbf{I}	inertia tensor	$\text{kg}\cdot\text{m}^2$
i	inclination	rad
K	kinetic energy	J
k_d	damping constant	$\text{kg}\cdot\text{m}^2\cdot\text{s}^{-1}$
M	ejecta mass	kg
m	mass	kg
\mathbf{M}	magnetic tensor	$\text{kg}^{-1}\cdot\text{m}^2\cdot\text{s}^3\cdot\text{A}^2$
N	Poisson process	
\mathbf{n}	inward surface normal	
\mathbf{n}_O	negative orbit normal	
P	probability	

$P_{l,m}$	Legendre functions	
P_n^m	Schmidt normalized associated Legendre functions	
$P^{m,n}$	Gauss functions	
\mathbf{p}	linear momentum	$\text{kg}\cdot\text{m}\cdot\text{s}^{-1}$
\mathbf{q}	quaternion	
r	geocentric distance	m
\mathbf{r}	position	m
\mathbf{r}_1	Sun position	m
\mathbf{r}_2	Moon position	m
$S_{l,m}$	spherical harmonic coefficient	
\mathbf{s}	incident light direction	
t	time	s
U	gravitational potential	$\text{J}(\cdot\text{kg}^{-1})$
V	geomagnetic potential	$\text{V}\cdot\text{s}\cdot\text{m}^{-1}$
v	velocity	$\text{m}\cdot\text{s}^{-1}$
\mathbf{v}	velocity vector	$\text{m}\cdot\text{s}^{-1}$
W	work	J
X	stochastic process	
Y	compound Poisson process	
α	size distribution parameter	
α_{alb}	albedo coefficient	
α_{ir}	emissivity coefficient	
α_p	surface normal - incident flow angle	rad
β	surface normal - incident light angle	rad
β_m	mass partitioning parameter	
γ	Earth surface element normal - satellite angle	rad
δ	size	m
θ	latitude	rad
θ_{DEC}	declination	rad
θ_{ECO}	ECO declination	rad
θ_{elev}	elevation	rad
θ_{GMST}	Greenwhich mean sidereal time	s (rad)
λ	longitude	rad
λ_{ECO}	ECO right ascension	rad

λ_m	mass proportionality factor	
λ_{RA}	right ascension	rad
μ_r	relative permeability	
ν	true anomaly	rad
ξ_k	jump sizes	
ρ	atmospheric density	$\text{kg}\cdot\text{m}^{-3}$
σ	conductivity	$\text{S}\cdot\text{m}^{-1}$
σ_a	absorption coefficient	
σ_{rd}	diffuse reflection coefficient	
σ_{rs}	specular reflection coefficient	
σ_θ	width of zenith distribution	rad
σ_ϕ	width of azimuth distribution	rad
τ_k	jump times	s
τ	torque	$\text{N}\cdot\text{m}$
ϕ	colatitude	rad
ϕ_{alb}	reflected radiation photon flux	$\text{W}\cdot\text{m}^{-2}$
ϕ_{azi}	azimuth	rad
ϕ_{ir}	emitted radiation photon flux	$\text{W}\cdot\text{m}^{-2}$
ϕ_R	radiation photon flux	$\text{W}\cdot\text{m}^{-2}$
ϕ_{solar}	direct solar radiation photon flux	$\text{W}\cdot\text{m}^{-2}$
Ψ	surface normal - impactor angle	rad
ψ	Earth surface element normal - Sun angle	rad
ψ_s	Earth shadow function	
Ω	right ascension of the ascending node	rad
ω_{aop}	argument of perigee	rad
ω	angular velocity vector	$\text{rad}\cdot\text{s}^{-1}$
ω_d	damper angular velocity	$\text{rad}\cdot\text{s}^{-1}$
I, J, K	Earth-Centered Earth-Fixed frame axes	
X, Y, Z	Earth-Centered Inertial frame axes	
x, y, z	Body-Frame axes	
x_c, y_c, z_c	collision frame axes	
x_o, y_o, z_o	Earth-Centered Orbital frame axes	
x_s, y_s, z_s	surface frame axes	
$x_{\text{sco}}, y_{\text{sco}}, z_{\text{sco}}$	Satellite-Centered Orbital frame axes	



John Lapsley

"Space Junk"

Ink on paper

Chapter 1

Introduction

October 4, 1957 is usually considered as the day of the launch of the first artificial Earth satellite, Sputnik 1, an incredible feat identifying a landmark moment of the Cold War era spaceflight rivalry; to a few people, however, it is now known as the day humans began polluting Space. In the last sixty years, over six thousand launches have put satellites in orbit, the data from which has led to just as many, if not more, groundbreaking scientific achievements. There is no denying that the Space Race and the following international aerospace cooperation has benefited all areas of life on Earth, but all the while stakeholders rarely thought twice of the lasting effect the accumulation of orbiting objects would have on the future of the near-Earth environment.

1.1 Space Debris Environment

The United States Space Surveillance Network (SSN) has continuously detected and catalogued artificial Earth satellites since that memorable day over six decades ago. As of July 2018, 19,137 objects are being tracked orbiting our planet, a number that has been steadily increasing since 1957, only a couple thousand of which are active mission payloads [10, 11]. Recent model estimates have put the total number of objects in orbit greater than 1 cm at 670,000, and it is thought that more than 170 million particles larger than 1 mm circle Earth [12]. Potential collisions between active satellites and these *space debris* are becoming an increasing threat to space operations [13]. Indeed, although collisions with *large* debris (>10 cm) causing major satellite break-ups occur at extremely low frequencies, impacts with smaller debris and micrometeoroids are common and have a significant influence on space missions [14, 15]. Occurring at speeds averaging $10\text{-}20 \text{ km s}^{-1}$, impacts from μm -sized particulates occur frequently, not only

deteriorating solar cells and other satellite surfaces, but also damaging spacecraft subsystems through plasma effects such as electrostatic discharges and electromagnetic interference [15].

The population of space debris is most critical in low-Earth orbit (LEO), below 2000 km, where it has been estimated that even if no new missions were launched the debris population would continue to increase gradually due to collisions for the next 200 years [16]. This warning has since been amplified due to two catastrophic events that have caused the debris population in LEO to escalate even further. On January 11, 2007, China intentionally launched an anti-satellite missile to destroy its Fengyun-1C weather satellite, dramatically increasing the number of tracked objects by 2800 (or 25%) in the 800-1000 km orbital altitude range [17]. In addition, the first-ever collision between intact satellites occurred on 10 February 2009, when the inactive Russian Cosmos 2251 satellite and the operational American Iridium 33 satellite, predicted to encounter a close-approach of 584 m, impacted at an altitude of 770 km, leading to over 2300 extra tracked fragments in orbit [14, 18]. Hundreds of fragmentation events, mostly explosions of satellites and upper stages, have also contributed to this uncontrolled growth, leading to concentrated debris densities in the 800-1000 km and 1400 km altitude range [19]. Moreover, geosynchronous equatorial orbit (GEO), an orbital regime at an altitude of 35,786 km vital for international communications, has become a cemetery for every satellite launched and left there since 1963 without the possibility of natural decay [20].

Defunct satellites and their fragmentation particles aren't the only pieces of debris orbiting Earth, however. First, other launch and mission-related objects (LMRO) constitute the non-fragment portion of the tracked debris population. These consist mostly of West Ford needles, approximately 480 million short pieces of thin copper wire released during the West Ford Project experiments in the 1960s at a mean altitude of 3650 km with the aim to create an artificial ionosphere for communications purposes [21]. This environmental disaster lead to the creation of the Committee on Space Research (COSPAR) Panel on Potentially Environmentally Detrimental Activities in Space (PEDAS). Second, exhaust particles from solid rocket motors (SRM) also contribute greatly to the total debris population [22]. During SRM firings, Al_2O_3 particles are expelled from two generation mechanisms: SRM dust (SRMD), μm -sized particles continuously generated throughout the engine burn, and SRM slag (SRMS), much larger particles leaving the nozzle towards the end of the burn. Third, sodium-potassium alloy droplets (NAKD) come from the ejected liquid coolant of nuclear reactors, mostly

restricted to orbits with an inclination of 65° and an altitude of 900-950 km, contributing to the debris population in the mm and cm scale [22]. Fourth, surface degradation particles, paint flakes (PAFL), also populate LEO orbits. Caused by reaction of satellite surfaces with atomic oxygen, thermal cycling creating cracks, and ultraviolet radiation exposure, these debris objects are thought to measure 2-200 μm [22]. Fifth, ejecta (EJEC), or secondary debris, measuring up to a few millimetres, come from the ejection of particles during hypervelocity impacts between primary debris and satellites [22]. Finally, a new source of debris was recently discovered in GEO-like highly eccentric orbits. These objects were attributed to multi-layer insulation (MLI) debris with high area-to-mass ratios (HAMR), thought to be material shed off old satellites [23].

Models do exist to evaluate the collisional risk of the current population and to predict the future near-Earth environment; nevertheless, it is very difficult to accurately estimate the evolution of the debris population due to large uncertainties. The National Aeronautics and Space Administration (NASA) and the European Space Agency (ESA) developed their own engineering models, known as the Orbital Debris Engineering Model (ORDEM) and the Meteoroid and Space Debris Terrestrial Environment Reference (MASTER) model, respectively, which evaluate the current debris population and estimate the debris flux a satellite in a particular orbit would encounter over a period of time using independent data sources and techniques [22, 24, 25]. They are mostly empirically-based, validated using in-situ data from various returned spacecraft surfaces as well as observational telescope and radar data, and include a historical data set as well as projection estimates. MASTER and ORDEM also make use of debris generation models predicting the evolution of the space debris environment: ESA's Debris Environment Long-Term Analysis (DELT) model and NASA's LEO-to-GEO Environment Debris (LEGEND) model. These tools have become indispensable for spacecraft designers, operators and debris researchers looking for a solution to the space debris problem.

In any case, the hazards arising from the debris population inflation are clear, as are the risks and costs associated with potential collisions. The popular response to the issue, though, is lingering, in an echo of the fabled "boiling frog" anecdote: put a frog in a pot of boiling water and it will jump out; put it in cool water and heat it gradually, however, and it will remain in place and be boiled alive. Governments and companies are slow to react to the changing pace of space debris pollution, but the threat is present, and stakeholders need to be convinced that acting now will benefit them in the long run [26].

1.2 Mitigation and Remediation

In 1978, a disaster scenario was theorized, now known as the Kessler syndrome, where the density of space debris would grow in a cascading effect due to collisions, making future space missions impossible [27]. The growing concern of this becoming reality has led space agencies to develop guidelines to limit the future generation of space debris from operations [28, 29, 30]. Furthermore, research into finding ways to remove current space debris has been plentiful. Such processes are known as Active Debris Removal (ADR) and although still in its early stages due to technical, financial and legal reasons, the idea of implementing ADR has been thoroughly investigated [31, 32].

1.2.1 International Guidelines

The Scientific and Technical Subcommittee of the United Nations (UN) Committee on the Peaceful Uses of Outer Space (COPUOS) first added space debris as an official agenda item in 1994. The Inter-Agency Space Debris Coordination Committee (IADC), grouping most of the world's leading space agencies, achieved a major milestone when they presented their Space Debris Mitigation Guidelines to UNCOPUOS in 2002 [29]. Since then, NASA, ESA and other space agencies have each published their set of space debris mitigation guidelines. While France is the only country so far to have implemented these guidelines in a legally-binding form with the French Space Operations Act in 2010, supervised by the Centre National d'Études Spatiales (CNES), everywhere else on Earth, they remain simple recommendations.

The IADC mitigation guidelines can be split into four objectives: the limitation of debris released during normal satellite operations; the minimization of the potential of on-orbit break-ups; post-mission satellite disposal; and the prevention of on-orbit collisions [29]. The first relates to space debris released during manoeuvres or experiments where particulates could be ejected into orbit. The second category concerns explosions due to: stored energy from batteries, residual propellants and high pressure vessels; risky operations that could lead to accidental fragmentation; or intentional destruction. The guidelines recommend spacecraft systems to be designed to limit these risks. The third involves removing satellites from already crowded areas in LEO and GEO. For LEO satellites, the natural decay lifetime after operations should be limited to

25 years, without any risk of casualties on the ground during re-entry. The recommendation for GEO is to place satellites in graveyard orbits with a minimum perigee more than 235 km over the geostationary altitude. Finally, during the mission design and development of new projects, the risk of accidental collisions should be estimated and minimized, while spacecraft should be designed in such a way to limit the potential damage if impacts with small debris occur.

Compliance to these guidelines, though, is still imperfect. Only 30-60% of the mass of LEO payloads that have reached end-of-life recently do so in orbits which comply with the 25-year rule; and 15-20% of non-compliant LEO payloads attempt to manoeuvre to compliant orbits, but only 5% succeed [33]. Compliance for rocket bodies has greatly improved due to the new practice of controlled re-entries: previously, a little over 20% of rocket body mass reached end-of-life in orbits adhering to the 25-year rule; that number is now at 70% [33]. In GEO, approximately 90% of recent end-of-life payloads attempted to comply with the mitigation guidelines, and 80% achieved it [33]. As these numbers show, much improvement is still required for global adherence to these recommendations. When the nominal duration of a mission is exceeded but the satellite is still fully operational, operators rarely want to retire their spacecraft in a compliant orbit and usually proceed to extend the mission time-line. While this provides further use to the satellite, it also increases the risk of unwanted mission failures and loss-of-contact in the current non-compliant orbit. One possible solution to comply with the mitigation requirements in these cases would then be through ADR.

1.2.2 Active Debris Removal

ADR consists of developing a mission to launch a removal spacecraft that would rendezvous with a large space debris target, analyze its motion from a distance, capture it using one of a variety of possible techniques, stabilize the target's rotation, and finally remove it from orbit. It has been found that 5-10 large targets from critical orbits should be removed per year simply to stabilize the debris population in the next 200 years [34]. One of the key issues is selecting the optimal target. Multiple indices have been developed to identify potential targets based on their mass, orbit, risk of fragmentation or the risk they would pose on others if they fragmented [35, 36, 37]. Missions which would consist of removing several targets one after the other by disposing them in sequence in low-altitude orbits have also been considered, the decisive parameter in this case being a similar orbital inclination [38]. Using either one of these methods,

several large debris are recurrent: the Soviet SL-16 upper stages, the French Ariane 4 rocket bodies, and the European Earth-observing satellite Envisat.

Techniques to capture such large targets have been widely studied and multiple examples of capture processes have been considered: tentacles, one or multiple robotic arms, tethered nets, or harpoons [32]. Similarly, various removal methods are possible: drag augmentation systems which would increase the surface area of the target and therefore increase aerodynamic drag; an electrodynamic tether making use of the Earth's magnetic field; solar sails using the Sun's radiation; laser systems pulsating beams to reduce the target's velocity; or a high-velocity ion beam from an ion beam shepherd spacecraft [32]. All of these techniques have their benefits and drawbacks, and some of them have already been or are currently being tested or planned in actual missions.

In December 2016, the Japan Aerospace Exploration Agency (JAXA) launched a spacecraft containing an experimental electrodynamic tether to demonstrate its de-orbiting technology; however, the deployment of the tether was unsuccessful. Furthermore, a consortium of European institutions launched in June 2018 the RemoveDEBRIS platform from the International Space Station (ISS), a demonstration mission aimed at testing multiple ADR technologies including the net capture of a spinning cubesat, a vision-based navigation experiment, a harpoon, and an inflatable dragsail [39]. A start-up, called Astroscale, is also developing an end-of-life spacecraft for ADR purposes. Its technology demonstration mission, ELSA-d, is planned for 2020; it will release a target and proceed to analyze its rotational motion, match it, perform a magnetic capture, and de-orbit by propulsion [40]. In addition, the CleanSpace One project, led by the École Fédérale Polytechnique de Lausanne in Switzerland, is aiming to recapture its defunct cubesat SwissCube using a tentacle structure [41]. Finally, ESA has been planning to remove its defunct spacecraft Envisat that it lost contact with in April 2012. Now considered as a primary target for ADR, ESA has been developing its e.Deorbit mission for launch in 2024, consisting of a robotic capture mechanism [42]. These are just a few of the missions and technologies being developed as interest in the issue has seen a reassuring increase, even in the last year or so.

1.3 Satellite Rotational Dynamics

ADR efforts, however, may encounter potential challenges in orbit. Uncontrolled objects like debris targets experience multiple perturbations that arise in the space environment which may lead to tumbling. Stabilizing and capturing a large rotating debris can therefore pose difficulties and an ADR mission can only succeed if an accurate estimation of the target's rotational state is obtained prior to launch. In this light, multiple observation campaigns of high-value targets in densely populated orbits are underway, and, in parallel, modelling efforts are trying to characterize the long-term evolution of the attitude dynamics of defunct satellites, which, combined, will benefit the understanding and forecasting of the dynamics of these possible targets.

1.3.1 Observing Inoperative Spacecraft

Multiple observation techniques can provide the community with estimates of a space object's rotational motion. Three methods are currently being used to estimate the angular velocity and spin axis orientation of observed targets: satellite laser ranging (SLR), photometric measurements, or light curves, as well as inverse synthetic aperture radar (ISAR) images.

SLR consists of reflecting ground-based lasers on retroreflectors on-board a satellite to estimate precisely its position in orbit. When a satellite is rotating, the position of the reflector with respect to the satellite's center of mass will vary, inducing oscillations in the distance from the ground station to the reflector, and high-repetition-rate (kHz) SLR can therefore provide a measurement of the spin period and the spin axis orientation [43]. The International Laser Ranging Service (ILRS) is a collaboration between over 40 stations providing support to geodetic and geophysical research activities through their SLR campaigns [44]. Although usually used to observe active satellites, some stations have also focused on space debris objects for the estimation of their rotation. In 2013, after a request from ESA, a special ILRS campaign dedicated to observing Envisat began; 15 SLR stations started to regularly track and obtain high-repetition-rate data from the large space debris [43]. From this, an initial estimate of its attitude motion was obtained. Similarly, another large space debris of interest, namely the French-American Ocean Topography Experiment TOPEX/Poseidon, inoperative since 2006, became a target of a new campaign initiated by the Graz SLR station in Austria in 2014 followed by the entire ILRS Space Debris Study Group in 2015 [7].

A second widely-used observation technique is by means of photometric measurements, also called light curves. Objects illuminated by the Sun will reflect light which can be captured by observatories on the ground. From repeated peaks in the intensity of the signal received, an estimate of the object's spin period can be obtained [45]. Historically, this technique was mainly used for the analysis of the rotation of asteroids but is now gaining interest from the space debris community. Envisat has been of popular interest, as well as TOPEX/Poseidon, but the main benefit of this method is that other defunct satellites without retroreflectors can also be investigated [46, 47]. The Astronomical Institute at the University of Bern (AIUB) has been cataloguing space debris observations from light curves since 2007 using its 1-meter telescope at the Zimmerwald Observatory [48]. Other stations have also investigated and determined the rotation rate of a diverse set of debris, including many retired box-wing geosynchronous satellites [49, 50, 51, 52].

The final observation method has only recently started being used to calculate the rotational parameters of defunct spacecraft. ISAR is a technique consisting of generating a two-dimensional snapshot of an object using radar imaging. After obtaining multiple consecutive images detailing the target's attitude evolution, an estimate of the rotational parameters can be determined. This is an algorithmically complex procedure dealing with a multitude of computer vision issues [53]. The largest study to date of a space debris object has been one of Envisat using the Tracking and Imaging Radar (TIRA) in Germany [54]. Using these three observation methods in parallel has been shown to be advantageous for obtaining more precise estimates of a target's rotational motion [55]. Combining these observational efforts with theoretical and computational work therefore becomes of paramount importance to obtain a complete understanding of the attitude dynamics of large space debris.

1.3.2 Modeling Efforts

Studying the long-term rotational dynamics of uncontrolled space objects is a relatively new field of research. Since most operational satellites are attitude-controlled and the influence of external forces are compensated, information on the cumulative effect of environmental perturbations on the rotational dynamics of spacecraft was not a priority for mission planning. For tumbling space debris in uncontrolled attitude states, however, small torques will add up and alter the object's attitude dynamics in the long run.

The dominant torques affecting a satellite are highly dependent on its geometry, orbit, inertia parameters and material properties [56, Ch. 8]. The most prominent torques in the near-Earth environment include the gravity-gradient torque, arising from variations in the Earth's gravitational field over the body of the debris, radiation torques, as photons exert pressure on surfaces of the debris, the aerodynamic torque, due to aerodynamic drag at lower altitudes, and magnetic torques, coming from the interactions between the orbiting debris and Earth's magnetic field [56, Ch. 8].

Much recent effort has been made in trying to understand the relationship between the conductive surfaces of spinning spacecraft and the Earth's magnetic field [57, 58, 59]. Early studies of the influence of the Earth's gravitational field on the attitude of free satellites have also contributed to our understanding of the rotational dynamics of space debris [60, 61]. Research into the effect of both gravitational and magnetic torques on satellites in specific orbits, namely sun-synchronous polar orbits, have been of much interest due to their high debris density [59, 62]. It has been found that under the influence of these two torques, satellites in these orbits will follow a clear process consisting of three stages: a transient process to a flat spin due to internal energy dissipation, where the spin axis is aligned with the satellite's major principal axis of inertia; an exponential deceleration due to the eddy-current torque; and a chaotic transition to a final regime that will depend on the satellite's properties [62]. Furthermore, the rotational motion of Envisat, which is in its second deceleration stage as described above, has been investigated in more detail, and its angular velocity decay rate has been determined using a novel form of the eddy-current torque [58].

An important class of environmental torques for box-wing satellites is radiation torques. Due to the asymmetry of the satellite geometry, the radiation coming from the Sun, as well as emitted and reflected radiation from the Earth can have a substantial effect on a satellite's orientation and spin [7]. Furthermore, the Yarkovsky-O'Keefe-Radzievskii-Paddack (YORP) effect, consisting of absorbed sunlight being re-emitted as thermal radiation, can have significant influence on these types of satellites as well. Although historically used to explain the changes in the angular velocity of asteroids, recent research has applied this effect to defunct satellites and work on this is still active; more specifically, the YORP effect has been used to explain the observed behaviour of GOES satellites [63, 64].

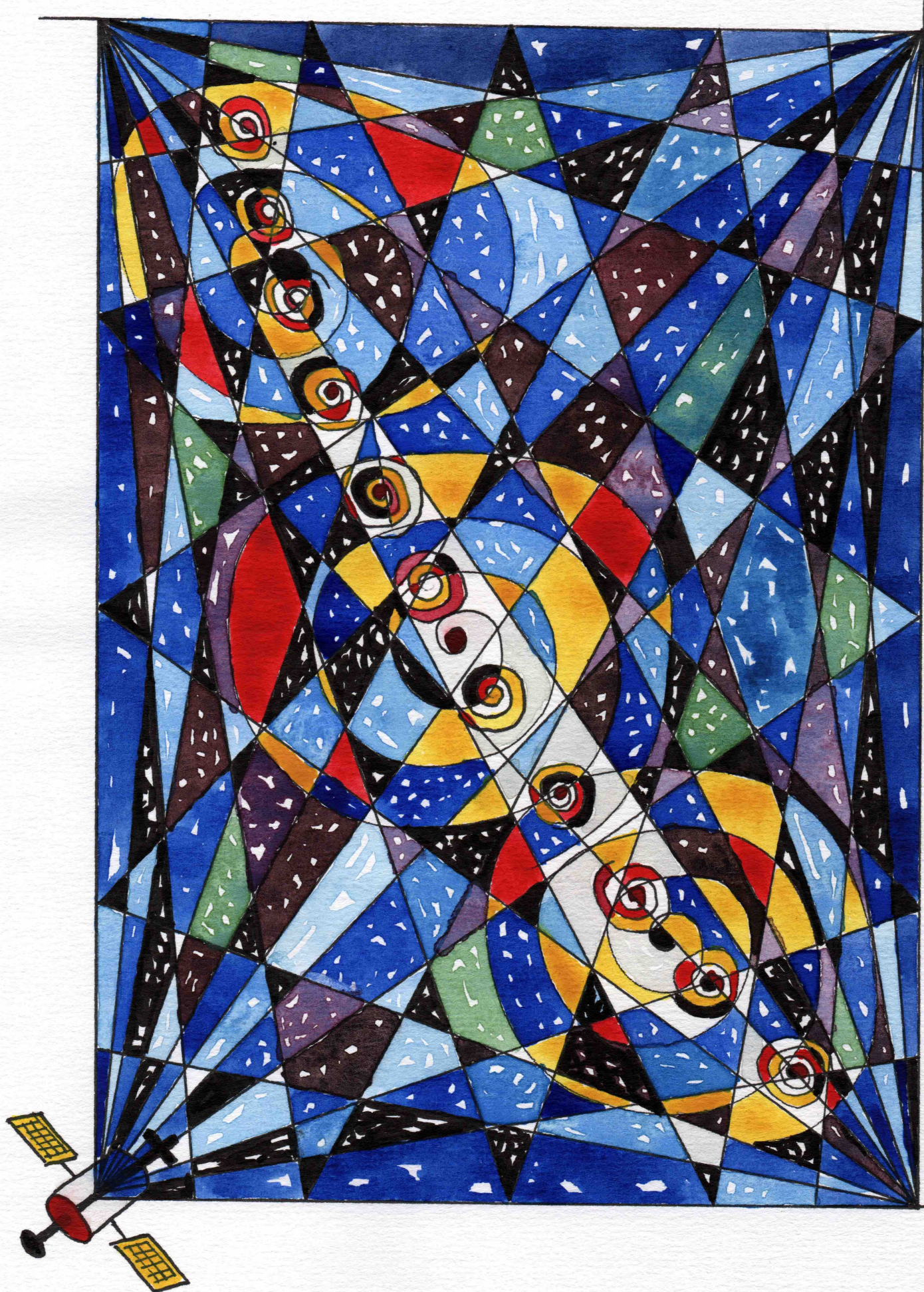
Coupling the attitude motion of uncontrolled space objects to their orbital motion can also be used to more accurately determine or estimate their orbital evolution. The recently discovered HAMR objects have been found to be highly influenced by solar

radiation pressure, which affects their orbit greatly in a very attitude-dependent manner [65, 66]. Similarly, space weather related effects can have a noticeable impact on HAMR objects due to the attitude dependence of the spacecraft charging from interaction with different currents in the plasma surrounding Earth [67].

To comprehensively address the modeling issues, ESA has recently contracted the development of a comprehensive coupled orbit-attitude model for large space debris called *iOTA* (In-Orbit Tumbling Analysis). Preliminary results with this model, which is still under development and not open to the public, have been published, focusing on reproducing synthetic measurements such as light curves and SLR residuals to compare to observations [68]. The goal of the work on *iOTA* is to present short-term simulations to help observers validate their measurements and to provide ADR missions with quick estimates of their target’s rotational dynamics during the mission, as well as medium- to long-term predictions for the preparation of such a mission [68].

1.4 Thesis Outline

The format of this thesis is therefore as follows. First, a novel, publicly available, and comprehensive coupled orbit-attitude propagator developed for space debris remediation purposes, entitled the Debris SPin/Orbit Simulation Environment (D-SPOSE), will be outlined in Chapter 2. The various perturbations considered will be detailed, its mode of operation will be described, and a validation of the tool will be performed. Chapter 3 will then go through the framework to include a perturbation not investigated to date, namely the effect of the bombardment of small debris and micrometeoroids through hypervelocity impacts on the orbital and attitude motion of large space debris. Chapter 4 will apply D-SPOSE to the favoured ADR target Envisat; its complex attitude dynamics will be investigated and recommendations will be put forth for obtaining better future estimates of its rotational parameters from observations. Chapter 5 will be a second case study of another large defunct spacecraft and space debris of interest, TOPEX/Poseidon. Its rotational motion will be analyzed in detail making use of D-SPOSE. The spacecraft’s moments of inertia and magnetic properties will be identified from observations as values of these parameters are completely missing, making it impossible to forecast its future motion. Finally, Chapter 6 will summarize the contributions of this thesis and will provide suggestions for future work in this research area.



8402/60 S&B

Pierre Sagnières

"Tournebouling"

Watercolour on drawing paper

Chapter 2

D-SPOSE: Debris SPin/Orbit Simulation Environment

The capture and stabilization phases of Active Debris Removal (ADR) can only succeed if an accurate estimation of the target's rotational state is obtained prior to launch. In this light, a novel coupled orbit-attitude propagation tool called D-SPOSE was developed, the primary goal of which is the study of the long-term evolution of the attitude dynamics of large space debris. Containing the major torques that affect the attitude dynamics of spacecraft in orbit, the developed propagator will enable accurate analyses and predictions of the rotational motion of potential ADR targets before mission launch, benefiting future space debris remediation efforts.

Section 2.1 will first discuss the reference frames used and the equations governing the orbit and attitude dynamics of Earth satellites which are propagated numerically in D-SPOSE. Sections 2.2 and 2.3 will then go over the various gravitational and non-gravitational perturbations considered in D-SPOSE that satellites experience in orbit. The tool itself and its operating modes and inputs will be presented in Section 2.4. Finally, a validation of the tool will be performed in Section 2.5 by comparing simulation results to actual observations of the evolution of the attitude states of certain satellites for which an abundance of measurements exists.

2.1 Spacecraft Dynamics

2.1.1 Reference Frames

Various references frames and coordinate systems are used throughout this thesis and in the implementation of D-SPOSE to describe the effects of different external torques and accelerations. Keeping tabs on which reference frame is used under specific circumstances is important in order to correctly analyze results and describe physical phenomena.

Earth-Centered Inertial Frame

Multiple types of inertial frames exist in astrodynamics. For the study of Earth satellites, the most convenient choice is Earth-Centered Inertial (ECI) frames [1, Ch. 3 p. 151]. One commonly used ECI frame is J2000, which is defined by the Earth's mean equator and mean equinox on January 1, 2000 at noon. However, in D-SPOSE, a quasi-inertial frame, named the True-Equator Mean-Equinox (TEME) frame, is the selected frame in order to avoid tedious rotations and transformations leading to a potential build up of numerical errors. It was chosen as it corresponds to the reference frame of Two-Line Element sets (TLE) describing the position with time of space objects maintained by the the North American Aerospace Defense Command (NORAD) and used as input into D-SPOSE [69].

The TEME frame isn't truly inertial, however, and slowly rotates with time as the true equator shifts. Nevertheless, it was determined that currently a rate of change of approximately 0.005° per year occurs with respect to J2000. This was deemed negligible for studies of large space debris using D-SPOSE as the usual time scale is a decade.

In the inertial frame, it is useful to define the orientation of a vector by two angles. This notation will come in handy when discussing the spin axis of an object. Figure 2.1 shows the Earth in the inertial frame with the inertial X-axis, the inertial Y-axis, the inertial Z-axis and the two angles defining an arbitrary vector: the declination, θ_{DEC} and the right ascension, λ_{RA} .

Earth-Centered Earth-Fixed Frame

Although motion equations are propagated in an inertial frame, many environmental perturbations affecting satellites are dependent on the position of the satellite with

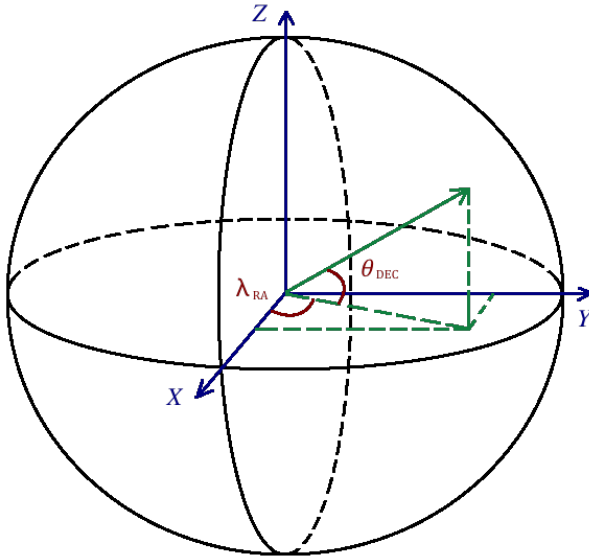


FIGURE 2.1: Earth-Centered Inertial Frame

respect to the Earth. The Earth's gravity and magnetic fields are fixed with Earth and atmospheric density models also contain latitudinal and longitudinal effects. For such cases, an Earth-Centered Earth-Fixed (ECEF) frame is selected [1, Ch. 3 p. 152]. In D-SPOSE, the usual ECEF frame is chosen, defined by the Earth's equator and the prime meridian. The equator is defined by the Earth-fixed I -axis and J -axis as seen in Fig. 2.2; the K -axis defines the North Pole; the prime meridian goes through the I -axis. In this frame one can define the position of an object by its geocentric distance, r , latitude, θ , longitude, λ , and colatitude, ϕ , as displayed in Fig. 2.2. Latitude is therefore defined by $\pm 90^\circ$ from the equator, with $+90^\circ$ being the North Pole. Longitude is defined Eastward from the prime meridian from 0 to 360° . Colatitude is defined as $\phi = 90^\circ - \theta$.

Rotating between an inertial and an Earth-fixed frame requires careful processing of the various effects contributing to the rotational motion of the Earth in the inertial frame, such as Earth's precession and nutation and the movement of the Pole with respect to Earth's surface. The process to do so is outlined in Vallado [1, Ch. 3, p. 203]. However, as these effects only have a large influence over a much longer time scale (centuries to millennia) than the ones used for space debris studies in D-SPOSE (years), a simple rotation from the inertial frame to the ECEF frame is done at every time step using the current Greenwich Mean Sidereal Time (GMST), θ_{GMST} in seconds

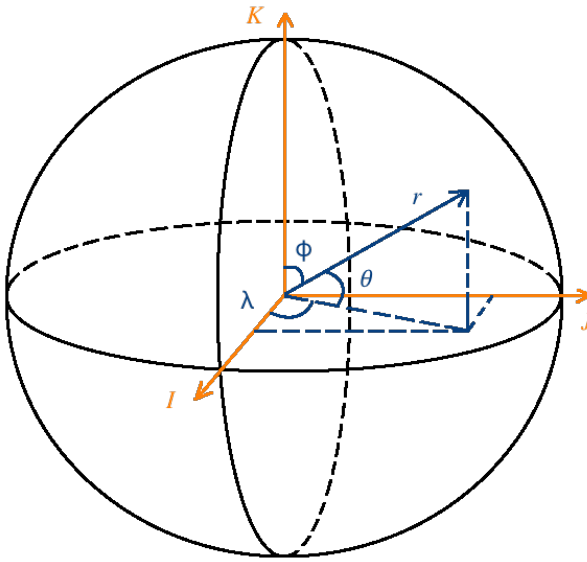


FIGURE 2.2: Earth-Centered Earth-Fixed Frame

[1, Ch. 3, p. 188]:

$$\theta_{GMST} = 67310.54841 + (876600.0 \times 3600.0 + 8640184.812866) T_{UTC} + 0.093104 T_{UTC}^2 - 6.2 \times 10^{-6} T_{UTC}^3 \quad (2.1)$$

where T_{UTC} is the time since the J2000.0 epoch on January 1, 2000 at 12:00 UTC. The rotation matrix to convert vectors between the two frames is determined as follows, after converting θ_{GMST} from seconds to radians [1, Ch. 3, p. 224]:

$$\mathbf{C}_{\text{ECI} \rightarrow \text{ECEF}} = \begin{bmatrix} \cos \theta_{GMST} & \sin \theta_{GMST} & 0 \\ -\sin \theta_{GMST} & \cos \theta_{GMST} & 0 \\ 0 & 0 & 1 \end{bmatrix} \quad (2.2)$$

A velocity transformation also needs to be performed as it involves a rotating frame [1, Ch. 3, p. 224]:

$$\mathbf{v}_{\text{ECI}} = \mathbf{C}_{\text{ECEF} \rightarrow \text{ECI}} (\mathbf{v}_{\text{ECEF}} + \boldsymbol{\omega}_E^\times \mathbf{r}_{\text{ECEF}}) \quad (2.3)$$

where $\boldsymbol{\omega}_E$ is the Earth's inertial angular velocity in the K (and Z) direction.

Orbital Elements and the Earth-Centered Orbital Frame

In orbital mechanics, six parameters, the orbital elements, characterize the shape and size of a satellite's orbit along with its position on that orbit. The classical set of orbital elements are the semi-major axis, a , defining the size of the orbit, the eccentricity, e , defining its shape, the inclination, i , the right ascension of the ascending node, Ω , the argument of perigee, ω_{aop} , the latter three defining the orientation of the orbit in the inertial frame, and the true anomaly, ν , defining the position of the satellite along the orbit. These are presented in Table 2.1. It is possible to switch between the position and velocity vector in the inertial frame and the orbital elements using a set of defined algorithms as presented in Vallado [1, Ch. 2, p. 112-120].

TABLE 2.1: List of Classical Orbital Elements

Symbol	Name	Unit
e	Eccentricity	
a	Semi-Major Axis	km
i	Inclination	rad
Ω	Right Ascension of the Ascending Node	rad
ω_{aop}	Argument of Perigee	rad
ν	True Anomaly	rad

As discussed previously, the initial orbit used as input into D-SPOSE is in the form of a TLE. Its format is very specific and has a rich heritage dating back to military operations in the 1960s. NORAD frequently publishes TLEs containing information on the epoch and orbital elements for the space objects contained in its catalog. A typical TLE has the following format, including a first line containing information on the object itself and a second line with information on the orbit:

```
1 27386U 02009A    13127.45641789 .00000089 00000-0 44087-4 0 3555
2 27386   98.4303 196.5510 0001204  87.6383 272.4946 14.37606880585289
```

Key information which is used in D-SPOSE is outlined in Table 2.2. The orbital elements presented are mean orbital elements from which the effects of perturbations are removed; the orbital elements at a specific point in time that evolve constantly due to perturbations are called osculating elements. Switching from mean elements to osculating elements can be done using the Simplified General Perturbations (SGP) models [69].

TABLE 2.2: Two-Line Element Set Content

TLE Data	Content
27386	Satellite Number
13	Epoch Year (last two digits of year)
127	Epoch Day of Year
.45641789	Fraction of Day
98.4303	Inclination ($^{\circ}$)
196.5510	Right Ascension of the Ascending Node ($^{\circ}$)
0001204	Eccentricity (with a decimal point before first digit)
87.6383	Argument of Perigee ($^{\circ}$)
272.4946	Mean Anomaly ($^{\circ}$)
14.37606880	Mean Motion (revolutions per day)

For a specific orbit, one can also define an Earth-Centered Orbital (ECO) frame which rotates with the precessing orbit and defined by x_o pointing towards the ascending node and z_o pointing along the orbit normal. Figure 2.3a shows the ECO frame with respect to the ECI frame as a function of the orbital inclination and right ascension of the ascending node.

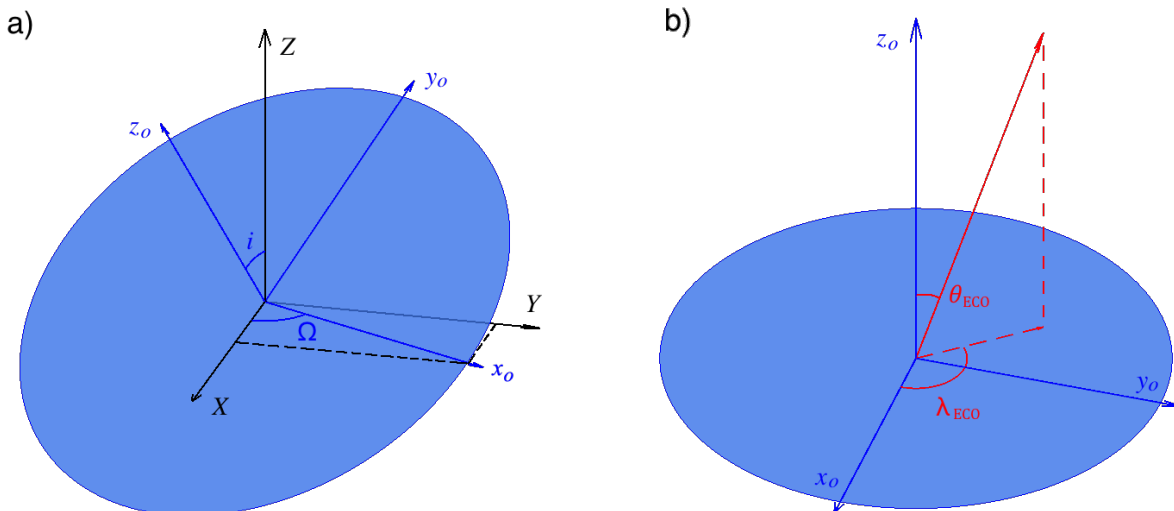


FIGURE 2.3: Earth-Centered Orbital Frame

The ECO frame is very convenient to visualize the motion of a spacecraft's spin axis. It has long been known that under the sole influence of the gravity-gradient torque, the motion of a spinning satellite's angular momentum vector forms a closed path in this frame [60, 61]. One can therefore define two angles that would characterize

the orientation of a vector in this frame. Figure 2.3b shows such two angles, denoted by θ_{ECO} and λ_{ECO} .

Satellite-Centered Orbital Frame

It is also possible to define a reference frame fixed with the motion of a satellite in orbit, which we will call the Satellite-Centered Orbital (SCO) frame. This frame is convenient when discussing perturbations which are dependent on the satellite's direction of motion, such as aerodynamic drag. We will show in Chapter 3 that this reference frame is also useful to characterize the effect of bombardment from small debris and micrometeoroids. Figure 2.4 displays the SCO frame for a satellite along its orbit with the x_{SCO} -axis in the spacecraft velocity direction, the z_{SCO} -axis pointing towards Earth in the orbital plane, and the y_{SCO} -axis completing the right hand rule.

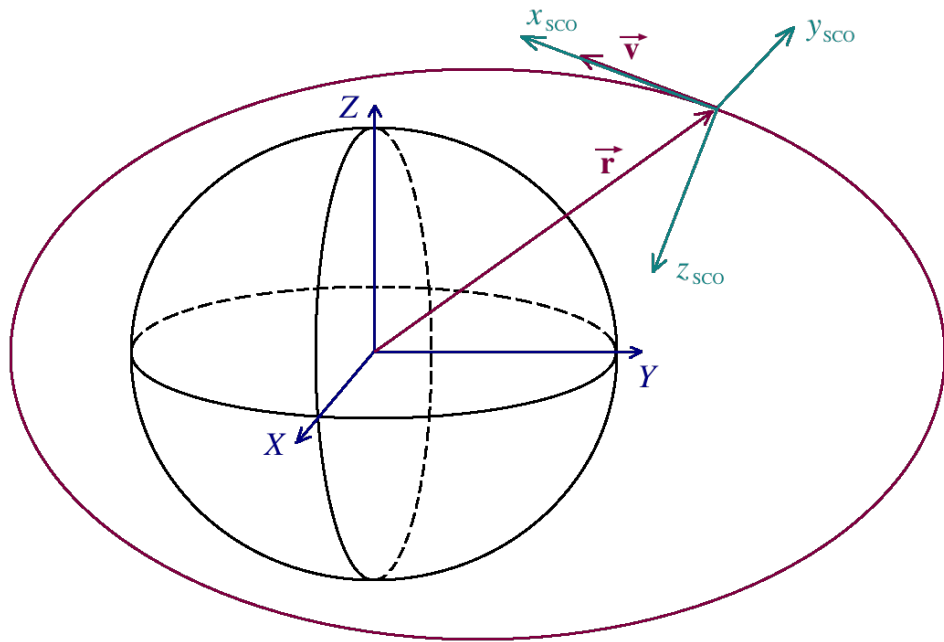


FIGURE 2.4: Satellite-Centered Orbital Frame

It is once more possible to characterize the orientation of a vector in this frame by defining two angles, the elevation, θ_{elev} , and the azimuth, ϕ_{azi} . Elevation is defined positive in the space-ward direction from the x_{SCO} -axis, opposite the z_{SCO} -axis, from -90° to 90° , and azimuth defined positive in the starboard direction, from the x_{SCO} -axis towards the y_{SCO} -axis, from -180° to 180° .

Body-Fixed Frame

Finally, the body-fixed frame is, as its name suggests, a reference frame which is fixed with the rigid body of the satellite. This frame is used in D-SPOSE to propagate the attitude equation defined in Eq. (2.5) and also to define the surface geometry of the satellite. A typical surface geometry model in the body-fixed frame is presented in Fig. 2.5 with the body-fixed x -axis, y -axis, and z -axis.

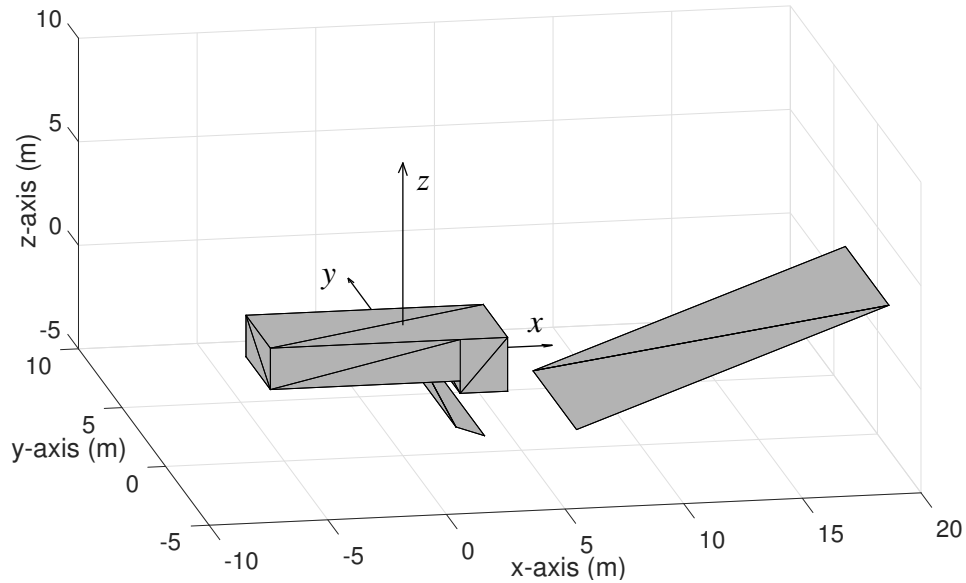


FIGURE 2.5: Body-Fixed Frame

2.1.2 Orbit and Attitude Equations

Dealing with satellite dynamics requires an analysis of the six degrees of freedom governing the orbit and attitude of spacecraft. Three coupled vector differential equations describe the evolution of the corresponding variables. First is the dynamics equation for orbital motion in an ECI coordinate frame [1, Ch. 8, p. 525]:

$$\ddot{\mathbf{r}}(t) = -\frac{\mu}{r(t)^3} \mathbf{r}(t) + \sum_j \mathbf{a}_j(t, \mathbf{r}(t), \mathbf{v}(t), \mathbf{q}(t), \boldsymbol{\omega}(t)) \quad (2.4)$$

where \mathbf{r} is the position as a function of time t , $r = \|\mathbf{r}\|$, \mathbf{v} is the velocity, \mathbf{q} is the attitude parametrization, chosen here to be a quaternion, $\mathbf{q} = [q_0 \mathbf{q}_v^T]^T$, $\boldsymbol{\omega}$ is the angular velocity of the body with respect to the inertial frame, μ is the Earth's gravitational

parameter, and \mathbf{a}_j represents the additional considered accelerations due to orbital perturbations, which are a function of the rigid body's position, velocity, and attitude state. Equation (2.4) is propagated in the TEME reference frame and all vectors with the exception of $\boldsymbol{\omega}$ represent components in the TEME frame.

The second differential equation, the dynamics equation for attitude motion, relates the evolution of absolute angular velocity to the sum of the external torques, $\boldsymbol{\tau}_j$, about the body's center of mass [56, Ch. 3 p. 59]:

$$\mathbf{I}\dot{\boldsymbol{\omega}}(t) + \boldsymbol{\omega}(t)^{\times}\mathbf{I}\boldsymbol{\omega}(t) = \sum_j \boldsymbol{\tau}_j(t, \mathbf{r}(t), \mathbf{v}(t), \mathbf{q}(t), \boldsymbol{\omega}(t)) \quad (2.5)$$

where \mathbf{I} is the matrix representation of the inertia tensor of the rigid body in the centroidal body-fixed frame. The external torques considered are not only dependent on the attitude state of the rigid body, but also on its position and velocity. All vectors in Eq. (2.5) with the exception of \mathbf{r} , \mathbf{v} , and \mathbf{q} represent components in the same body-fixed frame; the superscript \times denotes the skew-symmetric matrix representation of the cross-product.

Finally, the third differential equation is the kinematic equation for the absolute orientation of the spacecraft:

$$\dot{\mathbf{q}}(t) = \frac{1}{2}\boldsymbol{\Omega}(\boldsymbol{\omega})\mathbf{q}(t) \quad (2.6)$$

where, expressed in terms of the body-frame components of $\boldsymbol{\omega} = [\omega_x \ \omega_y \ \omega_z]^T$:

$$\boldsymbol{\Omega} = \begin{bmatrix} 0 & -\omega_x & -\omega_y & -\omega_z \\ \omega_x & 0 & \omega_z & -\omega_y \\ \omega_y & -\omega_z & 0 & \omega_x \\ \omega_z & \omega_y & -\omega_x & 0 \end{bmatrix} \quad (2.7)$$

In D-SPOSE, Eqs. (2.4)-(2.6) are numerically propagated at a fixed integration time step using a fifth-order Runge-Kutta method called the Runge-Kutta Dormand-Prince (RKDP) numerical integration method [70]. The same time step is used for propagating both the orbit and attitude equations as both are coupled, where information about one is used in the computation and propagation of the other.

The accelerations and torques due to external perturbations, as well as the environmental models considered, are summarized in Table 2.3. These include Earth's

TABLE 2.3: External Perturbations and Environmental Models

Perturbation	Environmental Model
Gravitational perturbations and gravity gradient torque	EGM2008 [71]
Third-body perturbations	Miriade Ephemerides [72]
Aerodynamic drag and torque	DTM-2013 [2]; NRLMSISE-00 [3]; JB2008 [5]; HWM14 [4]
Eddy-current torque	IGRF-12 [73]; WMM [74]
Solar radiation pressure and torque	Montenbruck and Gill [75]
Albedo acceleration and torque	Stephens [76]; CERES [77]; ECMWF [78]
Infrared acceleration and torque	Stephens [76]; CERES [77]; ECMWF [78]
Internal energy dissipation	Kane Damper [79]
Hypervelocity impacts	Sagrières and Sharf [80, 81]; MASTER-2009 [22]

gravitational acceleration due to its deviation from that of a homogeneous sphere, the gravity-gradient torque, and third-body gravitational accelerations from the Sun and the Moon, all of which are conservative, as well as the aerodynamic drag and torque, the eddy-current torque, and the radiation pressure and torque, which are non-conservative. Direct solar radiation as well as reflected radiation (albedo) and infrared emission from the Earth are considered. The effect of internal energy dissipation is also taken into account. More complete forms than usually employed are used for: the gravity-gradient torque, calculated from a spherical-harmonic representation of the Earth's gravitational potential; the aerodynamic drag and torque, for a spinning object; and the eddy-current torque, for a slowly rotating body. These perturbations will be discussed in detail in Section 2.2 and 2.3, while the associated environmental models will be presented in Section 2.4.2. Furthermore, the effect of bombardment from micrometeoroids and small space debris through hypervelocity impacts on the attitude and orbital motion of spacecraft, the long-term effect of which has not previously been studied, will be discussed in its entirety in Chapter 3 with the presentation of a novel stochastic framework.

2.2 Gravitational Perturbations

2.2.1 Earth's Gravitational Field

Earth is not a perfectly uniform sphere but rather an oblate and highly non-uniform body. In order to capture the gravitational perturbations from such a body, a spherical-harmonic expansion of the Earth's gravitational potential function, U , defined in the ECEF frame can be used, from which the acceleration of a point mass due to Earth's gravity field, as a function of its geocentric distance, r , its spherical geocentric latitude, θ , and its longitude, λ , can be obtained [1, Ch. 8, p. 545]:

$$U(r, \theta, \lambda) = \frac{\mu}{r} \left[1 + \sum_{l=2}^k \sum_{m=0}^l \left(\frac{R_E}{r} \right)^l P_{l,m}[\sin \theta] \{ C_{l,m} \cos(m\lambda) + S_{l,m} \sin(m\lambda) \} \right] \quad (2.8)$$

where R_E is Earth's equatorial radius, C and S are coefficients representing the mathematical modeling for the Earth's shape using spherical harmonics, and $P_{l,m}$ are Legendre functions evaluated at $\sin \theta$, which can be computed by a recursive algorithm, presented in Appendix A.

The sum in Eq. (2.8) is performed over the gravitational coefficients as obtained from the desired geopotential model up to a certain degree and order k . The acceleration due to Earth's gravitational field, including the standard spherical Earth term (first term on right hand side of Eq (2.4)), is then computed using the chain rule [1, Ch. 8, p. 550]:

$$\mathbf{a}_{\text{grav}} = \frac{\partial U}{\partial r} \left(\frac{\partial r}{\partial \mathbf{r}} \right)^T + \frac{\partial U}{\partial \lambda} \left(\frac{\partial \lambda}{\partial \mathbf{r}} \right)^T + \frac{\partial U}{\partial \theta} \left(\frac{\partial \theta}{\partial \mathbf{r}} \right)^T \quad (2.9)$$

Analytical expressions for the partial derivatives of the gravitational potential and the associated coordinate transformations in Eq. (2.9) are derived in Appendix A.

2.2.2 Gravity-Gradient Torque

From Eq. (2.8), it can be seen that for a rigid body the value of the geopotential will vary over its mass distribution, leading to differences in the gravitational acceleration witnessed by different parts of the spacecraft. This non-uniform distribution of the gravitational field over the spacecraft body will lead to a torque called the gravity-gradient torque. It is a conservative torque and will therefore not have a long-term effect on the rotational energy of a spacecraft but will have an influence on the evolution

of its spin axis. The gravity-gradient torque is usually calculated assuming a spherical model of Earth's gravity field. However, in D-SPOSE, in order to provide a more accurate analysis of the effect of the Earth's gravitational field on the long-term attitude dynamics of large space debris, it is computed for a general gravitational field from the spherical-harmonic expansion of the geopotential. Nevertheless, one simplifying assumption is made in this computation, which is that the gravitational acceleration in the vicinity of the center of mass varies linearly with distance. The gravity-gradient torque is then given as follows [82]:

$$\boldsymbol{\tau}_{\text{grav}} = \begin{bmatrix} g_{23}(I_{zz} - I_{yy}) - g_{13}I_{xy} + g_{12}I_{xz} + I_{yz}(g_{22} - g_{33}) \\ g_{13}(I_{xx} - I_{zz}) + g_{23}I_{xy} - g_{12}I_{yz} + I_{xz}(g_{33} - g_{11}) \\ g_{12}(I_{yy} - I_{xx}) - g_{23}I_{xz} + g_{13}I_{yz} + I_{xy}(g_{11} - g_{22}) \end{bmatrix} \quad (2.10)$$

where the g_{ij} and I_{ij} are the components of the matrices \mathbf{G} and \mathbf{I} , respectively, the former defined by [82]:

$$\mathbf{G} = \mathbf{C}^T \frac{\partial \mathbf{a}_{\text{grav}}}{\partial \mathbf{r}} \mathbf{C} \quad (2.11)$$

and where \mathbf{C} is the rotation matrix from the body-fixed frame to the inertial frame.

The evaluation of \mathbf{G} requires the derivative of \mathbf{a}_{grav} with respect to \mathbf{r} , which can be computed analytically. Thus, using the geopotential function of Eq. (2.8) directly, the derivative of the acceleration can be computed from Eq. (2.9) by again applying the chain rule:

$$\begin{aligned} \frac{\partial \mathbf{a}_{\text{grav}}}{\partial \mathbf{r}} = & \frac{\partial^2 U}{\partial r^2} \frac{\partial r}{\partial \mathbf{r}} \left(\frac{\partial r}{\partial \mathbf{r}} \right)^T + \frac{\partial^2 U}{\partial \theta^2} \frac{\partial \theta}{\partial \mathbf{r}} \left(\frac{\partial \theta}{\partial \mathbf{r}} \right)^T + \frac{\partial^2 U}{\partial \lambda^2} \frac{\partial \lambda}{\partial \mathbf{r}} \left(\frac{\partial \lambda}{\partial \mathbf{r}} \right)^T + \\ & \frac{\partial^2 U}{\partial \theta \partial r} \left(\frac{\partial r \partial \theta^T}{\partial \mathbf{r} \partial \mathbf{r}} + \frac{\partial \theta \partial r^T}{\partial \mathbf{r} \partial \mathbf{r}} \right) + \frac{\partial^2 U}{\partial \lambda \partial r} \left(\frac{\partial r \partial \lambda^T}{\partial \mathbf{r} \partial \mathbf{r}} + \frac{\partial \lambda \partial r^T}{\partial \mathbf{r} \partial \mathbf{r}} \right) + \\ & \frac{\partial^2 U}{\partial \theta \partial \lambda} \left(\frac{\partial \lambda \partial \theta^T}{\partial \mathbf{r} \partial \mathbf{r}} + \frac{\partial \theta \partial \lambda^T}{\partial \mathbf{r} \partial \mathbf{r}} \right) + \frac{\partial U}{\partial r} \frac{\partial^2 r}{\partial \mathbf{r}^2} + \frac{\partial U}{\partial \theta} \frac{\partial^2 \theta}{\partial \mathbf{r}^2} + \frac{\partial U}{\partial \lambda} \frac{\partial^2 \lambda}{\partial \mathbf{r}^2} \end{aligned} \quad (2.12)$$

The second partial derivatives and additional coordinate transformations in Eq. (2.12) can all be derived in closed form and are presented in Appendix A.

2.2.3 Third-body Interactions

The final gravitational perturbations considered are third-body accelerations. The Moon and the Sun both have an influence on the orbital dynamics of Earth satellites

and therefore need to be included in any long-term orbital analysis. Their effect is determined from μ_k and \mathbf{r}_k representing the gravitational parameter and position of the Sun and Moon ($k = 1, 2$) in the chosen ECI frame, respectively, and treating them as point masses [1, Ch. 8, p. 574]:

$$\mathbf{a}_k = \sum_{k=1,2} \mu_k \left(\frac{\mathbf{r}_k(t) - \mathbf{r}(t)}{\|\mathbf{r}_k(t) - \mathbf{r}(t)\|^3} - \frac{\mathbf{r}_k(t)}{r_k(t)^3} \right) \quad (2.13)$$

In D-SPOSE, the positions of the Sun and Moon are taken from available planetary ephemerides. This is discussed in Section 2.4.2. A potential difficulty from using Eq. (2.13) can arise, however. For example, if the third-body is the Sun, then the difference between the Earth-Sun position vector and the satellite-Sun position vector will be minute, and the cube of this as calculated in Eq. (2.13) will be even smaller, thus presenting a challenge when computing numerically. To get around this, another form of Eq. (2.13) can be used and is employed in D-SPOSE [1, Ch. 8, p. 575]:

$$\frac{\mathbf{r}_k(t) - \mathbf{r}(t)}{\|\mathbf{r}_k(t) - \mathbf{r}(t)\|^3} - \frac{\mathbf{r}_k(t)}{r_k(t)^3} = \mathbf{r}_s(t)Q - \frac{\mathbf{r}(t)}{r_k(t)^3} \quad (2.14)$$

where:

$$Q = \frac{(r(t)^2 + 2(\mathbf{r}(t) \cdot \mathbf{r}_s(t))(r_k(t)^2 + r_k(t)r_s(t) + r_s(t)^2))}{r_k(t)^3 r_s(t)^3 (r_k(t) + r_s(t))} \quad (2.15)$$

$$\mathbf{r}_s(t) = \mathbf{r}_k(t) - \mathbf{r}(t) \quad (2.16)$$

2.3 Non-Gravitational Perturbations

2.3.1 Aerodynamic Drag and Torque

Aerodynamic drag is one of the largest non-gravitational perturbation for satellites in Low-Earth Orbit (LEO). It is caused by particles interacting with the satellite body creating an acceleration in the opposite direction of its motion as the satellite is doing work on the atmosphere. Its effect will lead to an eventual decay of the satellite's orbital altitude. Understanding aerodynamic drag requires an accurate knowledge of the atmosphere, the spacecraft surfaces, and the interaction between both. The effect of aerodynamic drag quickly reduces at higher orbits due to the atmospheric density's

exponential decrease. The acceleration due to aerodynamic drag can be obtained from the following equation [1, Ch. 8, p. 551]:

$$\mathbf{a}_{\text{drag}} = -\frac{1}{2} \frac{c_D A}{m} \rho v_{\text{rel}} \mathbf{v}_{\text{rel}} \quad (2.17)$$

where c_D is the drag coefficient, A is the satellite cross-sectional area normal to the incident flow, m is the spacecraft mass, ρ is the atmospheric density at the current position, and \mathbf{v}_{rel} is the relative velocity of the satellite with respect to the atmosphere. Multiple atmospheric density and velocity models can be used in D-SPOSE and each are detailed in Section 2.4.2.

However, in our model we refine the computation of aerodynamic drag by considering additional terms due to the velocity component of the spacecraft rotation with respect to the atmosphere, and obtain a slightly modified equation for the aerodynamic drag. By dividing the spacecraft in tessellated surfaces defined by the three vertices and the unit inward surface normal, \mathbf{n}_p , as shown in Fig. 2.5, the drag acceleration can be calculated as a sum over each triangular surface p in view of the relative wind as follows, with components in the inertial frame [56, Ch. 8, p. 252]:

$$\mathbf{a}_{\text{drag}} = -\sum_p \frac{1}{2} \frac{c_D A_p}{m} \rho \left(\cos \alpha_p v_{\text{rel}} \mathbf{v}_{\text{rel}} + (\mathbf{n}_p^T (\mathbf{c}_p^\times \boldsymbol{\omega}_{\text{rel}})) \mathbf{v}_{\text{rel}} - v_{\text{rel}} \cos \alpha_p \mathbf{c}_p^\times \boldsymbol{\omega}_{\text{rel}} \right) \quad (2.18)$$

where A_p is the area of surface p , $\cos \alpha_p = -\mathbf{n}_p \cdot \frac{\mathbf{v}_{\text{rel}}}{v_{\text{rel}}}$, \mathbf{c}_p is the position of the center of pressure of surface p from the center of mass of the spacecraft and $\boldsymbol{\omega}_{\text{rel}}$ the relative angular velocity of the spacecraft with respect to the atmosphere. Surfaces are considered to be in view of the relative wind when $\cos \alpha_p > 0$.

The force arising from the Earth's atmosphere will also have an associated torque which depends highly on the geometry of the satellite surface exposed to the incoming flow. The aerodynamic torque for a spinning spacecraft can be calculated by computing a surface integral over the area of surface p and summing over all the exposed surfaces. For components in the body-fixed frame, it is expressed as follows [56, Ch. 8, p. 252]:

$$\begin{aligned} \boldsymbol{\tau}_{\text{drag}} = & -\sum_p \frac{1}{2} c_D \rho \left(v_{\text{rel}} A_p \cos \alpha_p \mathbf{c}_p^\times \mathbf{v}_{\text{rel}} + \iint_A (\mathbf{n}_p^T (\mathbf{r}_p^\times \boldsymbol{\omega}_{\text{rel}})) (\mathbf{r}_p^\times \mathbf{v}_{\text{rel}}) dA - \right. \\ & \left. \iint_A v_{\text{rel}} \cos \alpha_p \mathbf{r}_p^\times \mathbf{r}_p^\times \boldsymbol{\omega}_{\text{rel}} dA \right) \end{aligned} \quad (2.19)$$

with \mathbf{r}_p the position of the surface element dA with respect to the body's center of mass. For a general spacecraft geometry model defined by triangular surfaces, an analytical solution to the surface integrals in Eq. (2.19) as a function of the positions of the three vertices can be obtained and is summarized in Appendix B.

2.3.2 Eddy-current Torque

The interaction between a spinning satellite's conductive surfaces and the Earth's magnetic field will lead to a perturbing torque called the eddy-current torque. This phenomenon arises from the rotation of an electrically conducting body as moving electrons are resisted by the surface material. For slowly spinning spacecraft, the time variation of the magnetic field as seen by the orbiting spacecraft also needs to be considered, an effect which isn't always considered in the literature. The equation for the eddy-current torque, in body frame components, is [62]:

$$\boldsymbol{\tau}_{\text{eddy}} = \left[\mathbf{M} \left(\boldsymbol{\omega}^{\times} \mathbf{B} - \left(\frac{d\mathbf{B}}{dt} \right)_I \right) \right]^{\times} \mathbf{B} \quad (2.20)$$

where \mathbf{M} is the magnetic tensor of the object, \mathbf{B} is the Earth's magnetic field, and $\left(\frac{d\mathbf{B}}{dt} \right)_I$ is the time derivative of the Earth's magnetic field measured in the inertial frame as experienced along the satellite's orbit and expressed in the body-fixed frame.

The Earth's magnetic field can be calculated similarly to the effect of the Earth's gravity field from the spherical-harmonic expansion of the Earth's magnetic potential in the ECEF frame. It can be written as [83, App. H, p. 779]:

$$\mathbf{B} = -\nabla V \quad (2.21)$$

$$V(r, \phi, \lambda) = a_M \sum_{n=1}^k \left(\frac{a}{r} \right)^{n+1} \sum_{m=0}^n (g_n^m \cos(m\lambda) + h_n^m \sin(m\lambda)) P_n^m[\cos \phi] \quad (2.22)$$

where ϕ is the colatitude, λ is the longitude, a_M is the geomagnetic convention for Earth's mean reference spherical radius, g_n^m and h_n^m are Gauss coefficients obtained from a magnetic potential model up to degree and order k , which is dependent on the chosen model, and P_n^m are the Schmidt normalized associated Legendre functions evaluated at $\cos \phi$, which can be obtained from a recursive algorithm, given in Appendix C.

The time derivative of the Earth's magnetic field can be calculated from the magnetic field in a rotating ECEF frame:

$$\left(\frac{d\mathbf{B}}{dt} \right)_I = \left(\frac{d\mathbf{B}}{dt} \right)_E + \boldsymbol{\omega}_E^\times \mathbf{B} \quad (2.23)$$

where $\boldsymbol{\omega}_E$ is the angular velocity of the Earth with respect to the inertial frame. The time derivative of the magnetic field measured in the ECEF frame can then be expanded:

$$\left(\frac{d\mathbf{B}}{dt} \right)_E = (\mathbf{v}_E \cdot \nabla) \mathbf{B} + \left(\frac{\partial \mathbf{B}}{\partial t} \right)_E \quad (2.24)$$

where \mathbf{v}_E is the spacecraft velocity measured in the rotating ECEF frame:

$$\mathbf{v}_E = \mathbf{v} - \boldsymbol{\omega}_E^\times \mathbf{r} \quad (2.25)$$

Considering a local spherical coordinate frame, S :

$$\left(\frac{\partial \mathbf{B}}{\partial t} \right)_E = \left(\frac{\partial \mathbf{B}}{\partial t} \right)_S + \boldsymbol{\omega}_S^\times \mathbf{B} \quad (2.26)$$

where $\boldsymbol{\omega}_S$ is the angular velocity of the spherical coordinate frame with respect to the ECEF frame due to the orbiting spacecraft, defined by:

$$\boldsymbol{\omega}_S = \frac{\mathbf{r}^\times \mathbf{v}_E}{r^2} \quad (2.27)$$

The analytical expressions for these terms can all be obtained from the spherical-harmonic expression for the Earth's magnetic potential. The analytical expressions derived for $\left(\frac{d\mathbf{B}}{dt} \right)_I$ from the spherical-harmonic expansion of the Earth's magnetic field are detailed in Appendix C. Multiple geomagnetic models can be selected in D-SPOSE in order to obtain the value of the Earth's magnetic field at the satellite position; these are presented in Section 2.4.2.

2.3.3 Radiation Perturbations

The pressure that an incoming flux of photons has on satellite surfaces can lead to a non-negligible acceleration and torque, depending on the spacecraft shape. Similarly to aerodynamic drag, the force associated with radiation can be calculated as a sum

over every lit surface p and expressed in inertial frame components [56, Ch. 8, p. 263]:

$$\mathbf{a}_{\text{rad}} = \sum_p \frac{\phi_R}{mc} \left[(\sigma_a + \sigma_{rd}) \mathbf{s} + \frac{2}{3} \sigma_{rd} \mathbf{n}_p + 2\sigma_{rs} \cos \beta \mathbf{n}_p \right] A_p \cos \beta \quad (2.28)$$

where σ_a , σ_{rd} , and σ_{rs} represent the coefficients of absorption, diffuse reflection, and specular reflection for that surface and for the appropriate light spectrum, respectively, c is the speed of light, ϕ_R is the photon flux from the incoming source of radiation, \mathbf{s} is the unit vector of the incident light direction, and $\cos \beta = \mathbf{s} \cdot \mathbf{n}_p$. Surfaces are considered to be in view of the radiation source when $\cos \beta > 0$. Three sources of radiation leading to three photon fluxes are considered: first, direct solar radiation from the Sun, ϕ_{solar} ; second, radiation reflected from the Earth's surface (albedo), ϕ_{alb} ; and third, emitted infrared radiation from the Earth, ϕ_{ir} .

The torque associated with the radiation can then be obtained from the acceleration derived above, summed over every lit surface p , and expressed in the body-fixed frame [56, Ch. 8, p. 263]:

$$\boldsymbol{\tau}_{\text{rad}} = \sum_p mc_p^{\times} \mathbf{a}_{\text{rad},p} \quad (2.29)$$

Direct Solar Radiation

The first and largest source of radiation is the direct radiation coming from the Sun. In this case, the incident light direction is calculated by [1, Ch. 8, p. 580]:

$$\mathbf{s} = -\frac{\mathbf{r}_1}{r_1} \quad (2.30)$$

with \mathbf{r}_1 the Earth-Sun vector, as specified in Section 2.2.3. The solar radiation photon flux varies with time and can be calculated as [7]:

$$\phi_{\text{solar}} = \psi_S S_R \left(\frac{a_u}{r_1} \right)^2 \quad (2.31)$$

where S_R is the solar radiation constant, a_u is the Astronomical Unit (AU), and ψ_S is the Earth shadow function, which equals 0 when the satellite is in the Earth's shadow and 1 when the satellite is sunlit. A geometrical model of the penumbra transition when $0 < \psi_S < 1$ is used [75, Ch. 3, p. 80].

Earth's Albedo and Infrared Emissions

The albedo and infrared radiation from the Earth has a smaller effect than direct solar radiation but still needs to be taken into account. The effect of the albedo will be greatest when the satellite is on the dayside, where the Earth's surface below it is illuminated, while Earth's infrared emissions are independent of illumination. Photon fluxes also vary with time and location. By dividing Earth's surface into grids defined by latitude and longitude, one can calculate them as follows [7]:

$$\phi_{\text{alb}} = S_R \left(\frac{a_u}{r_1} \right)^2 \sum_{\theta} \sum_{\lambda} \alpha_{\text{alb},\theta,\lambda} \cos \psi \cos \gamma \frac{A_{\theta,\lambda}}{\pi d} \quad (2.32)$$

$$\phi_{\text{ir}} = S_R \left(\frac{a_u}{r_1} \right)^2 \sum_{\theta} \sum_{\lambda} \alpha_{\text{ir},\theta,\lambda} \cos \gamma \frac{A_{\theta,\lambda}}{4\pi d} \quad (2.33)$$

where α_{alb} and α_{ir} are the albedo and emissivity coefficients, respectively, $A_{\theta,\lambda}$ is the Earth surface element area, d is the Earth surface element-satellite distance, and with ψ and γ representing the angles between the Earth surface element normal and the direction to the Sun and satellite, respectively. Earth surface elements are only considered when $\cos \gamma > 0$ for both albedo and infrared emissions, and also only when the surface element is lit, *i.e.*, when $\cos \psi > 0$, for the albedo. The incident light direction is calculated from the center of the considered Earth surface element.

Multiple available models for the Earth albedo and emissivity coefficients can be chosen in D-SPOSE. These will be discussed in more detail in Section 2.4.2.

2.3.4 Internal Energy Dissipation

Internal energy dissipation is the last torque included in D-SPOSE as its effect is known to be significant in the long-term attitude motion of spacecraft. No physical body is truly rigid and damping can arise in a satellite from multiple sources, including the sloshing of fuel, vibrations, or moving appendages [56, Ch. 6, p. 139]. However, including its effect in the equations of attitude motion can quickly become complex. Various modeling techniques exist, including using a point mass damper consisting of a point mass constrained in its motion and associated with a damping constant and spring constant [56, Ch. 3, p. 65]. Within the rigid-body modeling framework, a simple way to capture the effect of internal energy dissipation is by using a Kane damper [79]. This mechanism consists of a spherical mass contained inside a cavity full of

viscous fluid at the spacecraft's center of mass. Assuming that the centers of mass of the spacecraft and the damper remain coincident, a torque proportional to their relative angular velocity will arise:

$$\tau_{\text{damper}} = k_d(\omega_d - \omega) \quad (2.34)$$

where ω_d is the angular velocity of the damper with respect to the inertial frame, expressed in the body-fixed frame, and k_d is a damping constant. The damper can be treated as a separate rigid body, with its own equations of motion, similarly to Eqs. (2.5)-(2.7), but as a function of ω_d , \mathbf{q}_d and \mathbf{I}_d , and with only $-\tau_{\text{damper}}$ as an external torque.

2.4 Propagator Inputs and Operating Modes

One of the key aspects of the developed propagator is its flexibility. Because of the complexity of the tool, various input-files are required and external code is used for various environmental models. Although D-SPOSE is coded in C, it also incorporates pre-developed software in Fortran, C++ and C. As it was built over a relatively long period of time and used initially for diverse studies not necessarily specifically related to the final primary goal as stated in this thesis, it contains a large set of parameters and options making it also useful for other research (re-entry analyses, atmospheric modeling studies, and mission planning, for example). Section 2.4.1 will discuss the format of the propagator, the inputs required for it to function, and its modes of operation. Section 2.4.2 will review the external models and code used.

2.4.1 Input Files Format

Five user-input text files are expected to initialize the coupled propagation: one file for each of the initial conditions, the perturbation model parameters, and the propagation parameters, and two files for the spacecraft parameters.

First, a file containing a TLE set for the desired object in the standard format provides the information necessary to characterize the orbit and the initial epoch. This is preferred instead of using accurate position data from the International Laser Ranging Service (ILRS) so as to have the possibility of use with objects which aren't necessarily

tracked by laser ranging. The TLE is then converted into a set of osculating orbital elements and an initial translational state vector (\mathbf{r} and \mathbf{v}) by using the SGP4 propagator, which is provided in an external C++ function [69].

Second is a file containing the propagation parameters, specifically information on the desired propagation time step, time length, and the frequency at which the user requires information on the state of the system throughout the propagation.

The third file contains the model parameters: the user has the option to include or exclude every considered acceleration and torque, and to choose the desired environmental model for each. In this file, the user also needs to set up the parameters required for each model. These include: the maximum degree and order considered for the geopotential (k in Eq. (2.8)) for the calculation of the gravitational acceleration and gravity-gradient torque (up to degree and order 100); the drag coefficient for the calculation of the aerodynamic drag and torque (c_D in Eqs. (2.18) and (2.19)); the solar activity indices used in the external atmospheric models for the calculation of the atmospheric density, which can either be set up to be the actual observed values or user-inputted values (see Section 2.4.2); and the damper properties for the calculation of internal energy dissipation (\mathbf{I}_d and k_d in Eq. (2.34)). The last two files are related to the spacecraft itself. The first contains information on the spacecraft geometry. Any spacecraft shape can easily be considered since the input consists of a list of triangular surfaces defined by the position of its three vertices in the body-fixed frame, the direction of its inward surface normal (\mathbf{n}_p in Eq. (2.18) and (2.19)), and the optical coefficients in the visible and infrared spectra (σ_a , σ_{rd} , and σ_{rs} in Eq. (2.28)). The second file contains the other properties of the spacecraft: its mass (m), its moments of inertia (\mathbf{I} in Eqs. (2.5) and (2.10)) and magnetic tensor (\mathbf{M} in Eq. (2.20)) in the same body-fixed frame. The initial orientation of the spacecraft either in the inertial frame or in the orbital frame, in order to initialize the attitude, and the initial angular velocity are also requested here.

Finally, four output files are generated by the propagator: the first contains the evolution of the system state with information on the position (\mathbf{r}) and velocity (\mathbf{v}) of the spacecraft in the inertial frame, its attitude with respect to the inertial frame (\mathbf{q}), and its angular velocity in the body-fixed frame ($\boldsymbol{\omega}$), as well as information on all the simulation inputs; the second contains the values of the accelerations and torques as evaluated throughout the propagation; the third contains the total work done by the non-conservative perturbations on the spacecraft as well as the gravitational potential energy from the Earth, Sun, and Moon if the associated perturbations are considered.

Finally, the geometry file is reproduced for housekeeping purposes.

2.4.2 Environmental Models

As was previously mentioned, different environmental models are used as input into D-SPOSE to calculate the external perturbations affecting the considered satellite. They are either set up as their own files containing coefficients used in the associated equations or as external functions called in the main D-SPOSE software.

Geopotential Model

The gravitational coefficients $C_{l,m}$ and $S_{l,m}$ used in the calculation of the geopotential in Eq. (2.8) can be obtained from various models. The one available in D-SPOSE is the Earth Gravitational Model 2008 (EGM2008), a highly accurate geopotential model developed from a wide set of terrestrial and satellite data sources [71]. It is complete to degree and order 2159, although only coefficients up to degree and order 100 are included in D-SPOSE as an external text file.

Solar System Ephemerides

The positions of the Sun and the Moon (\mathbf{r}_1 and \mathbf{r}_2 in Eqs. (2.13) and (2.30)) are obtained from planetary ephemerides provided by the Virtual Observatory of the Institut de Mécanique Céleste et de Calcul des Éphémérides [72]. In D-SPOSE, they are set up as external text files providing the positions of each in the ECI frame in AU, with 12-hour increments for the Sun, and 4-hour increments for the Moon, starting from January 1, 2000 to December 31, 2030. It is easily possible to append future ephemerides to the text files for studies at a later date.

Atmospheric Models

In the calculation of the aerodynamic drag and torque, it is necessary to provide the time-dependent atmospheric density at the position of the satellite (ρ in Eqs. (2.18) and (2.19)). Modeling the Earth's atmosphere is incredibly complex as many phenomena exist and influence the dynamics of the constantly-evolving upper atmosphere. Density decreases exponentially with altitude, and changes in geomagnetic and solar activity can cause large density variations on top of seasonal and diurnal effects. There

exists a large variety of atmospheric models, and in the last few decades, empirical atmospheric density modeling has evolved significantly due to the increased availability of satellite data. To date, three state-of-the-art comprehensive models have been most widely used and are incorporated in D-SPOSE in order to provide accurate orbital propagation for LEO satellites: first, the 2013 version of the Drag-Temperature Model (DTM-2013) [2]; second, the Jacchia-Bowman 2008 (JB2008) model [5]; and third the NRLMSISE-00 model developed by the Naval Research Laboratory (NRL) as an extension to Mass Spectrometer and Incoherent Scatter (MSIS) class of atmospheric models [3]. The three models use independent techniques based on various data sets to predict atmospheric densities as a function of location (latitude, longitude, altitude) and time (time of day and of year). Furthermore, different indices for solar and geomagnetic activity are used in the three models. The three models and their inputs will be outlined briefly here, but recent and comprehensive reviews of atmospheric density modeling can be found in Emmert [84] and He et al. [85].

Originally developed in 1978, DTM is a three-dimensional thermospheric model based on the diffusive equilibrium and spherical harmonics of individual atmospheric constituents combined with satellite drag data and in-situ measurements. New data and improvements of the algorithms, leading to better agreements for extreme solar and geomagnetic conditions, were added in later versions and further improvements were made by including incoherent scatter radar and satellite interferometer data as well as different proxies for solar activity. The latest version, released as DTM-2013, includes a large data set from the Gravity Recovery and Climate Experiment (GRACE), the Challenging Minisatellite Payload (CHAMP), and the Gravity Field and Steady-State Ocean Circulation Explorer (GOCE) satellites and uses F30 as a solar activity proxy, covering the 200-900 km altitude range and using K_p as its geomagnetic index [2].

In D-SPOSE, DTM-2013 is called as an external Fortran function and requires three input files: one containing the daily and previous 81-day average F30 index; one containing the 3-hour K_p index; and the last containing the 24-hour average K_p index for every 3-hour period. The observed indices in the files currently span the range from January 1, 2000 to December 31, 2017, but can easily be appended with later values for future studies. The geomagnetic indices are obtained by a global network of observatories and can be found in the publications of the National Oceanic and Atmospheric Administration (NOAA) [86]. Solar activity indices can similarly be obtained from

publications of the Collecte Localisation Satellites (CLS) as directed by the Centre National d'Études Spatiales (CNES) [87].

The Jacchia atmospheric models solve the diffusion equation to obtain temperature, density and composition data from 90 km to 2500 km [88]. Systematic variations with the solar cycle, with solar activity over one solar rotation, semiannual variations, seasonal-latitudinal variations, diurnal variations, variation with geomagnetic activity and rapid fluctuations from gravity waves are deduced from satellite drag data and are also taken into account in the model equations. Improvements were made over the years by improving the boundary conditions of the diffusion equations and with new satellite data.

The Jacchia-Bowman 2008 (JB2008) model improves on the Jacchia models by incorporating new solar indices obtained from on-orbit sensor data and using a new semiannual density model and geomagnetic index model with temperature correction equations for high altitudes up to 4000 km [5]. Furthermore, JB2008 includes more data sources such as daily density values from drag analysis of numerous satellites, accelerometer data from CHAMP and GRACE as well as density values from the High Accuracy Satellite Drag Model (HASDM) [89]. This model uses as input a combination of solar parameters ($F_{10.7}$, S_{10} , M_{10} , Y_{10} and their 81-day centered averages with 1, 1, 2, and 5-day lags, respectively) and the Dst geomagnetic index. In D-SPOSE, JB2008 is also called as an external Fortran function and provides two external files for the geomagnetic and solar indices it uses [5]. Unlike for DTM-2013, it is not possible to have user-inputted indices to calculate the atmospheric density.

The third category, the MSIS-class models, differs from the Jacchia models in that they are thermospheric models based directly on measurements of atmospheric densities from satellites and temperatures obtained from incoherent scatter measurements at ground stations. A major upgrade to the MSIS-class of models is the more recent NRLMSISE-00 model [3]. In addition to a more extensive data set in spatial range and time period, the model also includes the satellite drag data which are the basis of the Jacchia models, bringing forward the advantages of both types of models. Furthermore, NRLMSISE-00 includes the effect of anomalous oxygen (O^+ and hot atomic oxygen) in the mass density above 500 km, an important component to satellite drag at these altitudes [3]. Space weather inputs include the previous day observed $F_{10.7}$, the 81-day centered average $F_{10.7}$ and the 3-hour magnetic index a_p . The outputs are two temperature values—the local neutral temperature and the asymptotic value at the exosphere, *i.e.*, exospheric temperature—as well as number densities for various

neutral species, anomalous oxygen and the total mass density. NRLMSISE-00 is provided as an external C function and two input files are needed for each the solar and geomagnetic indices. The current files contain indices spanning the time period from January 1, 2000 to December 31, 2017 and it is also possible to append the files with later indices.

Although all these models have their benefits and limitations, large uncertainties are present and should be kept in mind when using them [90]. A visual representation of the discrepancies between models can be obtained by considering a globally-averaged density profile for a specific altitude and time frame, as for example, is shown in Fig. 2.6 for 400 km using inputs for the year 2014. The globally-averaged density was obtained by discretizing Earth into 5° latitude by 5° longitude bins and averaging the density values at each bin, weighing them according to their surface area. One can see that the density profiles share a similar shape; however, differences of up to a factor of 2 are present for short time periods. Propagating orbits by using the atmospheric densities from different models can therefore lead to diverging orbital parameters as the instantaneous differences accumulate over time.

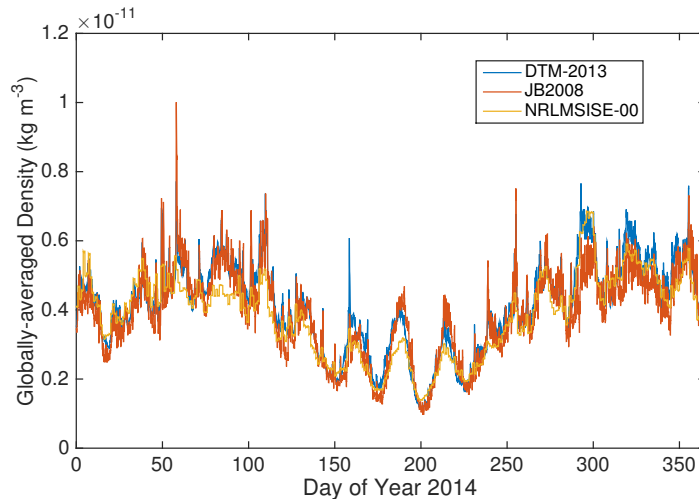


FIGURE 2.6: Globally-Averaged Atmospheric Density at 400 km for 2014

In addition to atmospheric density, the calculation of aerodynamic drag and torque requires knowledge of the relative velocity of the spacecraft with respect to the atmosphere (\mathbf{v}_{rel} in Eqs. (2.18) and (2.19)). This is calculated from the horizontal velocity of the atmosphere at the position of the satellite. In D-SPOSE, two options exist: first, to use the classical assumption that the atmosphere is co-rotating with Earth, or second, to calculate deviations according to the NRL's Horizontal Wind Model 2014 (HWM14)

[4]. This model is called as an external Fortran function and asks for the same input as NRLMSISE-00.

Geomagnetic Field

Two different geomagnetic potential models can be selected in D-SPOSE in order to calculate the strength and direction of the magnetic field at the satellite position: the International Geomagnetic Reference Field (IGRF) or the World Magnetic Model (WMM) [73, 74]. These are provided as external text files containing each model's determined Gauss coefficients (g_n^m and h_n^m in Eq. (2.22)).

The IGRF is the product of an international collaboration of research institutes and laboratories with both modeling and observational expertise led by the International Association of Geomagnetism and Aeronomy (IAGA) since 1965 [73]. It continuously provides the scientific community with a set of mathematical tools to assess the Earth's magnetic field and its evolution from 1900 to the present, also supplying a short-term forecast, for use in geology, space weather, and satellite dynamics studies. It produces Gauss coefficients for every 5 year period with a maximum degree and order 13 (k in Eq. (2.22)).

The WMM is a joint project between the United States and the United Kingdom. Funded by the American National Geospatial-Intelligence Agency (NGA) and the Defence Geographic Centre (DGC) in the UK, the model was developed by the NOAA's National Centers for Environmental Information (NCEI) and the British Geological Survey (BGS). Its primary goal is to provide the magnetic declination, the difference between a magnetic bearing and a true bearing, at every point on Earth's surface, but the Gauss coefficients it produces every 5 years can be used in many other applications. In its publications, it contains Gauss coefficients up to degree and order 12 for that 5-year period as well as an estimated time evolution of the coefficients for applications beyond the 5-year period [73].

Earth's Radiation Budget

Lastly, three model choices for the Earth albedo and emissivity (α_{alb} and α_{ir} in Eqs. (2.32) and (2.33)) are available in D-SPOSE. The first is a set of monthly-averaged values derived from satellite observations between 1964 and 1977 [76]. The second and third are obtained from two different observation centers: the Clouds and the Earth's

Radiant Energy System (CERES), an experiment funded by the National Aeronautics and Space Administration (NASA), and the European Centre for Medium-Range Weather Forecasts (ECMWF), both data sets obtained from monthly-averaged values from 2000-2015 satellite data [77, 78]. These encompass the final three external files incorporated in D-SPOSE containing the values for each the albedo and emissivity coefficients for every month of the year and for each Earth surface element, divided in $9^\circ \times 9^\circ$ latitude-longitude bins [6].

2.5 Validation

In the interest of giving credence to the developed propagator, comparing simulation results to observations of satellites for which there exists abundant measurements of the evolution of their attitude state would demonstrate its utility and benefits. Spherical non-attitude-controlled geodetic satellites prove to be ideal candidates for this due to the fact that they are equipped with multiple corner cube reflectors (CCRs), a necessity for geodesy studies. In this light, D-SPOSE is applied to three such passive spacecraft that have been continuously tracked by the ILRS since launch using high-repetition-rate (kHz) satellite laser ranging (SLR) from which attitude estimates have been determined: the American and Italian Laser Geodynamics Satellite 2 (LAGEOS-2) and Laser Relativity Satellite (LARES), and the Japanese Ajisai satellite [91, 92, 93]. In addition to SLR, photometric measurements (light curves) leading to further observations of their attitude state when the satellites are illuminated by the Sun have also been obtained for LAGEOS-2 and Ajisai [9, 8].

Previous spin models have already been developed for these satellites, most notably the LageOS Spin Axis Model (LOSSAM) and its recent upgrade, the LArase Satellites Spin mOdel Solutions (LASSOS) model [94, 95]. However, these models were tailored specifically for these geodetic spherical satellites and can not be applied to any generic spacecraft. The development of D-SPOSE fills a gap in ongoing research into the spin dynamics of space debris, with the possibility of being applied to large satellites where any of the multiple torques included can manifest itself as the dominant external perturbation.

Much effort has already been made to try and understand the spin dynamics of these satellites [91, 94, 95, 96]. The goal of this study is not to try and improve these

satellite-specific models, but to see whether the tool constructed for space debris remediation purposes could reproduce past observation results. Simulations were therefore performed and compared to these observations. The core of this Section can be found in Sagnières et al. [97].

2.5.1 LAGEOS-2

As a result of the success of the LAGEOS mission launched in 1976, NASA and the Italian Space Agency (ASI) joined forces to build a twin satellite in order to continue the scientific endeavours of the original mission. LAGEOS-2 was finally launched on October 22, 1992 in a 52.6° inclined, nearly circular orbit at approximately 5,800 km altitude. Its mission objective was to provide laser ranging measurements for a variety of geodetic studies. As such, precise observations of the satellite's position have been made since its launch [91]. Furthermore, high-repetition-rate SLR data have made possible the determination of its spin period and spin axis orientation, which have enabled studies of general relativity effects such as the Lense-Thirring effect [98]. In addition, light curves coming off the spacecraft have been analyzed, providing another source of estimates of its spin period and spin axis orientation [9].

Two major spacecraft parameters influence greatly the spacecraft's spin dynamics due to the dominance of the torques associated with them: the moments of inertia, affecting the gravity-gradient torque, and the magnetic tensor, influencing the eddy-current torque. However, as it was not thought at the time of launch that such precise orbit measurements would be obtained or could be improved by measuring satellite's spin state, these were not determined before launch [99]. Nevertheless, multiple efforts have been made to estimate them.

An in-depth review and critical analysis of past estimates of the mass and inertia properties of LAGEOS-2 were made as part of the LASer RAnged Satellites Experiment (LARASE) research program [99]. This project aims to improve modelling and measurements of general relativity effects from satellite laser ranging data [98]. Conclusions on the LAGEOS-2 properties were drawn from all available information in the literature and from an analysis of the satellite's spin dynamics using the LOSSAM model; the estimated mass and moments of inertia of the satellite were $m = 405.38 \text{ kg}$, $I_z = 11.45 \pm 0.03 \text{ kg m}^2$ and $I_x = I_y = 11.00 \pm 0.03 \text{ kg m}^2$ [94, 99]. Furthermore, the satellite's center of mass was found to be $-0.053 \pm 0.025 \text{ cm}$ from the geometric centre of the slightly oblate sphere along its symmetry axis, assumed here to be the z-axis,

and the sphere's radius was estimated to be 30 cm [94]. Figure 2.7 shows the spacecraft geometry, divided into 264 surfaces, used as input into D-SPOSE along with all of the parameters presented in Table 2.4.

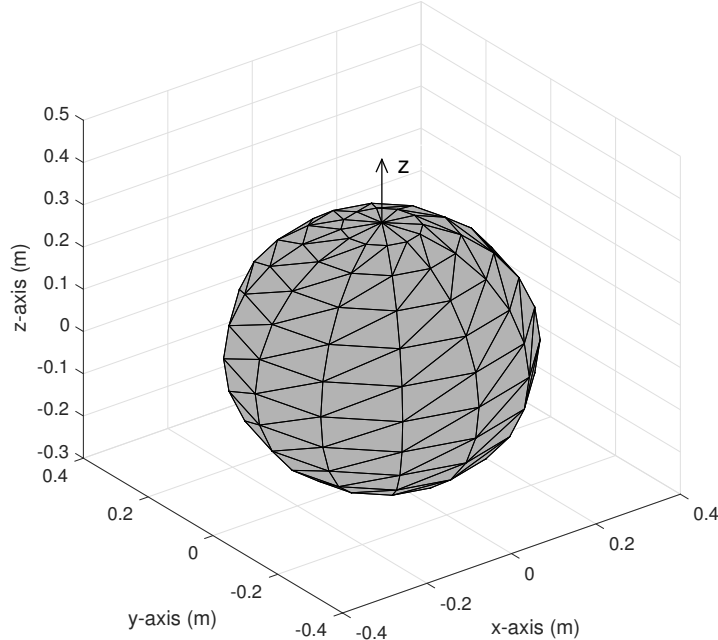


FIGURE 2.7: LAGEOS-2 Surface Geometry Model

TABLE 2.4: Parameters of the Spherical Geodetic Satellites

Spacecraft	m (kg)	$I_x = I_y$ (kg m^2)	I_z (kg m^2)	r (cm)	h_{com} (cm)	C_r	ΔC_r	M (S m^4)
LAGEOS-2	405.38	11.00	11.45	30	-0.053	1.12	0.012	5900
LARES	386.8	4.76	4.77	18.2	0	1.07	0	450
Ajisai	685.1	485	525	107.5	0	1.12	0	625

The magnetic tensor, on the other hand, has never been estimated. In the case of LAGEOS-2, an initial estimate for the magnetic tensor can be obtained by considering the satellite as a thick spherical shell whose matrix representation of the magnetic tensor in the centroidal body-fixed frame has previously been shown to be approximated by:

$$\mathbf{M} = \text{diag}\{M, M, M\} \quad (2.35)$$

with [100]:

$$M = \frac{2}{15}\pi\sigma\mu_r^2(b^5 - a^5) \quad (2.36)$$

where σ is the body's electrical conductivity, μ_r is its relative permeability, and b and a are the shell's outer and inner radius, respectively.

Although the structure of the LAGEOS-2 spacecraft is complex, made up of elements composed of various materials, we can use the formulation in Eq. (2.36) to derive an estimate of the magnetic tensor. As LAGEOS-2 is coated with aluminum, whose conductivity is $2.459 \times 10^7 \text{ S m}^{-1}$ and relative permeability approximated to 1, we can consider the spacecraft as an aluminum shell [94]. With a radius of 30 cm and a shell thickness of 1.5 cm, we obtain $M = 5662 \text{ S m}^4$; however, multiple simulations were executed by varying this value to obtain the best fit when comparing to observations.

The initial conditions of the satellite were selected from observations in early March 2000 and propagated for a period of 8 years with a time step of 1 s. A simulation with a time step of 0.1 s was also performed, showing no difference in the results, confirming internal conservation of energy. The following TLE was chosen to initialize the orbit:

```
1 22195U 92070B    00063.73989110 -.00000009 00000-0 10000-3 0   8627
2 22195   52.6411 214.8667 0137462 309.2891 49.5566 6.47294321174037
```

The initial spin period and orientation of the spin axis were taken from light curve observations at the same epoch: a spin period of 17.27 s, the declination and right ascension (RA) of the spin axis of the satellite -65.78° and 272.36° , respectively, determined to be the major principal axis, and body-frame z -axis in Fig. 2.7 [9]. All of the initial conditions are presented for LAGEOS-2 in Table 2.5 with the semi-major axis (a), the inclination (i), the eccentricity (e), the right ascension of the ascending node (Ω), and the argument of perigee (ω_{aop}).

TABLE 2.5: Initial Conditions for Spherical Geodetic Satellites

Spacecraft	Date	a (km)	i ($^\circ$)	e	Ω ($^\circ$)	ω_{aop} ($^\circ$)	Spin Period (s)	Declination ($^\circ$)	RA ($^\circ$)
LAGEOS-2	2000-03-03	12162	52.64	0.0137	214.87	309.29	17.2712	-65.78	272.36
LARES	2012-02-15	7820	69.49	0.0011	234.48	296.06	11.8	-73	186.5
Ajisai	2003-01-01	7867	50.01	0.0011	211.16	333.89	1.905	-87.5	-20

The optical coefficients for direct solar radiation were determined from previous studies [95]. A reflectivity coefficient of $C_r = 1.12$ with a reflectivity difference between the north and south hemispheres of the satellite of $\Delta C_r = 0.012$ were found. From these, assuming that radiation is emitted diffusely, approximate values of σ_{rd} and σ_a of 0.17 and 0.83 for the north hemisphere, and 0.19 and 0.81 for the south hemisphere, respectively, were set.

In the simulations of LAGEOS-2, reflected and emitted radiation were not considered due to the negligible impact on a satellite of spherical shape. Aerodynamic drag and torque were also neglected due to the altitude of the satellite orbit. Similarly, as the satellite is initially in a major-axis spin, internal energy dissipation was not considered. The magnetic potential model used was IGRF-12 and EGM2008 coefficients up to degree and order 2 were adopted.

Figure 2.8 shows the evolution of a) the spin period, b) the spin axis declination, and c) the spin axis right ascension in the inertial frame, for the entire propagation. The best fit simulation results obtained by varying the value of M only are presented with the black line, and observations made from SLR data are shown in blue [91], while the ones made from photometric measurements are shown in red [9]. The SLR data covers the period from 2000 to the end of 2007, while estimates obtained from light curves are available from 2000 to the end of 2004. As can be seen from the figure, using the input parameters stated in Table 2.4, simulations and observations agree well. The simulation shown was obtained with the value of $M = 5900 \text{ S m}^4$ used in the magnetic tensor, which is very close to the initial analytical estimate of 5662 S m^4 . An almost perfect agreement can be seen with light curve observations of the spin axis orientation, which show much less scatter than its SLR counterparts. The differences observed with SLR observations can most likely be attributed to uncertainty in the measurements, but could also come from uncertainty in input parameters. As was mentioned, the moments of inertia and other spacecraft parameters are not perfectly known and would have a noticeable impact on simulation results.

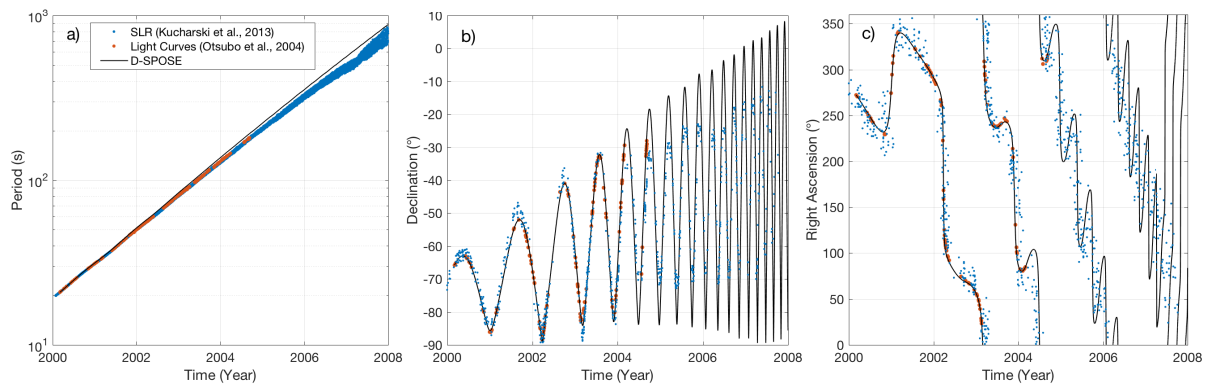


FIGURE 2.8: Evolution of LAGEOS-2 Spin Parameters in Inertial Frame

As mentioned in Section 2.1.1, a more convenient way to visualize the motion of

a spacecraft's spin axis is through the ECO frame. When influenced by the gravity-gradient torque only, the motion of a spinning satellite's angular momentum vector will form a closed path; as the eddy-current torque slows down its rotation, however, the closed path will evolve. Figure 2.9 contains the evolution of the spin axis orientation from the simulation throughout the entire propagation in this frame. Figure 2.9c characterizes the evolution of the spin axis in the ECO frame in an equidistant azimuthal projection along the line of sight of the orbit normal direction (z_0 -axis) from the negative to the positive. The starting point of the motion on March 3, 2000 is indicated by a plus sign. As one can see, the LAGEOS-2 spin axis evolves towards a rotation about a point slightly displaced from the negative orbit normal with an increasing amplitude and decreasing period, a much less chaotic motion than it seems by looking at the motion in the inertial frame in Fig. 2.8.

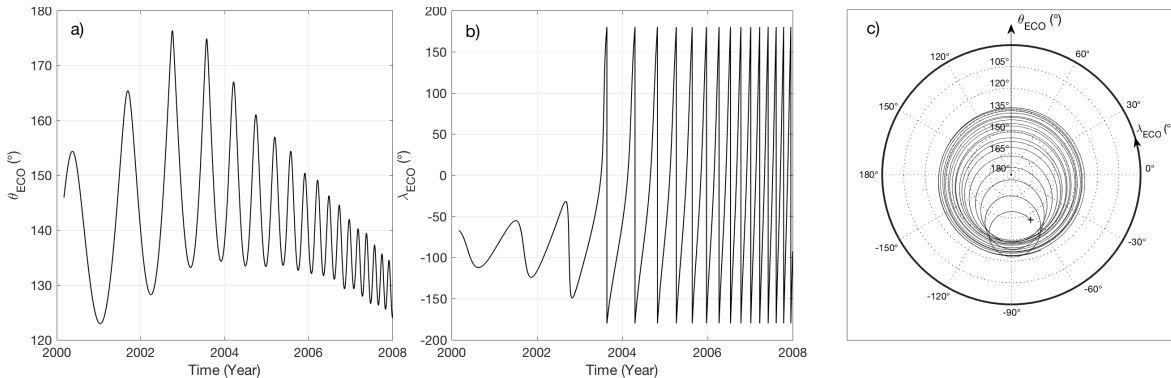


FIGURE 2.9: Evolution of LAGEOS-2 Spin Axis in ECO Frame from Simulation

2.5.2 LARES

On February 13, 2012, the European Space Agency (ESA) launched the new Italian LARES spacecraft and placed it in a circular orbit at an altitude of 1450 km and an inclination of 69.5° . Its main mission was to send back observations of Earth's gravity field and provide much-needed geodetic measurements in combination with the LAGEOS program. Just like LAGEOS-2, it is a fully passive spherical satellite containing multiple CCRs on its surface for SLR observations.

First SLR measurements were obtained shortly after its launch, showing that although the body was made of a non-magnetic alloy so that the interaction with the

Earth's magnetic field would be minimal, eddy-currents still occurred and slowed-down the satellite's spin [101]. A longer observation campaign, from February 2012 to April 2013, was then performed showing a precession of the spin axis; the LOSSAM model was applied to LARES and showed an agreement between simulation results and these observations [92].

Recently, the LASSOS model was developed to further the efforts of providing accurate modelling of the LAGEOS and LARES spin parameters [95], also providing accurate information on the input parameters for their model. Using these parameters, we tried to replicate the observations using D-SPOSE.

The surface geometry of LARES was assumed to be a sphere with a radius of 18.2 cm divided into 264 surfaces, similarly to LAGEOS-2 as shown in Fig. 2.7 but with the center of mass assumed to be at the sphere's geometric center, with moments of inertia values of $I_x = I_y = 4.76 \pm 0.03 \text{ kg m}^2$ and $I_z = 4.77 \pm 0.03 \text{ kg m}^2$ and a spacecraft weight of $m = 386.8 \text{ kg}$ [95]. The reflectivity coefficient was previously determined to be 1.07; so, under similar assumptions as for LAGEOS-2, the coefficients of absorption and diffuse reflection were set as 0.9 and 0.1, respectively, with no difference in reflectivity among both hemispheres [95]. The parameters that were used as input into the propagator for LARES are summarized in Table 2.4.

Again, aerodynamic perturbations, internal energy dissipation, and emitted and reflected radiation were not considered. The initial TLE was taken right after launch, in mid-February 2012, and the propagation length and time step were set to 1.5 years and 1 s, respectively:

1	38077U	12006A	12046.96446026	-.00000022	00000-0	10000-3	0	130
2	38077	69.4848	234.4843	0011091	296.0553	63.9332	12.54929120	333

The initial spin period and orientation of the spin axis were taken from SLR measurements right after launch: a spin period of 11.8 s, a spin axis orientation with a -73° declination and a 186.5° right ascension, assuming the spin axis of the satellite to be the z -axis [92]. These initial conditions, including the spin parameters and orbital elements at the TLE epoch are presented in Table 2.5. Figure 2.10 shows the evolution of a) the spin period, b) the spin axis declination, and c) the spin axis right ascension in the inertial frame for the entire propagation in black, with the SLR observations and a fit of the inertial spin period shown in blue [92].

Similarly to LAGEOS-2, an initial value for the magnetic tensor was obtained from Eq. (2.36). Assuming a similar structure to what was used for LAGEOS-2 but for an

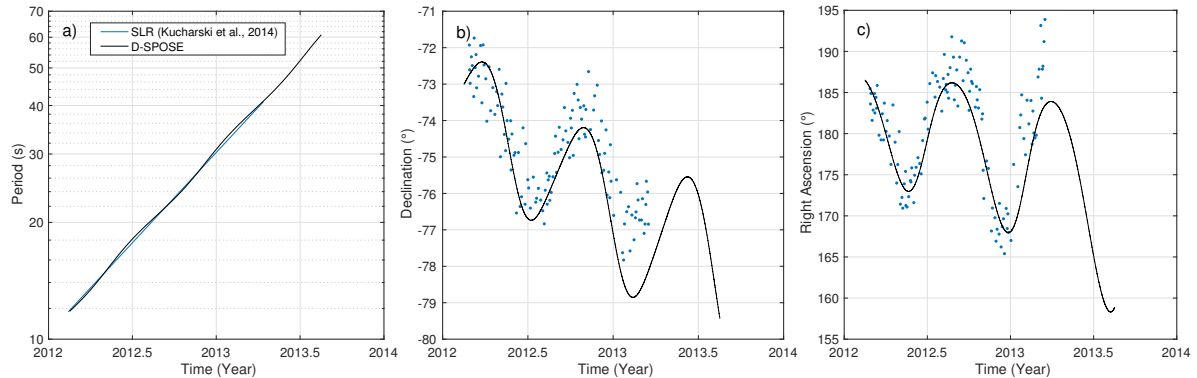


FIGURE 2.10: Evolution of LARES Spin Parameters in Inertial Frame

aluminum shell with a radius of 18.2 cm and a thickness of 1 cm, the initial value of $M = 506 \text{ S m}^4$ was set. In order to reproduce the spin period increase, however, a magnetic tensor with $M = 450 \text{ S m}^4$ was determined to provide the best fit, agreeing reasonably well with the initial estimate.

Once more, a good agreement exists between observations and simulation results. Nevertheless, a departure between both seems to appear towards the end of the propagation, again likely due to uncertainties in observations, but also in the input parameters used, particularly the moments of inertia, which play a crucial role in the precession motion of the spin axis under the influence of the gravity-gradient torque. More observations would be needed to investigate this further.

As was done for LAGEOS-2, the motion of the LARES spin axis in the ECO frame was analyzed. Figure 2.11 displays the evolution of the two angles θ_{ECO} and λ_{ECO} fixed with the precessing orbit for the 1.5-year propagation. Throughout the simulation, the spin axis seems to be rotating about a point approximately 110° from the orbit normal and -90° from the ascending node. The amplitude of the motion also seems to be decreasing with time, with one revolution completed in a little over six months. However, this represents only one and a half years and more observations would be needed to compare to simulations at a future date and to fully characterize the resulting motion.

2.5.3 Ajisai

Originally named the Experimental Geodetic Payload, Ajisai is a Japanese satellite that was launched in August 1986 in an orbit of 1500 km and 50° inclination. It is a

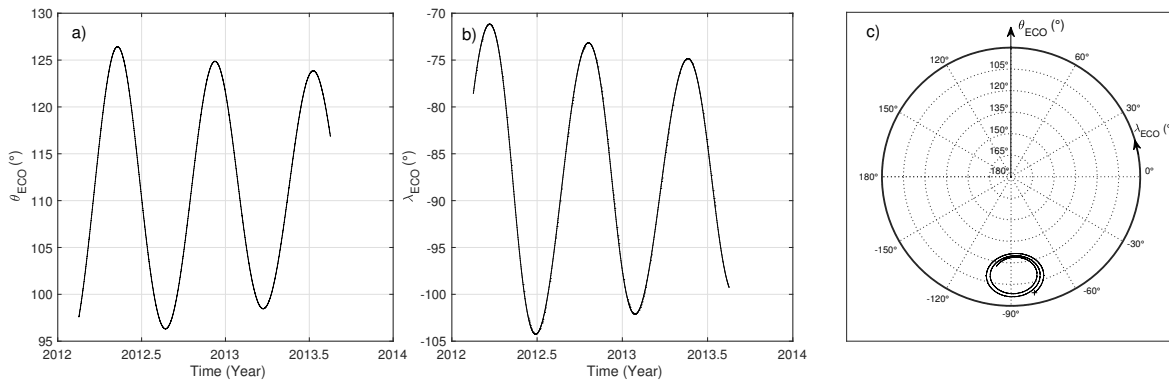


FIGURE 2.11: Evolution of LARES Spin Axis in ECO Frame from Simulation

passive geodetic satellite that had the purpose of improving Japan’s geodetic network and calculating the accurate positions of the many Japanese islands. It contains 1436 CCRs as well as a nutation damper, limiting the effect of external perturbations helping to maintain a major-axis spin [102]. However, being much larger than the two previous satellites with a radius of 107.5 cm but in the same mass range ($m = 685.1$), its high area-to-mass ratio leads to higher uncertainties from non-gravitational perturbations [102]. The spacecraft was originally launched in a spinning state with a spin period of 1.5 s and with its spin axis aligned with the Earth’s rotation axis.

Like LAGEOS-2 and LARES, it has been continuously tracked by SLR stations and photometric measurements have been made throughout its lifetime. In Graz, Austria, thousands of satellite passes have been observed from a high-repetition-rate SLR station. An analysis of 4599 passes from October 2003 to November 2014 from which the spin axis orientation was obtained revealed a precession and nutation of the Ajisai spin axis, similar to what was seen for the previous two satellites [93]. Moreover, 279 photometric observations have been analyzed from 2009 to the end of 2015 providing additional measurements of the satellite’s spin axis orientation and spin period [8]. These two data sets are shown in Fig. 2.12 and represent the largest observation data set among the three spacecraft considered.

In order to validate our propagator, a simulation was run for Ajisai and compared to these observations. The satellite mass and radius were set to be 685.1 kg and 1.075 m [102]. The surface geometry was divided into 264 surfaces. The same reflectivity coefficient as LAGEOS-2 was used, with no difference between the hemispheres and no offset of the center of mass with the geometric center as no accurate data was available.

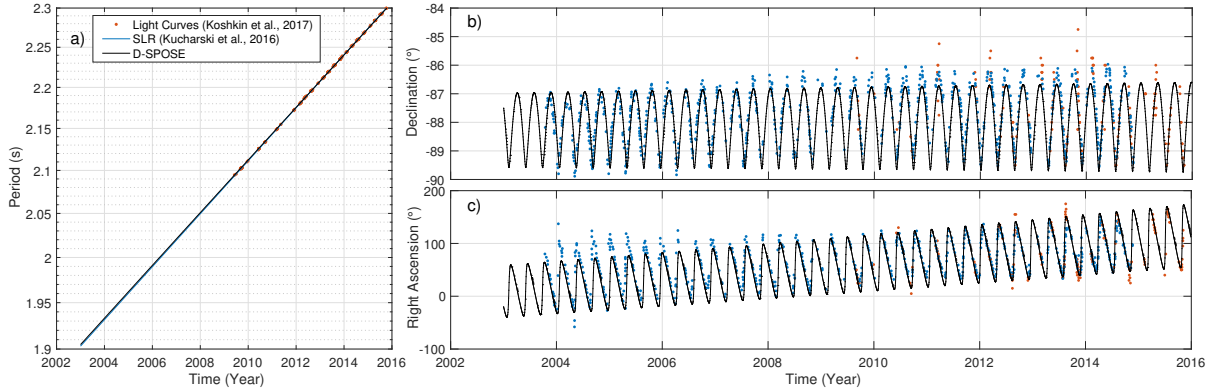


FIGURE 2.12: Evolution of Ajisai Spin Parameters in Inertial Frame

Similarly to LAGEOS-2 and LARES, little information exists in the literature on Ajisai's inertia properties. During the analysis of the SLR measurements, an estimate of $I_z = 527.7 \text{ kg m}^2$ and a ratio of the principal moments of inertia of 1.09 was determined [93, 103]. Approximate values of $I_x = I_y = 485 \text{ kg m}^2$ and $I_z = 525 \text{ kg m}^2$ were therefore used in our simulations.

The estimation of the magnetic tensor is more complicated for Ajisai than it was for the other two spacecraft. The composition of Ajisai is very different from LAGEOS-2 and LARES; Ajisai was built to minimize the effect of eddy currents, with dielectric film placed in layers in the body's external structure [93]. Eddy-currents therefore have a much smaller influence than they do for the other spacecraft, a fact that is observable in the slow increase of its spin period over the 13-year observation time frame shown in Fig. 2.12. Nevertheless, the best fit for the magnetic tensor was found to be 625 S m^4 . The parameters that were used as input into the propagator for Ajisai are summarized in Table 2.4.

The initial spin period and orientation of the spin axis were estimated for early 2003: a spin period of 1.905 s, and a spin axis orientation with a -87.5° declination and a -20° right ascension were used for initial conditions, again assuming the spin axis of the satellite to be the z-axis. The initial TLE was taken at the beginning of 2003, at the start of the SLR observations:

```
1 16908U 86061A 03001.47495629 -.00000083 00000-0 10000-3 0 7483
2 16908 50.0093 211.1607 0011280 333.8863 26.1414 12.44446750413909
```

The initial conditions for Ajisai, including the spin parameters and orbital elements at the TLE epoch are presented in Table 2.5. The results of the propagation are presented

in Fig. 2.12, with a) the spin period, b) the spin axis declination, and c) the spin axis right ascension in the inertial frame for the entire propagation in black. The SLR and light curve observations are shown in blue and red, respectively [8, 93]. Aerodynamic perturbations, internal energy dissipation, and emitted and reflected radiation were once more not considered in the simulations. A propagation length of 13 years was selected to cover the observation time span. A time step of 0.5 s was chosen as Ajisai is spinning very quickly compared to the other two spacecraft and the usual time step of 1 s was not adequate to conserve energy; a subsequent check with a time step of 0.1 s did not show any differences compared to the results obtained with a time step of 0.5 s.

Once more, the results agree well with the observations, taking into account the uncertainty related to both data sets. Both sources of observations, SLR and light curves, show a similar scatter of observations and a similar agreement with the simulation results. The spin period increase is well captured using the determined magnetic tensor value of 625 S m^4 . There is, however, a small discrepancy seen in the right ascension at the beginning of the propagation. Nevertheless, if we take into account the fact that the declination is very close to -90° , for large fluctuations of the right ascension, the actual angular difference in the spin axis orientation at that declination is very small.

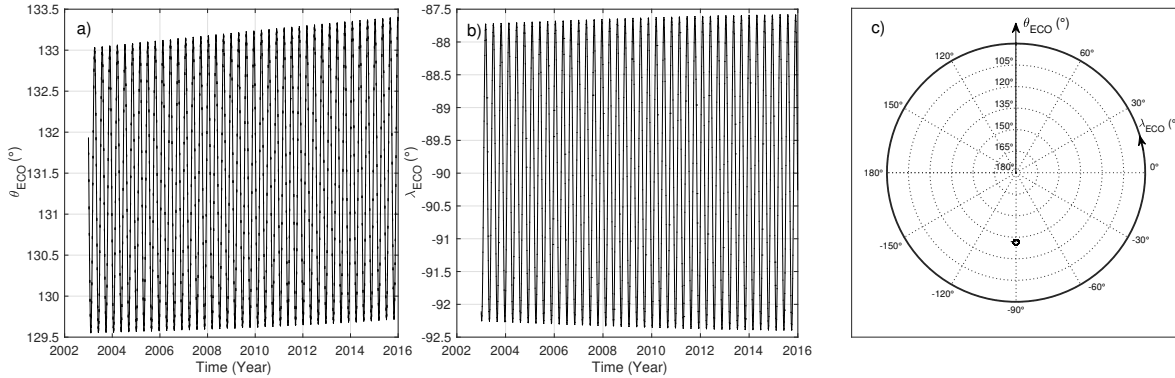


FIGURE 2.13: Evolution of Ajisai Spin Axis in ECO Frame from Simulation

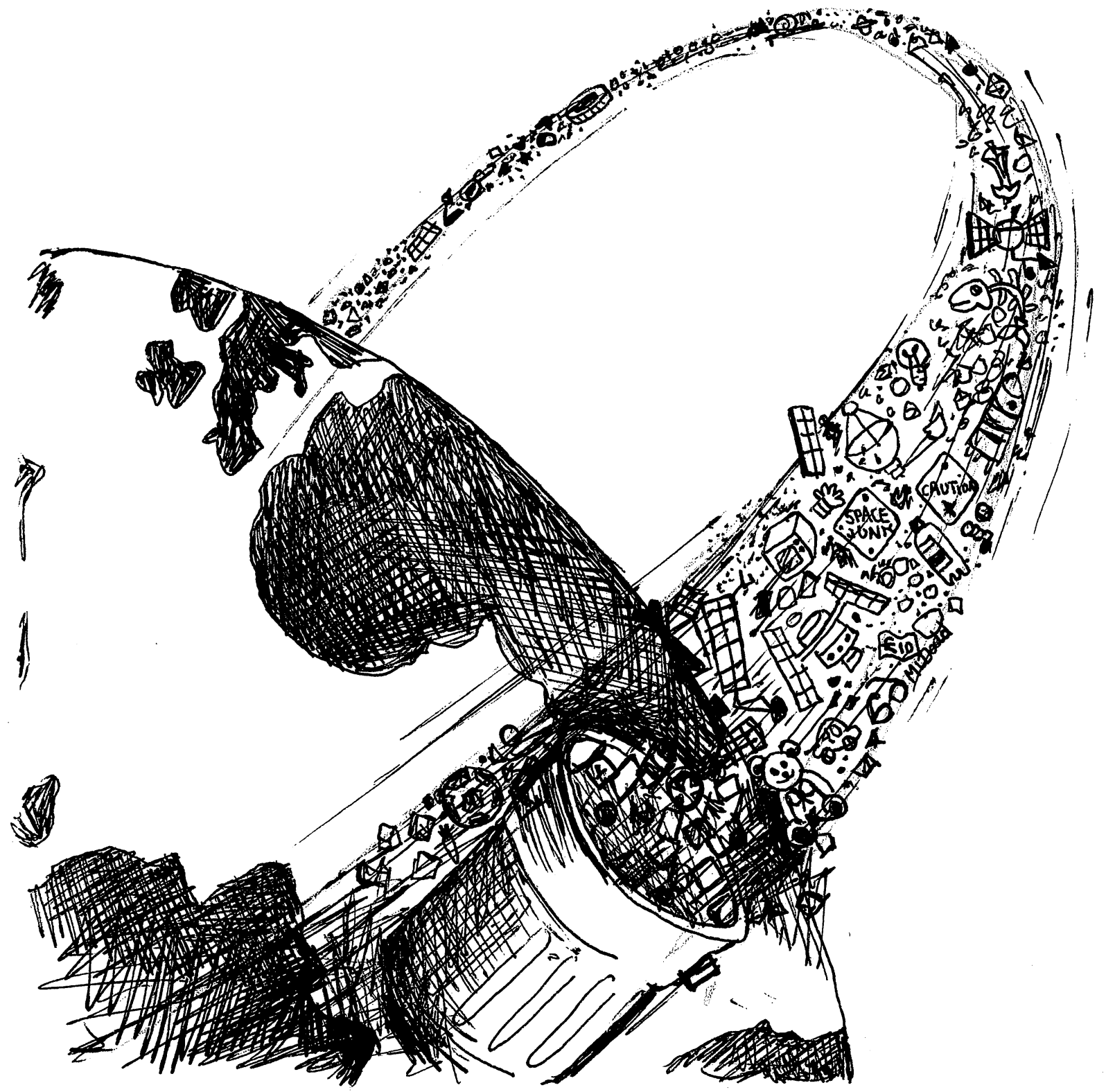
Switching over to the orbital frame, Fig. 2.13 shows the evolution of the two angles θ_{ECO} and λ_{ECO} fixed with the precessing orbit for the 13-year propagation. As we can see, the spin axis is very much fixed in this reference frame at a point close to 131° from the orbit normal and -90° from the ascending node. A small increase in the amplitude of the oscillation can be seen, showing the increasing effect of the external perturbations as the spacecraft steadily slows down.

2.6 Concluding Remarks

Studying the spin dynamics of defunct spacecraft is of the utmost importance when considering their retrieval from orbit. The novel coupled orbit-attitude propagator developed for such studies, called D-SPOSE, was presented and the underlying model was described, with an emphasis on its comprehensiveness and flexibility of operation. The dynamics and external perturbations considered were presented; the environmental models and external software used were described; and the modes of operation were outlined.

High-repetition-rate SLR observations and light curve measurements from three passive spherical geodetic satellites, LAGEOS-2, LARES, and Ajisai, for which observations of their spin state are abundant, were compared to simulation results, confirming the benefit of the presented attitude dynamics model for future application to defunct satellites as part of space debris remediation efforts. Some discrepancies exist, especially when comparing simulations results to SLR observations, but these are due to the fact that a relatively large spread in observations exists and that the inertia and magnetic properties of the spacecraft are not well known leading to uncertainties. Furthermore, it was shown that studying the spin dynamics of satellites orbiting Earth is more convenient when looked at from the perspective of the rotating reference frame precessing with the orbit. This is due to the fact that, when dominant, the gravity-gradient torque forces a closed-loop motion of a satellite's spin axis in this frame.

While a preliminary validation was performed, confirming the reliability of the gravity-gradient torque and eddy-current torque computations, it needs to be kept in mind that the effect of aerodynamic torque was not assessed. Moreover, radiation pressure only had a minimal influence on the attitude evolution of the spherical satellites. These effects will be tested for a different type of satellite in Chapters 4 and 5. The influence of hypervelocity impacts on the attitude and orbit of Earth satellites will now be discussed.



Marion Dodd

"Wish Upon a Coke Can"

Drawing ink on paper

Chapter 3

Stochastic Modeling of Hypervelocity Impacts

Collisions between small orbital debris and micrometeoroids, on the one hand, and active and inoperative satellites, on the other, are typically considered in the context of the increasing threat that they present to space operations and missions [13]. From a somewhat different perspective, the impacts between the small debris flux and a large object, be it a functional or defunct spacecraft, will lead to a transfer of momentum from the impactor to the target, thus modifying its orbital and rotational parameters. Moreover, at such high velocities, the particles ejected during crater formation provide an additional momentum transfer, an effect known as momentum enhancement [104]. While many of the environmental factors influencing an object's orbit in space introduced in the previous Chapter have been extensively studied, the effect of bombardment of debris and meteoroids on spacecraft orbit propagation is a research area that is still in its infancy [56, 105, 106].

The core of this Chapter will discuss a methodology for including hypervelocity impacts into spacecraft orbit and attitude propagation models by considering the transfer of linear and angular momentum from collisions as a stochastic jump process known as a compound Poisson process, as was put forward by Sagnières and Sharf [80, 81, 107]. The differential equations for orbital and attitude motion then become stochastic differential equations (SDE) and are solved in a Monte Carlo simulation by employing independent sets of randomly generated collisions that can be obtained using impact fluxes converted into probability density functions (PDF) and obtained from the European Space Agency's (ESA) Meteoroid and Space Debris Terrestrial Environment Reference (MASTER) model describing the debris and meteoroid population around Earth [22]. Furthermore, the additional effect of momentum enhancement, which is

dependent on the orientation of the spacecraft, can also be implemented, calculated for every collision by considering the velocity, mass and direction distribution of the ejecting particles from another model developed for ESA defining the characteristics of such ejecta [104].

First, a review of the problem and of past work on the subject will be detailed in Section 3.1. Second, an introduction to stochastic processes and an explanation of how and why hypervelocity impacts can be thought of as a compound Poisson process will be given in Section 3.2. Third, Section 3.3 will discuss the implementation of such a stochastic process in the equations of motion and its numerical solution. Fourth, the method to include the momentum associated with ejecta created during the hypervelocity impacts is outlined in Section 3.4. Finally, in Section 3.5, the developed procedure is applied to two space debris objects: the defunct European satellite Envisat and a high area-to-mass ratio (HAMR) object modeled after a multi-layer insulation (MLI) material.

3.1 Particle Impacts

Changes in angular velocity due to debris and meteoroid collisions have already been witnessed in several space missions. When the spacecraft Giotto went through the dust tail of comet 26P/Grigg-Skjellerup in July 1992, a decrease in the spin period of 0.8 ms and a nutation of 0.1° was determined by two-way Doppler measurements [108]. Similarly, during the Hipparcos mission, more than 150 changes in angular velocity were seen and attributed to impacts from debris or meteoroids, with values ranging from the lower sensitivity threshold of 0.03 milliarcseconds (mas) s^{-1} up to a few 100 mas s^{-1} [109]. Furthermore, the Gaia spacecraft is expected to face up to 20,000 impacts per year during its mission, although smaller collisions below the detection threshold will also most likely occur [109]. More recently, the Russian Ball Lens In The Space (BLITS) satellite saw its mission end abruptly in January 2013 after a three-year operation when it collided with a piece of space debris, most likely a fragment of the Chinese Fengyun-1C weather satellite destroyed in 2007. Its spin period was reduced from 5.6 s to 2.1 s after impact [110].

The earliest studies dealing with impact effects of meteoroids on spacecraft attitude date back to the middle of the Space Race. A simple probabilistic study on the angular disturbance to a spacecraft resulting from meteoroid bombardment was performed,

deriving an equation for the change in angular velocity as a function of the probability of being hit for any given spacecraft parameters [111]. The equation was applied to a satellite in geosynchronous orbit, finding that over one year the most probable angular disturbance of such a spacecraft would be $10^{-3} \text{ }^\circ \text{ s}^{-1}$ with a probability of 36.8%, and that approximately 1% of spacecraft would notice a change of $0.34 \text{ }^\circ \text{ s}^{-1}$. A similar analysis specifically for gravity-gradient stabilized satellites also found that a deflection of 5° or more from the earth-oriented orientation would only happen once every several years and that a complete overturn of the satellite due to a single impact would only occur once in 250 years on average, or up to 1000 years depending on the satellite geometry and meteoroid flux used. It was therefore concluded that impacts with meteoroids are not a serious issue [112]. It was also shown in a later study that an anisotropy in the meteoroid flux combined with an asymmetry in the spacecraft geometry would lead to a steady-state attitude disturbance for attitude-stabilized spacecraft, but that any calculation would contain large uncertainties due to the effect known as momentum enhancement, when an additional transfer of momentum to the target is generated from the ejecta material being thrown backwards during these hypervelocity impacts [105].

As a comparison to other torques, Hughes [56, Ch. 8, p. 266] also provided a rough estimate of the incident normal pressure arising from meteoroid collisions and saw that it was more than four orders of magnitude smaller than the value of solar radiation pressure. He concluded that the meteoroid impact torque is therefore negligible. However, this estimate was obtained using a 1969 meteoroid flux model and did not include the current space debris population. In addition, the momentum enhancement effect was not taken into account.

The most complete study of momentum transfer to spacecraft from hypervelocity impacts to date was documented as an internal report by the ESA European Space Research and Technology Centre (ESTEC) [109]. The goal of the study was to obtain an estimate of the collisional flux as a function of angular velocity change, specifically for the preparation of the Gaia mission. Subsequently, the model was fitted empirically to obtain an equation of the number of impacts per year as a function of momentum transfer and it was then incorporated into Gaia's Dynamical Attitude Model [113]; however, this model was not an attitude propagation model. Due to the stochastic nature of collisions in the space environment, implementing collisions into the differential equations of motion as seen in Chapter 2 will need to make use of stochastic processes.

3.2 Collisions as a Compound Poisson Process

3.2.1 Stochastic Processes

A stochastic process describes the evolution of a system's random variables over time. In contrast to deterministic processes which can evolve in only one particular way, given an initial condition, these stochastic processes can evolve in multiple, or infinitely many, directions (or paths). As such, they are very useful when wanting to characterize uncertainties of any kind. Stochastic processes are commonly classified either as discrete-time or continuous-time, depending on the possible set of time values associated with the process. A Lévy process is a class of continuous-time stochastic processes with independent, stationary increments: it is used to characterize the evolution of a random variable where the successive displacements are random, independent, and follow the same distribution for the same time interval [114, Ch. 1, p. 13].

The most well known Lévy processes are the Wiener process and the Poisson process. The Wiener process, also called standard Brownian motion, is widely used to represent uncertainties in dynamical systems as it represents the integral of ideal white noise. The Poisson process, on the other hand, is a jump process which counts events, *i.e.*, where the jump size is of value one. A classic example of the Poisson process is counting the number of phone calls arriving at a call center over a period of time, assuming all the calls are independent from one another. A Poisson process $N = \{N_t, t \geq 0\}$ with intensity $\lambda > 0$ is a piecewise constant stochastic process with initial value $N_0 = 0$ such that $N_t - N_s$ follows a Poisson distribution with intensity λ , with probability [114, Ch. 1, p. 8]:

$$P[N_t - N_s = k] = \frac{e^{-\lambda(t-s)} (\lambda(t-s))^k}{k!} \quad (3.1)$$

for $k \in \mathbb{N}$, $t \geq 0$ and $s \in [0, t]$. The time between two independent consecutive jumps is further described by an exponential distribution with the following PDF:

$$f(t; \lambda) = \lambda e^{-\lambda t} \quad (3.2)$$

for $t \geq 0$.

A Poisson process where the jump size is not one, but follows any given distribution, is called a compound Poisson process, $Y = \{Y_t, t \geq 0\}$, where $Y_0 = 0$ and [114,

Ch. 1, p. 11]:

$$Y_t = \sum_{k=1}^{N_t} \xi_k \quad (3.3)$$

for $t \geq 0$, jump sizes ξ_k and a Poisson process N_t with jump times τ_k . A compound Poisson process then produces a succession of jumps, where the time between two jumps again follows an exponential distribution and jump sizes follow any given distribution. The entire process is defined by the set of pairs $(\tau_k, \xi_k)_{k \in \mathbb{N}}$.

In order to represent collisions as a stochastic process, one can make an helpful analogy between the space environment and kinetic gas theory. In the same manner that a rapidly moving particle collides with other particles in a gas, an object in the space environment can be thought to be sweeping a large volume filled with other debris and micrometeoroids. From this analogy, one can say that collisions follow Poisson statistics by assuming that the collisions are independent and arrive at a constant average rate. This assumption is the basis of the flux determination software of the MASTER-2009 model and has previously been used to calculate debris collisional fluxes with spacecraft [22, 113, 115, 116]. More specifically, one can assume that the time between two collisions will therefore follow an exponential distribution. Departure from Poisson statistics, however, are to be expected for cases such as satellite breakups and meteoroid streams when a sudden increase in the number of collisions can occur. If an exponential distribution can be used to define the time between collisions, then it follows that a compound Poisson process can describe these collisions if a distribution for the jump size, and a definition of what the jumps represent, can be determined. By considering the jumps as the linear momentum associated with each collision, with jump sizes equal to the varying associated momentum magnitudes, one can then develop a three-dimensional compound Poisson process describing the collisions to be experienced by an object in space. PDFs describing the linear momentum for these impactors can be obtained using outputs of the MASTER-2009 model.

3.2.2 ESA's MASTER-2009 Model

MASTER-2009, the latest version of the software released in 2011, was developed by the Institute of Aerospace Systems at the Technische Universität of Braunschweig under contract by the European Space Operations Centre (ESOC) [22]. Its purpose is to characterize the population of natural and artificial particulates in the near-Earth environment. It consists of a full three-dimensional description of the debris distribution

from Low-Earth Orbit (LEO) to Geosynchronous Equatorial Orbit (GEO) and incorporates a model for the background meteoroid environment and seasonal meteoroid streams. Furthermore, the software can simulate the future evolution of the debris population and includes a historical component.

The software has multiple modes of operation; the one of interest for this study is the Target Orbit Scenario. In this case, the user can define a certain orbit, and the model will compute a debris and meteoroid impact flux (in $\#/m^2/year$) that an object in such an orbit would encounter. The impact fluxes per unit area per unit time can be extracted as a function of impactor characteristics or orbital parameters. Each flux bin represents the number of collisions a randomly tumbling one-sided $1\ m^2$ surface would encounter per year in orbit from particles falling in that specific parameter bin. Some of the parameters, and the ones of interest here, include impactor mass, impact velocity, and azimuth and elevation angles (ϕ_{azi} and θ_{elev} as defined in Section 2.1.1 of Chapter 2; for clarity, the subscripts will be dropped in this Chapter). A 3D directional impact flux as a function of azimuth and elevation angle can also be obtained. The mass range goes from 10^{-15} to $10^5\ kg$ while the velocity range is from 0 to $60\ km\ s^{-1}$. Figures 3.1, 3.2 and 3.3 show the output impact fluxes as a function of mass, velocity and direction generated for the following orbit characteristics representing that of the defunct European satellite Envisat: a semi-major axis (SMA) of 7136 km, an eccentricity of 0.0001, and an inclination of 98.3° .

The fluxes in the figures are broken down according to impactor type, which were discussed briefly in Chapter 1. The model's reference population is that of 1 May 2009 and consists of objects ranging in size from $1\ \mu m$ to $10\ m$ with an orbiting radius from 6,564 to 43,164 km. The total debris population is divided into source types according to origin and each group is generated by various sub-models. As mentioned in Chapter 1, these include explosion and collision fragments (EXPL and COLL in the figure legend), launch and mission related objects (LMRO), Solid rocket motor dust and slag (SRMD and SRMS), sodium-potassium alloy droplets (NAKD), paint flakes (PAFL), ejecta particles (EJEC), population clouds (CLOUD), and the meteoroid background (MTBG). A complete description of each source type can be found in Flegel et al. [22].

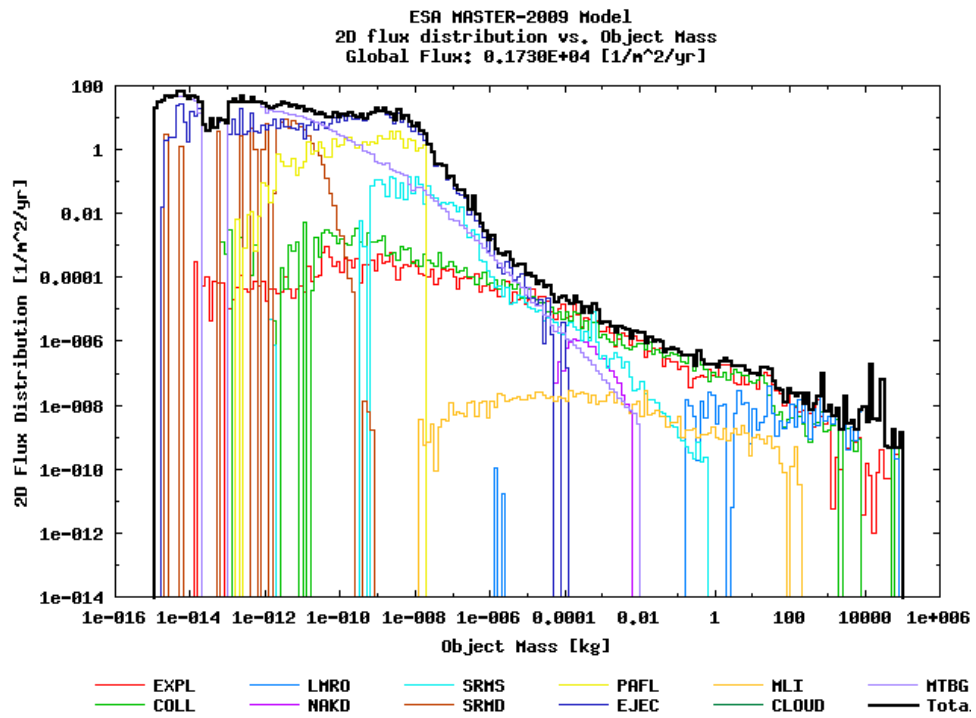


FIGURE 3.1: MASTER-2009 Impactor Mass Flux Distribution

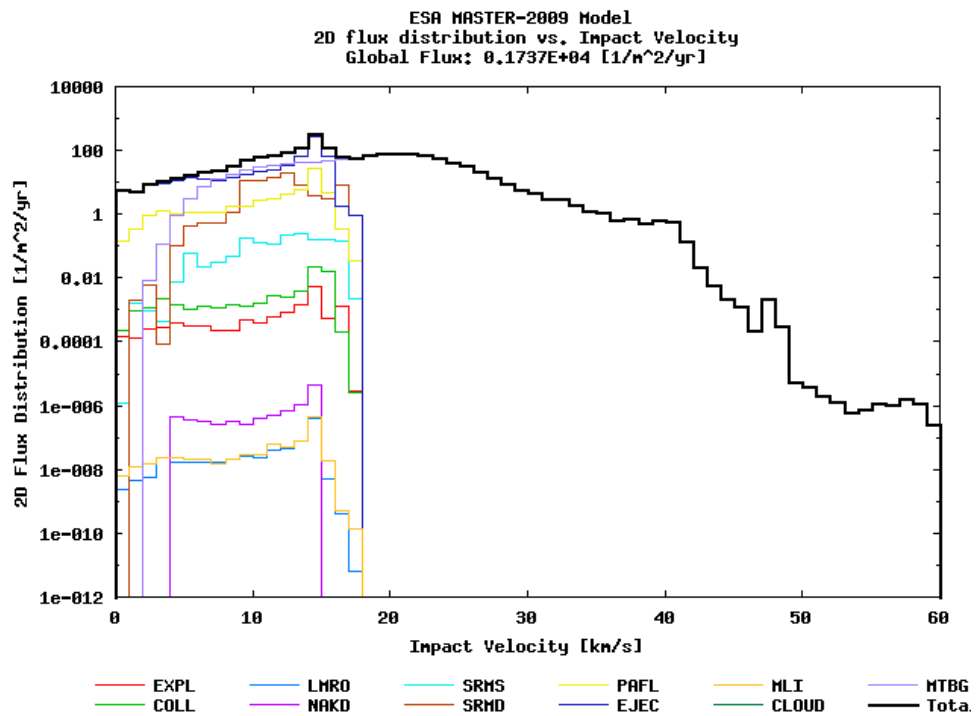


FIGURE 3.2: MASTER-2009 Impact Velocity Flux Distribution

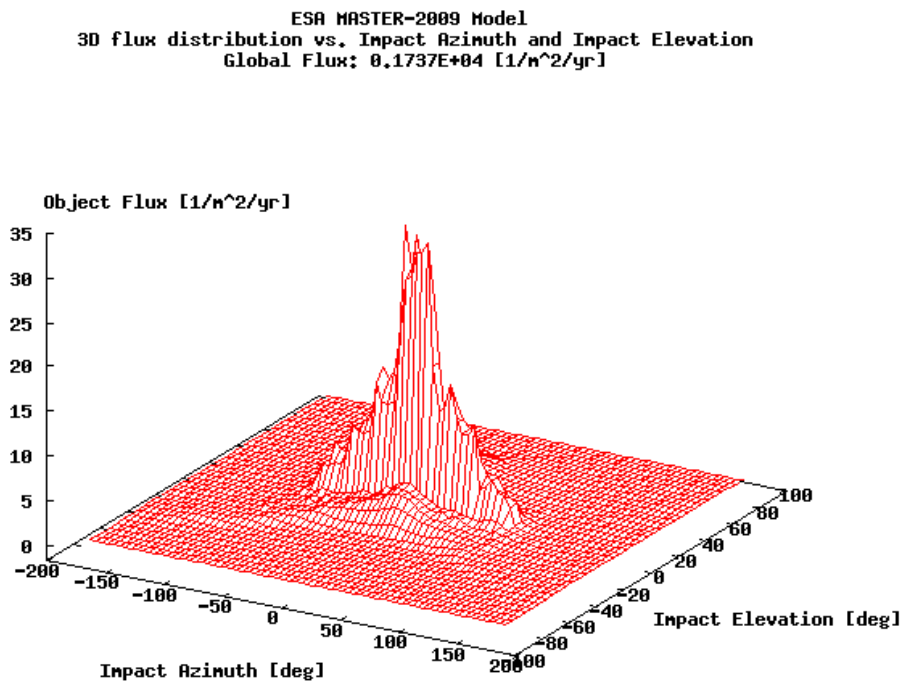


FIGURE 3.3: MASTER-2009 3D Impact Direction Flux Distribution

3.2.3 Converting Impact Fluxes to Probability Density Functions

If a PDF for a continuous random variable X is given by $f_X(x)$ then the probability of X falling between values a and b is defined as:

$$P[a \leq X \leq b] = \int_a^b f_X(x) dx \quad (3.4)$$

In order to obtain a PDF from the fluxes in Figs. 3.1 and 3.2, one needs to divide the value of the flux at every bin by the bin width and by the global flux over the entire range so that $\int_{-\infty}^{\infty} f_X(x) dx = 1$. The derived PDFs can be interpreted in the following way: if an impactor collides with the orbiting target at a certain time, the probability of the impactor having a mass (or relative velocity) between values a and b will follow the distribution defined by Eq. (3.4). A similar two-dimensional joint PDF for direction can be obtained as a function of azimuth and elevation angle. Dividing the value of the flux in Fig. 3.3 at each bin by its area and the global flux, one can obtain a 2D analog to

the PDF defined in Eq. (3.4):

$$P[a \leq \theta \leq b, c \leq \phi \leq d] = \int_a^b \int_c^d f_{\theta,\phi}(x,y) dy dx \quad (3.5)$$

where $f_{\theta,\phi}(x,y)$ is the joint PDF and $P[a \leq \theta \leq b, c \leq \phi \leq d]$ is the probability of the elevation θ falling between a and b and azimuth ϕ falling between c and d .

Using this method, PDFs for impactor mass, impact velocity and a 2D PDF for direction as a function of azimuth and elevation angle can be obtained separately for micrometeoroids and for space debris. It is important to separate the two cases as only micrometeoroids can reach velocities above 20 km s^{-1} and therefore the distributions obtained otherwise would not be independent. The last step is obtaining the exponential distribution describing the time between collisions. From the outputs of the MASTER-2009 run for the orbit specified earlier, a randomly tumbling one-sided 1 m^2 surface will encounter 1737 collisions every year, while 1009 of them are from micrometeoroids. Therefore the intensity of the exponential distribution for such an object will be $\lambda = 1737 / (365.25 \times 24 \times 60 \times 60) = 5.504 \times 10^{-5} \text{ s}^{-1}$ with about 58% of collisions occurring from micrometeoroids. The PDF for such a distribution is shown in Fig. 3.4. Together, the PDFs will define the jump size and jump times representing the compound Poisson process for the linear momentum associated with collisions. As the orbit of the target will vary with time, it is important to remember that these PDFs could also change since the impact fluxes will also differ with the evolving orbit. The assumptions made here are that they remain the same throughout the entire propagation and that they are independent of the position in orbit.

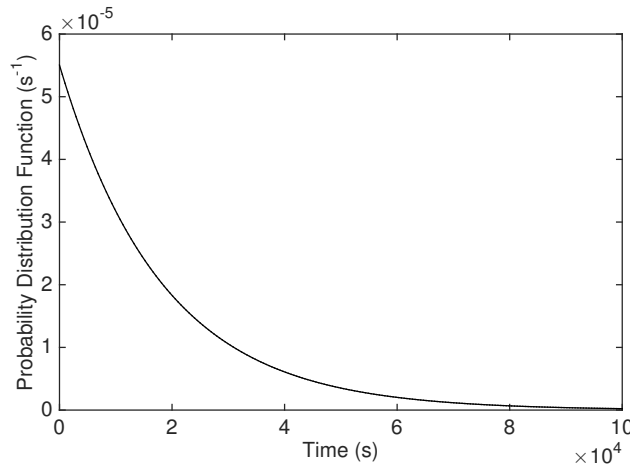


FIGURE 3.4: PDF for Time Between Collisions from MASTER-2009

3.3 Numerical Solution to Stochastic Differential Equations with Jumps

Including a stochastic process in a differential equation transforms it into a stochastic differential equation. First, an SDE with a compound Poisson process representing collisions will be formulated before describing how to solve such an SDE. An explanation of the generation process of the random collisions used to obtain a sample path solution to the SDE will then follow.

3.3.1 Implementing Collisions in Spacecraft Motion Equations

If we consider a stochastic process, X_t , undergoing a compound Poisson process, Y_t , as well as a deterministic process, then the SDE describing its evolution is written in the following way in differential form [114, Ch. 1, p. 43]:

$$dX_t = a(t, X_t)dt + c(t, X_{t^-})dY_t \quad (3.6)$$

where $t^- = \lim_{\epsilon \rightarrow 0} t - \epsilon$ is the time at the left-hand limit of the jump at time t .

From Eqs. (2.4) and (2.5) in Chapter 2, the differential equations for orbital and attitude motion can be set up in differential form:

$$d\dot{\mathbf{r}}(t) = \left(-\frac{\mu}{r(t)^3} \mathbf{r}(t) + \sum_j \mathbf{a}_j(t, \mathbf{r}(t), \mathbf{v}(t), \mathbf{q}(t), \boldsymbol{\omega}(t)) \right) dt \quad (3.7)$$

$$Id\boldsymbol{\omega}(t) = \left(-\boldsymbol{\omega}(t)^\times \mathbf{I} \boldsymbol{\omega}(t) + \sum_j \boldsymbol{\tau}_j(t, \mathbf{r}(t), \mathbf{v}(t), \mathbf{q}(t), \boldsymbol{\omega}(t)) \right) dt \quad (3.8)$$

Considering the momentum of the satellite, defined as $\mathbf{p} = m\dot{\mathbf{r}}$ with m the mass of the spacecraft, Eq. (3.7) can be rewritten as:

$$d\mathbf{p}(t) = m \left(-\frac{\mu}{r(t)^3} \mathbf{r}(t) + \sum_j \mathbf{a}_j(t, \mathbf{r}(t), \mathbf{v}(t), \mathbf{q}(t), \boldsymbol{\omega}(t)) \right) dt \quad (3.9)$$

Including the term for the angular momentum transfer from hypervelocity impacts, as a function of the compound Poisson process for linear momentum, Y_t , and the location of impact, $\mathbf{r}_i(t, \mathbf{q}(t))$, which is also random following a uniform distribution, Eqs. (3.9)

and (3.8) are transformed into SDEs:

$$d\mathbf{p}(t) = m \left(-\frac{\mu}{r(t)^3} \mathbf{r}(t) + \sum_j \mathbf{a}_j(t, \mathbf{r}(t), \mathbf{v}(t), \mathbf{q}(t), \boldsymbol{\omega}(t)) \right) dt + d\mathbf{Y}_t \quad (3.10)$$

$$\mathbf{I}d\boldsymbol{\omega}(t) = \left(-\boldsymbol{\omega}(t)^\times \mathbf{I}\boldsymbol{\omega}(t) + \sum_j \boldsymbol{\tau}_j(t, \mathbf{r}(t), \mathbf{v}(t), \mathbf{q}(t), \boldsymbol{\omega}(t)) \right) dt + \mathbf{r}_i(t, \mathbf{q}(t))^\times d\mathbf{Y}_t \quad (3.11)$$

Solving such SDEs can be done to obtain a sample path solution of the stochastic process in question by generating a random set of values for each random variable. A probability measure for the solution of the process can then be obtained by computing many sample paths in a Monte Carlo simulation and analyzing the distribution of the results. In our case, obtaining an estimate for the distribution of the evolution of the rotational and orbital parameters is of interest. Generating a random set of collisions, characterized by a linear momentum vector and a location of impact, will therefore produce a sample path solution to Eqs. (3.10) and (3.11).

3.3.2 Solving the Stochastic Differential Equation

The numerical integration method used to solve the stochastic jump process in Eqs. (3.10) and (3.11) requires a jump-adapted time discretization method, where the time discretization is constructed to include the jump times on top of the regular time step [114, Ch. 8, p. 347]. Once the jump times are known, solving Eqs. (3.10) and (3.11) then reduces to first using any numerical integration method to propagate momentum and angular velocity without considering collisions, *i.e.*, integrating forward the following first-order ODEs:

$$\frac{d\mathbf{p}(t)}{dt} = m \left(-\frac{\mu}{r(t)^3} \mathbf{r}(t) + \sum_j \mathbf{a}_j(t, \mathbf{r}(t), \mathbf{v}(t), \mathbf{q}(t), \boldsymbol{\omega}(t)) \right) \quad (3.12)$$

$$\frac{d\boldsymbol{\omega}(t)}{dt} = \mathbf{I}^{-1} \left(-\boldsymbol{\omega}(t)^\times \mathbf{I}\boldsymbol{\omega}(t) + \sum_j \boldsymbol{\tau}_j(t, \mathbf{r}(t), \mathbf{v}(t), \mathbf{q}(t), \boldsymbol{\omega}(t)) \right) \quad (3.13)$$

Second, if time step t_{n+1} is a jump time, the estimates of momentum and angular velocity obtained from Eqs. (3.10) and (3.11) at the next time step, $\mathbf{p}_{t_{n+1}^-}$ and $\boldsymbol{\omega}_{t_{n+1}^-}$, are

updated using the following jump condition:

$$\mathbf{p}_{t_{n+1}} = \mathbf{p}_{t_{n+1}^-} + \Delta \mathbf{Y}_{t_{n+1}} \quad (3.14)$$

$$\boldsymbol{\omega}_{t_{n+1}} = \boldsymbol{\omega}_{t_{n+1}^-} + \mathbf{I}^{-1} \mathbf{r}_i(t_{n+1}, \mathbf{q}(t_{n+1}))^\times \Delta \mathbf{Y}_{t_{n+1}} \quad (3.15)$$

where:

$$\Delta \mathbf{Y}_{t_{n+1}} = \mathbf{p}_{\text{rel}} \quad (3.16)$$

is the jump size of the compound Poisson process at jump time t_{n+1} , describing the relative linear momentum of the impactor and generated randomly as shown in the following section.

The derivation of Eq. (3.16) starts by looking at the momentum exchange between the impactor and the target at the moment of impact t_{n+1} in the inertial frame, where the subscript i here represents the impactor, and t^- represents the time at the left-hand limit of the impact. Thus, using conservation of momentum over the duration of impact, we have:

$$\Delta \mathbf{p}_{t_{n+1}} = -\Delta \mathbf{p}_{i,t_{n+1}} \quad (3.17)$$

or equivalently:

$$\mathbf{p}_{t_{n+1}} = \mathbf{p}_{t_{n+1}^-} + \mathbf{p}_{i,t_{n+1}^-} - \mathbf{p}_{i,t_{n+1}} \quad (3.18)$$

In terms of velocity, where m is the mass of the target and m_i is the mass of the impactor:

$$m \mathbf{v}_{t_{n+1}} = m \mathbf{v}_{t_{n+1}^-} + m_i \mathbf{v}_{i,t_{n+1}^-} - m_i \mathbf{v}_{i,t_{n+1}} \quad (3.19)$$

The velocities after impact are equal, assuming the impactor is absorbed by the target:

$$m \mathbf{v}_{t_{n+1}} = m \mathbf{v}_{t_{n+1}^-} + m_i \mathbf{v}_{i,t_{n+1}^-} - m_i \mathbf{v}_{t_{n+1}} \quad (3.20)$$

The velocity of the impactor right before impact can be written in terms of the velocity of the target and the relative velocity of the impactor:

$$\mathbf{v}_{i,t_{n+1}^-} = \mathbf{v}_{t_{n+1}^-} + \mathbf{v}_{\text{rel}} \quad (3.21)$$

Therefore:

$$m \mathbf{v}_{t_{n+1}} = m \mathbf{v}_{t_{n+1}^-} + m_i \mathbf{v}_{t_{n+1}^-} + m_i \mathbf{v}_{\text{rel}} - m_i \mathbf{v}_{t_{n+1}} \quad (3.22)$$

and solving for $\mathbf{v}_{t_{n+1}}$:

$$(m + m_i)\mathbf{v}_{t_{n+1}} = (m + m_i)\mathbf{v}_{t_{n+1}^-} + m_i\mathbf{v}_{\text{rel}} \quad (3.23)$$

Simplifying for $m \gg m_i$ gives:

$$m\mathbf{v}_{t_{n+1}} = m\mathbf{v}_{t_{n+1}^-} + m_i\mathbf{v}_{\text{rel}} \quad (3.24)$$

or in terms of momentum:

$$\mathbf{p}_{t_{n+1}} = \mathbf{p}_{t_{n+1}^-} + \mathbf{p}_{\text{rel}} \quad (3.25)$$

This is the jump condition used for propagating the momentum of the target during a collision as seen in Eq. (3.14) and in its attitude equivalent in Eq. (3.15).

3.3.3 Generating Independent Collisions

In order to solve the above SDEs with their associated jump conditions, randomly generated impactor momentum vectors and their impact time need to be obtained.

Computing Random Linear Momentum

Producing random values from any given PDF can be done using a method known as inverse transform sampling [114, Ch. 2, p. 64]. This is a procedure where a pseudo-random number generator is used to uniformly sample a number u at random between 0 and 1 and find the value x such that $F_X(x) = u$, where $F_X(x)$ is the random variable's cumulative distribution function (CDF) defined as:

$$F_X(x) = P[X \leq x] = \int_{-\infty}^x f_X(t)dt \quad (3.26)$$

The CDF for the exponential distribution for times between collisions, for $t \geq 0$, is:

$$F(t; \lambda) = 1 - e^{-\lambda t} \quad (3.27)$$

From this, one can obtain the jump times for each collision, t_n , iteratively until the end of the desired propagation period by randomly generating waiting times, t_r , according

to Eq. (3.27) and setting the impact times to:

$$t_n = t_{n-1} + t_r \quad (3.28)$$

with $t_0 = 0$.

At each impact time, the impactor type needs to be determined based on the proportion of collisions that come from either micrometeoroids or space debris. Once that is determined from a pseudo-random number generator, the linear momentum vector can be obtained by calculating the CDF for impactor mass, impact velocity, and impact direction for that specific impactor type and using inverse transform sampling. For the impact direction, a joint CDF can be calculated in the following way:

$$F_{\theta,\phi}(x, y) = P[\theta \leq x, \phi \leq y] = \int_{-\frac{\pi}{2}}^x \int_{-\pi}^y f_{\theta,\phi}(t, s) ds dt \quad (3.29)$$

Obtaining random values for the elevation angle θ and azimuth ϕ is done first by calculating the CDF for the elevation angle, obtained from Eq. (3.30), and using inverse transform sampling. Second, the conditional PDF for azimuth at that specific elevation angle, $\hat{\theta}$, needs to be calculated and inverse transform sampling is used on that particular distribution, obtained from Eq. (3.31) [114, Ch. 2, p. 64]:

$$F_\theta(x) = F_{\theta,\phi}(x, \pi) \quad (3.30)$$

$$f_\phi(y|\theta = \hat{\theta}) = f_{\theta,\phi}(\hat{\theta}, y) / f_\theta(\hat{\theta}) \quad (3.31)$$

where $f_\theta(\hat{\theta}) = \int_{-\frac{\pi}{2}}^{\frac{\pi}{2}} f_{\theta,\phi}(\hat{\theta}, y) dy$.

Having obtained random values for impactor mass m_i , impact velocity v_i , elevation angle θ_i , and azimuth ϕ_i , an impactor relative linear momentum vector in the Satellite-Centered Orbital (SCO) frame (see Secion 2.1.1) can be computed by switching from spherical coordinates to Cartesian coordinates:

$$\mathbf{p}_{\text{rel}} = \begin{bmatrix} -m_i v_i \cos \theta_i \cos \phi_i \\ -m_i v_i \cos \theta_i \sin \phi_i \\ m_i v_i \sin \theta_i \end{bmatrix} \quad (3.32)$$

The vector then needs to be rotated into the inertial frame for use in Eq. (3.14) and into the body-fixed frame for Eq. (3.15).

Computing Random Impact Location

To complete the computation of angular momentum transferred to the body as a result of collisions, the random location of impact needs to be generated. An object geometry needs to be determined and is split into triangular surfaces defined by their three vertices and their inward surface normal (see Fig. 2.5). During the attitude propagation, the potential surfaces of impact have to be identified based on the object orientation and the impact direction. To this end, a new reference frame is defined, the collision frame, where the body frame is rotated so that the given linear momentum vector is aligned with the negative z_c -axis. The surfaces in view of the impactor are then only considered as potential surfaces of impact if the angle between the inward surface normal and the negative z_c -axis is smaller than 90° . Self-shadowing is not considered in the present implementation as it is deemed negligible for the two cases studied below due to their convex shapes. In order to obtain a random surface of impact among the n eligible surface candidates, $i \in \{1, \dots, n\}$, a pseudo-random number generator is used with the impact probability for each surface, P_i , calculated as being proportional to the projected area of that surface onto the x_c - y_c plane of the collision frame, that is:

$$P_i = \frac{A_i \cos \Psi_i}{\sum_{i=1}^n A_i \cos \Psi_i} \quad (3.33)$$

where A_i is the area of surface i and Ψ_i is the angle between the inward normal of surface i and the impactor linear momentum vector.

Once a triangular surface of impact has been determined, the location of impact on the particular surface can be obtained as a function of the position of the three vertices, \mathbf{r}_1 , \mathbf{r}_2 and \mathbf{r}_3 , assuming a uniform distribution with randomly generated numbers, $s, t \in [0, 1]$ as:

$$\mathbf{r}_i = (1 - \sqrt{t})\mathbf{r}_1 + \sqrt{t}((1 - s)\mathbf{r}_2 + s\mathbf{r}_3) \quad (3.34)$$

With a value for the location of impact and the linear momentum in hand for every collision, the angular momentum transfer to the object can be computed, assuming a total transfer of momentum to the target by absorption of the impactor and that the mass of the impactor is negligible compared to the mass of the target (*i.e.*, the mass and inertia properties of the target remain unchanged throughout the propagation).

To obtain a more accurate value for the transfer of linear and angular momentum, the effect known as momentum enhancement mentioned earlier can be included. To do so, a calculation of the momentum associated with the ejecta created during crater formation following these hypervelocity impacts needs to be done. This computation is explained in the following section. The orbital and attitude propagation can then be performed for each set of independently generated random collisions in a Monte Carlo simulation.

3.4 Ejecta Momentum

During hypervelocity impacts, when an impactor strikes the target, a large amount of particulates in the neighbourhood of the location of impact are broken off and ejected as a crater is formed on the surface. These particles all have an associated outgoing momentum, which increases the total transfer of momentum from the impactor to the target. This momentum enhancement effect is particularly important for brittle materials often used in spacecraft. Experimental work on this multiplication of momentum has been carried out since the early 1960s with a view to studying impact detectors and shielding for satellites [117, 118]. This phenomenon is also of particular interest for the potential deflection of near-Earth asteroids [119]. However, it is difficult to obtain accurate estimates due to the dependence on impactor shape, density, size and speed, and target characteristics [120].

Although these aforementioned experiments have attempted to replicate collisions in the space environment, there is only a limited amount of data on the subject and it is therefore difficult to properly estimate the momentum enhancement factor for every debris and meteoroid collision. Additionally, laboratory experiments to date on hypervelocity impacts have produced collision velocities only up to about 10 km/s, depending on impactor mass, while debris and meteoroid collisions occur at higher velocities. However, a model was developed primarily for ESA trying to describe the ejecta population from these collisions for implementation into the ESABASE space environment analysis tool [104]. This model is also included in the MASTER-2009 software to calculate the total ejecta population [22]. From this model, it is possible to calculate the total momentum associated with the ejecta and it is used here to derive the additional momentum transfer to the target during each collision as a function of impactor mass, velocity, and direction.

Three ejection processes are postulated to occur during these impacts: jetting, cone fragments, and spallation [104]. Jetting occurs as small particles are ejected at grazing angles and high velocities during the early stages of the impact. Cone fragments are small and fast particles ejected at a constant elevation angle creating a cone around the impact crater. Spall products are large fragments ejected at low velocities normal to the impact surface. The particles can be in liquid, solid, or gaseous form and come from both the impactor and the target. Downrange scattered ejecta, propelled in the half-space behind the target, are not taken into account by the model. Furthermore, jetting is neglected from the model as it accounts for less than 1% of the total ejected mass.

Spall fragments are assumed to be ejected vertically at a low velocity along the direction normal to the surface. Cone fragments, on the other hand, are described by their size, velocity, zenith and azimuth distributions in the frame fixed with the surface. From these, the linear momentum vector of the ejecta can be calculated. After switching to the body frame, it can be subtracted from the relative linear momentum of the impactor for calculation of the total momentum transfer:

$$\mathbf{p}_{\text{total}} = \mathbf{p}_{\text{rel}} - (\mathbf{p}_{\text{cone}} + \mathbf{p}_{\text{spalls}}) \quad (3.35)$$

A full description of the model and the equations describing the computation of the ejecta characteristics can be found in Rival and Mandeville [104]. The derivation of \mathbf{p}_{cone} and $\mathbf{p}_{\text{spalls}}$ from the model is detailed in Appendix D. A combination of input parameters to the model were used and are shown in Table 3.1 [22, 104]. In the current implementation, only impacts with brittle material were considered.

The above methodology has certain limitations, however. The ejecta model is only valid for a specific range of impact characteristics: the model is only reasonable for an impactor size between 5 μm and 1 mm and an impact velocity between 1 km s^{-1} and 20 km s^{-1} [22]. To adjust to these limitations, whenever the impactor characteristics lie outside of the given range, the closest limit is used as input to the ejecta model. Adjusting to lower values of impactor mass and velocity will therefore underestimate the actual momentum contribution from ejecta. Nevertheless, it is important to note that from the MASTER-2009 software, only impacts with meteoroids occur at velocities higher than 20 km s^{-1} . For an orbit similar to that of Envisat's, about 0.3% of impacts will occur at velocities smaller than 1 km s^{-1} and 26% of collisions will be

TABLE 3.1: Ejecta Model Parameters

Symbol	Definition	Value	Reference
ρ_i	Impactor density	2700 kg m^{-3}	[22]
ρ_t	Target density	2500 kg m^{-3}	[22]
β_m	Mass partitioning parameter	1 if $d_i < 1 \mu\text{m}$ 0.4 if $d_i > 100 \mu\text{m}$ $-0.3 \log_{10} d_i - 0.8$ otherwise	[104]
v_{spalls}	Velocity of spall products	10 m s^{-1}	[22]
α_s	Size distribution parameter	-3.5	[104]
δ_{\min}	Minimal cone fragment size	$0.1 \mu\text{m}$	[104]
λ_m	Proportionality of largest cone fragment mass to total ejected mass	0.1 if $\theta_i \leq 60^\circ$ 0.5 if $\theta_i > 60^\circ$	[104]
σ_θ	Width of zenith distribution	3°	[22]
$\theta_{\max0}$	Mean zenith angle for normal impacts	30°	[22]
$\theta_{\max60}$	Mean zenith angle for grazing impacts	80°	[22]
σ_φ	Width of azimuth distribution for grazing impacts	5°	[104]
v_{\min}	Minimal velocity of cone fragments	10 m s^{-1}	[22]

from meteoroids at velocities higher than 20 km s^{-1} . Similarly, less than $10^{-3}\%$ of impactors have a characteristic size larger than 1 mm. As the minimal impactor size from MASTER-2009 is $1 \mu\text{m}$, this value was chosen as a lower limit instead of $5 \mu\text{m}$ so as to not exaggerate the effect of momentum enhancement. It is important to note that for such an orbit, 40% of collisions will be with objects between $1 \mu\text{m}$ and $5 \mu\text{m}$.

3.5 Case Studies

The framework explained above was split into two analyses. First, in Section 3.5.1, the effect of hypervelocity impacts solely on the attitude of space debris was explored. In this case, the orbital motion is propagated without any perturbations but collisions are generated randomly and their long-term effect on attitude is determined. Second, in Section 3.5.2, the influence on orbital motion is examined. In this case, the equation for orbital motion is coupled to its attitude analog in order to capture the orientation-dependent effect of momentum transfer from collisions, but the attitude motion is simply propagated without external perturbations.

3.5.1 Influence on Attitude

The influence of hypervelocity impacts on the attitude dynamics of two different categories of space debris were investigated: the defunct European environmental satellite Envisat, and a HAMR object modeled after a MLI debris. The simulations

were performed over a period of ten years assuming only collisions with debris and meteoroids and no other external torques. Figure 3.5 summarizes the algorithm that was developed. The inputs include the orbital parameters of the target, the object geometry and inertia properties, and the initial conditions of the SDE; the output of the procedure is the evolution of the distribution of the rotational parameters. The fraction of the algorithm which is a part of the Monte Carlo loop is presented inside the box. Each ten-year run was repeated 20,000 times to obtain a yearly evolution of the distribution for rotational kinetic energy. For each case, a run including ejecta momentum and one excluding it were made in order to observe the influence of the momentum enhancement effect on long-term attitude propagation.

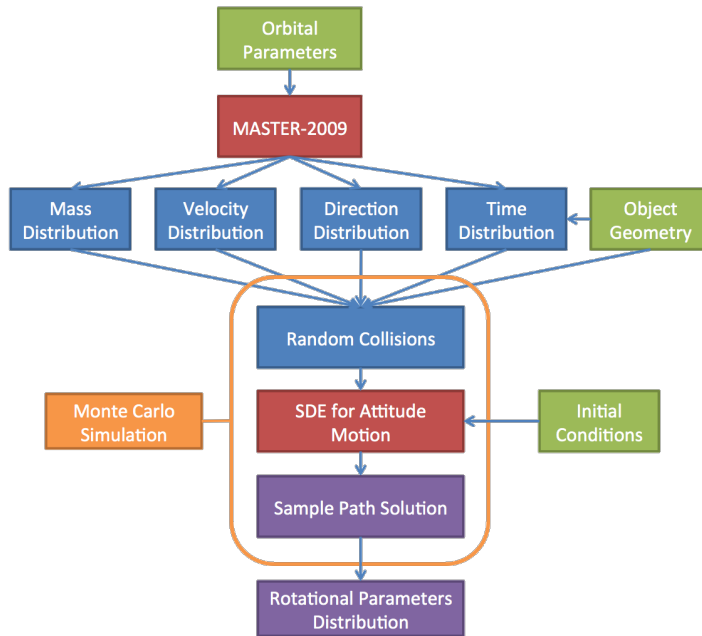


FIGURE 3.5: Flowchart of the Algorithm for Attitude Propagation from Hypervelocity Impacts

Envisat

As was introduced in Chapter 1, Envisat is a European Earth-observing environmental satellite launched by ESA on 1 March 2002. It was sent in a Sun synchronous polar orbit at an altitude of 790 km and inclination of about 98° with a purpose to monitor climate change and the Earth's environmental resources. The expected mission lifetime was 5 years but it lasted until 8 April 2012, when ESA lost contact with the

satellite for unknown causes, and then announced its end of mission on 9 May 2012. To this day, Envisat remains in orbit and is one of the largest space debris objects currently being tracked by the United States Space Surveillance Network (SSN). Due to its large size and busy polar orbit, Envisat has been of much interest to the community as a potential Active Debris Removal (ADR) target.

For the present analysis, the body of Envisat is assumed to have a mass of approximately 7828 kg and to be a $10\text{ m} \times 4\text{ m} \times 4\text{ m}$ cuboid with a $14\text{ m} \times 5\text{ m}$ solar array inclined at 30° towards the z -axis, therefore having an exposed total surface of 332 m^2 [121]. Figure 3.6 shows the simplified geometry for Envisat split into triangular surfaces in the body-fixed frame. The orbit parameters used for Envisat as input to the MASTER-2009 software are those mentioned earlier. The impact fluxes used are therefore the outputs in Figs. 3.1-3.3 for the MASTER-2009 reference epoch of 1 May 2009 and are assumed to be constant for the ten year propagation. The matrix representation of the centroidal inertia tensor in the body-fixed frame is taken to be the following [121]:

$$\mathbf{I} = \begin{bmatrix} 17023.3 & 397.1 & -2171.4 \\ 397.1 & 124825.7 & 344.2 \\ -2171.4 & 344.2 & 129112.2 \end{bmatrix} \text{ kg m}^2 \quad (3.36)$$

while the initial angular velocity of the body frame with respect to the inertial frame, expressed in body frame coordinates, is $\boldsymbol{\omega}_0 = [0, 0, 2.67]^T \text{ }^\circ \text{s}^{-1}$ and the initial attitude of the body frame with respect to the orbital frame (Yaw, Pitch, Roll) as a 3-2-1 Euler transformation is $[180, 0, 62]^\circ$ [43]. These initial conditions are the results of an observation campaign that lasted from 30 May 2013 to 25 September 2013 and that was launched by the International Laser Ranging Service (ILRS) based on a request from ESA to monitor Envisat so as to better predict the trajectory and spin parameters of this large debris object. In order to demonstrate sensitivity to initial conditions, an alternate initial orientation was also considered. A random attitude of $[32.2, 16.7, -125.1]^\circ$ was chosen while the angular velocity in body-fixed frame was kept as specified above (keeping in mind that the rotation axis in the inertial frame therefore also changes). A deeper investigation into Envisat's spin motion will be performed in Chapter 4.

As the total spacecraft surface measures 332 m^2 , and since the intensity of the exponential distribution derived earlier from the total number of expected collisions per m^2 per year for Envisat's orbit was $5.504 \times 10^{-5} \text{ s}^{-1} \text{ m}^{-2}$, the value for the intensity now becomes $\lambda = 332 \times 5.504 \times 10^{-5} = 0.0183 \text{ s}^{-1}$. Every year, approximately 5.77×10^5

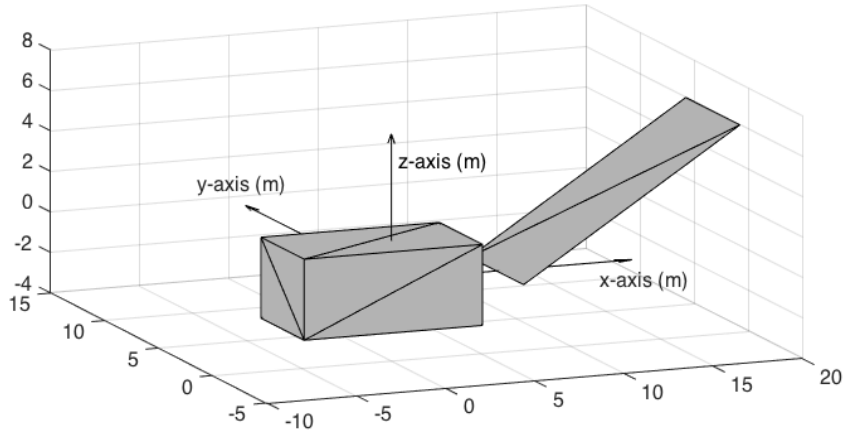


FIGURE 3.6: Simplified Model of Envisat in Body Frame

impacts, about one per minute, are expected on Envisat, with 58% coming from micrometeoroids. The magnitude of the angular momentum transfer for each collision from the impactor to Envisat is described by the CDFs in Fig. 3.7a for the cases with and without momentum enhancement (solid and dashed lines, respectively). As anticipated, the computed expected value of the angular momentum transfer per collision is larger when the momentum from ejecta is included, by approximately a factor of 3: $1.04 \times 10^{-4} \text{ kg m}^2 \text{ s}^{-1}$ with momentum enhancement and $3.54 \times 10^{-5} \text{ kg m}^2 \text{ s}^{-1}$ without. One of the assumptions of the model is that the mass and inertia tensor of Envisat do not change throughout each simulation. However, when an impactor collides with the target, some mass is added to the system while some is removed with the ejecta. After 10 years though, the total added mass to the system, calculated as the sum of the individual impactor masses, usually varies in the 10^{-3} kg range. The sum of the total ejecta masses, on the other hand, amounts to a few kg.

Figures 3.8a and 3.8b show the yearly PDFs for rotational kinetic energy after 1 to 10 years with and without considering ejecta momentum, respectively. The initial energy is shown by the vertical dotted line. In both cases and for every year, the widths of the distributions increase over time, and are always larger when ejecta momentum is considered. This is in agreement with the fact that more angular momentum is transferred with the inclusion of the contribution from ejecta. Furthermore, a slight yearly increase in the energy value of the distribution center is observed displaying a tendency for the satellite to spin up over time: 0.04% after 10 years with momentum enhancement, and 0.01% without. Nevertheless, most of the simulations do not result in a large change in

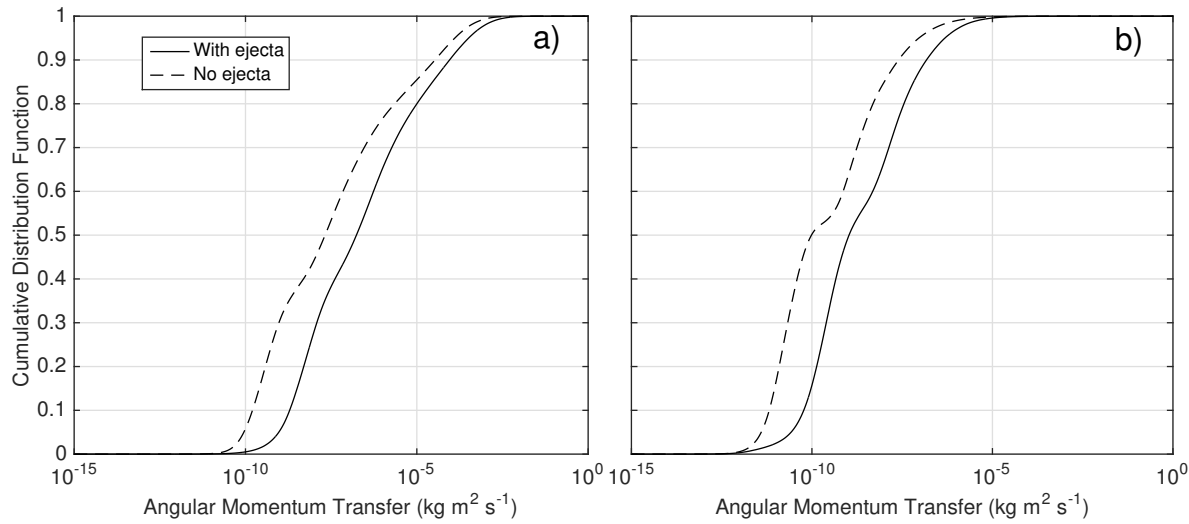


FIGURE 3.7: Cumulative Distribution Function of Angular Momentum Magnitude Transfer for (a) Envisat and (b) a HAMR object

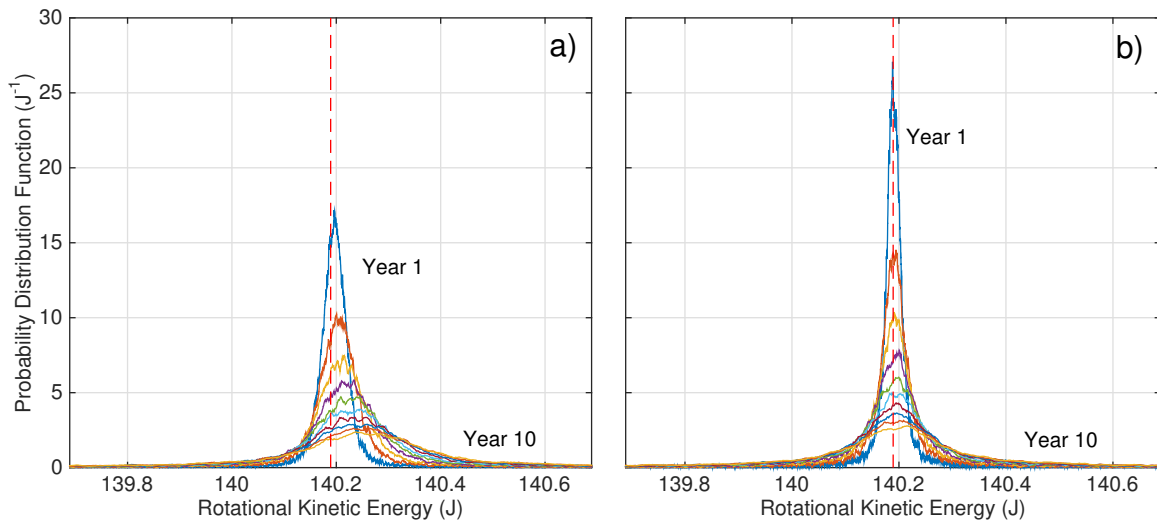


FIGURE 3.8: Evolution of PDF for Envisat's Rotational Kinetic Energy under Observed Initial Conditions: (a) with Momentum Enhancement and (b) without

rotational kinetic energy: collisions with impactors causing a change in energy larger than 5% were relatively uncommon. The yearly values of the distribution center, calculated as the mean around the peak, and the distribution width, calculated as the spread from the distribution center which contains 50% of the runs, are shown in Table 3.2 for the runs with momentum enhancement, along with the cumulative percentage of runs leading to an energy change greater than 5%. Additionally, a break clause in the propagation was implemented to simulate a satellite breakup when a collision occurred with an impactor having a mass exceeding 0.01 kg. At an impact velocity of 15 km s^{-1} , this corresponds roughly to the energy released by the explosion of 0.25 kg of TNT. Table 3.2 also shows the cumulative percentage of the 20,000 runs that resulted in a satellite breakup.

TABLE 3.2: Envisat Simulation Results

Year	Center (J)	Width (J)	>5% Energy Change (%)	Breakups (%)
1	140.1966	0.018	0.64	0.50
2	140.2020	0.029	1.38	1.09
3	140.2092	0.041	2.19	1.80
4	140.2148	0.053	2.96	2.46
5	140.2217	0.066	3.68	3.09
6	140.2275	0.079	4.41	3.73
7	140.2318	0.096	5.07	4.38
8	140.2352	0.112	5.74	5.00
9	140.2420	0.130	6.48	5.79
10	140.2453	0.148	7.21	6.55

Figures 3.9a and 3.9b show the same PDFs, with and without momentum enhancement, respectively, assuming the random initial orientation mentioned previously. Similarly, the distributions display a larger width from year to year and when momentum enhancement is considered. A shift in the distribution center can be seen in the opposite direction to that in the first case. Furthermore, the decrease in the energy value of the distribution center is considerably more significant, about 1% after 10 years. These results highlight the dependence of the long-term effect of hypervelocity impacts on the initial conditions of the spacecraft, more specifically, the initial orientation and direction of the spin axis.

Comparing these results to another study, where it was shown that under the influence of eddy currents and the gravity gradient torque for the same initial conditions Envisat witnesses a 2.67% decrease in energy over a period of 20 days, it is evident that

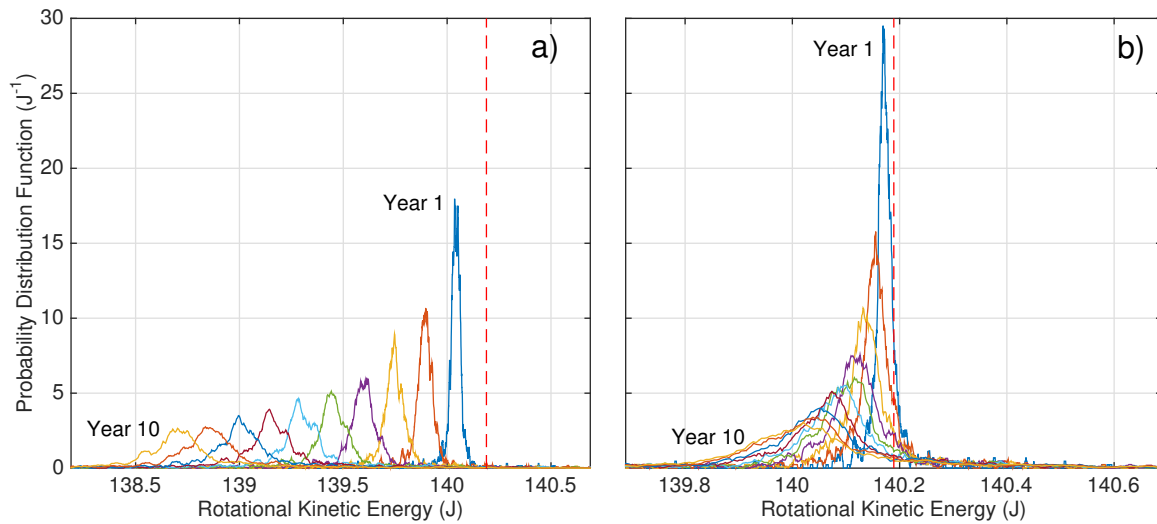


FIGURE 3.9: Evolution of PDF for Envisat’s Rotational Kinetic Energy for Random Initial Orientation: (a) with Momentum Enhancement and (b) Without

collisions do not play a large role in the attitude perturbations seen by Envisat compared to those of other environmental torques [58]. Overall, it can be concluded that hypervelocity impacts do not lead to significant changes in the rotational parameters of a space debris similar to Envisat, although the effect is not entirely negligible in the long-run, and highly dependent on initial conditions.

High Area-to-Mass Ratio Objects

The same procedure was repeated using the properties of a HAMR object. A flat two-sided $1\text{ m} \times 1\text{ m}$ plate with a mass of 0.1 kg was employed, therefore having an area-to-mass ratio of 20, simulating a piece of MLI debris [23]. The orbit used to calculate the impact fluxes from MASTER-2009 had an apogee at GEO, an eccentricity of 0.7 and an inclination of 15° [23]. An initial angular velocity of $\omega_0 = [1, 1, 1]^T \text{ } \circ \text{ s}^{-1}$ was used to simulate tumbling. The total number of expected collisions for that orbit was found to be 869.6 per year per m^2 , with about 93% coming from meteoroids, so the rate parameter for the exponential distribution defining the waiting time between impacts is therefore $\lambda = 5.511 \times 10^{-5} \text{ s}^{-1}$. Approximately 1739 collisions are expected to occur per year, or one every 5 hours, and the CDFs for the angular momentum transfer magnitude for each collision can be seen in Fig. 3.7b with and without momentum enhancement (solid and dashed lines, respectively). Again, the expected value for the

magnitude of the angular momentum transfer per collision is a factor of 3 higher when ejecta momentum is included: 4.02×10^{-7} kg m² s⁻¹ with momentum enhancement and 1.23×10^{-7} kg m² s⁻¹ without. These are smaller than the values for Envisat due to the relatively small size of the object, where the location of impact can't be as far away from the center of mass as for Envisat. After 10 years, the total added mass to the system varies in the 10⁻⁷ kg range, while the sum of the total ejecta masses amounts to about 10⁻⁴ kg.

Figures 3.10a and 3.10b show the evolution of the HAMR object's rotational kinetic energy for 10 years, with and without momentum enhancement, respectively. Similarly to Envisat, the spread of the distributions increase over time, and are always larger when ejecta momentum is considered. Unlike the previous case though, a distinct shift in the distribution center is difficult to characterize, although the upper tail of the distribution has a slower decrease than the lower tail, most likely due to the fact that the rotational kinetic energy is already quite low. A similar break clause was included as for the case of Envisat: a satellite breakup was simulated when the sum of the ejecta mass exceeded 1% of object's mass, or 0.001 kg. This is equivalent to an impact with a 10⁻⁷ kg object at a velocity of 30 km s⁻¹. Contrary to Envisat, a significant change in energy for the HAMR object was frequent. Table 3.3 shows the cumulative percentage of the 20,000 runs that resulted in a breakup after every year as well as the percentage of runs leading to an energy change larger than 50%, with and without momentum enhancement. From these values and from the evolution of the PDFs it can be concluded that for such a HAMR object, the influence of collisions is significant and should not be neglected when propagating attitude for long periods of time.

TABLE 3.3: HAMR Simulation Results

Year	Breakups (%)	Energy Change >50%	
		with Ejecta (%)	without Ejecta (%)
1	0.15	37.0	17.3
2	0.29	58.0	32.2
3	0.48	70.1	43.5
4	0.67	77.0	52.8
5	0.86	81.7	59.7
6	1.12	85.4	65.4
7	1.33	88.2	69.4
8	1.54	90.2	72.4
9	1.82	91.5	75.4
10	2.17	92.9	77.8

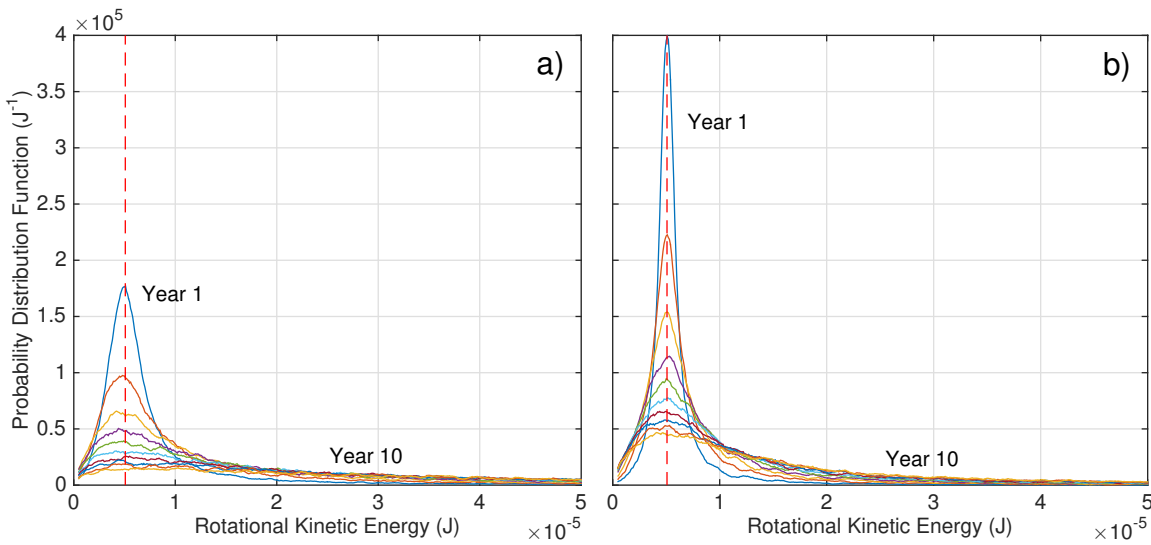


FIGURE 3.10: Evolution of PDF for the HAMR Object's Rotational Kinetic Energy: (a) with Momentum Enhancement and (b) without

There are a few caveats to these results, however. The discovered HAMR debris thought to be MLI material are not rigid, and are likely to change shape constantly. The effect of the collisions on such an object is likely to be very different when flexibility of the debris is taken into account. Moreover, one needs to keep in mind that the orbits of these debris are also evolving very rapidly [23]. As a result, the impact fluxes could vary significantly over the course of the propagation period, and therefore change the characteristics of the resulting randomly generated collisions and their influence on the long-term attitude propagation of the object.

3.5.2 Influence on Orbit

To understand the influence of hypervelocity impacts on orbital motion, the differential equations of motion were propagated for ten years considering only hypervelocity impacts and no external perturbations. The method was applied to the same targets: Envisat and a HAMR object. Each ten-year run was repeated 10,000 times for different randomly generated sets of collisions. To consider the effect of ejecta momentum, the attitude of the target was propagated in parallel. The equations for rotational motion and translational motion can be propagated separately and the coupling is only performed at the times of impact when information about attitude is used in the calculation of the momentum contribution from ejecta. As Envisat can be considered to

be relatively spin-stabilized as was determined from observations, a constant spin rate is assumed and external torques were neglected. The HAMR object is randomly tumbling, so excluding external torques will also not provide a bias in the results. The impact fluxes used are assumed to be constant throughout the propagation. The flowchart outlining the complete methodology is presented in Fig. 3.11. The inputs include the orbital parameters and the initial conditions of the differential equations. The output includes the probability distributions for the orbital parameters. The fraction of the algorithm which is in the Monte Carlo simulation is delineated with a box.

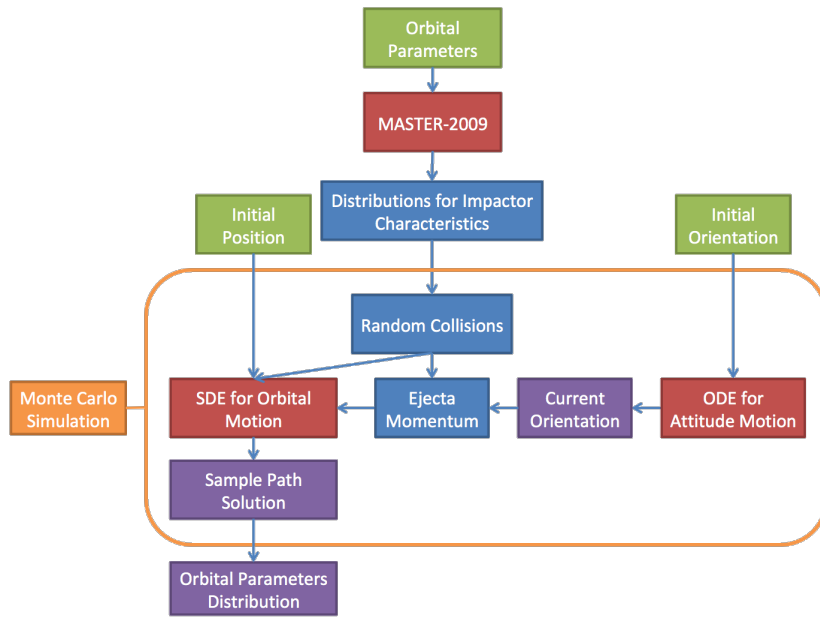


FIGURE 3.11: Flowchart of the Algorithm for Coupled Orbit-Attitude Propagation from Hypervelocity Impacts

A solution without momentum enhancement was also computed for Envisat in order to compare with an analytical test case that was derived to validate the stochastic model. This is detailed in Appendix E.

Envisat

The same spacecraft parameters and initial conditions as detailed above were used for the orbit analysis. Figures 3.12a and 3.12b show the PDFs for the change in SMA throughout the ten-year simulations for the case with and without momentum enhancement, where a yearly orbital decay of 0.96 m and 0.74 m are seen, respectively. Furthermore, the widths of the PDFs increase with time, as expected, and are larger

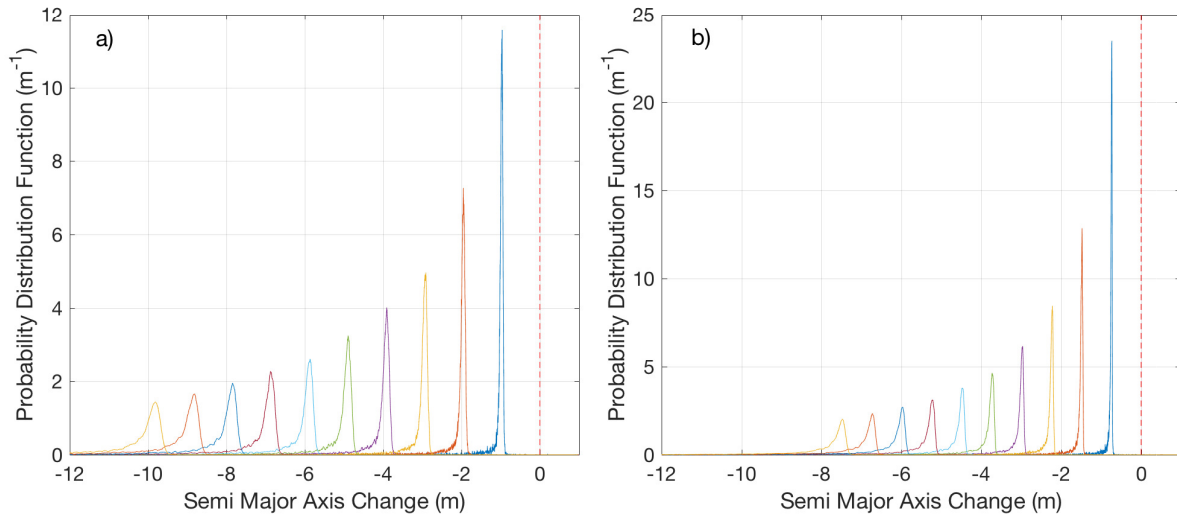


FIGURE 3.12: SMA PDF Evolution for Envisat (a) with Momentum Enhancement and (b) without

for the case with momentum enhancement, similarly to what was obtained for attitude motion. However, for such a large spacecraft at a relatively low orbit, aerodynamic drag will have a much larger influence on the orbital decay of the satellite, calculated using D-SPOSE to be up to 2 km per year depending on solar activity. PDFs were also obtained for the orbit eccentricity, inclination, right ascension of the ascending node and argument of perigee, but changes in them are minute and deemed negligible.

High Area-to-Mass Ratio Object

The same procedure was repeated using the properties and orbit of a HAMR object as detailed above. For such an object, the effect of hypervelocity impacts will be much greater. Indeed, Fig. 3.13 shows distributions with much larger widths (hundreds of meters compared to < 1 m for Envisat), and a decrease in the distribution center of about 8 m per year. Similar large variations in the distributions of other orbital elements can also be seen. Due to the small change in SMA and the large distribution widths, a non-negligible possibility of the orbit being raised exists. The widths of the distributions are related to the spread in directionality of the impacts: the wide spread is due to the fact that most impacts in this high-altitude orbit occur with meteoroids and these come from every direction. Because impacts are not mainly coming from the ram direction, as is the case for Envisat, some of the ten-year propagations end up with more collisions causing an increase in the SMA.

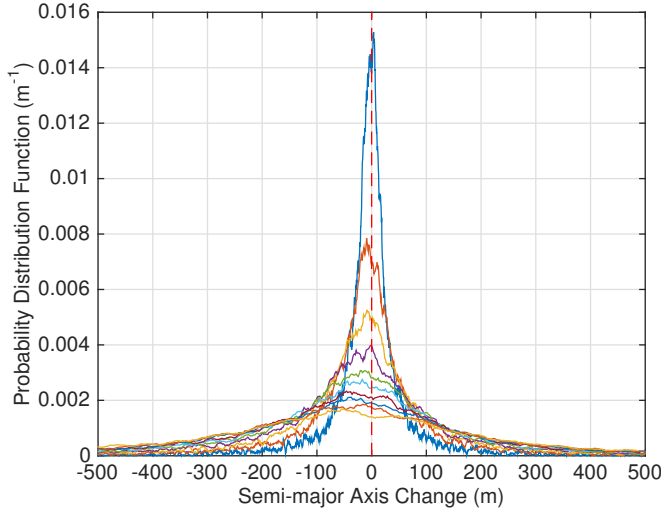


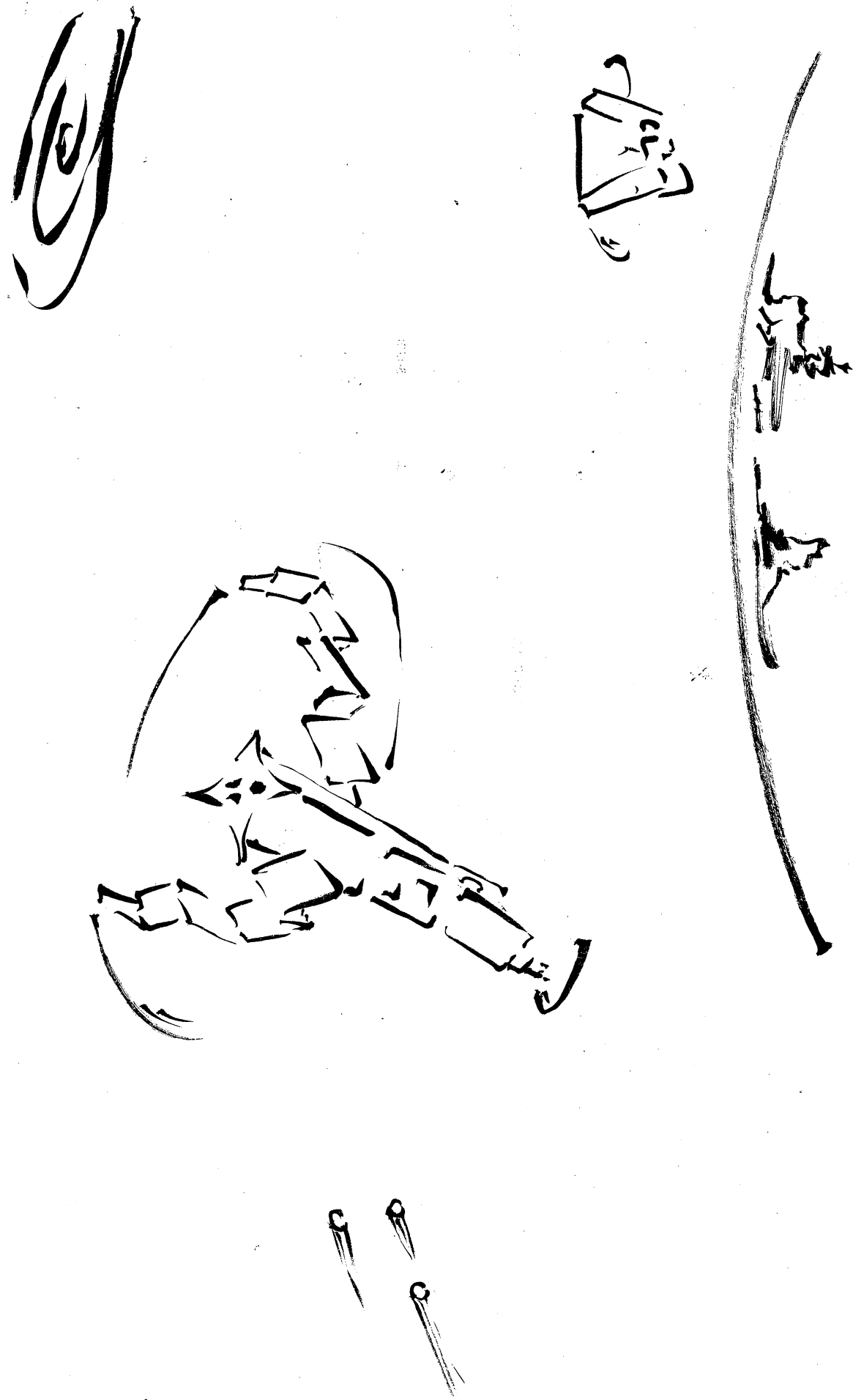
FIGURE 3.13: SMA PDF Evolution for the HAMR Object

3.6 Concluding Remarks

A method to include hypervelocity impacts with small debris and meteoroids in the orbit and attitude propagation of large space debris was developed. By considering the linear momentum associated with collisions as a compound Poisson process and incorporating it into the stochastic differential equations for orbital and attitude motion, distributions for the evolution of the rotational kinetic energy and orbital parameters of such space debris could be computed by randomly generating sets of collisions for the desired propagation period in a Monte Carlo simulation. The characteristics of each collision, the impactor type, mass, impact velocity and direction, and impact time, were shown to be obtained from output fluxes of the MASTER-2009 model for a specific input orbit.

The framework was applied to two cases of space debris. It was shown that for a large object like Envisat, even while experiencing a high frequency of impacts, the satellite did not show significant changes in its rotational or orbital parameters even after 10 years, although the effect is not entirely negligible and impacts leading to breakups events or large energy changes are possible. For a high area-to-mass ratio object the influence of collisions is stronger, although limitations in the current model implementation are highlighted. Large changes in its orbit and rotational parameters are frequent and highly probable even though for such an orbit and surface area fewer

collisions occur. Furthermore, the effect of including ejecta momentum into the computation was outlined. Using an ejecta model, the contribution to the total angular momentum transfer to the satellite from collisions was shown to approximate a momentum enhancement factor of 3 for the input parameters considered, although the directionality of the ejecta momentum is also considered. In addition, it was shown that this model can be used to compute the probability of a satellite breakup from collisions with impactors measuring less than the standard limit of 10 cm by considering a threshold impactor kinetic energy.



Hetty Schricke

"Lost in Space"

Chinese ink on rice paper

Chapter 4

The Envisat Enigma

In Chapter 3, the effect of hypervelocity impacts on the attitude and orbit of the European Space Agency (ESA) defunct environmental satellite Envisat was analyzed. A deeper investigation into its attitude dynamics considering other external perturbations will now be performed using D-SPOSE. As was previously mentioned, ESA lost contact with Envisat in April 2012 and is now planning the world's first Active Debris Removal (ADR) mission, called e.Deorbit, for 2024 [42]. A number of observatories around the world have since then tracked the spacecraft in order to determine its rotational state, as understanding the rotational dynamics of the target is fundamental for the success of such a mission. Three different methods have been used in the observation campaigns to date, including Satellite Laser Ranging (SLR), photometric measurements (light curves), and inverse synthetic aperture radar (ISAR) images [43, 46, 54]. These observations have revealed that Envisat experienced a significant angular velocity increase through May 2013, unexplained so far; and that since then the spacecraft has been undergoing a slow decay of its spin rate. Initial modelling efforts determined that this was due to the eddy-current torque as the spacecraft interacted with Earth's magnetic field [58]. Furthermore, ESA has contracted the development of a coupled orbit-attitude model for large space debris called *iOTA* (In-Orbit Tumbling Analysis). Preliminary results with this model, which is still under development and not open to the public, have been published, focusing on reproducing synthetic measurements such as light curves and SLR residuals in order to compare to observations [68]. Although the observation studies published to date mostly agree on the satellite's *spin rate*, there are contradictions about the observed or determined motion of its *spin axis* and these are truly puzzling.

It is in order to shine light on this mystery that an investigation on the rotational dynamics of the "most wanted" space debris Envisat over a four-year duration beginning

after its spin-up in May 2013 was performed. Using D-SPOSE and the inputs as specified in Section 4.1, through analysis of the simulation results detailed in Section 4.2, we achieve our principal goal, which is to gain insight and new understanding of the attitude evolution of large space debris objects over a long period of time, revealing that, unlike what has been assumed previously, the likelihood of Envisat’s spin axis remaining stable is small. With careful post-processing of attitude time histories of Envisat, we identify three distinct components of the rotational motion of this debris, the understanding of which will provide the community with new perspectives for further studies of Envisat’s rotation. A sensitivity study of the effect of various model parameters on simulation results is outlined in Section 4.3. In Section 4.4, a critical review of observational studies reported on Envisat’s rotational state is performed, in light of the knowledge gained from the simulations and with a comparison to the simulation results. In consideration of the highly anticipated planned removal mission, Section 4.5 will outline predictions of the evolution of its future attitude motion for the 2024-2025 ADR time frame. Finally, recommendations for future observation campaigns in order to provide better estimates of Envisat’s angular motion are put forward in Section 4.6. The core of this work can be found in Sagnières and Sharf [122].

4.1 Simulation Inputs

As was mentioned in Section 2.4 of Chapter 2, various input parameters are required in D-SPOSE: perturbation model parameters, spacecraft parameters, initial conditions, and propagation parameters. For the Envisat case study, not every perturbation was considered in the baseline scenario. Aerodynamic drag and torque were included, using DTM-2013 and the standard drag coefficient of 2.2; the eddy-current torque is included using the magnetic field modeling from IGRF-12; third-body interactions from the Moon and Sun are also included; and the gravity-gradient torque and gravitational accelerations up to degree and order 12 are considered. However, the solar radiation torque has previously been shown to cause only a short-term periodic behaviour in Envisat’s angular velocity and no change in its secular evolution or on the spin axis motion and was therefore initially excluded [123]; a deeper investigation is performed in Section 4.3. Hypervelocity impacts were excluded in light of the results obtained in Chapter 3. Internal energy dissipation was similarly excluded in the baseline scenario, but simulations including it and varying the various parameters are also

presented in Section 4.3. In addition, we investigate the effects of dropping some of the terms in the aerodynamic torque as well as varying the order of the gravitational potential. Supplementary simulations and the corresponding results are all summarized in Table 4.1 of Section 4.3.

Spacecraft parameters include the spacecraft mass, inertia tensor, magnetic tensor, and spacecraft geometry. The matrix representation of the centroidal magnetic tensor in the body-fixed frame is assumed to be [58]:

$$\mathbf{M} = \begin{bmatrix} 931500 & 0 & 0 \\ 0 & 1059000 & 0 \\ 0 & 0 & 1059000 \end{bmatrix} \text{ kg}^{-1} \text{ m}^2 \text{ s}^3 \text{ A}^2 \quad (4.1)$$

The spacecraft mass and inertia tensor were presented in Section 3.5.1. It is interesting to note that, although not so in appearance, Envisat's inertial distribution with respect to its principal frame is close to that of an axisymmetric body. The inertia tensor stated in Eq. (3.36) was determined directly by ESA and as no damage to the spacecraft has been observed, we have high confidence in the inertial parameters used [54, 121]. However, the magnetic tensor was obtained by dividing the spacecraft into parts with assumed magnetic properties according to their structural materials and, therefore, is subject to large uncertainty [58]. The effect of this uncertainty is investigated in the next section.

The geometry, specifically the surface model, is presented in Fig. 4.1. It consists of a more detailed and accurate representation of the satellite's geometry than the simplified version detailed in Fig. 3.6 of Chapter 3. As shown, Envisat's geometry is made up of 28 triangular surfaces. The model consists of the main satellite body ($10 \times 2.6 \times 2.8$ m), an antenna measuring (10×1.3 m), and a solar panel (14×5 m). The solar panel is assumed to be locked, making a 22° angle with respect to the x - y plane [124]. The body-fixed frame axes are shown in black in Fig. 4.1 while the maximum principal axis of inertia is shown in red, defined by the direction vector $[-0.0190 \ 0.0771 \ 0.9968]^T$ in the body-fixed frame. It is rotated approximately -4.5° from the z -axis about the x -axis.

The initial orbital conditions and initial attitude conditions are needed as well. As Envisat experienced an unexplained spin-up after contact was lost, the initial orbital conditions were set to a TLE obtained after this event occurred. The following TLE, from May 7, 2013, was used as input:

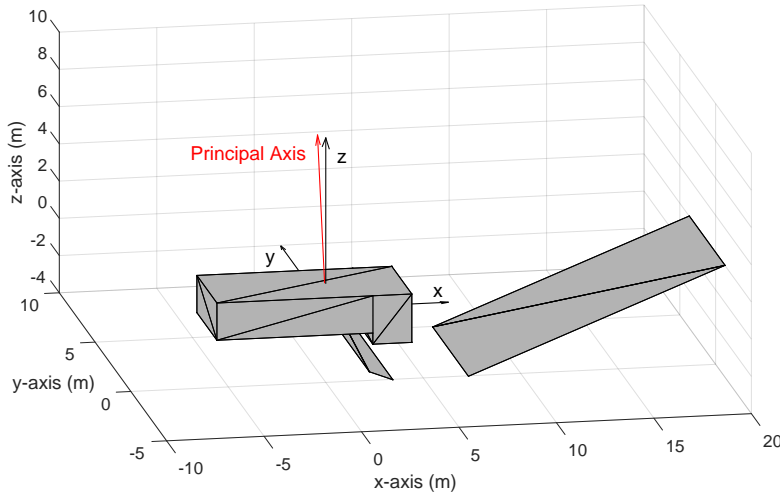


FIGURE 4.1: Tessellated Model of Envisat’s Surface Geometry in the Body-Fixed Frame

```

1 27386U 02009A 13127.45641789 .00000089 00000-0 44087-4 0 3555
2 27386 98.4303 196.5510 0001204 87.6383 272.4946 14.37606880585289

```

At the TLE epoch, from observations which will be reviewed in the Section 4.4, Envisat is estimated to be rotating at approximately 2.9° s^{-1} or, equivalently, having a rotation period of 125 s. For comparison, the satellite’s orbital period at that time is approximately 100 minutes. From observations, it is also widely accepted that Envisat is spinning in retrograde motion (opposite to its orbital motion). Its rotation axis is approximately parallel to the symmetry axis of its retroreflector panel, which in turn is close to the satellite’s maximum principal axis of inertia, indicated in Figure 4.1 [43]. Envisat’s initial angular velocity vector was therefore assumed to be along the body-fixed frame z-axis.

The initial orientation of the body was parametrized by the initial orientation of the angular velocity vector with respect to the negative orbital normal vector. Since no information exists on the exact attitude of the spacecraft for the epoch of the simulation, the baseline scenario for the propagation was chosen to have the initial angular velocity vector 30° away from the negative orbit normal. In order to explicitly characterize the motion of the spin axis and shed light on contradictions in current literature regarding this issue, various additional simulations were performed. Specifically, five

simulations were run by varying the initial inclination of the angular velocity vector, always lined-up with the body-fixed frame z -axis, from the negative orbit normal as: $0^\circ, 8.5^\circ, 17^\circ, 28^\circ, 45^\circ$. With the exception of 45° case, the other values correspond to the results deduced from observations and were chosen in order to provide a comparison to previous studies which will be presented in Section 4.4. Three supplementary scenarios related to the variation of initial angular velocity (magnitude and direction) were also investigated as per Table 4.1.

Finally, the propagation parameters involved are the duration of the propagation and the time step used in the numerical integration. For all propagation scenarios, the duration was set to four years (1461 days) with a time step of 1 s. This time step was considered to be sufficiently small as only a 0.12% energy loss was found after checking the work-energy balance throughout the simulation. A propagation with a time step of 0.1 s was also performed and the differences in the obtained results were found to be negligible.

4.2 Propagation Results

The rotational motion of Envisat is very complex, but significant insight can be gained by considering the evolution of the angular momentum and angular velocity of the satellite. Analysis of simulation results reveals three distinct angular motions that can be observed in the inertial frame, as shown in the schematic, not to scale, in Fig. 4.2: 1) a precession of the angular momentum vector, about the Earth's rotation axis, as the orbital plane precesses; 2) a revolution of the angular momentum vector about the orbit normal, composed of a nutation and a libration with locked periods; and 3) a wobbling of the angular velocity vector, about the body's angular momentum vector. The direction of each motion and of the spacecraft rotation are also shown. The precise definitions of the aforementioned motions employed in this work are stated as follows, making use of the angular momentum frame¹ and the Earth-Centered Orbital (ECO) frame as defined in Section 2.1.1:

Definition 1: A precession is a secular change in the first Euler angle of the 3-1-3 attitude parametrization of the angular momentum frame with respect to the inertial frame.

¹ The angular momentum frame definition employed in this study assumes the z_h -axis is fixed with the body's angular momentum vector.

Definition 2: A nutation is a secular change in the first Euler angle of the 3-1-3 attitude parametrization of the angular momentum frame with respect to the ECO frame.

Definition 3: A libration is an oscillation of the second Euler angle of the 3-1-3 attitude parametrization of the angular momentum frame with respect to the ECO frame. In this study, the corresponding angle is defined as the nutation amplitude.

Definition 4: Wobbling denotes the torque-free motion of the angular velocity vector about the angular momentum vector for an inertially asymmetric body.

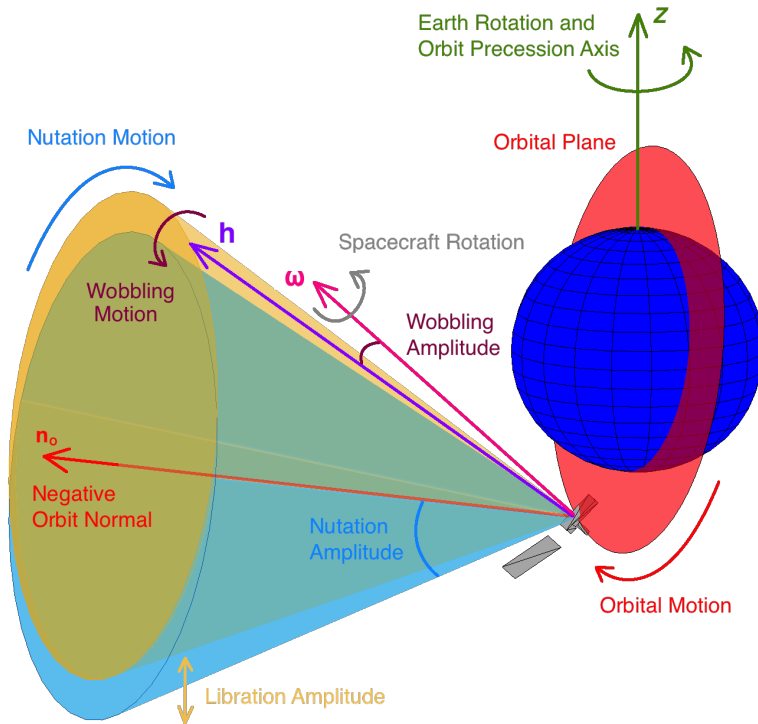


FIGURE 4.2: Schematic of Angular Motions Experienced by Envisat

The three angular motions were determined by comparing the satellite's angular momentum vector, $\mathbf{h} = \mathbf{I}\boldsymbol{\omega}$, to the inertial X-axis, the inertial Z-axis, the negative orbit normal, \mathbf{n}_O , and the angular velocity vector, $\boldsymbol{\omega}$. Figure 4.3 displays the relevant angular distance measures for the appropriate time durations for the baseline scenario. From the secular change in the minimum angle between \mathbf{h} and X over the four year propagation, as seen in Fig. 4.3a, the precession of Envisat's angular momentum vector can be deduced. It has a period of approximately one year as it follows the orbital plane's precession. It is the gravity gradient torque that fixes the motion of the angular momentum vector with and about the orbit normal. The high-frequency oscillations

seen in Fig. 4.3a represent the rotation of the angular momentum vector with respect to the orbit normal (nutation and libration), which quickens and widens over time.

The second motion is the rotation of the angular momentum vector with respect to the orbit normal. Figure 4.3b shows the \mathbf{h} -Z and \mathbf{h} - \mathbf{n}_O angles over the first month of the propagation. The \mathbf{h} -Z angle isolates the nutational motion: from its oscillations, the nutation period and amplitude can be deduced. Similarly, the evolution of the \mathbf{h} - \mathbf{n}_O angle allows to separate out the libration motion, and the libration period and amplitude can be derived. One can see that the libration and nutation periods are exactly the same. This motion is also due to the gravity gradient torque.

The third motion is the wobbling motion of the angular velocity vector, $\boldsymbol{\omega}$, around the angular momentum vector. Figure 4.3c shows this motion from a sample 258 seconds of the simulation (approximately one wobble period). The amplitude of the wobbling, measured as the maximum angular deviation between \mathbf{h} and $\boldsymbol{\omega}$, is approximately 2° in this case. This motion is due to the fact that the initial angular velocity is not aligned with the principal axis of inertia of the spacecraft.

Figure 4.4 shows the evolution of Envisat's (a) angular velocity magnitude (spin rate), (b)-(c) nutation period and amplitude, (d) libration amplitude, and (e)-(f) wobbling period and amplitude, for the five simulations corresponding to the five initial inclinations of $\boldsymbol{\omega}$ stated earlier. Multiple observations can be made from the simulations on the tendencies of these motions. First, the decay of the angular velocity magnitude due to the eddy-current torque is present, as noted previously [58]. Second, the amplitude of the nutation increases consistently in every case, while the period decreases over the four year propagation. Third, the libration and nutation periods, which are on the order of days, are locked together throughout the propagation and are longer for larger nutation amplitudes. Fourth, a larger initial deviation from the negative orbit normal (nutation amplitude) produces a slower decay of angular velocity. Fifth, the larger the nutation, the larger the libration amplitude as well. It is interesting to note that unless the rotation starts out perfectly about the axis perpendicular to the orbital plane, *i.e.*, the 0° case, the nutation motion will become larger and quicker: an increase in the amplitude of approximately 50% occurs after four years, for the cases where the initial angular velocity vector is 8.5° and 17° from the negative orbit normal, while the period decreases by a factor of 2.5 after four years, from approximately 5 days to 2. Furthermore, in each case, the wobbling amplitude decreases to below 0.5° , as the spacecraft approaches a major principal axis spin, with a larger decrease for the cases

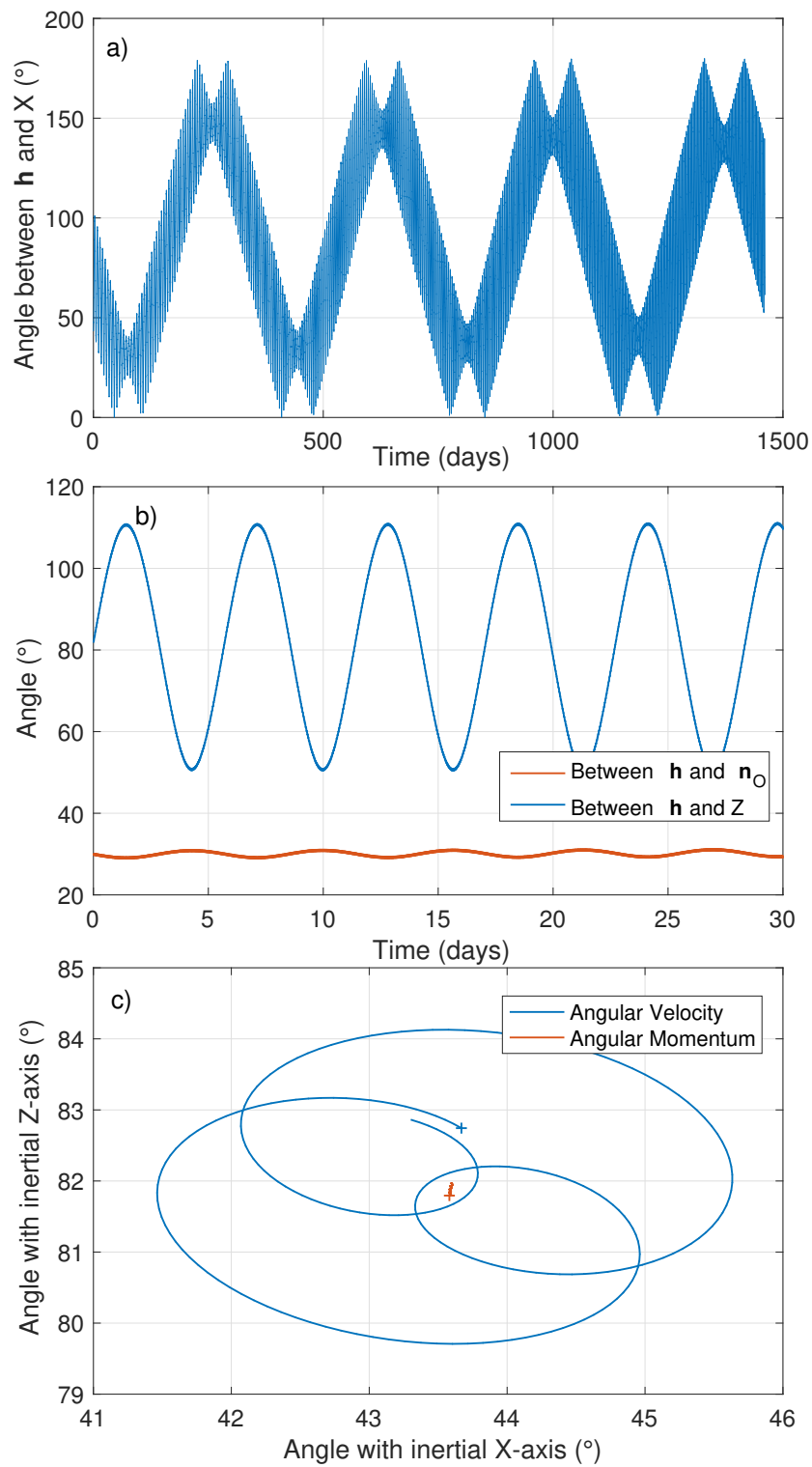


FIGURE 4.3: Examples of the Evolution of Envisat's Angular Motions for the Baseline Scenario

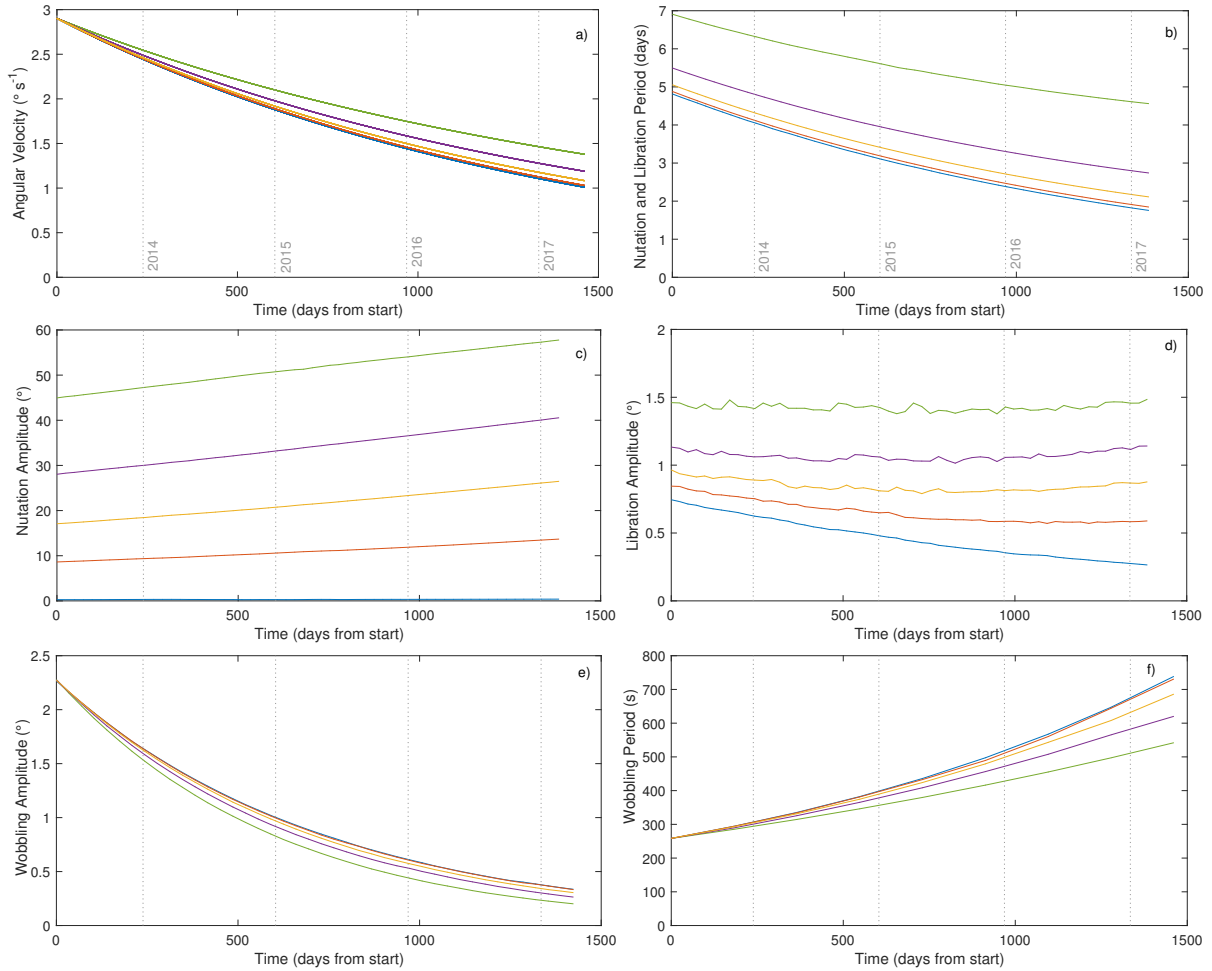


FIGURE 4.4: Evolution of Envisat's Angular Motion for the Four-Year Propagation

where the initial spin axes are farther away from the negative orbit normal. The wobbling slows down the quickest (200% increase of the period in four years) for the case when the angular velocity vector is aligned with the negative orbit normal.

4.3 Sensitivity Study on Input Parameters

While these results demonstrate that the expected wobbling motion is small and simulations have shown that it becomes smaller and slower with time, the nutation of Envisat's angular momentum vector is expected to become larger and faster with time, which could be worrying for future ADR missions. Nevertheless, the dependence of these results on the model parameters and initial conditions needs to be explored further.

Table 4.1 displays the supplementary simulations (SS) that were carried out by varying the indicated model parameters and initial rotation from the baseline scenario. First and foremost, it was found that the evolution of Envisat's orbital motion has a negligible effect on the rotational motion results: aerodynamic drag and third-body gravitational perturbations showed almost no influence on the evolution of Envisat's angular motion (SS1), neither did increasing the degree and order of the gravitational potential model from 12 to 24 (SS2). It was also shown that, in this case, not considering higher-order terms in the calculation of the gravity-gradient torque was negligible, at least when analyzing the motion of the spin axis (SS3). Excluding the extra terms in the aerodynamic torque and drag for a spinning spacecraft did not reveal any changes (SS4), neither did excluding the aerodynamic torque completely (SS5); however, as expected, removing either the gravity-gradient torque (SS6) or the eddy-current torque (SS7) led to significant differences, showing that they are indeed the dominating torques. In this light, the influence of the relevant parameters for these two torques was investigated further.

Reducing the initial angular velocity magnitude by approximately 10% led to a similar decrease of the nutation/libration period throughout the propagation (SS8). This occurs as the spin stabilization of the spacecraft weakens for a slower spin rate, thus amplifying the effect of the gravity gradient torque. No other change in the angular motion was found. Using the World Magnetic Model for the geomagnetic model [74] instead of IGRF-12 did not reveal any differences (SS9), but decreasing the magnetic

TABLE 4.1: Influence of Initial Conditions and Perturbation Model Parameters

Parameter	Baseline	Change	Difference in Angular Motion
SS1 Aerodynamic Drag	Included	Excluded	Negligible
SS2 Gravitational Field	Order and degree 12	Order and degree 24	Negligible
SS3 Gravity-Gradient Torque	Order and degree 12	Order and degree 1	Negligible
SS4 Aerodynamic Drag and Torque	Full Model	No Spin Terms	Negligible
SS5 Aerodynamic Torque	Included	Excluded	Negligible
SS6 Torques Considered	Gravity-gradient, eddy-current, aerodynamic	Only eddy-current	No precession, nutation or libration
SS7 Torques Considered	Gravity-gradient, eddy-current, aerodynamic	Only gravity-gradient	Angular velocity, nutation and libration remain constant throughout propagation
SS8 Initial Angular Velocity Magnitude	2.9° s^{-1}	2.6° s^{-1}	Nutation and libration period is proportionally $\sim 10\%$ smaller throughout propagation
SS9 Geomagnetic Model	IGRF-12	WMM	Negligible
SS10 Magnetic Tensor	[58]	Decreased by 10%	Angular velocity decrease is $\sim 6\%$ smaller
SS11 Initial Angular Velocity Direction	Body-fixed frame z-axis	Major principal axis	No wobbling
SS12 Initial Angular Velocity Direction	Body-fixed frame z-axis	Further away from principal axis (initial wobbling amplitude 100% larger)	Wobbling amplitude 100% larger throughout propagation
SS13 Solar Radiation Pressure and Torque	Excluded	Included	Evolution of angular velocity highly dependent on orientation of solar panel
SS14 Internal Energy Dissipation	Excluded	Included	Faster wobbling decrease
SS15 Time Step	1 s	0.1 s	Negligible

tensor values by 10% led to a slower decrease of the spin rate, after four years by approximately 6% (SS10). These simulations have shown that the precession, nutation, and libration motions due to the gravity-gradient torque persist regardless of the initial spin conditions, although the period of the nutation and libration depends on the angular velocity magnitude. Moreover, the spin rate decay due to the eddy-current torque was shown to be the cause of the evolution of the amplitude and period of these motions. Finally, the extent of the wobbling motion was found to only depend on the initial difference between the maximum principal axis and the spin axis direction, although its damping towards the major-axis spin will occur with time (SS11 and SS12).

As previously mentioned, the effect of solar radiation was excluded from the baseline scenario as it had been shown to cause only a short-term periodic behaviour in angular velocity for Envisat [123]. However, the effect of solar radiation on the spin characteristics of satellites is known to be highly dependent on the shape of the spacecraft and the optical properties of its surfaces; more specifically, the position and orientation of the solar panel can have a large influence on the evolution of a satellite's angular velocity [7]. Although Envisat was seen to have its solar panel in a position close to the way presented in Fig. 4.1, its exact rotation about the x -axis is difficult to determine and it could vary by a few degrees [124]. Multiple simulations were carried out, for small changes of the orientation of the solar panel, by rotating it about the axis going through the center of the solar panel and satellite body and aligned with the

body-fixed frame x -axis (SS13). The inertia matrix was kept constant in these simulations. The solar panel optical coefficients were taken from the International DORIS Service (IDS) macro-model for Envisat [125].

Figure 4.5a shows the evolution of the angular velocity magnitude for the simulations where the solar panel was rotated by -10° to 5° , with an increment of 1° . The black line represents the baseline scenario without solar radiation. As can be seen, even a small change in the orientation of the solar panel can cause a large difference in the evolution of angular velocity. From Fig. 4.5, it was found that the most likely orientation of the solar panel is in such a way that its surface normal points towards the satellite's major principal axis, which occurs when the solar panel is rotated between -4° and -5° about the x -axis (recall that the maximum principal axis as shown in red in Fig. 4.1 is inclined by approximately -4.5°). Any deviation from this by even one degree causes a significant, unrealistic change in the evolution of angular velocity. Adding solar radiation did not reveal any changes in the evolution of the nutation and wobbling amplitudes for the -4° and -5° cases, although the period of each motion did change, evolving proportionally to angular velocity. The libration amplitude showed a noticeable difference: an oscillation with a period of one year and an amplitude of approximately 0.1° on top of its secular evolution appears, as exhibited in Fig. 4.5b when adding solar radiation with the solar panel rotated at -4° and -5° .

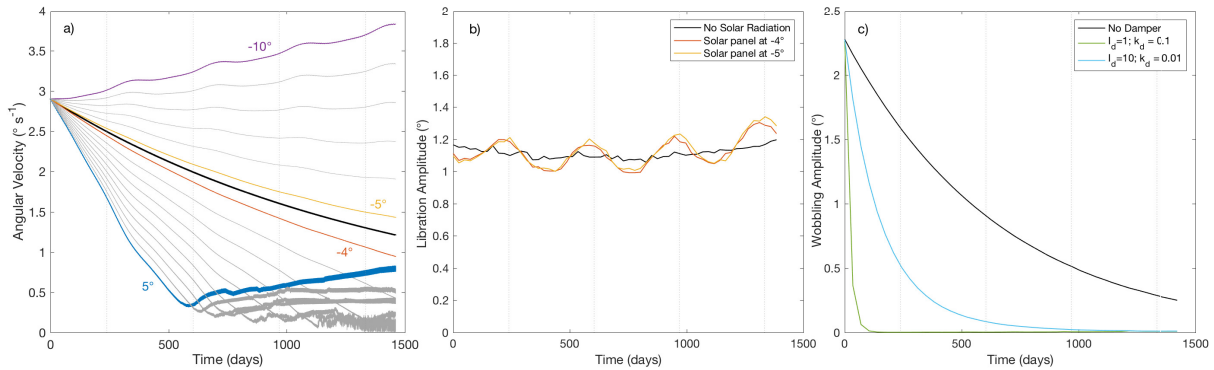


FIGURE 4.5: Evolution of Envisat's Angular Motions for Supplemental Simulations

Finally, including internal energy dissipation was also investigated (SS14). Multiple cases were analyzed: the moment of inertia of the damper I_d was varied between 1 and 10 kg m^2 ; damping constants from 0.01 to $1 \text{ kg m}^2 \text{ s}^{-1}$ were considered. No effects on the motion of the spin axis or angular velocity of the spacecraft were found, apart from a faster decrease of the wobbling motion, *i.e.*, a faster convergence to a major-axis spin.

Depending on the input parameters of the damper, the wobbling motion died down after 100 days to 3 years, bringing the spacecraft to a pure major-axis spin. Figure 4.5c shows such a decay in the wobbling amplitude for both the fastest and slowest decay seen from the simulations performed.

4.4 Review of Observational Results

Three observation methods have been used to estimate Envisat's rotational motion: satellite laser ranging, photometric measurements, and ISAR images. Figure 4.6 and Table 4.2 provide an overview of observational results to date that have dealt with Envisat's angular velocity and attitude motion. The vertical dashed line in Fig. 4.6 represents the time of loss of contact. The studies obtained estimates of Envisat's angular velocity over different but overlapping time frames using various methods. A good agreement on the observed decrease of the spacecraft's angular velocity magnitude from May 2013 onwards exists, which is also in line with the simulation results presented in Fig. 4.4a. However, four major sources of uncertainty are present in our simulation results that would lead to differences in the rate of decay of angular velocity: the initial orientation of ω , the initial angular velocity (SS8), the value of the magnetic tensor (SS10), and the orientation of the solar panel (SS13). Taking these into account, the observed angular velocity evolution agrees well with simulation results. Nevertheless, large differences in the motion of the spin axis have been observed and contradictions related to its stability are abundant. Moreover, some studies made certain assumptions in order to estimate Envisat's inertial angular velocity magnitude and spin axis direction, and uncertainty in these estimates are rarely discussed in detail. A review of all the measurements made so far, taking into account knowledge obtained from our simulation results, is therefore timely and crucial.

TABLE 4.2: Summary of Envisat Angular Motion Studies

Study	Time Frame	Method	Information Relevant to Spin Axis Orientation
[126] Shakun et al. (2013)	April - August 2013	Light Curves	Concluded that a precession of the spin axis is present
[43] Kucharski et al. (2014)	April - September 2013	SLR	Spin axis inclined 28° from n_O and fixed in the SCO frame over entire period
[46] Koskin et al. (2016)	2013-2015	Light Curves	Assumed a fixed spin axis in SCO frame and concluded it to be aligned with n_O
[55] Silha et al. (2017)	September 2016	Combination	Spin axis orientation obtained directly from ISAR images for each pass
[54] Sommer et al. (2017)	2011-2017	ISAR	Large spread in spin axis orientation is observed over the entire time frame
[127] Lin and Zhao (2018)	2013-2015	Light Curves	Included spin axis motion from gravity-gradient torque; concluded spin axis is nutating at 8.5° from n_O ; found presence of evolving nutation period (4.8 to 3.4 days from 2013 to 2015) and libration amplitude (0.7° to 0.5°)
[128] Pittet et al. (2018)	2013-2015	SLR	Spin axis orientation obtained for each pass and concluded fixed in ECO frame at 17° from n_O .

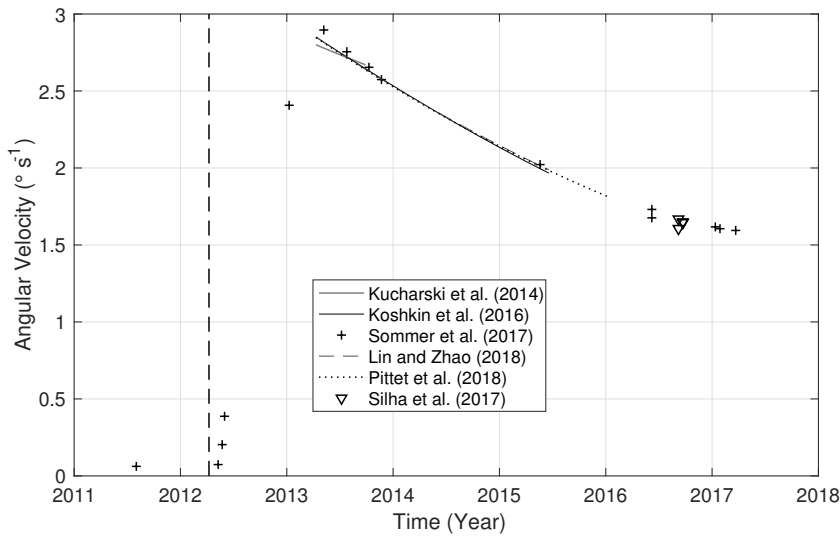


FIGURE 4.6: Reproduction of Envisat’s Angular Velocity Estimates as a Function of Time from Observational Studies

Envisat contains retroreflectors that can be used for satellite laser ranging; SLR residuals, defined as the difference between the laser range measured from the observatory on Earth to the retroreflector array (RRA) on-board the satellite and the predicted position of the satellite’s centre of mass with respect to the observatory, therefore provide a signal measuring the motion of the RRA as the spacecraft rotates around its centre of mass [43]. From oscillations in SLR residuals, an estimate of the satellite’s *apparent* spin period as measured from the observatory can be obtained [43]. Such measurements can only be taken when the satellite pass over the observatory is long enough relative to its rotation period so that such oscillations are observable, and when the RRA is visible to the ground station. In order to obtain the *inertial* spin parameters of the satellite, various methods can be used.

Some of the first post-mission observations dedicated to understanding what happened to Envisat were obtained by the International Laser Ranging Service (ILRS) at the request of ESA throughout 2013 [43]. From an analysis of 87 passes from various SLR stations, the campaign results obtained estimates of the apparent spin period of the satellite and determined that Envisat was witnessing a slow decrease of its angular velocity. The inertial spin periods were then obtained by assuming a specific spacecraft orientation. From the entire set of 347 passes during the seven-month period, the spacecraft’s spin axis was determined to be fixed in the Satellite-Centred Orbital (SCO) frame (see Section 2.1.1), inclined at approximately 28° from the negative orbit

normal and perpendicular to the spacecraft velocity direction [43]. Observations from 46 passes seen by the Glaz SLR station having a mean duration of 6.8 min were then used to estimate the inertial spin period of the satellite by assuming it was spinning opposite to its orbital motion (in retrograde motion). The spin axis orientation was assumed to be fixed in the SCO frame over the seven-month period, meaning that a precession is considered, and that a nutation equal to the orbital period of 100 minutes was assumed. However, simulation results for the 28° initial orientation of the spin axis with respect to the orbit normal (purple scenario in Fig. 4.4) show that this is impossible, as a nutation motion with period of a few days is expected in this case. Furthermore, if the assumed orientation of the spin axis is incorrect, an error on the inertial spin period will follow [43].

A more recent study dealing with SLR observations determined Envisat's spin parameters using SLR residuals from each single pass, instead of fitting over multiple passes [128]. Using the data from 31 passes observed from the Zimmerwald SLR station throughout 2013-2015, the study concluded that Envisat's spin axis was aligned with its principal axis of inertia and that it made a fixed 17° angle with the negative orbit normal, disregarding the possibility of a nutation, which again contradicts our simulation results (yellow scenario in Fig. 4.4). However, this conclusion should be taken lightly as a large spread of the spin axis orientation over the 2.5-year time frame is present in the results shown² [128].

The second method that has been applied to study Envisat's angular motion is light curve measurements obtained from variations of the target's brightness as seen from a ground telescope. From repeated peaks in the measurements, one can, in a similar way to SLR measurements, obtain an estimate of the *apparent* spin period of the target [45]. Converting to the *inertial* spin period, however, requires more care than doing so from SLR residuals, as a direction of the spin axis orientation cannot be obtained directly. Difficulties first exist in order to correctly obtain corresponding light peaks for slowly rotating spacecraft where the reflection geometry as seen from the ground changes from one peak to the next over one pass [46]. An assumption that the light reflections come from smooth flat surfaces and that the spin axis is fixed over one pass is also made in order to obtain valid inertial spin period values. Our results indicate that the latter is indeed a reasonable assumption for a short (few minutes) pass.

²The distribution of observations indicates a spread of the spin axis orientation inclined from 5° to 35° from the negative orbit normal with error bars between 1° and 12° ; the distribution of the azimuth of the spin axis in the ECO frame oscillates from 90° to 315° , with much smaller error bars.

First results from light curves were obtained using the KT-50 telescope and concluded from various observations ranging from April to August 2013 that, due to the spread of inertial spin period values, fluctuations of the spin axis orientation were present, and deduced a precession of the spin axis with the orbital plane [126]. More sets of results were also obtained from the same telescope for the period from April 2013 to May 2015. The inertial spin periods were derived by assuming that the actual attitude state can be determined by minimizing the spread of the resulting inertial spin period points; an assumption on the motion of the spin axis over the entire time frame is therefore made [46]. After assuming that the spin axis was fixed in the SCO frame and testing several inclinations of the spin axis with respect to the negative orbit normal from $0\text{--}30^\circ$, the study determined that the 0° case provided the best fit (*i.e.*, that the spin axis orientation was along the negative orbit normal) [46]. Once more, the assumption that the spin axis is fixed in the SCO frame is more than likely incorrect. If the spin axis is indeed aligned with the negative orbit normal, our 0° simulation results (blue scenario) confirm that the spin axis should be fixed in the SCO frame; however, as the gravity-gradient torque forces a rotation of the angular momentum vector about the negative orbit normal, an average best fit of 0° would also provide the smallest spread in the inertial spin period estimates.

A later study included the analytical expression for the gravity-gradient torque in the model employed to convert from the apparent to the inertial spin period values and therefore included the possibility of a nutation and libration, although no wobbling motion was considered [127]. A best fit was found when the angular momentum vector made approximately an 8.5° angle with the negative orbit normal; for that nutation amplitude, the nutation period (locked with the libration period) was found analytically to decrease from 4.8 days in 2013 to 3.4 days in 2015, and the libration amplitude from 0.7° in 2013 to 0.5° in 2015. These values are in an approximate agreement with what was found in our simulation as shown in Fig. 4.4 (orange scenario). Nevertheless, our results clearly show that the reduction of the spin rate, confirmed by all observations to date, goes hand in hand with an increase in the nutation amplitude over time; however, no indication of the evolution of the nutation amplitude is present in this study [127]. Including the gravity-gradient torque in the fitting model reduced the spread of the inertial spin period points as compared to results from the initial study, but not to the level of measurement errors stated [46]. The source of this discrepancy is still unexplained, but a significant wobbling and the evolution of the nutation amplitude as predicted by our simulations may contribute to an explanation.

ISAR imaging can also be used to determine the attitude state of a satellite in a more direct way than the other two methods. From multiple images obtained over a pass, a value for the angular velocity vector (magnitude and direction) can be deduced. The Tracking and Imaging Radar (TIRA) has focused on Envisat for multiple passes ranging from August 2011 to January 2017 [54]. During all of these observations, no specific motion of the spin axis is observed, and a large change in the spin axis direction can be seen in the inertial frame. The presence of the precession is witnessed, but a large nutation would also be needed to explain the spread in spin axis directions described.

Finally, these three methods have been used in conjunction: a study looking at four passes in September 2016, two on the 6th and two on the 21st, determined inertial spin periods from both light curve measurements and SLR residuals from the ZIMLAT telescope assuming a fixed rotation vector over one pass obtained by TIRA images [55]. A conclusion that Envisat's spin axis orientation was constant was made, although a 10° difference between two vectors on consecutive passes 100 minutes apart and a 24–34° difference between both days were observed. The fixed orientation concluded from these results is therefore debatable. Even though the two sets of passes are two weeks apart, the orbit's precession does not entirely explain the difference, which strongly suggests that a nutation is present.

4.5 Propagation to 2025: Removal Mission Date

So as to obtain predictions of the attitude state of Envisat for the time frame of the upcoming e.Deorbit mission, simulations were performed for a propagation length of 12 years until mid-2025. Because of the uncertainty in the various parameters mentioned, the magnetic tensor was varied in order to fit simulation results of the evolution of angular velocity with observations. This was done for the four previous cases of the initial orientation, where the initial angular velocity vector is 0°, 8.5°, 17°, and 28° from the negative orbit normal. In these simulations, the aerodynamic torque and hypervelocity impacts were excluded, but the gravity-gradient torque (up to order and degree 2), the eddy-current torque, the radiation torques (with a solar panel orientation at −4.5°), and internal energy dissipation (with $I_d = 1 \text{ kg m}^2$ and $k_d = 0.1 \text{ kg m}^2 \text{ s}^{-1}$) were included. The fitted values of $M_{yy} = M_{zz}$ for the four initial conditions were found to be 6×10^5 , 6×10^5 , 6.5×10^5 , and $7 \times 10^5 \text{ kg}^{-1} \text{ m}^2 \text{ s}^3 \text{ A}^2$, respectively, keeping

the proportionality between M_{xx} and M_{zz} the same as in Eq. (4.1). The TLE presented in Section 4.1 was used as input; however, in order to fit the curves of the angular velocity evolution to observations, an initial angular velocity of 2.8° s^{-1} was used. Figure 4.7a shows the evolution of the angular velocity as a function of time for the presented simulations as well as for observations. Figures 4.7b-d show the evolution of the characteristics of the nutation and libration for the same simulations.

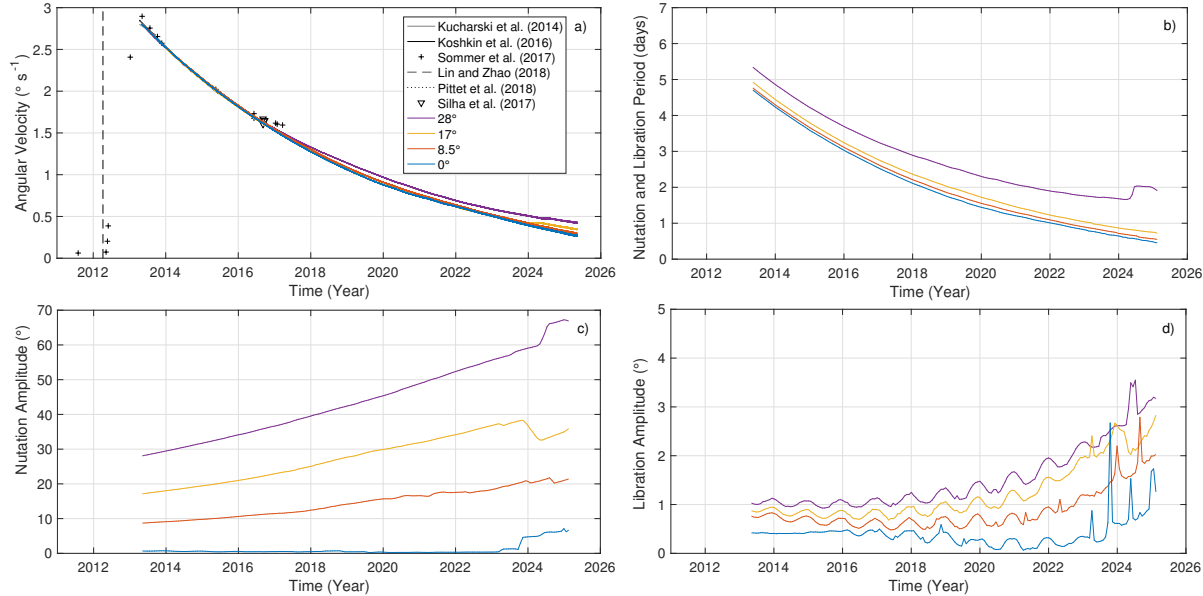


FIGURE 4.7: Long-Term Evolution of Envisat's Angular Velocity as a Function of Time

As can be seen from the results, the trends of the angular motions presented in Section 4.2 are expected to continue. By 2024, Envisat will slow down to approximately 0.5° s^{-1} , by which time the characteristics of the motions become less defined due to a smaller spin-stabilization and the beginning of a tumbling motion. This can be seen, for example, by the increase in the nutation amplitude for the 0° scenario in 2023, not representative of an actual nutation motion, but of the start of a tumbling motion. This can also be seen in the libration amplitude for every scenario, where variations start to occur during the same period.

The exact motion of the spacecraft in 2025 will be highly dependent on the current spin motion, as can be seen by the differences in the nutation motion for each scenario; furthermore, it is expected that as the spacecraft slows down and starts tumbling, the radiation pressure could lead the large debris into a different spin state or even into an increasing angular velocity scenario, as was seen in Fig. 4.5a, and as is currently

the case for TOPEX/Poseidon (see Chapter 5). Nevertheless, at these slow speeds, the attitude motion of tumbling debris becomes very chaotic and highly sensitive to the spacecraft parameters used as input, as has also been demonstrated in previous studies [59, 62, 129].

4.6 Recommendations

From the application of D-SPOSE to the defunct satellite Envisat, insights into the evolution of its rotational motion have been obtained. Its complex attitude dynamics has been found to be composed of three distinct angular motions: i) a precession of the satellite’s angular momentum vector with the orbital plane; ii) a revolution of its angular momentum vector about the orbit normal, composed of a nutation and libration with locked periods on the order of a few days and decreasing, and with the amplitude still uncertain; and iii) a wobbling of the angular velocity vector about angular momentum vector, although simulations have shown that any wobbling present after the satellite’s spin-up has most likely decayed by this time leaving Envisat in a major-axis spin.

The three observation methods employed to date for estimating the rotation of Envisat are quite different but complementary: SLR residuals can be used to determine both the spin rate and spin axis orientation over a single pass; photometric measurements will provide a continuous light signal from the satellite from which a spin rate can be obtained; ISAR images will detect the instantaneous attitude of the satellite, and with multiple consecutive images, the spin rate and spin axis orientation can be determined. While many of the observational studies to date using these three methods have concluded a fixed orientation of Envisat’s spin axis in the inertial frame or SCO frame, our analysis of the procedures used and data obtained shows that this is highly unlikely. Unless the spin axis is perfectly aligned with the orbit normal, an extremely unlikely scenario, an evolving nutation motion due to the gravity gradient torque will occur, contrary to what has been concluded so far. An agreement on the precession of the spin axis with the orbit seems to exist, but the presence of a nutation about the negative orbit normal and its time dependence needs to be acknowledged. The spread in the observed spin axis orientations, as determined by ISAR imaging and SLR, as well as the spread in the inertial spin periods from both SLR and light curves, even after

considering the gravity gradient torque, are indicative that such an evolving motion exists.

Characterizing this motion, however, is difficult, due to the complexity of such an angular motion and the scarcity of observations. However, any large motion observed after a few years will be due to a nutation of the spin axis. Our recommendations in order to obtain better estimates of Envisat's actual attitude motion are twofold. First, the attitude models used to obtain inertial spin period points from SLR measurements and light curves should include the possibility of a nutation and libration, as has previously been done for light curves, but should also allow for the evolution of the nutation amplitude. Second, in order to characterize these motions and fit simulation results with observations, a much larger observational data set is required on the time scale of each motion. Obtaining estimates for the nutation amplitude and period and their evolution with time could be done by analyzing SLR and ISAR data, first for multiple consecutive passes over a few days from various ground stations, and then by repeating these measurements several months later to detect their evolution.

The simulation results obtained from this study have provided multiple novel insights into Envisat's attitude motion in addition to the presence of the three angular motions. The derived high-order gravity-gradient torque and the complete formulation of the aerodynamic drag and torque for a spinning spacecraft were shown to be negligible for Envisat. Solar radiation was found to potentially have a large influence on the satellite, but when comparing to observations, it was deduced that the orientation of the solar panel was in a such a way that its effect is minimal. Most importantly, the simulated nutation motion was shown to become larger and faster with time. As Envisat's rotation slows down, its relative spin-stabilization effect will decrease, which will lead the gravity gradient torque and other environmental torques to push the satellite towards an even larger tumbling motion. Although Envisat's angular velocity magnitude is decreasing, this phenomenon indicates potential difficulties for the European Space Agency's upcoming e.Deorbit mission.



Philippe Cazalis

"Coup de chalut dans l'ether"

Watercolour on drawing paper

Chapter 5

TOPEX/Poseidon in Minor-Axis Spin

Another large space debris which has witnessed an increasing amount of interest in the last few years is the decommissioned joint NASA/CNES Ocean Topography Experiment called TOPEX/Poseidon, uncontrolled since January 2006 after one of its momentum wheels stopped working [7]. The spacecraft was initially launched in August 1992 into a circular orbit at 1,340 km with a 66° inclination, with a purpose to precisely map ocean surface topography in order to study various global weather phenomena [130]. Since its decommissioning, it has seen an increase in its angular velocity, as observed by Satellite Laser Ranging (SLR) and light curves, found to be due to solar radiation pressure [7, 47]. As the satellite contains a retroreflector array, precise measurements of its spin period and spin axis orientation have been obtained through high-repetition rate SLR data since 2014 from the Graz SLR station [7]. The International Laser Ranging Service (ILRS) and its Space Debris Working Group then initiated a global observation campaign in 2015. The interest in this debris has recently been even more pressing after a very close approach of 400 m was noticed in June 2017 between TOPEX/Poseidon and one of its successor spacecraft, the NASA/CNES Jason-2 satellite [7].

On top of understanding its rotational motion, needed if TOPEX/Poseidon ever becomes an Active Debris Removal (ADR) target, knowing its attitude dynamics is also beneficial to obtain precise orbital predictions for conjunction analyses to determine whether orbital manoeuvres of active satellites are necessary. However, accurate estimates of the spacecraft properties needed to predict the evolution of its rotation, such as its moments of inertia, are absent in the literature. This Chapter will aim to shed light on some of these missing parameters by analyzing the precise SLR measurements obtained for TOPEX/Poseidon and by applying D-SPOSE to this large debris and comparing simulation results to observations. While doing so, a better understanding of

the underlying rotational dynamics will be obtained.

Section 5.1 will first define a methodology to determine a relationship between the spacecraft's moments of inertia from observations of its spin motion. Section 5.2 will then make use of D-SPOSE to investigate the obtained parameters and will characterize the influence of external torques on the rotational dynamics of TOPEX/Poseidon. A comprehensive analysis of the system's energy and predictions of the satellite's future attitude state will be presented in Sections 5.3 and 5.4, respectively. Finally, a summary of the findings will be detailed in Section 5.5.

5.1 Determining Inertia Properties from Observations

5.1.1 Gravitational Effects on Angular Momentum

The equation for the rotational motion of a rigid body under external perturbations, seen in Eq. (2.5) in Section 2.1, can also be written as a function of its angular momentum, $\mathbf{h} = \mathbf{I}\boldsymbol{\omega}$, in the following way [56, Ch. 3, p. 59]:

$$\frac{d\mathbf{h}(t)}{dt} + \boldsymbol{\omega}(t)^\times \mathbf{h}(t) = \boldsymbol{\tau}(t, \mathbf{r}(t), \mathbf{v}(t), \mathbf{q}(t), \boldsymbol{\omega}(t)) \quad (5.1)$$

However, Eq. (5.1) can also be interpreted as the equation of motion of angular momentum expressed as components in the Earth-Centered Orbital (ECO) frame, $\mathbf{h} = [h_x \ h_y \ h_z]^T$, when perturbed by an oblate primary (see Fig. 2.3 in Section 2.1.1) [61]. In this interpretation, $\boldsymbol{\tau}$ is the sum of the external torques expressed in the ECO frame and $\boldsymbol{\omega}$ represents the angular velocity of the orbital plane, which is a function of the rate of change of the right ascension of the ascending node, Ω , and the inclination of the orbit, i . For a circular orbit, it is expressed as follows:

$$\boldsymbol{\omega} = \begin{bmatrix} 0 \\ \dot{\Omega} \sin i \\ \dot{\Omega} \cos i \end{bmatrix} \quad (5.2)$$

Under the influence of the gravity-gradient torque only, Eq. (5.1) becomes [61]:

$$\frac{d\mathbf{h}}{dt} = \frac{3\mu}{4r^3} \frac{H}{h^2} h_z \begin{bmatrix} -h_y \\ h_x \\ 0 \end{bmatrix} - \boldsymbol{\omega}^\times \mathbf{h} \quad (5.3)$$

where H is a complex function of the moments of inertia and angular velocity of the spacecraft, to be investigated in Section 5.1.2. Substituting for ω and \mathbf{h} into Eq. (5.2):

$$\begin{bmatrix} \dot{h}_x \\ \dot{h}_y \\ \dot{h}_z \end{bmatrix} = \frac{3\mu}{4r^3} \frac{H}{h^2} h_z \begin{bmatrix} -h_y \\ h_x \\ 0 \end{bmatrix} - \begin{bmatrix} -h_y \dot{\Omega} \cos i + h_z \dot{\Omega} \sin i \\ h_x \dot{\Omega} \cos i \\ -h_x \dot{\Omega} \sin i \end{bmatrix} \quad (5.4)$$

We can also write this equation in the spherical coordinate system of the ECO frame using h , θ_{ECO} , and λ_{ECO} , as defined in Fig. 2.3b in Section 2.1.1 (for clarity, the subscript ECO will be dropped in this Chapter):

$$\begin{aligned} h_x &= h \sin \theta \cos \lambda \\ h_y &= h \sin \theta \sin \lambda \\ h_z &= h \cos \theta \end{aligned} \quad (5.5)$$

and the time derivatives:

$$\begin{aligned} \dot{h}_x &= \dot{h} \sin \theta \cos \lambda + h \dot{\theta} \cos \theta \cos \lambda - h \dot{\lambda} \sin \theta \sin \lambda \\ \dot{h}_y &= \dot{h} \sin \theta \sin \lambda + h \dot{\theta} \cos \theta \sin \lambda + h \dot{\lambda} \sin \theta \cos \lambda \\ \dot{h}_z &= \dot{h} \cos \theta - h \dot{\theta} \sin \theta \end{aligned} \quad (5.6)$$

For a stable principal axis spin, under the sole influence of the gravity-gradient torque, which is conservative, h remains constant and Eq. (5.6) reduces to:

$$\begin{aligned} \dot{h}_x &= h \dot{\theta} \cos \theta \cos \lambda - h \dot{\lambda} \sin \theta \sin \lambda \\ \dot{h}_y &= h \dot{\theta} \cos \theta \sin \lambda + h \dot{\lambda} \sin \theta \cos \lambda \\ \dot{h}_z &= -h \dot{\theta} \sin \theta \end{aligned} \quad (5.7)$$

After the change of variables, Eq. (5.4) becomes:

$$\begin{bmatrix} \dot{\theta} \cos \theta \cos \lambda - \dot{\lambda} \sin \theta \sin \lambda \\ \dot{\theta} \cos \theta \sin \lambda + \dot{\lambda} \sin \theta \cos \lambda \\ -\dot{\theta} \sin \theta \end{bmatrix} = \frac{3\mu}{4r^3} \frac{H}{h} \cos \theta \begin{bmatrix} -\sin \theta \sin \lambda \\ \sin \theta \cos \lambda \\ 0 \end{bmatrix} - \begin{bmatrix} -\dot{\Omega} \sin \theta \sin \lambda \cos i + \dot{\Omega} \cos \theta \sin i \\ \dot{\Omega} \sin \theta \cos \lambda \cos i \\ -\dot{\Omega} \sin \theta \cos \lambda \sin i \end{bmatrix} \quad (5.8)$$

This is a system of three equations that defines the motion of the spin axis in the ECO frame through the angles θ and λ , if all other parameters are known. Alternatively, these equations can also be used to identify the value of parameter H/h if observations of the motion of the spin axis are available. As will be shown in the next section, this parameter is related to the three moments of inertia of the spacecraft and estimating it will therefore provide us with a relationship between them.

5.1.2 Moments of Inertia Relationship

As was mentioned earlier, an observation campaign of TOPEX/Poseidon has been on-going since 2014. Figure 5.2 displays observations of its spin axis orientation and period as determined by SLR for the time frame from 2014-2017 [7]. The reference frame that was used in that study was defined as an orbital coordinate system (OCS) with x_{ocs} pointing towards perigee and with z_{ocs} aligned with the orbit normal [7]. A comparison to the ECO frame can be seen in Fig. 5.1 where the orbital plane is shown by the blue circle. In this reference frame, the elevation is the angle made with the $x_{\text{ocs}}-y_{\text{ocs}}$ plane defined positive when angled towards z_{ocs} ; azimuth is the angle of the projection onto the $x_{\text{ocs}}-y_{\text{ocs}}$ plane defined positive when from the x_{ocs} -axis to the y_{ocs} -axis. In order to obtain the values in the ECO coordinate system used in the previous section, the following transformation needs to be made:

$$\theta = \frac{\pi}{2} - \theta_{\text{ocs}} \quad (5.9)$$

$$\lambda = \phi_{\text{ocs}} + \omega_{\text{aop}} \quad (5.10)$$

where θ_{ocs} and ϕ_{ocs} are the elevation and azimuth as described above, and ω_{aop} is the argument of perigee, which can be obtained from Two-Line Elements (TLE). Figure 5.3 shows the values of θ and λ after the transformation, along with the angular velocity of the spacecraft, ω , derived from the spin period.

From these observations, it is possible to determine approximate values for θ , λ , $\dot{\theta}$, $\dot{\lambda}$, and ω at a specific point in time. Equation (5.8) can then be solved for the ratio H/h .

If we assume that the spacecraft is spinning about its principal z -axis (see Fig. 5.4), as was determined from the SLR campaign, then H and h can be written as [7, 61]:

$$H = I_x + I_y - 2I_z \quad (5.11)$$

$$h = I_z\omega \quad (5.12)$$

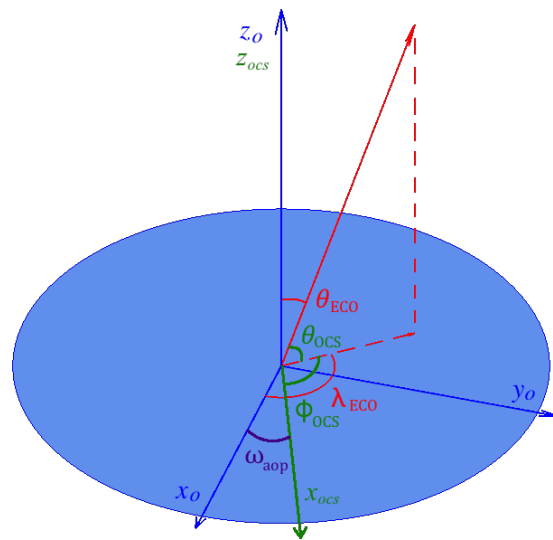


FIGURE 5.1: ECO and the Orbital Coordinate System [7]

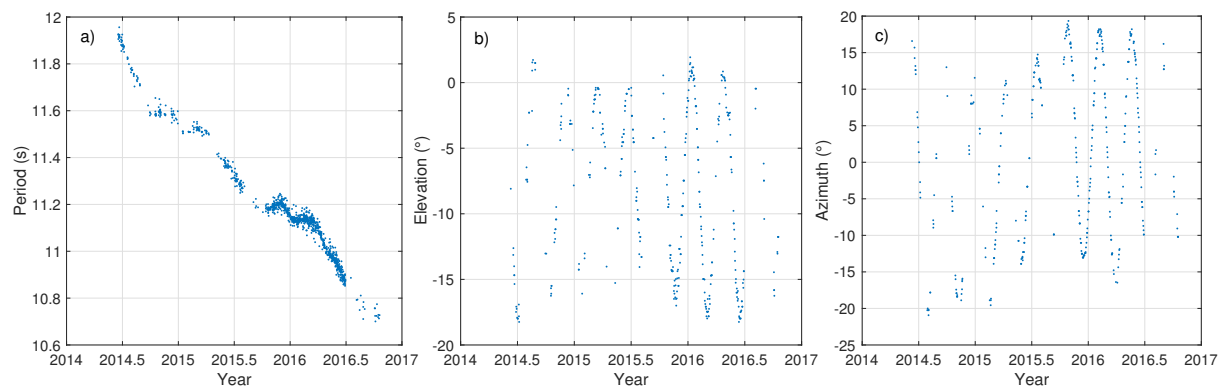


FIGURE 5.2: Observations of TOPEX/Poseidon a) Spin Period, b) Elevation, and c) Azimuth in the Orbital Coordinate System [7]

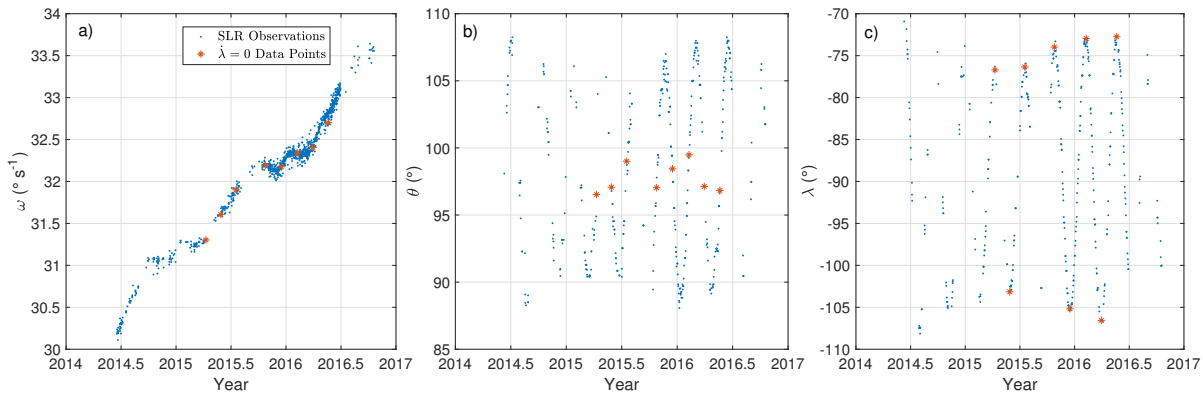


FIGURE 5.3: Observations of TOPEX/Poseidon Angular Velocity and Spin Axis Orientation in the ECO Frame

We can now write our unknown as a function of a non-dimensional parameter I^* which is purely a function of the moments of inertia:

$$I^* = \frac{I_x + I_y - 2I_z}{I_z} \quad (5.13)$$

so that:

$$\frac{H}{h} = \frac{I^*}{\omega} \quad (5.14)$$

The most simple observations that can be used from Fig. 5.3 in order to obtain an estimate of I^* occur at times when $\dot{\lambda} = 0$ using the second scalar equation of Eq. (5.8). Substituting for $\dot{\theta}$ from the third scalar equation of Eq. (5.8), $\dot{\lambda} = 0$, H/h from Eq. (5.14), and solving for I^* , yields:

$$I^* = \frac{4r^3\omega}{3\mu} (-\dot{\Omega} \sin i \csc \theta \sin \lambda + \dot{\Omega} \cos i \sec \theta) \quad (5.15)$$

This equation is valid as long as θ is not a multiple of $\pi/2$.

From Fig. 5.3c, it is possible to select 8 points which satisfy the $\dot{\lambda} = 0$ condition. The corresponding values of ω , θ , and λ are shown by red stars in Fig. 5.3 and are presented in Table 5.1 along with the values for r and i , which are obtained from TLEs at the corresponding dates. The value of $\dot{\Omega}$ was also determined from TLEs by assuming it constant over the 2014-2017 period and was found to be $\dot{\Omega} = -2.40433 \times 10^{-5} \text{ }^\circ \text{ s}^{-1}$. The derived I^* is presented for each point; the mean and standard deviation calculated from the set of 8 points was found to be $I^* = 0.79 \pm 0.15$, reflecting a significant spread in these estimates.

TABLE 5.1: Characteristics of Spin Axis Orientation Points where $\lambda = 0$

Date	θ ($^{\circ}$)	λ ($^{\circ}$)	ω ($^{\circ} \text{ s}^{-1}$)	i ($^{\circ}$)	r (km)	I^*
10-Apr-2015	96.531	-76.699	31.3030	66.0431	7714.164	0.9417
29-May-2015	97.072	-103.155	31.6061	66.0415	7714.158	0.8537
18-Jul-2015	99.012	-76.348	31.9004	66.0411	7714.153	0.6075
25-Oct-2015	97.036	-73.974	32.1933	66.0402	7714.146	0.8799
16-Dec-2015	98.446	-105.184	32.1751	66.0386	7714.139	0.6779
8-Feb-2016	99.483	-72.958	32.3387	66.0406	7714.136	0.5743
30-Mar-2016	97.133	-106.556	32.4048	66.0420	7714.132	0.87
20-May-2016	96.838	-72.744	32.7008	66.0409	7714.129	0.9311

Next, values for the individual moments need to be considered. First, we assume that the spacecraft, shown in Fig. 5.4, is axisymmetric (this assumption will be investigated in Section 5.2.2), and with $I_x = I_y$, Eq. (5.13) simplifies to:

$$I^* = 2 \frac{I_x - I_z}{I_z} \quad (5.16)$$

$$I_x = I_z \left(\frac{I^*}{2} + 1 \right) \quad (5.17)$$

Second, we note that from an analysis of observations during the SLR campaign, using an attitude dynamics model to fit simulation results with observations, it had been previously estimated that $I_z = 70,000 \text{ kg m}^2$ [7]. Making use of the value of I^* derived above and substituting for I_z , we obtain the following preliminary values for the moments of inertia:

$$\begin{aligned} I_x &= 97,650 \text{ kg m}^2 \\ I_y &= 97,650 \text{ kg m}^2 \\ I_z &= 70,000 \text{ kg m}^2 \end{aligned} \quad (5.18)$$

As the spacecraft was shown to be rotating about its body-frame z -axis, these initial estimates seem to indicate that the spacecraft is rotating about its *minor* principal axis. This will now be scrutinized in detail using D-SPOSE.

5.2 Investigation using D-SPOSE

5.2.1 Simulation Inputs

The initial orbital elements used for the coupled orbit-attitude propagations were taken from a TLE at the time of the first SLR observations shown in Fig. 5.2:

```
1 22076U 92052A 14163.17066206 -.00000054 00000-0 28497-4 0 2018
2 22076 66.0407 248.1072 0007707 272.4947 118.5262 12.80986122 21470
```

At approximately that epoch, on June 11, 2014, the spin period of TOPEX/Poseidon was determined to be approximately 11.92 s, with $\theta = 98.10^\circ$ and $\lambda = -70.92^\circ$.

The spacecraft surface geometry model used, made up of 16 triangular surfaces, is shown in Fig. 5.4 with the solar panel orientation identified by the red arrow. The spacecraft mass is taken as 2405.4 kg; the center of mass is assumed to be $\mathbf{c}_p = [0.160 \quad -0.418 \quad 0.049]^T$ from the center of the box with surface areas $\Delta x \Delta y = 8.32 \text{ m}^2$, $\Delta x \Delta z = 8.18 \text{ m}^2$, and $\Delta y \Delta z = 4.71 \text{ m}^2$; the solar array measures 3.3 m in width and has a surface area of 25.5 m² [125]. All of these parameters, as well as the surface optical coefficients, are taken directly from the International DORIS Service (IDS) macro-model for TOPEX/Poseidon [125]. The mass and center of mass are calculated from pre-launch estimates with the effect from manoeuvres removed [125]. Furthermore, the exact orientation of the solar panel is unknown as during the mission it rotated about the axis going through the center of the solar panel and satellite body and aligned with the body-frame y -axis; the orientation shown in Fig. 5.4a is considered to be the 0° case, where rotating it from its current $-z$ orientation towards the x -axis is considered positive.

Simulations were carried out for a period of three years (1096 days) with a time step of 0.5 s, which was determined to be sufficiently small after doing a work-energy balance check and obtaining almost exactly the same results for a simulation with a time step of 0.1 s. The gravity-gradient torque and gravitational acceleration were calculated using a geopotential up to order and degree 2. Aerodynamic drag and torque were neglected due to the altitude of the spacecraft, so was the effect of momentum transfer from hypervelocity impacts. The accelerations and torques due to direct solar radiation, as well as reflected (albedo) and emitted (infrared) radiation were considered, as well as the eddy-current torque using IGRF-12. Internal energy dissipation is investigated in detail in Section 5.3.

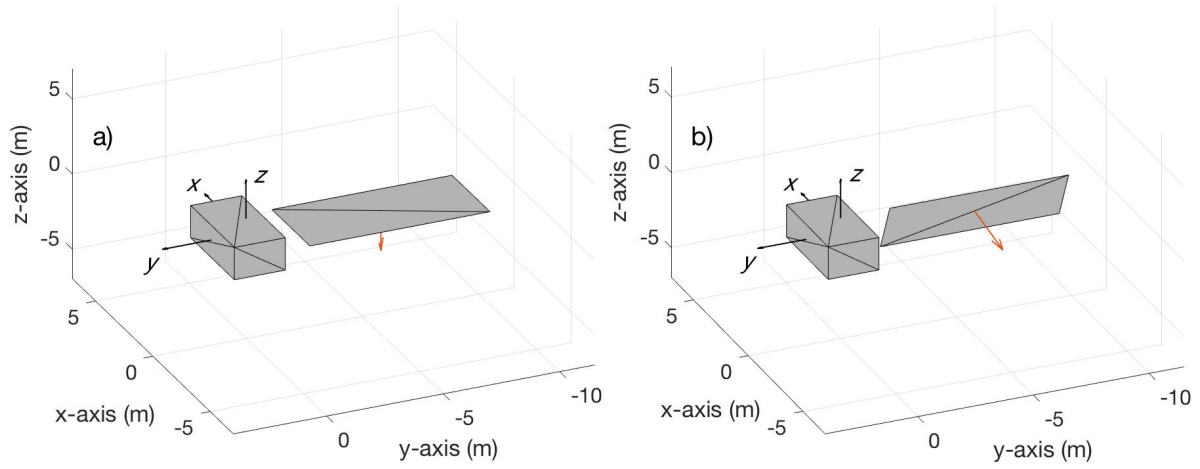


FIGURE 5.4: TOPEX/Poseidon Surface Geometry Model with Solar Panel Orientation at: a) 0° and b) 285°

As several parameter values of the spacecraft are uncertain, multiple simulations were executed by varying four types of parameters. First, the true moments of inertia are unknown: our estimates of them stated in Eq. (5.18) contain uncertainties and need to be validated; the axisymmetry assumption also needs to be checked; and the initial value of I_z should be investigated as the $70,000 \text{ kg m}^2$ estimate was obtained without considering the eddy-current torque. Second, although previously estimated to be rotated approximately 285° from the orientation in Fig. 5.4a, as determined in the study undertaken by the SLR campaign, the exact orientation of the solar panel is unknown [7]. Simulations were therefore performed varying this value from 275° to 295° in 1° increments. The 285° case is shown in Fig. 5.4b. Third, the effect of the eddy-current torque, which wasn't included in the attitude dynamics model of the SLR study used to propagate the spin period and estimate I_z , will be investigated here and the value of the magnetic tensor will be estimated. Finally, the finding that the spacecraft is spinning about its minor axis needs to be confirmed by analyzing the effect of internal energy dissipation using various Kane damper characteristics.

5.2.2 Propagation Results

In order to validate the methodology detailed in Section 5.1, an initial simulation was run considering only the gravity-gradient torque using the moments of inertia

from Eq. (5.18). Figure 5.5 displays the obtained evolution of the angular velocity magnitude and spin axis orientation. As can be seen, the oscillations are well captured, confirming the relationship derived in Section 5.1, but no evolution of the angular velocity is present as the gravity-gradient torque is conservative.

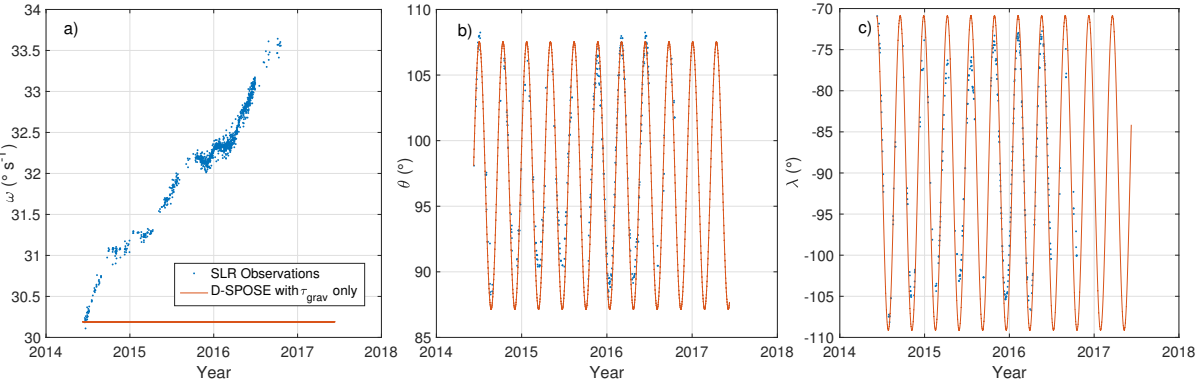
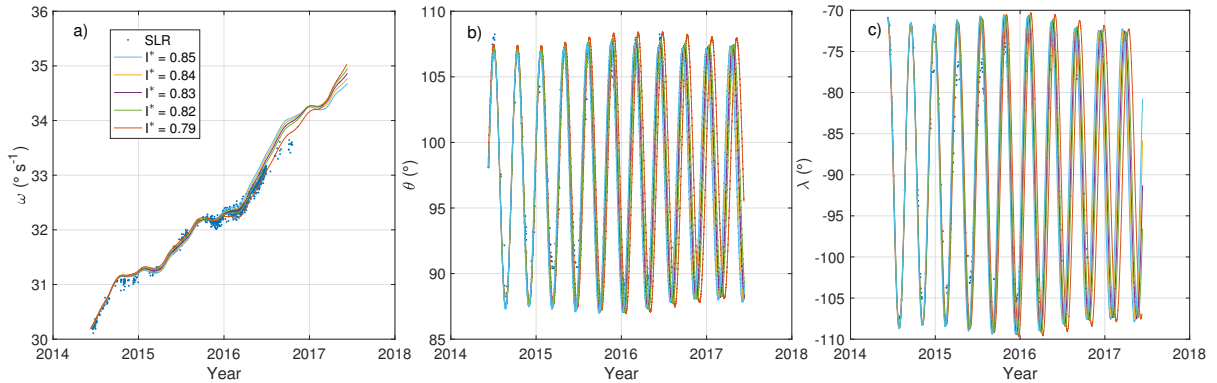


FIGURE 5.5: D-SPOSE Results Under the Gravity-Gradient Torque vs. Observations

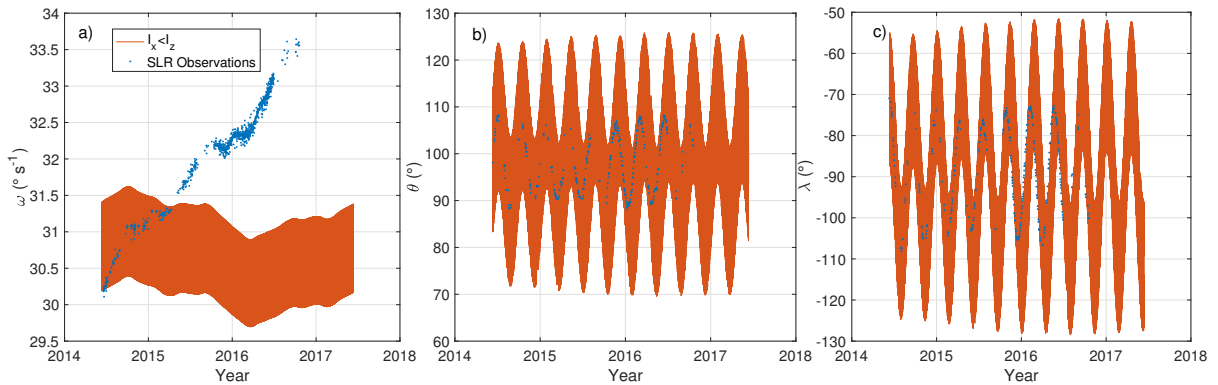
When including radiation pressure, which produces a good agreement between the simulation and observations for the evolution of angular velocity, similarly to what was found by the SLR study, it was seen that variations occurred in the amplitudes of the θ and λ oscillations when compared to the gravity-gradient only scenario, although they were determined to be slightly smaller than observations (see Fig. 5.6). In addition, a slight shift in the oscillations of the spin axis orientation occurs with respect to observations, indicating a need to correct the obtained value of I^* . Simulations varying I^* , but maintaining $I_z = 70,000 \text{ kg m}^2$ and the axisymmetry assumption, were therefore performed, keeping the solar panel orientation at 285° , and are shown in Fig. 5.6. The best fit between simulations and observations for the evolution of the spin axis orientation was found to occur when $I^* = 0.83$, well within the standard deviation of the original mean (0.79 ± 0.15). The axisymmetry condition was then checked by keeping the value of I_z constant, but varying I_x and I_y while satisfying this value of I^* , that is:

$$I_x + I_y = 2.83I_z \quad (5.19)$$

This showed no visible differences in the evolution of angular velocity and spin axis orientation for any of the scenarios, except for cases when either $I_x \leq I_z$ or $I_y \leq I_z$; these resulted in large high-frequency oscillations of the spin parameters, indicating that an intermediate principal axis spin about the body-frame z -axis is unstable, as can

FIGURE 5.6: Simulations Including Radiation Pressure and Varying I^*

be expected. An example simulation showing this instability can be seen in Fig. 5.7 for $I_x < I_z$, with $I_x = 60,000 \text{ kg m}^2$, $I_y = 138,100 \text{ kg m}^2$, and $I_z = 70,000 \text{ kg m}^2$.

FIGURE 5.7: D-SPOSE Results for $I_x < I_z$

When including the eddy-current torque, which is expected to slow down the rotation of a spinning spacecraft, decreasing the value of I_z is necessary in order to keep an agreement between the simulation results and observations. After performing a multitude of simulations, varying I_z from $70,000$ to $40,000 \text{ kg m}^2$ with increments of $10,000 \text{ kg m}^2$, assuming $I_x = I_y$, and adjusting for the orientation of the solar panel and the value of the magnetic tensor, assumed to be diagonal, $\mathbf{M} = \text{diag}\{M, M, M\}$, multiple simulations presented an agreement with observations. These are shown in Fig. 5.8 and the corresponding values for I_z , M , and the orientation of the solar panel γ are presented in Table 5.2. From the determined values of I_z and M , an approximate linear relationship between them emerged:

$$I_z = 75,000 - 0.25M \quad (5.20)$$

This relationship was found to hold well for values of $I_z \geq 50,000 \text{ kg m}^2$, but below that value, the larger difference in the solar panel orientation γ compared to the other cases, as seen in Table 5.2, brakes the linearity of the identity and the slope of the curve increases slightly.

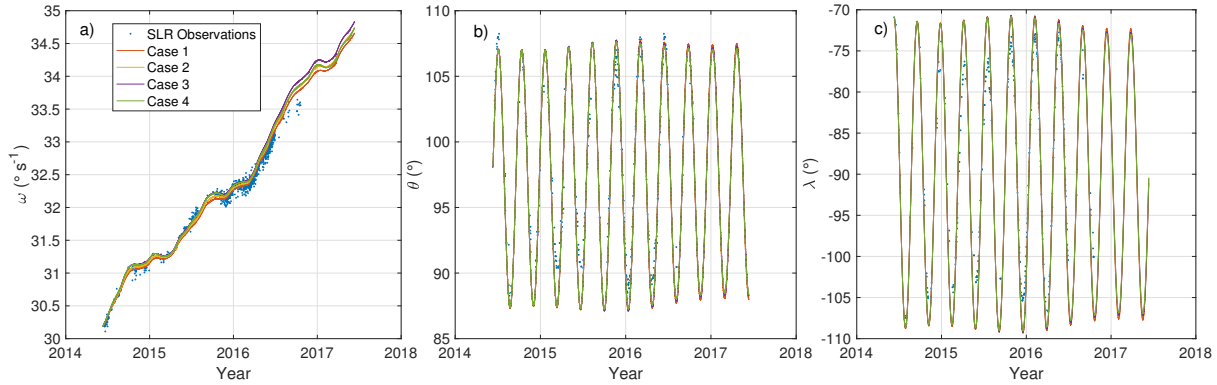


FIGURE 5.8: Best Fit Simulations Varying I_z , M , and γ vs. Observations

TABLE 5.2: Parameters of Best Fit Simulations

Simulation	$I_z (\text{kg m}^2)$	$M (\text{S m}^4)$	$\gamma (\text{°})$
Case 1	70,000	20,000	282
Case 2	60,000	60,000	281
Case 3	50,000	100,000	280
Case 4	40,000	150,000	278

Equations (5.19) and (5.20) relate the moments of inertia to the magnetic tensor of the spacecraft and define the spacecraft parameters as was determined by comparing propagation results to observations. However, an important effect was neglected in the previous simulations: internal energy dissipation is of great importance in the attitude dynamics of uncontrolled rigid bodies in space and its effect needs to be investigated, especially for a spacecraft which seems to be spinning about its minor principal axis.

5.3 Energy Analysis

5.3.1 Internal Energy Dissipation

It is usually expected that energy dissipation eventually transitions a rotating rigid body in space into a major-axis spin; it is in this light that additional simulations were

performed with D-SPOSE including the influence of a Kane damper (see Section 2.3.4) [79]. The characteristics of the damper were varied: two moments of inertia were considered, $I_d = 1 \text{ kg m}^2$ and $I_d = 10 \text{ kg m}^2$; and the damping coefficient k_d was selected to be 1, 0.1, and $0.01 \text{ kg m}^2 \text{ s}^{-1}$. These damper characteristics led to an initial perturbing torque on the order of 10^{-7} and 10^{-8} N m for the respective damper inertias considered, compared to approximately 10^{-2} , 10^{-4} , and 10^{-5} N m for the gravity-gradient, radiation, and eddy-current torques, respectively. Figure 5.9 shows the angular velocity and spin axis orientation of TOPEX/Poseidon for the corresponding simulations that were run for a period of three years using the parameters of Case 2 described in Table 5.2, but with no axisymmetry, randomly choosing $I_x = 94,800 \text{ kg m}^2$ and $I_y = 75,000 \text{ kg m}^2$, in order to have a clear major principal axis, in this case the body-frame x -axis.

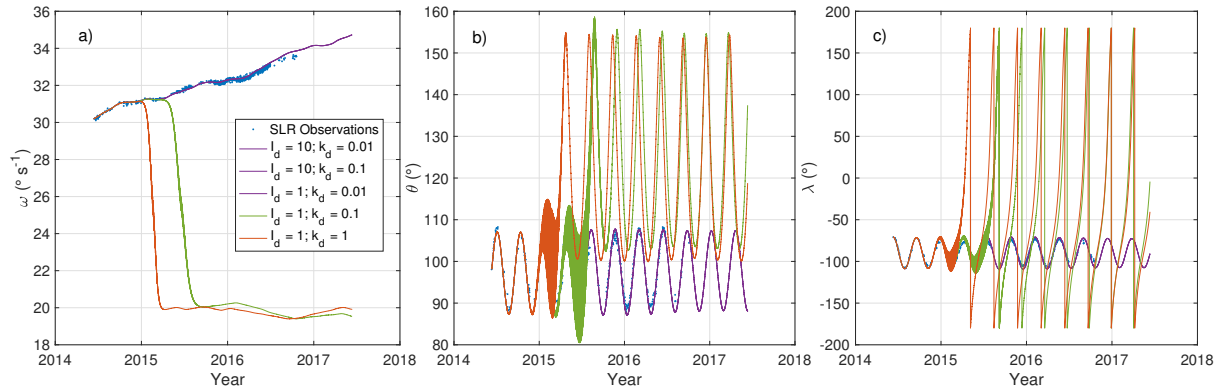


FIGURE 5.9: Simulations with Internal Energy Dissipation

As can be seen, for the cases where the effect of internal energy dissipation is expected to be the largest (either due to a small I_d or a large k_d), at some point during the simulation, a transition away from the minor-axis spin and into a major-axis spin occurs. The time taken for the system to transition, however, depends on the damper characteristics. Nevertheless, this phenomenon does not occur for every simulation in the time frame considered, indicating that a stable minor-axis spin has the potential to endure for quite some time, if internal energy dissipation is small enough. However, in order to confirm that the minor-axis spin is indeed feasible and representative of the system behaviour, a detailed examination of the total energy of the system was performed.

5.3.2 Work-Energy Balance

The equation for the work-energy balance of a rigid body under the influence of external perturbations is as follows [131]:

$$E_0 = U + K - W + \int_0^t \frac{\partial U}{\partial \tau} d\tau \quad (5.21)$$

where U and K are the potential and kinetic energy, W is the work done by the non-gravitational perturbations on the spacecraft, and E_0 is a constant, the initial energy of the system. In any analysis, the work-energy balance must be consistent with the approximations made in the description of the equations of motion, specifically the perturbations taken into account. Considering only the gravitational potential energy of a point mass due to the Earth, but not due to the Moon nor the Sun, the equation for the gravitational potential per unit mass defined by U in Chapter 2 (see Eq. (2.8) in Section 2.2) can be modified for the potential reference value of 0 at infinity to give the gravitational potential energy, U_E , as follows:

$$U_E = -\frac{\mu m}{r} \left[1 + \sum_{l=2}^k \sum_{m=0}^l \left(\frac{R_E}{r} \right)^l P_{l,m} [\sin \theta] \{ C_{l,m} \cos(m\lambda) + S_{l,m} \sin(m\lambda) \} \right] \quad (5.22)$$

This equation holds for a point mass orbiting a non-spherical Earth, but becomes more complex and dependent on orientation for a rigid body. For simplicity, instead of considering the orientation-dependent terms in the gravitational potential energy, which in turn lead to the effect of the gravity-gradient torque, the work done by this torque will be identified separately as W_{gg} , leading to a modified Eq. (5.21):

$$E_0 = U_E + K - W_{gg} - W + \int_0^t \frac{\partial U_E}{\partial \tau} d\tau \quad (5.23)$$

In this equation, the kinetic energy of the spacecraft arises from two sources, its translational kinetic energy, K_T , and its the rotational kinetic energy, K_R :

$$K = K_T + K_R = \frac{1}{2}mv^2 + \frac{1}{2}\boldsymbol{\omega}^T \mathbf{I} \boldsymbol{\omega} \quad (5.24)$$

The work done by the external perturbations similarly consists of the work done by the non-conservative forces, W_f , and the work done by the non-conservative torques,

W_τ , affecting the spacecraft:

$$W = W_f + W_\tau = \int_0^t \sum_i \mathbf{f}_i^T \mathbf{v} \, d\tau + \int_0^t \sum_j \boldsymbol{\tau}_j^T \boldsymbol{\omega} \, d\tau \quad (5.25)$$

Finally, the last term on the right hand side of Eq. (5.21) arises due to the time dependence of the potential function, related to the Earth's rotation about its axis. For a rotating Earth, the function in Eq. (5.22) varies in the inertial frame and the term associated with its time dependence was shown to be approximated by [131]:

$$\int_0^t \frac{\partial U_E}{\partial \tau} d\tau = \Delta U_t \approx -m\omega_E(r_x v_y - r_y v_x) \quad (5.26)$$

where $\mathbf{r} = [r_x \ r_y \ r_z]^T$ and $\mathbf{v} = [v_x \ v_y \ v_z]^T$ are the position and velocity of the satellite in the inertial frame, respectively, and ω_E is the rate of rotation of the Earth.

In order to analyze the evolution of the system's energy due to the non-conservative external perturbations, a one-year simulation was executed with all of the perturbations considered in Section 5.2.2, including damping ($I_d = 10 \text{ kg m}^2$ and $k_d = 0.01 \text{ kg m}^2 \text{ s}^{-1}$) but no third-body perturbations, using the spacecraft parameters of Case 2 in Table 5.2 but with no axisymmetry, and with a 0.01 s time step in order to reduce numerical errors and minimize possible losses of energy.

Figure 5.10a shows the evolution of the system's total mechanical energy, $U_E + K - W_{gg} + \Delta U_t$, for the one year propagation in blue. For comparison the mechanical energy associated with the satellite's orbital motion only, $U_E + K_T + \Delta U_t$, is presented in red. Figure 5.10b displays the evolution of the mechanical energy associated with the satellite's rotation, $K_R - W_{gg}$, in blue. A work-energy balance of the satellite's rotational motion was performed by calculating the work done by the external torques; a conservation of $K_R - W_{gg} - W_\tau$ is confirmed, as shown by the red line in Fig. 5.10b.

From these, we can see that the external perturbations do indeed increase the rotational energy of the spacecraft, and that the total energy of the system witnesses both periods of time when it decreases and periods of time when it increases. Although radiation pressure systematically increases the angular velocity of the spacecraft over the time frame of the simulations presented, the energy associated with the satellite's orbit (shown by the red curve in Fig. 5.10a) witnesses large oscillations due to the complex interaction between radiation pressure and the satellite's position and orientation. From the simulation results, a clearly defined pattern of evolution of the system's

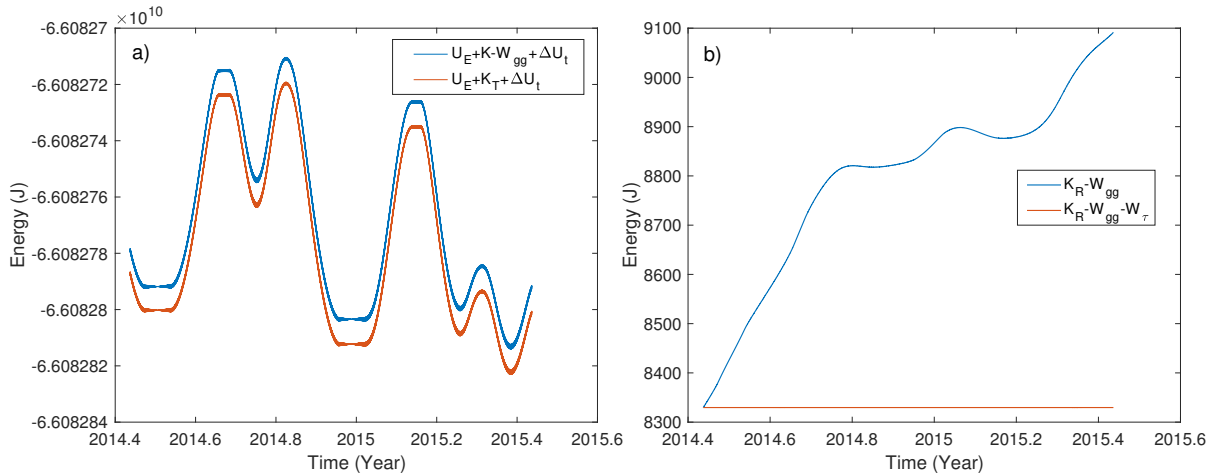


FIGURE 5.10: Evolution of the System Energy

energy can not be identified. Considering the energy of the system, it appears that TOPEX/Poseidon is indeed experiencing an increase of its angular velocity about its minor-axis spin. In order to determine whether this state of spin will persist and to predict the spacecraft's future attitude state, several simulations were performed to the year 2030.

5.4 Attitude Motion Predictions

Simulations for Cases 1 to 4 as presented in Table 5.2 were performed for a period of 15 years until 2030¹ in order to provide forecasts of the evolution of TOPEX/Poseidon's angular velocity and spin axis orientation and to determine whether even the smallest case of damping considered can result in an enduring stable minor-axis spin. The blue line in Fig. 5.11 shows the evolution of the spacecraft's spin motion for the entire propagation time frame for the Case 2 simulation without axisymmetry (using the random moments of inertia mentioned in Section 5.3.1) and considering a Kane damper with $I_d = 10 \text{ kg m}^2$ and $k_d = 0.01 \text{ kg m}^2 \text{ s}^{-1}$ (labeled as Case 2*). As can be seen, even in this "small" damping scenario a transition to a major-axis spin eventually occurs around 2023. The time to transition was found to be dependent on the chosen moment of inertia I_z . Since the time to transition was also shown to be dependent on the uncertain damping properties and since the resulting major-axis spin motion will

¹This time frame was chosen arbitrarily and is currently the largest time frame available in D-SPOSE due to Sun and Moon ephemerides only being included until then.

be dependent on the unknown moment of inertia associated with that principal axis (I_x or I_y), no reliable predictions can be put forward for the satellite's future spin motion if a transition ever occurs. The only useful information that D-SPOSE can provide in terms of attitude motion forecasts is if TOPEX/Poseidon stays in a stable minor-axis spin. As such, Fig. 5.11 shows the simulations for Cases 1 to 4 without internal energy dissipation.

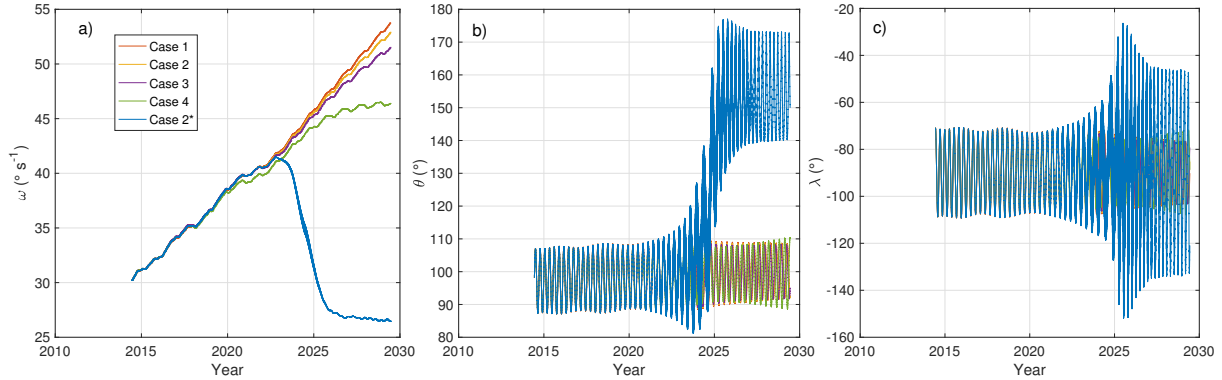


FIGURE 5.11: Predictions of TOPEX/Poseidon's Spin Motion

From these results, it can be concluded that, if a minor-axis spin is maintained, the satellite's angular velocity will continue to increase but with a decreasing rate, dependent on the moments of inertia of the spacecraft. In Case 1, where I_z is the highest, angular velocity increases the fastest. A departure from agreement between the four scenarios starts to occur around the year 2020. By 2030, the four simulations show that TOPEX/Poseidon's angular velocity magnitude will have reached approximately 50° s^{-1} . The decrease of the angular acceleration seen is most likely due to a balance being reached between radiation pressure accelerating the satellite's spin in a constant manner and the eddy-current torque resisting it increasingly due to its proportionality to the spacecraft angular velocity. As was mentioned, if a transition to a major-axis spin does indeed occur, it is impossible for now to predict when and how the satellite's spin motion will evolve.

As was seen in Chapter 2, an interesting way to visualize the spin motion of a satellite is by representing its spin axis orientation in an equidistant azimuthal projection of the ECO frame along the line of sight of the orbit normal direction from the negative to the positive z_o -axis. Figure 5.12 shows the spin axis orientation in such a projection for the entire Case 2 scenario (in yellow) and the Case 2* scenario after 2027, *i.e.*, after

the transition to major-axis spin has occurred (in blue). These results show that a nutation of the spin axis persists but with its center evolving throughout the transition to a major-axis spin along the $-y_0$ -axis. Once more, this exact transition will depend on the actual damping occurring in the spacecraft and its exact moments of inertia, both of which are unknown.

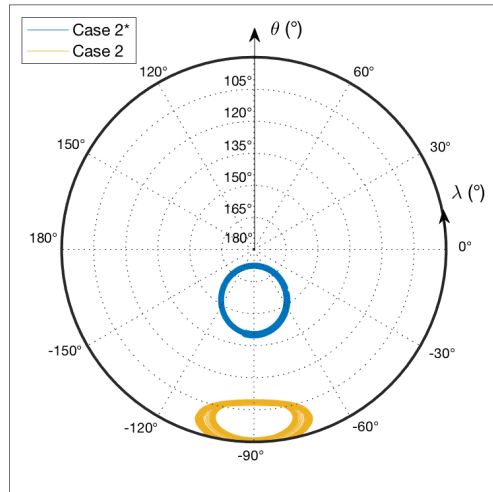


FIGURE 5.12: Evolution of the Spin Axis Orientation in ECO Frame

5.5 Summary of Findings

From observations of the spin period and spin axis orientation of a large space debris rotating about a principal axis, a procedure to estimate a relationship between its moments of inertia was derived. This methodology was applied to the inoperative spacecraft TOPEX/Poseidon, and it was found that the determined equation, $I_x + I_y = 2.83I_z$, represents a very good fit to the observations. However, the relationship between I_x and I_y is still unknown and can not be currently determined from observations. Nevertheless, comparing simulation results to observations and analyzing the energy of the system confirmed that TOPEX/Poseidon is spinning about its minor principal axis in a stable manner with an increasing angular velocity. Using D-SPOSE, the evolution of angular velocity magnitude and spin axis orientation as seen by SLR were well captured, validating the radiation torque model used; variations in the amplitudes of the oscillations in θ and λ were detected, but did not perfectly match

observations. This might be due to a missing external perturbation, possibly of thermal origins, such as the Yarkovsky-O’Keefe-Radzievskii-Paddack (YORP) effect [63].

The influence of the eddy-current torque, excluded from the study performed by the SLR campaign, was investigated and a linear relationship was found between the magnetic properties of the spacecraft and the moment of inertia of the axis about which the spacecraft is spinning. From observations, this was shown to be approximated by $I_z = 75,000 - 0.25M$. Assuming that the spacecraft is somewhat conductive (*i.e.*, $M > 0$) so that the eddy-current torque is playing a role in the attitude dynamics of TOPEX/Poseidon, then a maximum value for I_z of $75,000 \text{ kg m}^2$ can be assumed. Obtaining a better estimate of the magnetic tensor, for example using the finite elements method as has been done for Envisat, could help determine the exact value of I_z [58]. Finally, the orientation of the solar panel is still uncertain, but an approximate range was found to be between 278° and 282° from the position shown in Fig. 5.4a, very close to what was previously found during the SLR campaign [7]; observational techniques such as inverse synthetic aperture radar (ISAR) imaging could also provide additional information on the solar panel orientation. Obtaining better estimates of these properties will lead to more accurate attitude predictions needed for precise forecasts of the spacecraft orbit, crucial for space traffic management issues. Similarly, obtaining a better estimate of the exact orientation of the spin axis in the body-fixed frame, if the principal axis and the z-axis do not coincide, would help provide more accurate simulation results. Work on this is currently on-going by the SLR community [132].

Finally, analysis of the work-energy balance of the spacecraft showed that although the spacecraft angular velocity is increasing, and indeed, the mechanical energy associated with the rotational motion as well, the total energy of the system increases and decreases repeatedly over substantial periods of time due to the complex interaction between the satellite’s orbit, orientation, and radiation pressure. Internal energy dissipation was shown to eventually lead the spacecraft from a minor-axis spin to a major-axis spin, in a time frame that is dependent on the level of damping, which is unknown. Even the smallest damping considered in our simulations led to a transition after a period of 9 years. If the minor-axis spin endures until 2030, simulations have shown that the spacecraft will be spinning at approximately 50° s^{-1} at that time. If the motion does evolve into a major principal axis spin, its future motion is unpredictable for now, since its moments of inertia I_x and I_y are unknown. Alternatively, if future observations of TOPEX/Poseidon’s spin motion show that such a transition occurs, it might be possible to determine the other moments of inertia from those measurements.

I don't think
you realize the
GRAVITY of the
situation

Éloy Cariou

"Harry, you're an astro NOT!"

3D model using SketchUp Pro 2015 and Adobe Photoshop Elements

Chapter 6

Conclusion

6.1 Summary of Contributions

The primary goal of this thesis was to provide insights into the long-term rotational dynamics of large space debris, such as defunct satellites in Low Earth Orbits. In this light, a novel, comprehensive, publicly available and open-source software consisting of a coupled orbit-attitude propagator, named the Debris SPin/Orbit Simulation Environment (D-SPOSE), was developed¹. This tool bridges a gap in the research on the attitude motion of space debris by providing the community with a flexible way to study the short-term and long-term evolution of the spin motion of defunct satellites and other debris objects. Not only does the underlying model contain the critical perturbing accelerations and torques, including the aerodynamic drag and torque, radiation pressure and torque from the Sun and Earth, third-body interactions from the Sun and Moon, the eddy-current torque, gravitational accelerations, and the gravity-gradient torque, but more complete forms than usually employed were developed for several of them. Specifically, an analytical solution to calculate the additional effect of aerodynamic drag and torque for a spinning object as a function of its tessellated surface geometry was put forward; a high-order gravity-gradient torque from a spherical-harmonic representation of Earth's gravitational potential was derived; and the formulation for the eddy-current torque associated with a slowly rotating body under the influence of Earth's magnetic field represented by its spherical-harmonic expansion was also extracted. An initial validation of the tool was also performed by comparing simulation results to observations of the evolution of the spin period and spin axis orientation of uncontrolled spherical geodetic satellites for which an abundant amount of

¹The software is available on the McGill Aerospace Mechatronics Laboratory GitHub: <https://github.com/McGill-AML/D-SPOSE>

measurements exist.

The second main contribution was the development of a stochastic framework to consider the momentum transfer arising from bombardment of small debris and micrometeoroids in the dynamics of large space debris. The stochastic process known as the compound Poisson process was shown to adequately represent this effect in the attitude and orbit equations of motion of a large space debris, by using the impact fluxes of the European Space Agency's MASTER-2009 model to define the mass, velocity and direction of potential impactors. An analytical method to include the effect of momentum enhancement, consisting of the added momentum from surface particles ejected during impacts, was also put forward using ejecta characteristics established by another ESA model. Although these hypervelocity impacts were found to be negligible compared to other perturbations after applying the framework to the inoperative European satellite Envisat and a high area-to-mass ratio object, it was shown that the developed methodology can be used to compute the probability of a satellite-breakup due to small debris by considering the kinetic energy of the impactors.

Finally, D-SPOSE was applied to two defunct satellites and potential Active Debris Removal targets and key information on their spin motion was obtained by comparing simulation results to observations of their attitude state. First, a case study of the enigmatic Envisat was performed. Although observation campaigns of this spacecraft have been ongoing, discrepancies in the results obtained regarding its spin motion are intriguing. While an agreement on the evolution of its spin rate is present in the literature, contradictions about its spin axis orientation exist and were therefore investigated by analyzing simulation results for various scenarios of its attitude state. It was determined that Envisat is witnessing a complex rotational motion where its spin axis is undergoing a precession due to Earth's oblateness and a nutation about the orbit normal, the exact characteristics of which are unknown due to lack of reliable observations. Nevertheless these motions were shown to become larger and faster in every scenario analyzed. A critical review of observations was performed and recommendations were put forward to the community in order to obtain more accurate information on the satellite's spin motion, information which would be crucial to know in advance of any ADR mission. Propagation results to the proposed mission time frame were presented indicating that, at that time, a chaotic tumbling of the satellite will be highly likely.

For the second case study, the rotational dynamics of the joint NASA/CNES satellite TOPEX/Poseidon was studied. Witnessed to be increasing in angular velocity since

its decommissioning in 2006, the satellite has recently seen a rise in interest due to a recent close approach with its successor spacecraft, Jason-2. An investigation into its rotational dynamics has provided insights into its unknown parameters necessary for accurate predictions of its future attitude state and orbit, namely its moments of inertia and magnetic properties. A method to derive a relationship between the moments of inertia of a spinning satellite from observations of its spin period and spin axis orientation was presented and applied to TOPEX/Poseidon. It was determined that the spacecraft is spinning at an increasing angular velocity in a stable manner about its minor principal axis. Propagation results including internal energy dissipation showed that this motion will most likely eventually evolve into a major-axis spin due to internal damping, although the time frame for this transition is unknown. Furthermore, its future attitude state is currently unpredictable as it will depend on the exact moments of inertia which are still unknown.

6.2 Recommendations for Future Research

The software provided was developed to be highly flexible in its applications. However, multiple improvements to the model could be made. First, thermal effects, particularly the YORP effect, which have been found to explain the evolution of the spin period and spin axis orientation of certain asteroids and geostationary satellites, could be integrated [64]. Second, the residual magnetic torque, arising from the magnetic dipole moment of a spacecraft associated with permanent magnets and current loops in its structure, could also be included. Although this torque is usually negligible for satellites spinning at high angular velocities, it was shown to affect certain types of debris tumbling slowly [62]. Third, implementing a symplectic integrator instead of the numerical method currently used would be more appropriate and representative of the underlying physics of the system as it would provide better conservation of energy over the propagation time span. Taking these improvements into consideration would provide an even larger pool of application possibilities for D-SPOSE.

In order to obtain more precise predictions of the evolution of Envisat's spin motion, two recommendations were put forward. First, converting apparent spin periods obtained by Satellite Laser Ranging and light curves into apparent spin period points requires an accurate attitude dynamics model. Including the spin motion as determined in this thesis and its time evolution in the conversion process would provide

more accurate results. Second, a larger observational data set would provide the possibility to characterize the exact motion of the satellite's attitude. Obtaining estimates over a few days would help determine the nutation amplitude and period, while repeating these measurements after a few months would provide indications on the evolution of such a motion.

Similarly, more accurate information regarding TOPEX/Poseidon's rotational dynamics could be obtained by using a more accurate position of the spin axis in the body-fixed frame, work on which is currently being performed by the space debris community using photometric measurements [132]. In addition, obtaining an estimate of the satellite's magnetic tensor, possibly by using the same method applied to Envisat, would help narrow down the uncertainty on the moments of inertia of the spacecraft. These estimates would help provide a more accurate orientation of the solar panel, which, in turn, would lead to better predictions of its orbital and attitude motion.

In this thesis, D-SPOSE was applied to two inoperative satellites. However, similar studies could also be performed for defunct spacecraft and potential ADR targets such as upper stages and other retired satellites. Moreover, as was mentioned, the breadth of the developed tool's applications can enable studies on a large variety of topics. Although developed with space debris remediation purposes in mind and focused on the rotational dynamics of objects, the coupled orbit-attitude propagator can not only be used to obtain accurate predictions of a spinning satellite's attitude motion, but also to provide orbital propagations which take into account the varying area-to-mass ratio of the object of interest. This can be useful in multiple cases: to obtain better estimates for conjunction analyses; to determine precise atmospheric density values from observed satellite trajectories; or to determine optimal attitude states for missions which want the quickest re-entry after decommissioning. The characteristics of the tool could also be useful for mission planning purposes when needing to determine spacecraft properties required to fulfill mission requirements in terms of attitude stability. Furthermore, the large variety of input parameters and environmental models included and the software's ease of use are ideal for sensitivity and comparative studies. Finally, the software could also be used to provide accurate short-term attitude motion predictions for active missions. In all, the research area that is the long-term rotational dynamics of large space debris and uncontrolled satellites has much capacity for growth. D-SPOSE and the contributions laid out in this thesis will hopefully provide some groundwork for future investigations and analyses in this relatively new field.

Appendix A

Evaluating Gravitational Perturbations

The following Appendix will discuss the algorithms and analytical expressions used in D-SPOSE to obtain the acceleration and torque obtained from the spherical harmonic expansion of the Earth's gravitational potential, U [1, Ch. 8, p. 545]:

$$U(r, \theta, \lambda) = \frac{\mu}{r} \left[1 + \sum_{l=2}^k \sum_{m=0}^l \left(\frac{R_E}{r} \right)^l P_{l,m} [\sin \theta] \{ C_{l,m} \cos(m\lambda) + S_{l,m} \sin(m\lambda) \} \right] \quad (\text{A.1})$$

First, the Legendre functions in Eq. (A.1), $P_{l,m}$, can be obtained by recursion [1, Ch. 8, p. 543]. The starting values are:

$$\begin{aligned} P_{0,0} &= 1 \\ P_{1,0} &= \sin \theta \\ P_{1,1} &= \cos \theta \end{aligned} \quad (\text{A.2})$$

Then, for $l \geq 2$:

$$P_{l,0} = \frac{(2l-1) \sin(\theta) P_{l-1,0} - (l-1) P_{l-2,0}}{l} \quad (\text{A.3})$$

For $m \neq 0, m < l$:

$$P_{l,m} = P_{l-2,m} + (2l-1) \cos(\theta) P_{l-1,m-1} \quad (\text{A.4})$$

For $l \neq 0$:

$$P_{l,l} = (2l-1) \cos(\theta) P_{l-1,l-1} \quad (\text{A.5})$$

The first derivatives of the geopotential are required in Eqs. (2.9) and (2.12) and are as follows [1, Ch. 8, p. 550]:

$$\frac{\partial U}{\partial r} = -\frac{\mu}{r^2} \left[1 + \sum_{l=2}^k \sum_{m=0}^l \left(\frac{R_E}{r} \right)^l (l+1) P_{l,m} \{ C_{l,m} \cos(m\lambda) + S_{l,m} \sin(m\lambda) \} \right] \quad (\text{A.6})$$

$$\frac{\partial U}{\partial \theta} = \frac{\mu}{r} \sum_{l=2}^k \sum_{m=0}^l \left(\frac{R_E}{r} \right)^l \{ P_{l,m+1} - m \tan(\theta) P_{l,m} \} \times \{ C_{l,m} \cos(m\lambda) + S_{l,m} \sin(m\lambda) \} \quad (\text{A.7})$$

$$\frac{\partial U}{\partial \lambda} = \frac{\mu}{r} \sum_{l=2}^k \sum_{m=0}^l \left(\frac{R_E}{r} \right)^l m P_{l,m} \{ S_{l,m} \cos(m\lambda) - C_{l,m} \sin(m\lambda) \} \quad (\text{A.8})$$

The second derivatives of the geopotential are required in Eq. (2.12) and can be derived in a similar way:

$$\frac{\partial^2 U}{\partial r^2} = \frac{\mu}{r^3} \left[2 + \sum_{l=2}^k \sum_{m=0}^l \left(\frac{R_E}{r} \right)^l (l+1)(l+2) P_{l,m} \{ C_{l,m} \cos(m\lambda) + S_{l,m} \sin(m\lambda) \} \right] \quad (\text{A.9})$$

$$\begin{aligned} \frac{\partial^2 U}{\partial \theta^2} = & \frac{\mu}{r} \sum_{l=2}^k \sum_{m=0}^l \left(\frac{R_E}{r} \right)^l \{ P_{l,m+2} - (2m+1) \tan(\theta) P_{l,m+1} + m(m \tan(\theta) - \sec^2 \theta) P_{l,m} \} \times \\ & \{ C_{l,m} \cos(m\lambda) + S_{l,m} \sin(m\lambda) \} \end{aligned} \quad (\text{A.10})$$

$$\frac{\partial^2 U}{\partial \lambda^2} = \frac{\mu}{r} \sum_{l=2}^k \sum_{m=0}^l \left(\frac{R_E}{r} \right)^l m^2 P_{l,m} \{ -S_{l,m} \sin(m\lambda) - C_{l,m} \cos(m\lambda) \} \quad (\text{A.11})$$

$$\begin{aligned} \frac{\partial^2 U}{\partial \theta \partial r} = & -\frac{\mu}{r^2} \sum_{l=2}^k \sum_{m=0}^l \left(\frac{R_E}{r} \right)^l (l+1) \{ P_{l,m+1} - m \tan(\theta) P_{l,m} \} \times \{ C_{l,m} \cos(m\lambda) + \\ & S_{l,m} \sin(m\lambda) \} \end{aligned} \quad (\text{A.12})$$

$$\frac{\partial^2 U}{\partial \lambda \partial r} = -\frac{\mu}{r^2} \sum_{l=2}^k \sum_{m=0}^l \left(\frac{R_E}{r} \right)^l m(l+1) P_{l,m} \{ S_{l,m} \cos(m\lambda) - C_{l,m} \sin(m\lambda) \} \quad (\text{A.13})$$

$$\begin{aligned} \frac{\partial^2 U}{\partial \theta \partial \lambda} = & \frac{\mu}{r} \sum_{l=2}^k \sum_{m=0}^l \left(\frac{R_E}{r} \right)^l m \{ P_{l,m+1} - m \tan(\theta) P_{l,m} \} \times \{ S_{l,m} \cos(m\lambda) - C_{l,m} \sin(m\lambda) \} \end{aligned} \quad (\text{A.14})$$

Finally, the coordinate transformations used in the derivation of the gravitational

acceleration and gravity-gradient torque presented in Section 2.2 as a function of the position vector in the inertial reference frame $\mathbf{r} = [r_I \ r_J \ r_K]^T$ are, for Eq. (2.9), given as [1, Ch. 8, p. 550]:

$$\frac{\partial \mathbf{r}}{\partial \mathbf{r}} = \frac{\mathbf{r}^T}{r} \quad (\text{A.15})$$

$$\frac{\partial \theta}{\partial \mathbf{r}} = \frac{1}{\sqrt{r_I^2 + r_J^2}} \left(\frac{-\mathbf{r}^T \mathbf{r}_K}{r^2} + \frac{\partial r_K}{\partial \mathbf{r}} \right) \quad (\text{A.16})$$

$$\frac{\partial \lambda}{\partial \mathbf{r}} = \frac{1}{r_I^2 + r_J^2} \left(r_I \frac{\partial r_J}{\partial \mathbf{r}} - r_J \frac{\partial r_I}{\partial \mathbf{r}} \right) \quad (\text{A.17})$$

and for Eq. (2.12) can be derived as follow:

$$\frac{\partial^2 \mathbf{r}}{\partial \mathbf{r}^2} = -\frac{1}{r^3} \begin{bmatrix} r_I^2 - r^2 & r_I r_J & r_I r_K \\ r_I r_J & r_J^2 - r^2 & r_J r_K \\ r_I r_K & r_J r_K & r_K^2 - r^2 \end{bmatrix} \quad (\text{A.18})$$

$$\frac{\partial^2 \theta}{\partial \mathbf{r}^2} = \frac{1}{r^4 (r_I^2 + r_J^2)^{\frac{3}{2}}} \mathbf{R} \quad (\text{A.19})$$

with:

$$\mathbf{R} = \begin{bmatrix} r_K (2r_I^4 + r_I^2 r_J^2 - r_J^4 - r_I^2 r_K^2) & r_I r_J r_K (3r_I^2 + 3r_J^2 + r_K^2) & -r_I (r_I^2 + r_J^2) (r_I^2 + r_J^2 - r_K^2) \\ r_I r_J r_K (3r_I^2 + 3r_J^2 + r_K^2) & r_K (-r_I^4 + r_I^2 r_J^2 - r_I^2 r_K^2 + 2r_J^4) & -r_J (r_I^2 + r_J^2) (r_I^2 + r_J^2 - r_K^2) \\ -r_I (r_I^2 + r_J^2) (r_I^2 + r_J^2 - r_K^2) & -r_J (r_I^2 + r_J^2) (r_I^2 + r_J^2 - r_K^2) & -2r_K (r_I^2 + r_J^2)^2 \end{bmatrix} \quad (\text{A.20})$$

$$\frac{\partial^2 \lambda}{\partial \mathbf{r}^2} = \frac{1}{(r_I^2 + r_J^2)^2} \begin{bmatrix} 2r_I r_J & r_J^2 - r_I^2 & 0 \\ r_J^2 - r_I^2 & -2r_I r_J & 0 \\ 0 & 0 & 0 \end{bmatrix} \quad (\text{A.21})$$

$$\frac{\partial \mathbf{r}}{\partial \mathbf{r}} \left(\frac{\partial \mathbf{r}}{\partial \mathbf{r}} \right)^T = \frac{1}{r^2} \begin{bmatrix} r_I^2 & r_I r_J & r_I r_K \\ r_I r_J & r_J^2 & r_J r_K \\ r_I r_K & r_J r_K & r_K^2 \end{bmatrix} \quad (\text{A.22})$$

$$\frac{\partial \theta}{\partial \mathbf{r}} \left(\frac{\partial \theta}{\partial \mathbf{r}} \right)^T = \frac{1}{r^4(r_I^2 + r_J^2)} \begin{bmatrix} r_I^2 r_K^2 & r_I r_J r_K^2 & -r_I r_K (r_I^2 + r_J^2) \\ r_I r_J r_K^2 & r_J^2 r_K^2 & -r_J r_K (r_I^2 + r_J^2) \\ -r_I r_K (r_I^2 + r_J^2) & -r_J r_K (r_I^2 + r_J^2) & (r_I^2 + r_J^2)^2 \end{bmatrix} \quad (\text{A.23})$$

$$\frac{\partial \lambda}{\partial \mathbf{r}} \left(\frac{\partial \lambda}{\partial \mathbf{r}} \right)^T = \frac{1}{(r_I^2 + r_J^2)^2} \begin{bmatrix} r_J^2 & -r_I r_J & 0 \\ -r_I r_J & r_I^2 & 0 \\ 0 & 0 & 0 \end{bmatrix} \quad (\text{A.24})$$

$$\frac{\partial r \partial \theta^T}{\partial \mathbf{r} \partial \mathbf{r}} + \frac{\partial \theta \partial r^T}{\partial \mathbf{r} \partial \mathbf{r}} = \frac{1}{r^3 \sqrt{r_I^2 + r_J^2}} \begin{bmatrix} -2r_I^2 r_K & -2r_I r_J r_K & r_I (r_I^2 + r_J^2) - r_I r_K^2 \\ -2r_I r_J r_K & -2r_J^2 r_K & r_J (r_I^2 + r_J^2) - r_J r_K^2 \\ r_I (r_I^2 + r_J^2) - r_I r_K^2 & r_J (r_I^2 + r_J^2) - r_J r_K^2 & 2r_K (r_I^2 + r_J^2) \end{bmatrix} \quad (\text{A.25})$$

$$\frac{\partial r \partial \lambda^T}{\partial \mathbf{r} \partial \mathbf{r}} + \frac{\partial \lambda \partial r^T}{\partial \mathbf{r} \partial \mathbf{r}} = \frac{1}{r(r_I^2 + r_J^2)} \begin{bmatrix} -2r_I r_J & r_I^2 - r_J^2 & -r_J r_K \\ r_I^2 - r_J^2 & 2r_I r_J & r_I r_K \\ -r_J r_K & r_I r_K & 0 \end{bmatrix} \quad (\text{A.26})$$

$$\frac{\partial \lambda \partial \theta^T}{\partial \mathbf{r} \partial \mathbf{r}} + \frac{\partial \theta \partial \lambda^T}{\partial \mathbf{r} \partial \mathbf{r}} = \frac{1}{r^2 (r_I^2 + r_J^2)^{\frac{3}{2}}} \begin{bmatrix} 2r_I r_J r_K & r_K (r_J^2 - r_I^2) & -r_J (r_I^2 + r_J^2) \\ r_K (r_J^2 - r_I^2) & -2r_I r_J r_K & r_I (r_I^2 + r_J^2) \\ -r_J (r_I^2 + r_J^2) & r_I (r_I^2 + r_J^2) & 0 \end{bmatrix} \quad (\text{A.27})$$

Appendix B

Aerodynamic Torque Surface Integrals

The following will solve analytically the two surface integrals in Eq. (2.19), which are a function of the position of the three vertices of each triangular surface defining the spacecraft geometry model.

B.1 Theory

Consider a triangular surface A defined by the position of its three vertices, $\mathbf{r}_1 = [x_1 \ y_1 \ z_1]^T$, $\mathbf{r}_2 = [x_2 \ y_2 \ z_2]^T$, and $\mathbf{r}_3 = [x_3 \ y_3 \ z_3]^T$. Its unit normal vector is given, defined by $\mathbf{n} = [n_x \ n_y \ n_z]^T$. Evaluating a function $f(x, y, z)$ over A can be simplified to:

$$\iint_A f(x, y, z) dA = \iint_D f(x, y, z(x, y)) \sqrt{\left(\frac{\partial z}{\partial x}\right)^2 + \left(\frac{\partial z}{\partial y}\right)^2 + 1} dy dx \quad (\text{B.1})$$

where D is the projection of A on the x - y plane and $z(x, y)$ can be defined by one point (x_1, y_1, z_1) on its surface and by its normal:

$$z = \frac{n_x}{n_z}(x_1 - x) + \frac{n_y}{n_z}(y_1 - y) + z_1 \quad (\text{B.2})$$

The partial derivatives can be determined as follows:

$$\frac{\partial z}{\partial x} = -\frac{n_x}{n_z} \quad (\text{B.3})$$

$$\frac{\partial z}{\partial y} = -\frac{n_y}{n_z} \quad (\text{B.4})$$

Therefore the square root term simplifies to:

$$\begin{aligned} \sqrt{\left(\frac{\partial z}{\partial x}\right)^2 + \left(\frac{\partial z}{\partial y}\right)^2 + 1} &= \sqrt{\left(-\frac{n_x}{n_z}\right)^2 + \left(-\frac{n_y}{n_z}\right)^2 + 1} \\ &= \sqrt{\frac{n_x^2}{n_z^2} + \frac{n_y^2}{n_z^2} + \frac{n_z^2}{n_z^2}} \\ &= \left| \frac{1}{n_z} \right| \end{aligned} \quad (\text{B.5})$$

The surface integral in Eq. (B.1) simplifies to:

$$\iint_A f(x, y, z) dA = \iint_D \left| \frac{1}{n_z} \right| f(x, y, \frac{n_x}{n_z}(x_1 - x) + \frac{n_y}{n_z}(y_1 - y) + z_1) dy dx \quad (\text{B.6})$$

Now we parametrize using v from 0 to $1 - u$ and u from 0 to 1, with:

$$x(u, v) = x_1 + u(x_2 - x_1) + v(x_3 - x_1) \quad (\text{B.7})$$

$$y(u, v) = y_1 + u(y_2 - y_1) + v(y_3 - y_1) \quad (\text{B.8})$$

$$\begin{aligned} z(u, v) &= \frac{n_x}{n_z}(u(x_1 - x_2) + v(x_1 - x_3)) + \frac{n_y}{n_z}(u(y_1 - y_2) + v(y_1 - y_3)) + z_1 \\ &= \frac{u}{n_z}((x_1 - x_2)n_x + (y_1 - y_2)n_y) + \frac{v}{n_z}((x_1 - x_3)n_x + (y_1 - y_3)n_y) + z_1 \end{aligned} \quad (\text{B.9})$$

Eq. (B.6) becomes:

$$\iint_A f(x, y, z) dA = \int_0^1 \int_0^{1-u} \left| \frac{1}{n_z} \right| f(x(u, v), y(u, v), z(u, v)) |\mathbf{J}(u, v)| dv du \quad (\text{B.10})$$

where \mathbf{J} is the Jacobian of the change of variables. The absolute value of its determinant is computed with:

$$|\mathbf{J}(u, v)| = |(x_2 - x_1)(y_3 - y_1) - (x_3 - x_1)(y_2 - y_1)| \quad (\text{B.11})$$

Since both absolute value terms are not dependent on u and v , then:

$$\iint_A f(x, y, z) dA = \left| \frac{\mathbf{J}(u, v)}{n_z} \right| \int_0^1 \int_0^{1-u} f(x(u, v), y(u, v), z(u, v)) dv du \quad (\text{B.12})$$

If $n_z = 0$, then a similar approach can be done to obtain the following solutions for when $n_y \neq 0$ or $n_x \neq 0$, respectively:

$$\iint_S f(x, y, z) dS = \left| \frac{\mathbf{J}(u, v)}{n_y} \right| \int_0^1 \int_0^{1-u} f(x(u, v), y(u, v), z(u, v)) dv du \quad (\text{B.13})$$

with:

$$x(u, v) = x_1 + u(x_2 - x_1) + v(x_3 - x_1) \quad (\text{B.14})$$

$$y(u, v) = \frac{u}{n_y}((x_1 - x_2)n_x + (z_1 - z_2)n_z) + \frac{v}{n_y}((x_1 - x_3)n_x + (z_1 - z_3)n_z) + y_1 \quad (\text{B.15})$$

$$z(u, v) = z_1 + u(z_2 - z_1) + v(z_3 - z_1) \quad (\text{B.16})$$

$$|\mathbf{J}(u, v)| = |(x_2 - x_1)(z_3 - z_1) - (x_3 - x_1)(z_2 - z_1)| \quad (\text{B.17})$$

and:

$$\iint_S f(x, y, z) dS = \left| \frac{\mathbf{J}(u, v)}{n_x} \right| \int_0^1 \int_0^{1-u} f(x(u, v), y(u, v), z(u, v)) dv du \quad (\text{B.18})$$

with:

$$x(u, v) = \frac{u}{n_x}((y_1 - y_2)n_y + (z_1 - z_2)n_z) + \frac{v}{n_x}((y_1 - y_3)n_y + (z_1 - z_3)n_z) + x_1 \quad (\text{B.19})$$

$$y(u, v) = y_1 + u(y_2 - y_1) + v(y_3 - y_1) \quad (\text{B.20})$$

$$z(u, v) = z_1 + u(z_2 - z_1) + v(z_3 - z_1) \quad (\text{B.21})$$

$$|\mathbf{J}(u, v)| = |(y_2 - y_1)(z_3 - z_1) - (y_3 - y_1)(z_2 - z_1)| \quad (\text{B.22})$$

B.2 First Integral

Applying the solution method from Eq. (B.12) to the first integral in Eq. (2.19), with $\boldsymbol{\omega}_{\text{rel}} = [\omega_1 \ \omega_2 \ \omega_3]^T$, $\mathbf{v}_{\text{rel}} = [V_1 \ V_2 \ V_3]^T$, and $\mathbf{r}_p = [x \ y \ z]^T$:

$$\begin{aligned} f(x, y, z) &= (\mathbf{n}^T(\mathbf{r}_p^\times \boldsymbol{\omega}_{\text{rel}})) (\mathbf{r}_p^\times \mathbf{v}_{\text{rel}}) \\ &= (n_x(y\omega_3 - z\omega_2) + n_y(z\omega_1 - x\omega_3) + n_z(x\omega_2 - y\omega_1)) \begin{bmatrix} yV_3 - zV_2 \\ zV_1 - xV_3 \\ xV_2 - yV_1 \end{bmatrix} \end{aligned} \quad (\text{B.23})$$

Substituting in $x(u, v)$, $y(u, v)$, and $z(u, v)$ for $n_z \neq 0$ from Eqs. (B.7)-(B.9):

$$f(u, v) = \beta \begin{bmatrix} b_1 \\ b_2 \\ b_3 \end{bmatrix} \quad (\text{B.24})$$

where:

$$\begin{aligned} \beta = & n_x \left[(y_1 + u(y_2 - y_1) + v(y_3 - y_1))\omega_3 - \left(\frac{u}{n_z}((x_1 - x_2)n_x + (y_1 - y_2)n_y) + \right. \right. \\ & \left. \left. \frac{v}{n_z}((x_1 - x_3)n_x + (y_1 - y_3)n_y) + z_1 \right) \omega_2 \right] + n_y \left[\left(\frac{u}{n_z}((x_1 - x_2)n_x + (y_1 - y_2)n_y) + \right. \right. \\ & \left. \left. \frac{v}{n_z}((x_1 - x_3)n_x + (y_1 - y_3)n_y) + z_1 \right) \omega_1 - (x_1 + u(x_2 - x_1) + v(x_3 - x_1))\omega_3 \right] + \\ & n_z [(x_1 + u(x_2 - x_1) + v(x_3 - x_1))\omega_2 - (y_1 + u(y_2 - y_1) + v(y_3 - y_1))\omega_1] \end{aligned} \quad (\text{B.25})$$

$$\begin{aligned} b_1 = & (y_1 + u(y_2 - y_1) + v(y_3 - y_1))V_3 - \left(\frac{u}{n_z}((x_1 - x_2)n_x + (y_1 - y_2)n_y) + \right. \\ & \left. \frac{v}{n_z}((x_1 - x_3)n_x + (y_1 - y_3)n_y) + z_1 \right)V_2 \end{aligned} \quad (\text{B.26})$$

$$\begin{aligned} b_2 = & \left(\frac{u}{n_z}((x_1 - x_2)n_x + (y_1 - y_2)n_y) + \frac{v}{n_z}((x_1 - x_3)n_x + (y_1 - y_3)n_y) + z_1 \right)V_1 - \\ & (x_1 + u(x_2 - x_1) + v(x_3 - x_1))V_3 \end{aligned} \quad (\text{B.27})$$

$$b_3 = (x_1 + u(x_2 - x_1) + v(x_3 - x_1))V_2 - (y_1 + u(y_2 - y_1) + v(y_3 - y_1))V_1 \quad (\text{B.28})$$

The functions for the other two cases are, for $n_y \neq 0$ or $n_x \neq 0$, respectively:

$$\begin{aligned} \beta = & n_x \left(\left(\frac{u}{n_y}((x_1 - x_2)n_x + (z_1 - z_2)n_z) + \frac{v}{n_y}((x_1 - x_3)n_x + (z_1 - z_3)n_z) + y_1 \right) \omega_3 - \right. \\ & (z_1 + u(z_2 - z_1) + v(z_3 - z_1))\omega_2) + n_y ((z_1 + u(z_2 - z_1) + v(z_3 - z_1))\omega_1 - \\ & (x_1 + u(x_2 - x_1) + v(x_3 - x_1))\omega_3) + n_z ((x_1 + u(x_2 - x_1) + v(x_3 - x_1))\omega_2 - \\ & \left. \left(\frac{u}{n_y}((x_1 - x_2)n_x + (z_1 - z_2)n_z) + \frac{v}{n_y}((x_1 - x_3)n_x + (z_1 - z_3)n_z) + y_1 \right)\omega_1 \right) \end{aligned} \quad (\text{B.29})$$

$$\begin{aligned} b_1 = & \left(\frac{u}{n_y} ((x_1 - x_2)n_x + (z_1 - z_2)n_z) + \frac{v}{n_y} ((x_1 - x_3)n_x + (z_1 - z_3)n_z) + y_1 \right) V_3 - \\ & (z_1 + u(z_2 - z_1) + v(z_3 - z_1)) V_2 \end{aligned} \quad (\text{B.30})$$

$$b_2 = (z_1 + u(z_2 - z_1) + v(z_3 - z_1)) V_1 - (x_1 + u(x_2 - x_1) + v(x_3 - x_1)) V_3 \quad (\text{B.31})$$

$$\begin{aligned} b_3 = & (x_1 + u(x_2 - x_1) + v(x_3 - x_1)) V_2 - \left(\frac{u}{n_y} ((x_1 - x_2)n_x + (z_1 - z_2)n_z) + \right. \\ & \left. \frac{v}{n_y} ((x_1 - x_3)n_x + (z_1 - z_3)n_z) + y_1 \right) V_1 \end{aligned} \quad (\text{B.32})$$

and:

$$\begin{aligned} \beta = & n_x((y_1 + u(y_2 - y_1) + v(y_3 - y_1))\omega_3 - (z_1 + u(z_2 - z_1) + v(z_3 - z_1))\omega_2) + \\ & n_y((z_1 + u(z_2 - z_1) + v(z_3 - z_1))\omega_1 - \left(\frac{u}{n_x} ((y_1 - y_2)n_y + (z_1 - z_2)n_z) + \right. \\ & \left. \frac{v}{n_x} ((y_1 - y_3)n_y + (z_1 - z_3)n_z) + x_1 \right) \omega_3) + n_z \left(\frac{u}{n_x} ((y_1 - y_2)n_y + (z_1 - z_2)n_z) + \right. \\ & \left. \frac{v}{n_x} ((y_1 - y_3)n_y + (z_1 - z_3)n_z) + x_1 \right) \omega_2 - (y_1 + u(y_2 - y_1) + v(y_3 - y_1))\omega_1 \end{aligned} \quad (\text{B.33})$$

$$b_1 = (y_1 + u(y_2 - y_1) + v(y_3 - y_1)) V_3 - (z_1 + u(z_2 - z_1) + v(z_3 - z_1)) V_2 \quad (\text{B.34})$$

$$\begin{aligned} b_2 = & (z_1 + u(z_2 - z_1) + v(z_3 - z_1)) V_1 - \left(\frac{u}{n_x} ((y_1 - y_2)n_y + (z_1 - z_2)n_z) + \right. \\ & \left. \frac{v}{n_x} ((y_1 - y_3)n_y + (z_1 - z_3)n_z) + x_1 \right) V_3 \end{aligned} \quad (\text{B.35})$$

$$\begin{aligned} b_3 = & \left(\frac{u}{n_x} ((y_1 - y_2)n_y + (z_1 - z_2)n_z) + \frac{v}{n_x} ((y_1 - y_3)n_y + (z_1 - z_3)n_z) + x_1 \right) V_2 - \\ & (y_1 + u(y_2 - y_1) + v(y_3 - y_1)) V_1 \end{aligned} \quad (\text{B.36})$$

B.3 Second Integral

We now apply the solution method to the second integral in Eq. (2.19):

$$\begin{aligned} f(x, y, z) = & v_{\text{rel}} \cos \alpha \mathbf{r}_p^\times \mathbf{r}_p^\times \boldsymbol{\omega}_{\text{rel}} \\ = & v_{\text{rel}} \cos \alpha \begin{bmatrix} -(z^2 + y^2)\omega_1 + xy\omega_2 + xz\omega_3 \\ xy\omega_1 - (z^2 + x^2)\omega_2 + zy\omega_3 \\ xz\omega_1 + zy\omega_2 - (x^2 + y^2)\omega_3 \end{bmatrix} \end{aligned} \quad (\text{B.37})$$

Substituting in $x(u, v)$, $y(u, v)$, and $z(u, v)$ for $n_z \neq 0$, the three terms of the vector \mathbf{v} , where:

$$\mathbf{v} = \begin{bmatrix} v_1 \\ v_2 \\ v_3 \end{bmatrix} = \begin{bmatrix} -(z^2 + y^2)\omega_1 + xy\omega_2 + xz\omega_3 \\ xy\omega_1 - (z^2 + x^2)\omega_2 + zy\omega_3 \\ xz\omega_1 + zy\omega_2 - (x^2 + y^2)\omega_3 \end{bmatrix} \quad (\text{B.38})$$

become:

$$\begin{aligned} v_1 = & -\left(\left(\frac{u}{n_z}((x_1 - x_2)n_x + (y_1 - y_2)n_y) + \frac{v}{n_z}((x_1 - x_3)n_x + (y_1 - y_3)n_y) + z_1\right)^2 + \right. \\ & (y_1 + u(y_2 - y_1) + v(y_3 - y_1))^2\omega_1 + (x_1 + u(x_2 - x_1) + v(x_3 - x_1))(y_1 + \\ & u(y_2 - y_1) + v(y_3 - y_1))\omega_2 + (x_1 + u(x_2 - x_1) + v(x_3 - x_1))\left(\frac{u}{n_z}((x_1 - x_2)n_x + \right. \\ & \left. (y_1 - y_2)n_y) + \frac{v}{n_z}((x_1 - x_3)n_x + (y_1 - y_3)n_y) + z_1\right)\omega_3 \end{aligned} \quad (\text{B.39})$$

$$\begin{aligned} v_2 = & (x_1 + u(x_2 - x_1) + v(x_3 - x_1))(y_1 + u(y_2 - y_1) + v(y_3 - y_1))\omega_1 - \\ & \left(\left(\frac{u}{n_z}((x_1 - x_2)n_x + (y_1 - y_2)n_y) + \frac{v}{n_z}((x_1 - x_3)n_x + (y_1 - y_3)n_y) + z_1\right)^2 + \right. \\ & (x_1 + u(x_2 - x_1) + v(x_3 - x_1))^2\omega_2 + \left(\frac{u}{n_z}((x_1 - x_2)n_x + (y_1 - y_2)n_y) + \right. \\ & \left. \frac{v}{n_z}((x_1 - x_3)n_x + (y_1 - y_3)n_y) + z_1\right)(y_1 + u(y_2 - y_1) + v(y_3 - y_1))\omega_3 \end{aligned} \quad (\text{B.40})$$

$$\begin{aligned} v_3 = & (x_1 + u(x_2 - x_1) + v(x_3 - x_1))\left(\frac{u}{n_z}((x_1 - x_2)n_x + (y_1 - y_2)n_y) + \right. \\ & \left.\frac{v}{n_z}((x_1 - x_3)n_x + (y_1 - y_3)n_y) + z_1\right)\omega_1 + \left(\frac{u}{n_z}((x_1 - x_2)n_x + (y_1 - y_2)n_y) + \right. \\ & \left.\frac{v}{n_z}((x_1 - x_3)n_x + (y_1 - y_3)n_y) + z_1\right)(y_1 + u(y_2 - y_1) + v(y_3 - y_1))\omega_2 - \\ & ((x_1 + u(x_2 - x_1) + v(x_3 - x_1))^2 + (y_1 + u(y_2 - y_1) + v(y_3 - y_1))^2)\omega_3 \end{aligned} \quad (\text{B.41})$$

The double integral over u and v is now trivial and can be solved analytically. However these equations are only valid for $n_z \neq 0$. If $n_z = 0$, then a similar approach can be

done to obtain the following solutions for when $n_y \neq 0$ or $n_x \neq 0$, respectively:

$$\begin{aligned} v_1 = & -((z_1 + u(z_2 - z_1) + v(z_3 - z_1))^2 + (\frac{u}{n_y}((x_1 - x_2)n_x + (z_1 - z_2)n_z) + \\ & \frac{v}{n_y}((x_1 - x_3)n_x + (z_1 - z_3)n_z) + y_1)^2)\omega_1 + (x_1 + u(x_2 - x_1) + \\ & v(x_3 - x_1))(\frac{u}{n_y}((x_1 - x_2)n_x + (z_1 - z_2)n_z) + \frac{v}{n_y}((x_1 - x_3)n_x + (z_1 - z_3)n_z) + \\ & y_1)\omega_2 + (x_1 + u(x_2 - x_1) + v(x_3 - x_1))(z_1 + u(z_2 - z_1) + v(z_3 - z_1))\omega_3 \end{aligned} \quad (B.42)$$

$$\begin{aligned} v_2 = & (x_1 + u(x_2 - x_1) + v(x_3 - x_1))(\frac{u}{n_y}((x_1 - x_2)n_x + (z_1 - z_2)n_z) + \\ & \frac{v}{n_y}((x_1 - x_3)n_x + (z_1 - z_3)n_z) + y_1)\omega_1 - ((z_1 + u(z_2 - z_1) + v(z_3 - z_1))^2 + \\ & (x_1 + u(x_2 - x_1) + v(x_3 - x_1))^2)\omega_2 + (z_1 + u(z_2 - z_1) + v(z_3 - z_1)) \\ & (\frac{u}{n_y}((x_1 - x_2)n_x + (z_1 - z_2)n_z) + \frac{v}{n_y}((x_1 - x_3)n_x + (z_1 - z_3)n_z) + y_1)\omega_3 \end{aligned} \quad (B.43)$$

$$\begin{aligned} v_3 = & (x_1 + u(x_2 - x_1) + v(x_3 - x_1))(z_1 + u(z_2 - z_1) + v(z_3 - z_1))\omega_1 + \\ & (z_1 + u(z_2 - z_1) + v(z_3 - z_1))(\frac{u}{n_y}((x_1 - x_2)n_x + (z_1 - z_2)n_z) + \\ & \frac{v}{n_y}((x_1 - x_3)n_x + (z_1 - z_3)n_z) + y_1)\omega_2 - ((x_1 + u(x_2 - x_1) + v(x_3 - x_1))^2 + \\ & (\frac{u}{n_y}((x_1 - x_2)n_x + (z_1 - z_2)n_z) + \frac{v}{n_y}((x_1 - x_3)n_x + (z_1 - z_3)n_z) + y_1)^2)\omega_3 \end{aligned} \quad (B.44)$$

and:

$$\begin{aligned} v_1 = & -((z_1 + u(z_2 - z_1) + v(z_3 - z_1))^2 + (y_1 + u(y_2 - y_1) + v(y_3 - y_1))^2)\omega_1 + \\ & (\frac{u}{n_x}((y_1 - y_2)n_y + (z_1 - z_2)n_z) + \frac{v}{n_x}((y_1 - y_3)n_y + (z_1 - z_3)n_z) + x_1)(y_1 + \\ & u(y_2 - y_1) + v(y_3 - y_1))\omega_2 + (\frac{u}{n_x}((y_1 - y_2)n_y + (z_1 - z_2)n_z) + \frac{v}{n_x}((y_1 - \\ & y_3)n_y + (z_1 - z_3)n_z) + x_1)(z_1 + u(z_2 - z_1) + v(z_3 - z_1))\omega_3 \end{aligned} \quad (B.45)$$

$$\begin{aligned}
v_2 = & \left(\frac{u}{n_x} ((y_1 - y_2)n_y + (z_1 - z_2)n_z) + \frac{v}{n_x} ((y_1 - y_3)n_y + (z_1 - z_3)n_z) + x_1 \right) (y_1 + \\
& u(y_2 - y_1) + v(y_3 - y_1)) \omega_1 - ((z_1 + u(z_2 - z_1) + v(z_3 - z_1))^2 + \\
& \left(\frac{u}{n_x} ((y_1 - y_2)n_y + (z_1 - z_2)n_z) + \frac{v}{n_x} ((y_1 - y_3)n_y + (z_1 - z_3)n_z) + x_1 \right)^2) \omega_2 + \\
& (z_1 + u(z_2 - z_1) + v(z_3 - z_1))(y_1 + u(y_2 - y_1) + v(y_3 - y_1)) \omega_3
\end{aligned} \tag{B.46}$$

$$\begin{aligned}
v_3 = & \left(\frac{u}{n_x} ((y_1 - y_2)n_y + (z_1 - z_2)n_z) + \frac{v}{n_x} ((y_1 - y_3)n_y + (z_1 - z_3)n_z) + x_1 \right) (z_1 + \\
& u(z_2 - z_1) + v(z_3 - z_1)) \omega_1 + (z_1 + u(z_2 - z_1) + v(z_3 - z_1))(y_1 + u(y_2 - y_1) + \\
& v(y_3 - y_1)) \omega_2 - \left(\left(\frac{u}{n_x} ((y_1 - y_2)n_y + (z_1 - z_2)n_z) + \frac{v}{n_x} ((y_1 - y_3)n_y + \right. \right. \\
& \left. \left. (z_1 - z_3)n_z) + x_1 \right)^2 + (y_1 + u(y_2 - y_1) + v(y_3 - y_1))^2 \right) \omega_3
\end{aligned} \tag{B.47}$$

Appendix C

Magnetic Field Computation

The following will go through the analytical expressions of the terms in the equation for the eddy-current torque in Section 2.3.2 as a function of the spherical harmonic expansion of the Earth's magnetic potential. In the local spherical coordinate reference frame, S, defined by $\hat{\mathbf{r}}$ in the radial direction, $\hat{\phi}$ in the south direction, and $\hat{\lambda}$ in the east direction, the following can be written as:

$$\mathbf{B} = \begin{bmatrix} B_r \\ B_\phi \\ B_\lambda \end{bmatrix} = - \begin{bmatrix} \frac{\partial V}{\partial r} \\ \frac{1}{r} \frac{\partial V}{\partial \phi} \\ \frac{1}{r \sin \phi} \frac{\partial V}{\partial \lambda} \end{bmatrix} \quad (\text{C.1})$$

$$\left(\frac{\partial \mathbf{B}}{\partial t} \right)_S = \begin{bmatrix} \frac{\partial B_r}{\partial t} \\ \frac{\partial B_\phi}{\partial t} \\ \frac{\partial B_\lambda}{\partial t} \end{bmatrix} = - \begin{bmatrix} \frac{\partial^2 V}{\partial r \partial t} \\ \frac{1}{r} \frac{\partial^2 V}{\partial \theta \partial t} \\ \frac{1}{r \sin \phi} \frac{\partial^2 V}{\partial \lambda \partial t} \end{bmatrix} \quad (\text{C.2})$$

$$\begin{aligned} (\mathbf{v}_E \cdot \nabla) \mathbf{B} &= v_r \frac{\partial \mathbf{B}}{\partial r} + \frac{v_\phi}{r} \frac{\partial \mathbf{B}}{\partial \phi} + \frac{v_\lambda}{r \sin \phi} \frac{\partial \mathbf{B}}{\partial \lambda} \\ &= - \begin{bmatrix} v_r \frac{\partial^2 V}{\partial r^2} + \frac{v_\phi}{r} \frac{\partial^2 V}{\partial \phi \partial r} + \frac{v_\lambda}{r \sin \phi} \frac{\partial^2 V}{\partial \lambda \partial r} \\ \frac{v_r}{r} \frac{\partial^2 V}{\partial \phi \partial r} - \frac{v_r}{r^2} \frac{\partial V}{\partial \phi} + \frac{v_\phi}{r^2} \frac{\partial^2 V}{\partial \phi^2} + \frac{v_\lambda}{r^2 \sin \phi} \frac{\partial^2 V}{\partial \phi \partial \lambda} \\ \frac{v_r}{r \sin \phi} \frac{\partial^2 V}{\partial \lambda \partial r} - \frac{v_r}{r^2 \sin \phi} \frac{\partial V}{\partial \lambda} - \frac{v_\phi \cos \phi}{r^2 \sin^2 \phi} \frac{\partial V}{\partial \lambda} + \frac{v_\phi}{r^2 \sin^2 \phi} \frac{\partial^2 V}{\partial \lambda \partial \phi} + \frac{v_\lambda}{r^2 \sin^2 \phi} \frac{\partial^2 V}{\partial \lambda^2} \end{bmatrix} \quad (\text{C.3}) \end{aligned}$$

The first partial derivatives of the magnetic potential are as follows [83, App. H, p. 781]:

$$\frac{\partial V}{\partial r} = - \sum_{n=1}^k \left(\frac{a}{r}\right)^{n+2} (n+1) \sum_{m=0}^n (g_n^m \cos(m\lambda) + h_n^m \sin(m\lambda)) P_n^m[\cos \phi] \quad (\text{C.4})$$

$$\frac{\partial V}{\partial \phi} = a \sum_{n=1}^k \left(\frac{a}{r}\right)^{n+1} \sum_{m=0}^n (g_n^m \cos(m\lambda) + h_n^m \sin(m\lambda)) \frac{\partial P_n^m[\cos \phi]}{\partial \phi} \quad (\text{C.5})$$

$$\frac{\partial V}{\partial \lambda} = a \sum_{n=1}^k \left(\frac{a}{r}\right)^{n+1} \sum_{m=0}^n m(-g_n^m \sin(m\lambda) + h_n^m \cos(m\lambda)) P_n^m[\cos \phi] \quad (\text{C.6})$$

Similarly, the second partial derivatives of the magnetic potential can be calculated as follows:

$$\frac{\partial^2 V}{\partial r^2} = \frac{1}{r} \sum_{n=1}^k \left(\frac{a}{r}\right)^{n+2} (n+1)(n+2) \sum_{m=0}^n (g_n^m \cos(m\lambda) + h_n^m \sin(m\lambda)) P_n^m[\cos \phi] \quad (\text{C.7})$$

$$\frac{\partial^2 V}{\partial \phi \partial r} = - \sum_{n=1}^k \left(\frac{a}{r}\right)^{n+2} (n+1) \sum_{m=0}^n (g_n^m \cos(m\lambda) + h_n^m \sin(m\lambda)) \frac{\partial P_n^m[\cos \phi]}{\partial \phi} \quad (\text{C.8})$$

$$\frac{\partial^2 V}{\partial \lambda \partial r} = \sum_{n=1}^k \left(\frac{a}{r}\right)^{n+2} (n+1) \sum_{m=0}^n m(g_n^m \sin(m\lambda) - h_n^m \cos(m\lambda)) P_n^m[\cos \phi] \quad (\text{C.9})$$

$$\frac{\partial^2 V}{\partial t \partial r} = - \sum_{n=1}^k \left(\frac{a}{r}\right)^{n+2} (n+1) \sum_{m=0}^n (\dot{g}_n^m \cos(m\lambda) + \dot{h}_n^m \sin(m\lambda)) P_n^m[\cos \phi] \quad (\text{C.10})$$

$$\frac{\partial^2 V}{\partial \phi^2} = a \sum_{n=1}^k \left(\frac{a}{r}\right)^{n+1} \sum_{m=0}^n (g_n^m \cos(m\lambda) + h_n^m \sin(m\lambda)) \frac{\partial^2 P_n^m[\cos \theta]}{\partial \theta^2} \quad (\text{C.11})$$

$$\frac{\partial^2 V}{\partial \lambda \partial \phi} = a \sum_{n=1}^k \left(\frac{a}{r}\right)^{n+1} \sum_{m=0}^n m(-g_n^m \sin(m\lambda) + h_n^m \cos(m\lambda)) \frac{\partial P_n^m[\cos \theta]}{\partial \theta} \quad (\text{C.12})$$

$$\frac{\partial^2 V}{\partial t \partial \phi} = a \sum_{n=1}^k \left(\frac{a}{r}\right)^{n+1} \sum_{m=0}^n (\dot{g}_n^m \cos(m\lambda) + \dot{h}_n^m \sin(m\lambda)) \frac{\partial P_n^m[\cos \theta]}{\partial \theta} \quad (\text{C.13})$$

$$\frac{\partial^2 V}{\partial \lambda^2} = -a \sum_{n=1}^k \left(\frac{a}{r}\right)^{n+1} \sum_{m=0}^n m^2 (g_n^m \cos(m\lambda) + h_n^m \sin(m\lambda)) P_n^m[\cos \theta] \quad (\text{C.14})$$

$$\frac{\partial^2 V}{\partial t \partial \lambda} = a \sum_{n=1}^k \left(\frac{a}{r}\right)^{n+1} \sum_{m=0}^n m(-\dot{g}_n^m \sin(m\lambda) + \dot{h}_n^m \cos(m\lambda)) P_n^m[\cos \theta] \quad (\text{C.15})$$

The Schmidt normalized associated Legendre functions, P_n^m , are related to the Gauss functions, $P^{n,m}$, by the following [83, App. H, p. 780]:

$$P_n^m = S_{n,m} P^{n,m} \quad (\text{C.16})$$

using the transformations obtained by recursion [83, App. H, p. 781]:

$$S_{0,0} = 1 \quad (\text{C.17})$$

$$S_{n,0} = S_{n-1,0} \frac{2n-1}{n} \quad (\text{C.18})$$

$$S_{n,n} = S_{n,m-1} \sqrt{\frac{(n-m+1)(\delta_m^1 + 1)}{n+m}} \quad (\text{C.19})$$

The Gauss functions and its first derivatives can also be obtained by recursion [83, App. H, p. 781]:

$$P^{0,0} = 1 \quad (\text{C.20})$$

$$P^{1,0} = \cos \theta \quad (\text{C.21})$$

$$P^{n,n} = \sin \theta P^{n-1,n-1} \quad (\text{C.22})$$

$$P^{n,m} = \cos \theta P^{n-1,m} - K^{n,m} P^{n-2,m} \quad (\text{C.23})$$

$$\frac{\partial P^{0,0}}{\partial \theta} = 0 \quad (\text{C.24})$$

$$\frac{\partial P^{1,0}}{\partial \theta} = -\sin \theta \quad (\text{C.25})$$

$$\frac{\partial P^{n,n}}{\partial \theta} = \sin \theta \frac{\partial P^{n-1,n-1}}{\partial \theta} + \cos \theta P^{n-1,n-1} \quad (\text{C.26})$$

$$\frac{\partial P^{n,m}}{\partial \theta} = \cos \theta \frac{\partial P^{n-1,m}}{\partial \theta} - \sin \theta P^{n-1,m} - K^{n,m} \frac{\partial P^{n-2,m}}{\partial \theta} \quad (\text{C.27})$$

with [83, App. H, p. 781]:

$$\begin{aligned} K^{n,m} &= 0 && \text{for } n = 1 \\ K^{n,m} &= \frac{(n-1)^2 - m^2}{(2n-1)(2n-3)} && \text{for } n \geq 2 \end{aligned} \quad (\text{C.28})$$

The second partial derivatives are calculated as follows:

$$\frac{\partial^2 P^{0,0}}{\partial \phi^2} = 0 \quad (C.29)$$

$$\frac{\partial^2 P^{1,0}}{\partial \phi^2} = -\cos \phi \quad (C.30)$$

$$\frac{\partial^2 P^{n,n}}{\partial \phi^2} = 2 \cos \phi \frac{\partial P^{n-1,n-1}}{\partial \phi} - \sin \phi P^{n-1,n-1} + \sin \phi \frac{\partial^2 P^{n-1,n-1}}{\partial \phi^2} \quad (C.31)$$

$$\frac{\partial^2 P^{n,m}}{\partial \phi^2} = \cos \phi \frac{\partial^2 P^{n-1,m}}{\partial \phi^2} - 2 \sin \phi \frac{\partial P^{n-1,m}}{\partial \theta} - \cos \phi P^{n-1,m} - K^{n,m} \frac{\partial^2 P^{n-2,m}}{\partial \phi^2} \quad (C.32)$$

Appendix D

Computing Ejecta Momentum

This Appendix aims to provide an overview of how to compute the added transfer of momentum to spacecraft from ejecta during hypervelocity impacts as explained in Section 3.4. The ejecta model used is first described in Section D.1 [104]. The derivation of an analytical solution for ejecta momentum is then developed in Section D.2.

D.1 Ejecta Model by Rival and Mandeville (1999)

Every time a particle, either a small piece of space debris or a micrometeoroid, hits a spacecraft surface, secondary debris are ejected due to the high momentum associated with these hypervelocity impacts. During crater formation, particles in the neighbourhood of the collision area are broken off the primary impact surface. These particles add to the total debris population around Earth and also provide an additional momentum transfer to target, an effect known as momentum enhancement. Ejecta, or secondary particles, are defined as material ejected during hypervelocity impacts at significant velocity. The particles can be in liquid, solid, or gaseous form and come from both the impactor and the target. Three ejection processes are considered: jetting, cone fragments, and spallation.

The important characteristics defining a collision are the impact velocity, *i.e.*, the relative velocity of the impactor to the target, the impactor mass, the impact incident angle and the behaviour of the target, whether it is brittle or ductile. The ejecta itself is characterized by its mass, size and the direction of the ejected fragments. The surface reference frame fixed to the target surface and centered at the impact point used to describe the ejecta is shown in Fig. D.1.

One of the most important parameters describing the ejection mechanism is the total ejected mass, M_e , which is described as follows, taken from an empirical study

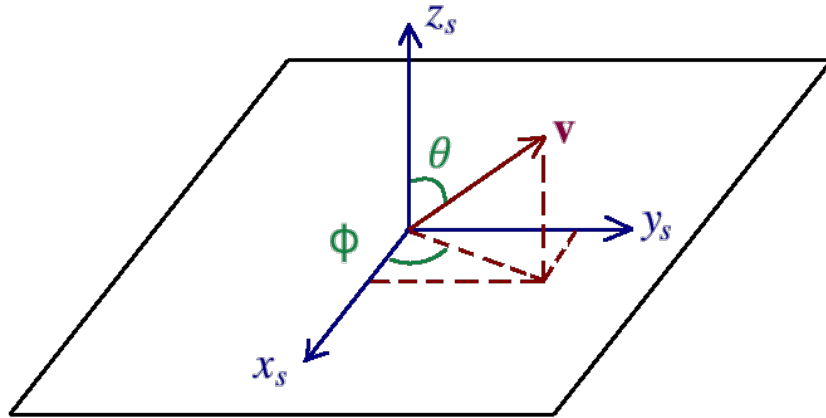


FIGURE D.1: Surface Reference Frame

correlating the total ejected mass to the kinetic energy of the impactor [133]:

$$M_e = 7.41 \times 10^{-6} (\rho_i / \rho_t)^{1/2} K_i^{1.133} (\cos \theta_i)^2 \quad (\text{D.1})$$

where \$\rho_i\$ is the impactor density, \$\rho_t\$ is the target density, \$K_i\$ is the impact kinetic energy based on the impact velocity and \$\theta_i\$ is the incident impact angle. This equation is valid for brittle targets. For ductile targets, a constant factor needs to be included; however, only brittle targets are considered here. The impactor and target densities are taken as 2700 and 2500 kg m\$^{-3}\$, respectively. During grazing impacts (\$\theta_i > 60^\circ\$), the ricochet phenomenon needs to be considered so \$\theta_i\$ is fixed at \$60^\circ\$.

The total ejected mass is split between spall products, cone fragments and jetting. However, since less than 1% of the total ejected mass is due to jetting, it is therefore neglected in the momentum computation. The fraction of the total ejected mass which is from cone fragments is determined by the parameter \$\beta_m\$, which is a function of the impactor size \$d_i\$. For a brittle target, \$\beta_m = 1\$ if \$d_i < 1 \mu\text{m}\$, \$\beta_m = 0.4\$ if \$d_i > 100 \mu\text{m}\$, and \$\beta_m = -0.3 \log_{10} d_i - 0.8\$ in between. In this case [104]:

$$\begin{aligned} M_{\text{cone}} &= \beta_m M_e \\ M_{\text{spalls}} &= (1 - \beta_m) M_e \end{aligned} \quad (\text{D.2})$$

Spallation therefore only occurs during impacts with large impactors and is only considered when \$d_i > 1 \mu\text{m}\$. Spall ejection velocity is usually low and is assumed to be 10 m s\$^{-1}\$.

Cone fragments are defined by three independent distributions defining the size

δ , zenith θ and azimuth φ of the ejecting particles. The ejection velocity, on the other hand, is a function of these three variables. The distribution describing the size of the cone fragments follows a power law [104]:

$$f_{\text{size}}(\delta) = \frac{\alpha + 1}{\delta_{\max}^{\alpha+1} - \delta_{\min}^{\alpha+1}} \delta^{\alpha} \mathbf{1}_{[\delta_{\min}, \delta_{\max}]} \quad (\text{D.3})$$

where $\mathbf{1}_{[\delta_{\min}, \delta_{\max}]}$ is the interval characteristic function, equal to 1 if $d \in [\delta_{\min}, \delta_{\max}]$, 0 otherwise, and $\alpha = -3.5$ for a brittle target. $\delta_{\min} = 0.1 \mu\text{m}$ is the minimal cut-off size for a cone fragment. $\delta_{\max} = \sqrt[3]{6m_{\max}/\pi\rho_t}$ is the maximal size for a cone fragment having spherical shape, where $m_{\max} = \lambda_m M_e$ is the largest cone fragment mass, proportional to the total ejected mass with $\lambda_m = 0.1$ for a brittle target when $\theta_i \leq 60^\circ$ and 0.5 when $\theta_i > 60^\circ$.

The zenith angle at which the cone fragments are ejected is described by a Gaussian distribution around the maximum angle θ_{\max} and defined between 0 and 90° [104]:

$$f_{\text{zen}}(\theta) = \frac{1}{\sigma_{\theta}\sqrt{2\pi}} \exp\left(-\frac{(\theta - \theta_{\max})^2}{2\sigma_{\theta}^2}\right) \mathbf{1}_{[0, \pi/2]} \quad (\text{D.4})$$

where $\sigma_{\theta} = 3^\circ$ is the width of the distribution and θ_{\max} is dependent on the impact incident angle θ_i and the material of the target and the impactor. Empirically, it was observed to have the following dependence [104]:

$$\begin{aligned} \text{for } \theta_i \leq 60^\circ : \theta_{\max} &= \frac{\theta_{\max60} - \theta_{\max0}}{\pi/3} \theta_i + \theta_{\max0} \\ \text{for } \theta_i > 60^\circ : \theta_{\max} &= \theta_{\max60} \end{aligned} \quad (\text{D.5})$$

with $\theta_{\max60} = 80^\circ$ and $\theta_{\max0} = 30^\circ$.

The azimuth distribution requires three conditions. First, rotational symmetry occurs for normal impacts; second, there is a relative increase in the number of fragments in the downstream impact direction compared to the backstream direction for oblique impacts; third, for collisions at high incident angles ($\theta_i > 60^\circ$), a transformation of the distribution from cone to beam shape occurs.

For the case when $\theta_i \leq 60^\circ$, the azimuth distribution follows a sinusoidal function [104]:

$$f_{\text{azi}}(\varphi) = \frac{1}{2\pi} \left(\frac{3\theta_i}{2\pi - 3\theta_i} \cos(\varphi - \varphi_{\max}) + 1 \right) \mathbf{1}_{[0, 2\pi]} \quad (\text{D.6})$$

where $\varphi_{\max} = \varphi_i$ is the azimuthal direction for which the number of cone fragments is maximum. For an oblique impact, the density is maximum for $\varphi = \varphi_i$ and minimum for $\varphi = \varphi_i + \pi$. The ratio between downstream and backstream densities increases from 1 for a normal impact to infinity for $\theta_i = 60^\circ$. For the case when $\theta_i > 60^\circ$, the beam is represented by a Gaussian distribution centred at $\varphi_{\max} = \varphi_i$ [104]:

$$f_{\text{azi}}(\varphi) = \frac{1}{\sigma_\varphi \sqrt{2\pi}} \exp\left(-\frac{(\varphi - \varphi_{\max})^2}{2\sigma_\varphi^2}\right) \mathbf{1}_{[0,2\pi]} \quad (\text{D.7})$$

where $\sigma_\varphi = 5^\circ$ is the width of the distribution

The velocity function is dependent on size and azimuth. It is assumed that there is no dependence on the zenith angle. The function satisfies an inverse relation between fragment size and velocity and considers a relative increase of the ejection velocity in the downstream direction for oblique impacts. Furthermore, as the incident impact angle increases, so will the maximum ejection velocity. The velocity function is formulated as follows [104]:

$$\begin{aligned} v(\delta, \varphi) &= D(\varphi)/\delta + E(\varphi) \\ D(\varphi) &= \frac{v_{\max}(\varphi) - v_{\min}}{\delta_{\max} - \delta_{\min}} \delta_{\max} \delta_{\min} \\ E(\varphi) &= \frac{v_{\min} \delta_{\max} - v_{\max}(\varphi) \delta_{\min}}{\delta_{\max} - \delta_{\min}} \end{aligned} \quad (\text{D.8})$$

where $v_{\min} = 10 \text{ m s}^{-1}$ and v_{\max} is dependent on azimuth only for non-grazing impacts [104]:

$$\text{for } \theta_i \leq 60^\circ : v_{\max}(\varphi) = v_i \left(1 + \frac{6\theta_i}{\pi}\right) \left(\frac{3\theta_i}{4\pi} \cos(\varphi - \varphi_{\max}) + 1 - \frac{3\theta_i}{4\pi}\right) \quad (\text{D.9})$$

$$\text{for } \theta_i > 60^\circ : v_{\max} = 3v_i$$

D.2 Computation of Ejecta Momentum

To get an accurate computation of the momentum provided by the ejecta, a calculation needs to be done for both the spall products and cone fragments. While the momentum associated with spall products can be easily obtained from the total mass and ejection velocity of the spall products, shown below in Section D.2.1, the momentum associated with cone fragments requires integrating the distributions over the whole

ejection range. The derivation for this will be shown in Section D.2.2 and is split into two cases, grazing and oblique impacts.

D.2.1 Momentum from Spall Products

The total mass of spall products is given by M_{spalls} in Eq. (D.2) and since we assume that the ejection velocity of spall products is constant at $v_{\text{spalls}} = 10 \text{ m s}^{-1}$ in the surface normal direction, we can write the momentum associated with spall products in the surface reference frame defined in Fig. D.1 as:

$$\mathbf{p}_{\text{spalls}} = \begin{bmatrix} 0 \\ 0 \\ M_{\text{spalls}} v_{\text{spalls}} \end{bmatrix} \quad (\text{D.10})$$

D.2.2 Momentum from Cone Fragments

A general solution for the momentum contribution from cone fragments can be obtained by calculating the expected value of momentum as a function of mass and velocity and integrating over the zenith and azimuth distributions. The result needs to be normalized over the expected mass from cone fragments:

$$\mathbf{p}_{\text{cone}} = \frac{M_{\text{cone}}}{\int_{m_{\min}}^{m_{\max}} m f_m(m) dm} \left[\begin{array}{l} \int_0^{\pi/2} \int_0^{2\pi} \int_{m_{\min}}^{m_{\max}} \sin(\theta) f_{\text{zen}}(\theta) \cos(\varphi) f_{\text{azi}}(\varphi) mv(m, \varphi) f_m(m) dm d\varphi d\theta \\ \int_0^{\pi/2} \int_0^{2\pi} \int_{m_{\min}}^{m_{\max}} \sin(\theta) f_{\text{zen}}(\theta) \sin(\varphi) f_{\text{azi}}(\varphi) mv(m, \varphi) f_m(m) dm d\varphi d\theta \\ \int_0^{\pi/2} \int_0^{2\pi} \int_{m_{\min}}^{m_{\max}} \cos(\theta) f_{\text{zen}}(\theta) f_{\text{azi}}(\varphi) mv(m, \varphi) f_m(m) dm d\varphi d\theta \end{array} \right] \quad (\text{D.11})$$

Mass distribution

In order to calculate the momentum associated with cone fragments, a distribution for the mass of the particles needs to be obtained, as shown in Eq. (D.11). This can be derived from the size distribution given in Eq. (D.3) assuming that the ejecta are spheres with constant density (i.e. $m = g(\delta) = \delta^3 \pi \rho_t / 6$). A change of variable can be performed as follows:

$$f_m(m) = \left| \frac{d}{dm} (g^{-1}(m)) \right| f_{\text{size}}(g^{-1}(m)) \quad (\text{D.12})$$

where:

$$g^{-1}(m) = \left(\frac{6m}{\pi\rho_t} \right)^{1/3} \quad (\text{D.13})$$

$$\frac{d}{dm}(g^{-1}(m)) = \frac{2}{\pi\rho_t} \left(\frac{6m}{\pi\rho_t} \right)^{-2/3} \quad (\text{D.14})$$

From this it follows that the distribution for the mass of the cone fragments is given by the following:

$$f_m(m) = \frac{2}{\pi\rho_t} \left(\frac{\alpha+1}{\delta_{\max}^{\alpha+1} - \delta_{\min}^{\alpha+1}} \right) \left(\frac{6m}{\pi\rho_t} \right)^{\frac{\alpha-2}{3}} \mathbf{1}_{[m_{\min}, m_{\max}]} \quad (\text{D.15})$$

where $m_{\min} = \delta_{\min}^3 \pi \rho_t / 6$.

Grazing Impacts

The simplest case is for grazing impacts, when the distribution for azimuth is a Gaussian distribution implying that the ejecta is concentrated into a beam going in one particular direction. In this case, velocity is also not a function of azimuth. The mean zenith angle is given by $\theta_{\max} = 80^\circ$ while the ejecta is going in the same azimuthal direction as the incoming impactor. Eq. (D.11) can then be split into a calculation of momentum magnitude and a calculation of direction. The magnitude of the momentum due to cone fragments is then calculated as follows:

$$p_{\text{cone}} = \frac{M_{\text{cone}}}{\int_{m_{\min}}^{m_{\max}} m f_m(m) dm} \int_{m_{\min}}^{m_{\max}} m v(m) f_m(m) dm \quad (\text{D.16})$$

An analytical solution to each integral can be obtained in the following way:

$$\begin{aligned}
\int_{m_{\min}}^{m_{\max}} m f_m(m) dm &= \int_{m_{\min}}^{m_{\max}} m \left(\frac{2}{\pi \rho_t} \right) \left(\frac{\alpha + 1}{\delta_{\max}^{\alpha+1} - \delta_{\min}^{\alpha+1}} \right) \left(\frac{6m}{\pi \rho_t} \right)^{\frac{\alpha-2}{3}} dm \\
&= \left(\frac{2}{\pi \rho_t} \right) \left(\frac{\alpha + 1}{\delta_{\max}^{\alpha+1} - \delta_{\min}^{\alpha+1}} \right) \left(\frac{6}{\pi \rho_t} \right)^{\frac{\alpha-2}{3}} \int_{m_{\min}}^{m_{\max}} m^{\frac{\alpha+1}{3}} dm \\
&= \left(\frac{2}{\pi \rho_t} \right) \left(\frac{\alpha + 1}{\delta_{\max}^{\alpha+1} - \delta_{\min}^{\alpha+1}} \right) \left(\frac{6}{\pi \rho_t} \right)^{\frac{\alpha-2}{3}} \left[\frac{3m^{\frac{\alpha+4}{3}}}{\alpha + 4} \right] \Big|_{m_{\min}}^{m_{\max}} \\
&= \left(\frac{2}{\pi \rho_t} \right) \left(\frac{\alpha + 1}{\delta_{\max}^{\alpha+1} - \delta_{\min}^{\alpha+1}} \right) \left(\frac{6}{\pi \rho_t} \right)^{\frac{\alpha-2}{3}} \left(\frac{3}{\alpha + 4} \right) \left(m_{\max}^{\frac{\alpha+4}{3}} - m_{\min}^{\frac{\alpha+4}{3}} \right)
\end{aligned} \tag{D.17}$$

$$\begin{aligned}
\int_{m_{\min}}^{m_{\max}} m v(m) f_m(m) dm &= \int_{m_{\min}}^{m_{\max}} m \left(\frac{D}{\left(\frac{6m}{\pi \rho_t} \right)^{1/3}} + E \right) \left(\frac{2}{\pi \rho_t} \right) \left(\frac{\alpha + 1}{\delta_{\max}^{\alpha+1} - \delta_{\min}^{\alpha+1}} \right) \left(\frac{6m}{\pi \rho_t} \right)^{\frac{\alpha-2}{3}} dm \\
&= \left(\frac{2}{\pi \rho_t} \right) \left(\frac{\alpha + 1}{\delta_{\max}^{\alpha+1} - \delta_{\min}^{\alpha+1}} \right) \left(\frac{6}{\pi \rho_t} \right)^{\frac{\alpha-2}{3}} \int_{m_{\min}}^{m_{\max}} \left(D \left(\frac{\pi \rho_t}{6m} \right)^{1/3} + E \right) m^{\frac{\alpha+1}{3}} dm \\
&= \left(\frac{2}{\pi \rho_t} \right) \left(\frac{\alpha + 1}{\delta_{\max}^{\alpha+1} - \delta_{\min}^{\alpha+1}} \right) \left(\frac{6}{\pi \rho_t} \right)^{\frac{\alpha-2}{3}} \left[\frac{3m^{\frac{\alpha+4}{3}} \left((\alpha + 4) D \left(\frac{\pi \rho_t}{6m} \right)^{1/3} + (\alpha + 3) E \right)}{(\alpha + 3)(\alpha + 4)} \right] \Big|_{m_{\min}}^{m_{\max}}
\end{aligned} \tag{D.18}$$

Simplifying from Eq. (D.16):

$$\begin{aligned}
p_{\text{cone}} &= M_{\text{cone}} \frac{\left[m^{\frac{\alpha+4}{3}} \left((\alpha + 4) D \left(\frac{\pi \rho_t}{6m} \right)^{1/3} + (\alpha + 3) E \right) \right] \Big|_{m_{\min}}^{m_{\max}}}{\left(m_{\max}^{\frac{\alpha+4}{3}} - m_{\min}^{\frac{\alpha+4}{3}} \right) (\alpha + 3)} \\
&= M_{\text{cone}} \left(\left(\frac{D (\alpha + 4)}{\alpha + 3} \right) \left(\frac{\pi \rho_t}{6} \right)^{1/3} \left(\frac{m_{\max}^{\frac{\alpha+3}{3}} - m_{\min}^{\frac{\alpha+3}{3}}}{m_{\max}^{\frac{\alpha+4}{3}} - m_{\min}^{\frac{\alpha+4}{3}}} \right) + E \right)
\end{aligned} \tag{D.19}$$

When considering the directionality of the ejecta, one has to integrate over zenith and azimuth. In the surface reference frame, the closed-form solution for the momentum

associated with cone fragments therefore becomes:

$$\begin{aligned} \mathbf{p}_{\text{cone}} &= p_{\text{cone}} \begin{bmatrix} \int_0^{\pi/2} \sin(\theta) f_{\text{zenith}}(\theta) d\theta \int_0^{2\pi} \cos(\varphi) f_{\text{azimuth}}(\varphi) d\varphi \\ \int_0^{\pi/2} \sin(\theta) f_{\text{zenith}}(\theta) d\theta \int_0^{2\pi} \sin(\varphi) f_{\text{azimuth}}(\varphi) d\varphi \\ \int_0^{\pi/2} \cos(\theta) f_{\text{zenith}}(\theta) d\theta \end{bmatrix} \\ &= p_{\text{cone}} \begin{bmatrix} \sin(\theta_{\max}) \cos(\sigma_\theta) \cos(\varphi_{\max}) \cos(\sigma_\varphi) \\ \sin(\theta_{\max}) \cos(\sigma_\theta) \sin(\varphi_{\max}) \cos(\sigma_\varphi) \\ \cos(\theta_{\max}) \cos(\sigma_\theta) \end{bmatrix} \end{aligned} \quad (\text{D.20})$$

since:

$$\begin{aligned} \int_0^{\pi/2} \sin(\theta) f_{\text{zen}}(\theta) d\theta &= \int_0^{2\pi} \sin(\theta) \frac{1}{\sigma_\theta \sqrt{2\pi}} \exp\left(-\frac{(\theta - \theta_{\max})^2}{2\sigma_\theta^2}\right) d\theta \\ &= \sin(\theta_{\max}) \cos(\sigma_\theta) \end{aligned} \quad (\text{D.21})$$

$$\begin{aligned} \int_0^{\pi/2} \cos(\theta) f_{\text{zen}}(\theta) d\theta &= \int_0^{2\pi} \cos(\theta) \frac{1}{\sigma_\theta \sqrt{2\pi}} \exp\left(-\frac{(\theta - \theta_{\max})^2}{2\sigma_\theta^2}\right) d\theta \\ &= \cos(\theta_{\max}) \cos(\sigma_\theta) \end{aligned} \quad (\text{D.22})$$

$$\begin{aligned} \int_0^{\pi/2} \sin(\varphi) f_{\text{azi}}(\varphi) d\varphi &= \int_0^{2\pi} \sin(\varphi) \frac{1}{\sigma_\varphi \sqrt{2\pi}} \exp\left(-\frac{(\varphi - \varphi_{\max})^2}{2\sigma_\varphi^2}\right) d\varphi \\ &= \sin(\varphi_{\max}) \cos(\sigma_\varphi) \end{aligned} \quad (\text{D.23})$$

$$\begin{aligned} \int_0^{\pi/2} \cos(\varphi) f_{\text{azi}}(\varphi) d\varphi &= \int_0^{2\pi} \cos(\varphi) \frac{1}{\sigma_\varphi \sqrt{2\pi}} \exp\left(-\frac{(\varphi - \varphi_{\max})^2}{2\sigma_\varphi^2}\right) d\varphi \\ &= \cos(\varphi_{\max}) \cos(\sigma_\varphi) \end{aligned} \quad (\text{D.24})$$

Furthermore, by choosing a surface reference frame where $\varphi_i = 0^\circ$, one can impose a simplification where there is no momentum contribution from cone fragments in the

y_s -direction:

$$\begin{aligned} \mathbf{p}_{\text{cone}} &= p_{\text{cone}} \cos(\sigma_\theta) \begin{bmatrix} \sin(\theta_{\max}) \cos(\sigma_\varphi) \\ 0 \\ \cos(\theta_{\max}) \end{bmatrix} \\ &= M_{\text{cone}} \cos(\sigma_\theta) \left(\left(\frac{D(\alpha+4)}{\alpha+3} \right) \left(\frac{\pi \rho_t}{6} \right)^{1/3} \left(\frac{m_{\max}^{\frac{\alpha+3}{3}} - m_{\min}^{\frac{\alpha+3}{3}}}{m_{\max}^{\frac{\alpha+4}{3}} - m_{\min}^{\frac{\alpha+4}{3}}} \right) + E \right) \begin{bmatrix} \sin(\theta_{\max}) \cos(\sigma_\varphi) \\ 0 \\ \cos(\theta_{\max}) \end{bmatrix} \end{aligned} \quad (\text{D.25})$$

Oblique Impacts

Because the velocity function for non-grazing impacts is a function of azimuth, as shown in Eq. (D.9), and that for $\theta_i \leq 60^\circ$ the distribution for azimuth is sinusoidal, the closed-form solution becomes more complex. Directionality needs to be considered for the magnitude of momentum due to cone fragments as well, and therefore an analog to Eq (D.16) for oblique impacts can not be obtained. However, mass and azimuth are independent from the zenith angle, therefore the reduction factor for zenith angle in Eq. (D.20) can be used. The normalization factor for mass also needs to be included. The momentum due to cone fragments then needs to be integrated over mass and azimuth as follows:

$$\mathbf{p}_{\text{cone}} = \frac{M_{\text{cone}} \cos(\sigma_\theta)}{\int_{m_{\min}}^{m_{\max}} m f_m(m) dm} \begin{bmatrix} \sin(\theta_{\max}) \int_0^{2\pi} \int_{m_{\min}}^{m_{\max}} \cos(\varphi) f_{\text{azi}}(\varphi) mv(m, \varphi) f_m(m) dm d\varphi \\ \sin(\theta_{\max}) \int_0^{2\pi} \int_{m_{\min}}^{m_{\max}} \sin(\varphi) f_{\text{azi}}(\varphi) mv(m, \varphi) f_m(m) dm d\varphi \\ \cos(\theta_{\max}) \int_0^{2\pi} \int_{m_{\min}}^{m_{\max}} f_{\text{azi}}(\varphi) mv(m, \varphi) f_m(m) dm d\varphi \end{bmatrix} \quad (\text{D.26})$$

The first integral has the same analytical solution as in Eq. (D.17). Again, by choosing a surface reference frame where $\varphi_i = 0^\circ$, the momentum contribution from cone fragments in the y_s -direction becomes $p_{\text{cone}}^y = 0$. Furthermore, the momentum from

cone fragments in the x_s -direction can be simplified using the results from Eq. (D.19):

$$\begin{aligned}
 p_{\text{cone}}^x &= \frac{M_{\text{cone}} \cos(\sigma_\theta) \sin(\theta_{\max})}{\int_{m_{\min}}^{m_{\max}} m f_m(m) dm} \int_0^{2\pi} \cos(\varphi) f_{\text{azi}}(\varphi) \int_{m_{\min}}^{m_{\max}} m v(m, \varphi) f_{\text{mass}}(m) dm d\varphi \\
 &= M_{\text{cone}} \cos(\sigma_\theta) \sin(\theta_{\max}) \int_0^{2\pi} \cos(\varphi) f_{\text{azi}}(\varphi) \\
 &\quad \left(\left(\frac{D(\varphi)(\alpha+4)}{\alpha+3} \right) \left(\frac{\pi \rho_t}{6} \right)^{1/3} \left(\frac{m_{\max}^{\frac{\alpha+3}{3}} - m_{\min}^{\frac{\alpha+3}{3}}}{m_{\max}^{\frac{\alpha+4}{3}} - m_{\min}^{\frac{\alpha+4}{3}}} \right) + E(\varphi) \right) d\varphi \\
 &= M_{\text{cone}} \cos(\sigma_\theta) \sin(\theta_{\max}) \left[\int_0^{2\pi} \cos(\varphi) f_{\text{azi}}(\varphi) E(\varphi) d\varphi + \right. \\
 &\quad \left. \left(\frac{\pi \rho_t}{6} \right)^{1/3} \left(\frac{m_{\max}^{\frac{\alpha+3}{3}} - m_{\min}^{\frac{\alpha+3}{3}}}{m_{\max}^{\frac{\alpha+4}{3}} - m_{\min}^{\frac{\alpha+4}{3}}} \right) \left(\frac{\alpha+4}{\alpha+3} \right) \int_0^{2\pi} \cos(\varphi) f_{\text{azi}}(\varphi) D(\varphi) d\varphi \right] \tag{D.27}
 \end{aligned}$$

The two integrals in the previous equation can be simplified:

$$\begin{aligned}
 \int_0^{2\pi} \cos(\varphi) f_{\text{azi}}(\varphi) D(\varphi) d\varphi &= \int_0^{2\pi} \cos(\varphi) f_{\text{azi}}(\varphi) \frac{v_{\max}(\varphi) - v_{\min}}{\delta_{\max} - \delta_{\min}} \delta_{\max} \delta_{\min} d\varphi \\
 &= \frac{\delta_{\max} \delta_{\min}}{\delta_{\max} - \delta_{\min}} \left(\int_0^{2\pi} \cos(\varphi) f_{\text{azi}}(\varphi) v_{\max}(\varphi) d\varphi - v_{\min} \int_0^{2\pi} \cos(\varphi) f_{\text{azi}}(\varphi) d\varphi \right) \tag{D.28}
 \end{aligned}$$

$$\begin{aligned}
 \int_0^{2\pi} \cos(\varphi) f_{\text{azi}}(\varphi) E(\varphi) d\varphi &= \int_0^{2\pi} \cos(\varphi) f_{\text{azimuth}}(\varphi) \frac{v_{\min} \delta_{\max} - v_{\max}(\varphi) \delta_{\min}}{\delta_{\max} - \delta_{\min}} d\varphi \\
 &= \frac{v_{\min} \delta_{\max}}{\delta_{\max} - \delta_{\min}} \int_0^{2\pi} \cos(\varphi) f_{\text{azi}}(\varphi) d\varphi - \frac{\delta_{\min}}{\delta_{\max} - \delta_{\min}} \int_0^{2\pi} \cos(\varphi) f_{\text{azi}}(\varphi) v_{\max}(\varphi) d\varphi \tag{D.29}
 \end{aligned}$$

with:

$$\begin{aligned}
 \int_0^{2\pi} \cos(\varphi) f_{\text{azi}}(\varphi) d\varphi &= \int_0^{2\pi} \cos(\varphi) \left(\frac{1}{2\pi} \right) \left(\frac{3\theta_i}{2\pi - 3\theta_i} \cos(\varphi - \varphi_{\max}) + 1 \right) d\varphi \\
 &= \frac{3\theta_i}{4\pi - 6\theta_i} \tag{D.30}
 \end{aligned}$$

$$\begin{aligned}
\int_0^{2\pi} \cos(\varphi) f_{\text{azi}}(\varphi) v_{\max}(\varphi) d\varphi &= \int_0^{2\pi} \cos(\varphi) \left(\frac{1}{2\pi} \right) \left(\frac{3\theta_i}{2\pi - 3\theta_i} \cos(\varphi - \varphi_{\max}) + 1 \right) \\
&\quad v_i \left(1 + \frac{6\theta_i}{\pi} \right) \left(\frac{3\theta_i}{4\pi} \cos(\varphi - \varphi_{\max}) + 1 - \frac{3\theta_i}{4\pi} \right) d\varphi \\
&= \left(\frac{v_i}{2\pi} \right) \left(1 + \frac{6\theta_i}{\pi} \right) \left(\frac{9(\pi - \theta_i)\theta_i \cos(\varphi_{\max})}{4\pi - 6\theta_i} \right)
\end{aligned} \tag{D.31}$$

Similarly, in the z_s -direction:

$$\begin{aligned}
P_{\text{cone}}^z = M_{\text{cone}} \cos(\sigma_\theta) \cos(\theta_{\max}) &\left[\int_0^{2\pi} f_{\text{azi}}(\varphi) E(\varphi) d\varphi + \right. \\
&\left. \left(\frac{\pi\rho_t}{6} \right)^{1/3} \left(\frac{m_{\max}^{\frac{\alpha+3}{3}} - m_{\min}^{\frac{\alpha+3}{3}}}{m_{\max}^{\frac{\alpha+4}{3}} - m_{\min}^{\frac{\alpha+4}{3}}} \right) \left(\frac{\alpha+4}{\alpha+3} \right) \int_0^{2\pi} f_{\text{azi}}(\varphi) D(\varphi) d\varphi \right]
\end{aligned} \tag{D.32}$$

The integrals can again be simplified:

$$\begin{aligned}
\int_0^{2\pi} f_{\text{azi}}(\varphi) D(\varphi) d\varphi &= \int_0^{2\pi} f_{\text{azimuth}}(\varphi) \frac{v_{\max}(\varphi) - v_{\min}}{\delta_{\max} - \delta_{\min}} \delta_{\max} \delta_{\min} d\varphi \\
&= \frac{\delta_{\max} \delta_{\min}}{\delta_{\max} - \delta_{\min}} \left(\int_0^{2\pi} f_{\text{azi}}(\varphi) v_{\max}(\varphi) d\varphi - v_{\min} \int_0^{2\pi} f_{\text{azi}}(\varphi) d\varphi \right) \\
&= \frac{\delta_{\max} \delta_{\min}}{\delta_{\max} - \delta_{\min}} \left(\int_0^{2\pi} f_{\text{azi}}(\varphi) v_{\max}(\varphi) d\varphi - v_{\min} \right)
\end{aligned} \tag{D.33}$$

$$\begin{aligned}
\int_0^{2\pi} f_{\text{azi}}(\varphi) E(\varphi) d\varphi &= \int_0^{2\pi} f_{\text{azi}}(\varphi) \frac{v_{\min} \delta_{\max} - v_{\max}(\varphi) \delta_{\min}}{\delta_{\max} - \delta_{\min}} d\varphi \\
&= \frac{v_{\min} \delta_{\max}}{\delta_{\max} - \delta_{\min}} \int_0^{2\pi} f_{\text{azi}}(\varphi) d\varphi - \frac{\delta_{\min}}{\delta_{\max} - \delta_{\min}} \int_0^{2\pi} f_{\text{azi}}(\varphi) v_{\max}(\varphi) d\varphi \\
&= \frac{v_{\min} \delta_{\max}}{\delta_{\max} - \delta_{\min}} - \frac{\delta_{\min}}{\delta_{\max} - \delta_{\min}} \int_0^{2\pi} f_{\text{azi}}(\varphi) v_{\max}(\varphi) d\varphi
\end{aligned} \tag{D.34}$$

with:

$$\begin{aligned} \int_0^{2\pi} f_{\text{azi}}(\varphi) v_{\max}(\varphi) d\varphi &= \int_0^{2\pi} \frac{1}{2\pi} \left(\frac{3\theta_i}{2\pi - 3\theta_i} \cos(\varphi - \varphi_{\max}) + 1 \right) \\ &\quad v_i \left(1 + \frac{6\theta_i}{\pi} \right) \left(\frac{3\theta_i}{4\pi} \cos(\varphi - \varphi_{\max}) + 1 - \frac{3\theta_i}{4\pi} \right) d\varphi \\ &= \left(\frac{v_i}{2\pi} \right) \left(1 + \frac{6\theta_i}{\pi} \right) \left(\frac{27\theta_i^2 - 36\pi\theta_i + 16\pi^2}{8\pi - 12\theta_i} \right) \end{aligned} \quad (\text{D.35})$$

Combining Eqs. (D.27) to (D.31), and simplifying $\cos(\varphi_{\max}) = 1$:

$$\begin{aligned} P_{\text{cone}}^x &= \frac{3\theta_i M_{\text{cone}} \cos(\sigma_\theta) \sin(\theta_{\max})}{(\delta_{\max} - \delta_{\min})(4\pi - 6\theta_i)} \left[v_{\min} \delta_{\max} - 3\delta_{\min} \left(\frac{v_i}{2\pi} \right) \left(1 + \frac{6\theta_i}{\pi} \right) (\pi - \theta_i) + \right. \\ &\quad \left. \delta_{\max} \delta_{\min} \left(\frac{\pi \rho_t}{6} \right)^{1/3} \left(\frac{m_{\max}^{\frac{\alpha+3}{3}} - m_{\min}^{\frac{\alpha+3}{3}}}{m_{\max}^{\frac{\alpha+4}{3}} - m_{\min}^{\frac{\alpha+4}{3}}} \right) \left(\frac{\alpha+4}{\alpha+3} \right) \left(\left(\frac{3v_i}{2\pi} \right) \left(1 + \frac{6\theta_i}{\pi} \right) (\pi - \theta_i) - v_{\min} \right) \right] \end{aligned} \quad (\text{D.36})$$

Similarly, combining Eqs. (D.32) to (D.35):

$$\begin{aligned} P_{\text{cone}}^z &= \frac{M_{\text{cone}} \cos(\sigma_\theta) \cos(\theta_{\max})}{\delta_{\max} - \delta_{\min}} \left[v_{\min} \delta_{\max} - \delta_{\min} \left(\frac{v_i}{2\pi} \right) \left(1 + \frac{6\theta_i}{\pi} \right) \left(\frac{27\theta_i^2 - 36\pi\theta_i + 16\pi^2}{8\pi - 12\theta_i} \right) + \right. \\ &\quad \left. \delta_{\max} \delta_{\min} \left(\frac{\pi \rho_t}{6} \right)^{1/3} \left(\frac{m_{\max}^{\frac{\alpha+3}{3}} - m_{\min}^{\frac{\alpha+3}{3}}}{m_{\max}^{\frac{\alpha+4}{3}} - m_{\min}^{\frac{\alpha+4}{3}}} \right) \left(\frac{\alpha+4}{\alpha+3} \right) \left(\left(\frac{v_i}{2\pi} \right) \left(1 + \frac{6\theta_i}{\pi} \right) \left(\frac{27\theta_i^2 - 36\pi\theta_i + 16\pi^2}{8\pi - 12\theta_i} \right) - v_{\min} \right) \right] \end{aligned} \quad (\text{D.37})$$

Once the momenta for spall products and cone fragments have been computed, the ejecta momentum can be calculated as the sum of both:

$$\mathbf{p}_{\text{ejecta}} = \mathbf{p}_{\text{cone}} + \mathbf{p}_{\text{spalls}} \quad (\text{D.38})$$

The total linear momentum transfer associated with the collision will therefore be:

$$\mathbf{p}_{\text{total}} = \mathbf{p}_{\text{rel}} - \mathbf{p}_{\text{ejecta}} \quad (\text{D.39})$$

where \mathbf{p}_{rel} is the relative momentum associated with the incoming impactor.

Appendix E

Analytical Momentum Transfer from Hypervelocity Impacts

Additional confidence in the validity of the stochastic orbit propagation model from hypervelocity impacts is given from two analytical test cases: one with a hypothetical spacecraft undergoing simple collisions, and the other with Envisat and its collisions according to MASTER-2009. The validation process involves comparing two solutions for each test case: on the one hand, a simulation of bombardment of impactors leading to orbital decay; and on the other hand, a Hohmann transfer from the same initial orbit to the resulting decayed orbit obtained by two hypothetical large impacts. The validation involves comparing the total mass of the impactors in the simulation to the sum of the impactors in the equivalent analytical Hohmann transfer.

E.1 Hohmann Transfer from Hypervelocity Impacts

From its definition, a Hohmann transfer from a circular orbit at (r_A, v_A) to a lower orbit at (r_B, v_B) , with:

$$v_k = \frac{\mu}{r_k}, k \in \{A, B\} \quad (\text{E.1})$$

where μ is Earth's gravitational parameter, is a two-impulse maneuver using an elliptical transfer orbit with eccentricity:

$$e = \frac{r_A - r_B}{r_A + r_B} \quad (\text{E.2})$$

The velocity changes to go from the outer circular orbit to the Hohmann transfer orbit, and from the Hohmann transfer orbit to the inner circular orbit, are, respectively:

$$\begin{aligned}\Delta v_A &= v_{A_H} - v_A \\ \Delta v_B &= v_B - v_{B_H}\end{aligned}\tag{E.3}$$

where v_{A_H} is the velocity of the spacecraft at the point that joins the outer orbit and the transfer orbit and v_{B_H} is the velocity of the spacecraft at the intersection of the inner orbit and the transfer orbit, calculated as:

$$v_{k_H} = \frac{\sqrt{(1+e)r_k\mu}}{r_k}, k \in \{A, B\}\tag{E.4}$$

By considering the two impulses leading to Δv_A and Δv_B as caused by collisions with large masses, m_1 and m_2 , impacting at some relative velocity, v_{rel} , one can apply conservation of momentum over the two impulses as:

$$mv_A + m_1(v_A - v_{\text{rel}}) = (m + m_1)v_{A_H}\tag{E.5}$$

$$mv_{B_H} + m_2(v_{B_H} - v_{\text{rel}}) = (m + m_2)v_B\tag{E.6}$$

Solving for m_1 and m_2 gives:

$$m_1 = \frac{m\Delta v_A}{-\Delta v_A - v_{\text{rel}}}\tag{E.7}$$

$$m_2 = \frac{m\Delta v_B}{-\Delta v_B - v_{\text{rel}}}\tag{E.8}$$

The validation exercise is now applied to the two aforementioned test cases, by comparing the sum of m_1 and m_2 to the sum of the debris and meteoroid flux throughout the orbital propagation time-frame, between the corresponding two orbits.

E.2 Hypothetical Spacecraft

The first test case involves a $m = 100$ kg satellite in a circular orbit at an initial altitude of 1000 km. A propagation was computed constraining the general formulation in Chapter 3 to allow only the bombardment from head-on collisions every 60 s, with

impactors having a mass of 10^{-12} kg and with an impact velocity of 15 km s^{-1} . This simulation showed a decay in the semi-major axis of 0.1582 m after one year. The sum of the impactor masses experienced during the one-year simulation is:

$$\begin{aligned}\sum_j m_j &= 365.25 \times 60 \times 24 \times 10^{-12} \\ &= 5.2596 \times 10^{-7} \text{ kg}\end{aligned}\quad (\text{E.9})$$

Substituting in Eqs. (E.2) through (E.8) the corresponding values for $m = 100 \text{ kg}$, $v_{\text{rel}} = 15 \text{ km s}^{-1}$, $r_A = 7371 \text{ km}$ and $r_B = 7371 - (0.1582 \times 10^{-3}) \text{ km}$, we obtain:

$$m_1 = m_2 = 2.6298 \times 10^{-7} \text{ kg} \quad (\text{E.10})$$

so that:

$$m_1 + m_2 = 5.2597 \times 10^{-7} \text{ kg} \quad (\text{E.11})$$

Comparing the results of Eqs. (E.9) and (E.11) gives credence to the validity of our propagator and stochastic model.

E.3 Envisat

The second, and more general, test case involves the results of the case study presented in Section 3.5.2. As shown in Fig. 3.12b, the decrease in SMA witnessed by Envisat after one year due to collisions only, without including the effect of ejecta momentum, is approximately 0.736 m . From the MASTER-2009 impact fluxes, the expected value for the impact velocity is calculated as $16.1449 \text{ km s}^{-1}$ and the median sum of the impactor masses from each of the 10,000 runs is approximately $3.00 \times 10^{-4} \text{ kg}$.

Following the same methodology as in the previous section, one can calculate the masses of the two impactors needed to perform the corresponding Hohmann transfer. In this case, $m = 7828 \text{ kg}$, $v_{\text{rel}} = 16.1449 \text{ km s}^{-1}$, $r_A = 7136 \text{ km}$, and $r_B = 7136 - (0.736 \times 10^{-3}) \text{ km}$. From Eqs. (E.2)-(E.8), the two impact masses are therefore found to be:

$$m_1 = m_2 = 9.3436 \times 10^{-5} \text{ kg} \quad (\text{E.12})$$

so that:

$$m_1 + m_2 = 1.8687 \times 10^{-4} \text{ kg} \quad (\text{E.13})$$

Comparing the result in Eq. (E.13) to the value of 3×10^{-4} kg, as predicted by the Monte Carlo simulations, shows a significant difference. This is to be expected, as the directionality of the impactors, included in the stochastic orbital propagation but not in the analytical Hohmann transfer, where the two collisions are assumed to be head-on, will produce a smaller effect in the reduction of the SMA. Indeed, from the MASTER-2009 direction flux, approximately 60% of the collisions occur with $\pm 45^\circ$ elevation and azimuth.

However, it is possible to take this directionality spread into account analytically by looking at the spacecraft's derived PDF for direction. A reduction factor can be obtained by integrating the direction-dependent flux over the entire sphere of directions in the SCO frame:

$$\mathbf{D} = \begin{bmatrix} -\int_{-\pi}^{\pi} \int_{-\frac{\pi}{2}}^{\frac{\pi}{2}} F(\theta_{\text{elev}}, \phi_{\text{azi}}) \cos \theta_{\text{elev}} \cos \phi_{\text{azi}} d\theta_{\text{elev}} d\phi_{\text{azi}} \\ -\int_{-\pi}^{\pi} \int_{-\frac{\pi}{2}}^{\frac{\pi}{2}} F(\theta_{\text{elev}}, \phi_{\text{azi}}) \cos \theta_{\text{elev}} \sin \phi_{\text{azi}} d\theta_{\text{elev}} d\phi_{\text{azi}} \\ -\int_{-\pi}^{\pi} \int_{-\frac{\pi}{2}}^{\frac{\pi}{2}} F(\theta_{\text{elev}}, \phi_{\text{azi}}) \sin \theta_{\text{elev}} d\theta_{\text{elev}} d\phi_{\text{azi}} \end{bmatrix} \quad (\text{E.14})$$

Applying this to Envisat, we obtain:

$$\mathbf{D} = \begin{bmatrix} -0.6001 \\ -0.0073 \\ 0.0986 \end{bmatrix} \quad (\text{E.15})$$

As one can see, the integrated flux is still mostly in the incoming ram direction due to the symmetry of the directional flux. The reduction factor obtained is therefore $\|\mathbf{D}\| = 0.6082$, which, when applied to the sum of the impactor masses from the Monte Carlo simulations yields:

$$\begin{aligned} \sum_j m_j &= 0.6082 \times 3.00 \times 10^{-4} \text{ kg} \\ &= 1.8246 \times 10^{-4} \text{ kg} \end{aligned} \quad (\text{E.16})$$

The above value is very close to the sum of the two impactors computed in Eq. (E.13) and therefore provides a satisfactory validation of the propagator and stochastic model.

Bibliography

- [1] D. Vallado. *Fundamentals of Astrodynamics and Applications*. Microcosm Press, Hawthorne, California, fourth edition, 2013. ISBN [978-1881883180](#).
- [2] S. L. Bruinsma. The DTM-2013 thermosphere model. *Journal of Space Weather and Space Climate*, 5:A1, 2015. doi:[10.1051/swsc/2015001](#).
- [3] J. M. Picone, A. E. Hedin, D. P. Drob, and A. C. Aikin. NRLMSISE-00 empirical model of the atmosphere: Statistical comparisons and scientific issues. *Journal of Geophysical Research*, 107(A12):1468, 2002. doi:[10.1029/2002JA009430](#).
- [4] D. P. Drob, J. T. Emmert, J. W. Meriwether, J. J. Makela, E. Doornbos, M. Conde, G. Hernandez, J. Noto, K. A. Zawdie, S. E. McDonald, J. D. Huba, and J. H. Klenzing. An update to the Horizontal Wind Model (HWM): The quiet time thermosphere. *Earth and Space Science*, 2:301–319, 2015. doi:[10.1002/2014EA000089](#).
- [5] B. R. Bowman, W. K. Tobiska, F. A. Marcos, C. Y. Huang, C. S. Lin, and W. J. Burke. A New Empirical Thermospheric Density Model JB2008 Using New Solar and Geomagnetic Indices. In *Proceedings of the AIAA/AAS Astrodynamics Specialist Conference and Exhibit*, AIAA 2008-6438, Honolulu, Hawaii, 2008. doi:[10.2514/6.2008-6438](#).
- [6] F. Deleflie, M. A. Sammuneh, R. Biancale, L. Sagnières, D. Coulot, A. Pollet, and J. Mahenc. A New Model of the Mean Albedo of the Earth: Estimation and Validation from the GRACE Mission and SLR Satellites. In *Proceedings of the 21st International Workshop on Laser Ranging*, Canberra, Australia, 2018.
- [7] D. Kucharski, G. Kirchner, J. C. Bennett, M. Lachut, K. Sośnica, N. Koshkin, L. Shakun, F. Koidl, M. Steindorfer, P. Wang, C. Fan, X. Han, L. Grunwaldt, M. Wilkinson, J. Rodríguez, G. Bianco, F. Vespe, M. Catalán, K. Salmins, J. R. del Pino, H.-C. Lim, E. Park, C. Moore, P. Lejba, and T. Suchodolski. Photon Pressure Force on Space Debris TOPEX/Poseidon Measured by Satellite Laser Ranging. *Earth and Space Science*, 4(10):661–668, 2017. doi:[10.1002/2017EA000329](#).

- [8] N. Koshkin, L. Shakun, N. Burlak, E. Korobeynikova, S. Strakhova, S. Melikyants, S. Terpan, and A. Ryabov. Ajisai spin-axis precession and rotation-period variations from photometric observations. *Advances in Space Research*, 60(7):1389–1399, 2017. doi:[10.1016/j.asr.2017.06.045](https://doi.org/10.1016/j.asr.2017.06.045).
- [9] T. Otsubo, R. A. Sherwood, P. Gibbs, and R. Wood. Spin Motion and Orientation of LAGEOS-2 From Photometric Observation. *IEEE Transactions on Geoscience and Remote Sensing*, 42(1):202–208, 2004. doi:[10.1109/TGRS.2003.817191](https://doi.org/10.1109/TGRS.2003.817191).
- [10] NASA Orbital Debris Program Office. Satellite Box Score. *Orbital Debris Quarterly News*, 22(3):12, 2018.
- [11] CelesTrak. Satcat boxscore, 2018. URL <https://celestak.com/satcat/boxscore.php>.
- [12] European Space Agency. How many space debris objects are currently in orbit?, 2018. URL https://www.esa.int/Our_Activities/Space_Engineering_Technology/Clean_Space/How_many_space_debris_objects_are_currently_in_orbit.
- [13] J.-C. Liou and N. L. Johnson. Risks in Space from Orbiting Debris. *Science*, 311:340–341, 2006. doi:[10.1126/science.1121337](https://doi.org/10.1126/science.1121337).
- [14] C. Pardini and L. Anselmo. Review of past on-orbit collisions among cataloged objects and examination of the catastrophic fragmentation concept. *Acta Astronautica*, 100:30–39, 2014. doi:[10.1016/j.actaastro.2014.03.013](https://doi.org/10.1016/j.actaastro.2014.03.013).
- [15] G. Drolshagen. Impact effects from small size meteoroids and space debris. *Advances in Space Research*, 41:1123–1131, 2008. doi:[10.1016/j.asr.2007.09.007](https://doi.org/10.1016/j.asr.2007.09.007).
- [16] J.-C. Liou and N. L. Johnson. Instability of the present LEO satellite populations. *Advances in Space Research*, 41(7):1046–1053, 2008. doi:[10.1016/j.asr.2007.04.081](https://doi.org/10.1016/j.asr.2007.04.081).
- [17] J.-C. Liou and N. L. Johnson. Characterization of the cataloged Fengyun-1C fragments and their long-term effect on the LEO environment. *Advances in Space Research*, 43:1407–1415, 2009. doi:[10.1016/j.asr.2009.01.011](https://doi.org/10.1016/j.asr.2009.01.011).
- [18] T. S. Kelso. Analysis of the Iridium 33-Cosmos 2251 collision. *Advances in the Astronautical Sciences*, 135:1099–1112, 2009.

- [19] European Space Agency. About space debris, 2018. URL https://www.esa.int/Our_Activities/Operations/Space_Debris/About_space_debris.
- [20] N. L. Johnson. Protecting the GEO environment: policies and practices. *Space Policy*, 15:127–135, 1999. doi:[10.1016/S0265-9646\(99\)00022-3](https://doi.org/10.1016/S0265-9646(99)00022-3).
- [21] I. I. Shapiro, H. M. Jones, and C. W. Perkins. Orbital properties of the West Ford dipole belt. *Proceedings of the IEEE*, 52(5):469–518, 1964. doi:[10.1109/PROC.1964.2992](https://doi.org/10.1109/PROC.1964.2992).
- [22] S. Flegel, J. Gelhaus, M. Mockel, C. Wiedemann, and D. Kempf. **Maintenance of the ESA MASTER Model - Final Report**. Technical Report 21705/08/D/HK, European Space Agency, 2011.
- [23] T. Schildknecht, R. Musci, and T. Flohrer. Properties of the high area-to-mass ratio space debris population at high altitudes. *Advances in Space Research*, 41: 1039–1045, 2008. doi:[10.1016/j.asr.2007.01.045](https://doi.org/10.1016/j.asr.2007.01.045).
- [24] P. H. Krisko. The New NASA Orbital Debris Engineering Model ORDEM 3.0. In *Proceedings of the 2014 AIAA/AAS Astrodynamics Specialist Conference*, AIAA 2014-4227, San Diego, California, 2014. doi:[10.2514/6.2014-4227](https://doi.org/10.2514/6.2014-4227).
- [25] P. H. Krisko, S. Flegel, M. J. Matney, D. R. Jarkey, and V. Braun. ORDEM 3.0 and MASTER-2009 modeled debris population comparison. *Acta Astronautica*, 113: 204–211, 2015. doi:[10.1016/j.actaastro.2015.03.024](https://doi.org/10.1016/j.actaastro.2015.03.024).
- [26] H. Schaub, L. E. Z. Jasper, P. V. Anderson, and D. S. McKnight. Cost and risk assessment for spacecraft operation decisions caused by the space debris environment. *Acta Astronautica*, 113:66–79, 2015. doi:[10.1016/j.actaastro.2015.03.028](https://doi.org/10.1016/j.actaastro.2015.03.028).
- [27] D. J. Kessler and B. G. Cour-Palais. Collision Frequency of Artificial Satellites: The Creation of a Debris Belt. *Journal of Geophysical Research*, 83(A6):2637–2646, 1978. doi:[10.1029/JA083iA06p02637](https://doi.org/10.1029/JA083iA06p02637).
- [28] International Academy of Astronautics. **Position Paper on Space Debris Mitigation: Implementing Zero Debris Creation Zones**. Technical Report SP-1301, European Space Agency, 2006.

- [29] Inter-Agency Space Debris Coordination Committee. **IADC Space Debris Mitigation Guidelines**. Technical Report IADC-02-01, Inter-Agency Space Debris Coordination Committee, 2007.
- [30] National Aeronautics and Space Administration. **Process for Limiting Orbital Debris**. Technical Report NASA-STD-8719.14A, National Aeronautics and Space Administration, 2012.
- [31] C. Bonnal, J.-M. Ruault, and M.-C. Desjean. Active debris removal: Recent progress and current trends. *Acta Astronautica*, 85:51–60, 2013. doi:[10.1016/j.actaastro.2012.11.009](https://doi.org/10.1016/j.actaastro.2012.11.009).
- [32] M. Shan, J. Guo, and E. Gill. Review and comparison of active debris capturing and removal methods. *Progress in Aerospace Sciences*, 80:18–32, 2016. doi:[10.1016/j.paerosci.2015.11.001](https://doi.org/10.1016/j.paerosci.2015.11.001).
- [33] ESA Space Debris Office. **ESA’s Annual Space Environment Report**. Technical Report GEN-DB-LOG-00239-OPS-GR, European Space Agency, 2018.
- [34] J.-C. Liou, N. L. Johnson, and N. M. Hill. Controlling the growth of future LEO debris populations with active debris removal. *Acta Astronautica*, 66(5–6):648–653, 2010. doi:[10.1016/j.actaastro.2009.08.005](https://doi.org/10.1016/j.actaastro.2009.08.005).
- [35] F. Letizia, C. Colombo, H. G. Lewis, and H. Krag. Assessment of breakup severity on operational satellites. *Advances in Space Research*, 58(7):1255–1274, 2016. doi:[10.1016/j.asr.2016.05.036](https://doi.org/10.1016/j.asr.2016.05.036).
- [36] A. Rossi, G. B. Valsecchi, and E. M. Alessi. The Criticality of Spacecraft Index. *Advances in Space Research*, 56(3):449–460, 2015. doi:[10.1016/j.asr.2015.02.027](https://doi.org/10.1016/j.asr.2015.02.027).
- [37] L. Anselmo and C. Pardini. Ranking upper stages in low Earth orbit for active removal. *Acta Astronautica*, 122:19–27, 2016. doi:[10.1016/j.actaastro.2016.01.019](https://doi.org/10.1016/j.actaastro.2016.01.019).
- [38] N. van der Pas, J. Lousada, C. Terhes, M. Bernabeu, and W. Bauer. Target selection and comparison of mission design for space debris removal by DLR’s advanced study group. *Acta Astronautica*, 102:241–248, 2014. doi:[10.1016/j.actaastro.2014.06.020](https://doi.org/10.1016/j.actaastro.2014.06.020).
- [39] Surrey Space Center. Removedebris, 2018. URL <https://www.surrey.ac.uk/surrey-space-centre/missions/removedebris>.

- [40] ASTROSCALE. Elsa-d, 2018. URL <https://astroscale.com/services/elsa-d>.
- [41] École Fédérale Polytechnique de Lausanne. Cleanspace one, 2018. URL https:////espace.epfl.ch/CleanSpaceOne_1.
- [42] R. Biesbroek, L. Innocenti, A. Wolahan, and S. M. Serrano. e.Deorbit - ESA's active debris removal mission. In *Proceedings of the 7th European Conference on Space Debris*, Darmstadt, Germany, 2017. ESA Space Debris Office.
- [43] D. Kucharski, G. Kirchner, F. Koidl, C. Fan, R. Carman, C. Moore, A. Dmytrotsa, M. Ploner, G. Bianco, M. Medvedskij, A. Makeyev, G. Appleby, M. Suzuki, J.-M. Torre, Zhang Z., L. Grunwaldt, and Q. Feng. Attitude and Spin Period of Space Debris Envisat Measured by Satellite Laser Ranging. *IEEE Transactions on Geoscience and Remote Sensing*, 52(12):7651–7657, 2014. doi:[10.1109/TGRS.2014.2316138](https://doi.org/10.1109/TGRS.2014.2316138).
- [44] M. R. Pearlman, J. J. Degnan, and J. M. Bosworth. The International Laser Ranging Service. *Advances in Space Research*, 30(2):135–143, 2002. doi:[10.1016/S0273-1177\(02\)00277-6](https://doi.org/10.1016/S0273-1177(02)00277-6).
- [45] J. Šilha, J.-N. Pittet, M. Hamara, and T. Schildknecht. Apparent rotation properties of space debris extracted from photometric measurements. *Advances in Space Research*, 61(3):844–861, 2018. doi:[10.1016/j.asr.2017.10.048](https://doi.org/10.1016/j.asr.2017.10.048).
- [46] N. Koshkin, E. Korobeynikova, L. Shakun, S. Strakhova, and Z. H. Tang. Remote Sensing of the EnviSat and Cbers-2B satellites rotation around the centre of mass by photometry. *Advances in Space Research*, 58(3):358–371, 2016. doi:[10.1016/j.asr.2016.04.024](https://doi.org/10.1016/j.asr.2016.04.024).
- [47] V. I. Kudak, V. P. Epishev, V. M. Perig, and I. F. Neybauer. Determining the orientation and spin period of TOPEX/Poseidon satellite by a photometric method. *Astrophysical Bulletin*, 72(3):340–348, 2017. doi:[10.1134/S1990341317030233](https://doi.org/10.1134/S1990341317030233).
- [48] J. Silha, T. Schildknecht, and J.-N. Pittet. Light curve database of Astronomical Institute of the University of Bern. In *Proceedings of the 67th International Astro-nautical Congress*, Guadalajara, Mexico, 2016. doi:[10.7892/boris.91306](https://doi.org/10.7892/boris.91306).
- [49] M. A. Earl and G. A. Wade. Observations of the Spin-Period Variations of Inactive Box-Wing Geosynchronous Satellites. *Journal of Spacecraft and Rockets*, 52(3):968–977, 2015. doi:[10.2514/1.A33077](https://doi.org/10.2514/1.A33077).

- [50] C. R. Binz, M. A. Davis, B. E. Kelm, and C. I. Moore. Optical Survey of the Tumble Rates of Retired GEO Satellites. In *Proceedings of the 2014 Advanced Maui Optical and Space Surveillance Technologies Conference*, Maui, Hawaii, 2014.
- [51] C. J. Benson, D. J. Scheeres, W. H. Ryan, E. V. Ryan, and N. Moskovitz. Rotation state evolution of retired geosynchronous satellites. In *Proceedings of the 2017 Advanced Maui Optical and Space Surveillance Technologies Conference*, Maui, Hawaii, 2017.
- [52] P. Papushev, Y. Karavaev, and M. Mishina. Investigations of the evolution of optical characteristics and dynamics of proper rotation of uncontrolled geostationary artificial satellites. *Advances in Space Research*, 43(9):1416–1422, 2009. doi:[10.1016/j.asr.2009.02.007](https://doi.org/10.1016/j.asr.2009.02.007).
- [53] J. Rosebrock. Absolute Attitude From Monostatic Radar Measurements of Rotating Objects. *IEEE Transactions on Geoscience and Remote Sensing*, 49(10):3737–3744, 2011. doi:[10.1109/TGRS.2011.2159727](https://doi.org/10.1109/TGRS.2011.2159727).
- [54] S. Sommer, J. Rosebrock, D. Cerutti-Maori, and L. Leushacke. Temporal Analysis of Envisat’s Rotational Motion. In *Proceedings of the 7th European Conference on Space Debris*, Darmstadt, Germany, 2017. ESA Space Debris Office.
- [55] J. Šilha, T. Schildknecht, J.-N. Pittet, G. Kirchner, M. Steindorfer, D. Kucharski, D. Cerutti-Maori, J. Rosebrock, S. Sommer, L. Leushacke, P. Kärräng, R. Kanzler, and H. Krag. Debris Attitude Motion Measurements and Modelling by Combining Different Observation Techniques. In *Proceedings of the 7th European Conference on Space Debris*, Darmstadt, Germany, 2017. ESA Space Debris Office.
- [56] P. C. Hughes. *Spacecraft Attitude Dynamics*. Dover Publications, Inc., Mineola, New York, 2006. ISBN [978-0-486-43925-9](https://doi.org/10.1016/j.actaastro.2012.03.004).
- [57] N. Praly, M. Hillion, C. Bonnal, J. Laurent-Varin, and N. Petit. Study on the eddy current damping of the spin dynamics of space debris from the Ariane launcher upper stages. *Acta Astronautica*, 76:145–153, 2012. doi:[10.1016/j.actaastro.2012.03.004](https://doi.org/10.1016/j.actaastro.2012.03.004).
- [58] N. Ortiz Gómez and S. J. I. Walker. Earth’s gravity gradient and eddy currents effects on the rotational dynamics of space debris objects: Envisat case study. *Advances in Space Research*, 56:494–508, 2015. doi:[10.1016/j.asr.2014.12.031](https://doi.org/10.1016/j.asr.2014.12.031).

- [59] S. Efimov, D. Pritykin, , and V. Sidorenko. Long-term attitude dynamics of space debris in Sun-synchronous orbits: Cassini cycles and chaotic stabilization. *Celestial Mechanics and Dynamical Astronomy*, 130:62, 2018. doi:[10.1007/s10569-018-9854-4](https://doi.org/10.1007/s10569-018-9854-4).
- [60] J. W. Crenshaw and P. M. Fitzpatrick. Gravity Effects on the Rotational Motion of a Uniaxial Artificial Satellite. *American Institute of Aeronautics and Astronautics Journal*, 6:2140–2145, 1968. doi:[10.2514/3.4946](https://doi.org/10.2514/3.4946).
- [61] R. L. Holland and H. J. Sperling. A First-Order Theory for the Rotational Motion of a Triaxial Rigid Body Orbiting an Oblate Primary. *The Astronomical Journal*, 74: 490–496, 1969. doi:[10.1086/110826](https://doi.org/10.1086/110826).
- [62] S. Efimov, D. Pritykin, and V. Sidorenko. Defunct Satellites in Nearly Polar Orbits: Long-term Evolution of Attitude Motion. *Open Astronomy*, 27(1):264–277, 2018. doi:[10.1515/astro-2018-0029](https://doi.org/10.1515/astro-2018-0029).
- [63] A. A. Albuja, D. J. Scheeres, and J. W. McMahon. Evolution of angular velocity for defunct satellites as a result of YORP: An initial study. *Advances in Space Research*, 56(2):237–251, 2015. doi:[10.1016/j.asr.2015.04.013](https://doi.org/10.1016/j.asr.2015.04.013).
- [64] A. A. Albuja, D. J. Scheeres, R. L. Cognion, W. Ryan, and E. V. Ryan. The YORP effect on the GOES 8 and GOES 10 satellites: A case study. *Advances in Space Research*, 61(1):122–144, 2018. doi:[10.1016/j.asr.2017.10.002](https://doi.org/10.1016/j.asr.2017.10.002).
- [65] C. Früh, T. M. Kelecy, and M. K. Jah. Coupled orbit-attitude dynamics of high area-to-mass ratio (HAMR) objects: influence of solar radiation pressure, Earth’s shadow and the visibility in light curves. *Celestial Mechanics and Dynamical Astronomy*, 117:385–404, 2013. doi:[10.1007/s10569-013-9516-5](https://doi.org/10.1007/s10569-013-9516-5).
- [66] C. Früh and M. K. Jah. Coupled orbit-attitude motion of high area-to-mass ratio (HAMR) objects including efficient self-shadowing. *Acta Astronautica*, 95:227–241, 2014. doi:[10.1016/j.actaastro.2013.11.017](https://doi.org/10.1016/j.actaastro.2013.11.017).
- [67] J. Hughes and H. Schaub. Space Weather Influence on Electromagnetic Geosynchronous Debris Perturbations Using Statistical Fluxes. *Space Weather*, 16(4):391–405, 2018. doi:[10.1002/2017SW001768](https://doi.org/10.1002/2017SW001768).

- [68] R. Kanzler, J. Silha, T. Schildknecht, B. Fritsche, T. Lips, and H. Krag. Space debris attitude simulation - *iOTA* (In-Orbit Tumbling Analysis). In *Proceedings of the 2015 Advanced Maui Optical and Space Surveillance Technologies Conference*, Maui, Hawaii, 2015.
- [69] D. A. Vallado, P. Crawford, R. Hujasak, and T. S. Kelso. *Revisiting Spacetrack Report #3: Rev 2*. In *Proceedings of the 2006 AIAA/AAS Astrodynamics Specialist Conference*, AIAA 2006-6753-Rev2, Keystone, Colorado, 2006.
- [70] J. R. Dormand and P. J. Prince. A family of embedded Runge-Kutta formulae. *Journal of Computational and Applied Mathematics*, 6(1):19–26, 1980. doi:[10.1016/0771-050X\(80\)90013-3](https://doi.org/10.1016/0771-050X(80)90013-3).
- [71] N. K. Pavlis, S. A. Holmes, S. C. Kenyon, and J. K. Factor. The development and evaluation of the Earth Gravitational Model 2008 (EGM2008). *Journal of Geophysical Research*, 117:B04406, 2012. doi:[10.1029/2011JB008916](https://doi.org/10.1029/2011JB008916).
- [72] Institut de Mécanique Céleste et de Calcul des Éphémérides. Miriade - the virtual observatory solar system object ephemeris generator, 2018. URL <http://vo.imcce.fr/webservices/miriade/>.
- [73] E. Thébault, C. C. Finlay, C. D. Beggan, P. Alken, J. Aubert, O. Barrois, F. Bertrand, T. Bondar, A. Boness, L. Brocco, E. Canet, A. Chambodut, A. Chulliat, P. Coisson, F. Civet, A. Du, A. Fournier, I. Fratter, N. Gillet, B. Hamilton, M. Hamoudi, G. Hulot, T. Jager, M. Korte, W. Kuang, X. Lalanne, B. Langlais, J.-M. Léger, V. Lesur, F. J. Lowes, S. Macmillan, M. Mandea, C. Manoj, S. Maus, N. Olsen, V. Petrov, V. Ridley, M. Rother, T. J. Sabaka, D. Saturnino, R. Schachtschneider, O. Sirol, A. Tangborn, A. Thomson, L. Tøffner-Clausen, P. Vigneron, I. Wardinski, and T. Zvereva. International Geomagnetic Reference Field: the 12th generation. *Earth, Planets and Space*, 67:79, 2015. doi:[10.1186/s40623-015-0228-9](https://doi.org/10.1186/s40623-015-0228-9).
- [74] A. Chulliat, S. Macmillan, P. Alken, C. Beggan, M. Nair, B. Hamilton, A. Woods, V. Ridley, S. Maus, and A. Thomson. The US/UK World Magnetic Model for 2015-2020. *Tehcnical Report, National Geophysical Data Center, NOAA*, 2015. doi:[10.7289/V5TB14V7](https://doi.org/10.7289/V5TB14V7).
- [75] O. Montenbruck and E. Gill. *Satellite Orbits: Models, Methods, Applications*. Springer-Verlag Berlin Heidelberg, 2013. ISBN [978-3-540-67280-7](https://doi.org/10.1007/978-3-540-67280-7).

- [76] G. L. Stephens, G. G. Campbell, and T. H. Vonder Haar. Earth Radiation Budgets. *Journal of Geophysical Research*, 86:9739–9760, 1981. doi:[10.1029/JC086iC10p09739](https://doi.org/10.1029/JC086iC10p09739).
- [77] N. G. Loeb, B. A. Wielicki, D. R. Doelling, G. L. Smith, D. F. Keyes, S. Kato, N. Manalo-Smith, and T. Wong. Toward Optimal Closure of the Earth’s Top-of-Atmosphere Radiation Budget. *Journal of Climate*, 22(3):748–766, 2009. doi:[10.1175/2008JCLI2637.1](https://doi.org/10.1175/2008JCLI2637.1).
- [78] European Centre for Medium-Range Weather Forecasts. Public datasets, 2018. URL <https://apps.ecmwf.int/datasets/>.
- [79] T. R. Kane and P. M. Barba. Effects of Energy Dissipation on a Spinning Satellite. *American Institute of Aeronautics and Astronautics Journal*, 4:1392–1394, 1966. doi:[10.2514/3.3683](https://doi.org/10.2514/3.3683).
- [80] L. B. M. Sagnières and I. Sharf. Stochastic modeling of hypervelocity impacts in attitude propagation of space debris. *Advances in Space Research*, 59(4):1128–1143, 2017. doi:[10.1016/j.asr.2016.11.030](https://doi.org/10.1016/j.asr.2016.11.030).
- [81] L. B. M. Sagnières and I. Sharf. Evolution of spacecraft orbital motion due to hypervelocity impacts with debris and meteoroids. In *Proceedings of the 7th European Conference on Space Debris*, Darmstadt, Germany, 2017. ESA Space Debris Office.
- [82] R. G. Gottlieb. **Fast Gravity, Gravity Partials, Normalized Gravity, Gravity GradientTorque and Magnetic Field: Derivation, Code and Data.** Technical Report 188243, National Aeronautics and Space Administration, 1993.
- [83] J. R. Wertz, editor. *Spacecraft Attitude Determination and Control*. D. Reidel Publishing Company, Dordrecht, Holland, 1978. doi:[10.1007/978-94-009-9907-7](https://doi.org/10.1007/978-94-009-9907-7).
- [84] J. T. Emmert. Thermospheric mass density: A review. *Advances in Space Research*, 56:773–824, 2015. doi:[10.1016/j.asr.2015.05.038](https://doi.org/10.1016/j.asr.2015.05.038).
- [85] C. He, Y. Yang, B. Carter, E. Kerr, S. Wu, F. Deleflie, H. Cai, K. Zhang, L. Sagnières, and R. Norman. Review and comparison of empirical thermospheric mass density models. *Progress in Aerospace Sciences*, 103:31–51, 2018. doi:[10.1016/j.paerosci.2018.10.003](https://doi.org/10.1016/j.paerosci.2018.10.003).

- [86] National Oceanic and Atmospheric Administration. Geomagnetic kp and ap indices, 2018. URL https://www.ngdc.noaa.gov/stp/GEOMAG/kp_ap.html.
- [87] Collecte Localisation Satellites. Solar radio flux for orbit determination: nowcast and forecast, 2018. URL <https://spaceweather.cls.fr/services/radioflux/>.
- [88] L. G. Jacchia. *Static Diffusion Models of the Upper Atmosphere with Empirical Temperature Profiles*. *Smithsonian Contributions to Astrophysics*, 8:215–257, 1965.
- [89] M. F. Storz, B. R. Bowman, J. I. Branson, S. J. Casali, and W. K. Tobiska. High accuracy satellite drag model (HASDM). *Advances in Space Research*, 36:2497–2505, 2005. doi:[10.1016/j.asr.2004.02.020](https://doi.org/10.1016/j.asr.2004.02.020).
- [90] D. A. Vallado and D. Finkleman. A critical assessment of satellite drag and atmospheric density modeling. *Acta Astronautica*, 95:141–165, 2014. doi:[10.1016/j.actaastro.2013.10.005](https://doi.org/10.1016/j.actaastro.2013.10.005).
- [91] D. Kucharski, H.-C. Lim, G. Kirchner, and J.-Y. Hwang. Spin parameters of LAGEOS-1 and LAGEOS-2 spectrally determined from Satellite Laser Ranging data. *Advances in Space Research*, 52(7):1332–1338, 2013. doi:[10.1016/j.asr.2013.07.007](https://doi.org/10.1016/j.asr.2013.07.007).
- [92] D. Kucharski, H.-C. Lim, G. Kirchner, T. Otsubo, G. Bianco, and J.-Y. Hwang. Spin Axis Precession of LARES Measured by Satellite Laser Ranging. *IEEE Geoscience and Remote Sensing Letters*, 11(3):646–650, 2014. doi:[10.1109/LGRS.2013.2273561](https://doi.org/10.1109/LGRS.2013.2273561).
- [93] D. Kucharski, G. Kirchner, T. Otsubo, H.-C. Lim, J. Bennett, F. Koidl, Y.-R. Kim, and J.-Y. Hwang. Confirmation of gravitationally induced attitude drift of spinning satellite Ajisai with Graz high repetition rate SLR data. *Advances in Space Research*, 57(4):983–990, 2016. doi:[10.1016/j.asr.2015.12.010](https://doi.org/10.1016/j.asr.2015.12.010).
- [94] J. I. Andrés de la Fuente. *Enhanced Modelling of LAGEOS Non-Gravitational Perturbations*. PhD thesis, Technische Universiteit Delft, 2007.
- [95] M. Visco and D. M. Lucchesi. Comprehensive model for the spin evolution of the LAGEOS and LARES satellites. *Physical Review D*, 98(4):044034, 2018. doi:[10.1103/PhysRevD.98.044034](https://doi.org/10.1103/PhysRevD.98.044034).

- [96] J. I. Andrés, R. Noomen, G. Bianco, D. G. Currie, and T. Otsubo. Spin axis behavior of the LAGEOS satellites. *Journal of Geophysical Research*, 109(B6):501, 2004. doi:[10.1029/2003JB002692](https://doi.org/10.1029/2003JB002692).
- [97] L. B. M. Sagnières, I. Sharf, and F. Deleflie. Validation of a novel coupled orbit-attitude propagator by comparison to SLR data and light curves. In *Proceedings of the 69th International Astronautical Congress*, Abstract ID 46562, Bremen, Germany, 2018.
- [98] D. M. Lucchesi, C. Magnafico, R. Peron, M. Visco, L. Anselmo, C. Pardini, M. Basan, G. Pucacco, and R. Stanga. The LARASE research program. State of the art on Modelling and Measurements of General Relativity effects in the field of the Earth: a preliminary measurement of the Lense-Thirring effect. In *Proceedings of the 2017 IEEE International Workshop on Metrology for AeroSpace*, pages 131–145, Padua, Italy, 2017. doi:[10.1109/MetroAeroSpace.2017.7999552](https://doi.org/10.1109/MetroAeroSpace.2017.7999552).
- [99] M. Visco and D. M. Lucchesi. Review and critical analysis of mass and moments of inertia of the LAGEOS and LAGEOS II satellites for the LARASE program. *Advances in Space Research*, 57(9):1928–1938, 2016. doi:[10.1016/j.asr.2016.02.006](https://doi.org/10.1016/j.asr.2016.02.006).
- [100] R. A. Wilson. *Rotational Magnetodynamics and Steering of Space Vehicles*. In *Proceedings of the XIth International Astronautical Congress 1960*, Paper 65, pages 525–536, Stockholm, Sweden, 1961.
- [101] D. Kucharski, T. Otsubo, G. Kirchner, and G. Bianco. Spin rate and spin axis orientation of LARES spectrally determined from Satellite Laser Ranging data. *Advances in Space Research*, 50(11):1473–1477, 2012. doi:[10.1016/j.asr.2012.07.018](https://doi.org/10.1016/j.asr.2012.07.018).
- [102] H. Hashimoto, S. Nakamura, H. Shirai, A. Sengoku, M. Fujita, M. Sato, H. Kuni-mori, and T. Otsubo. Japanese Geodetic Satellite AJISAI: development, observation and scientific contributions to geodesy. *Journal of the Geodetic Society of Japan*, 58(1):9–25, 2012. doi:[10.11366/sokuchi.58.9](https://doi.org/10.11366/sokuchi.58.9).
- [103] D. Kucharski, H.-C. Lim, G. Kirchner, T. Otsubo, G. Bianco, F. Koidl, and J.-Y. Hwang. Modeling spin parameters of Ajisai, LARES and the other geodetic satellites with SLR data. In *Proceedings of the 18th International Workshop on Laser Ranging*, 13-0304, Fujiyoshida, Japan, 2013.

- [104] M. Rival and J. C. Mandeville. Modeling of ejecta produced upon hypervelocity impacts. *Space Debris*, 1:45–57, 1999. doi:[10.1023/A:1010021403591](https://doi.org/10.1023/A:1010021403591).
- [105] G. J. Cloutier. Attitude Perturbation of Space Vehicles by Meteroid Impacts. *Journal of Spacecraft and Rockets*, 3(4):523–530, 1966. doi:[10.2514/3.28485](https://doi.org/10.2514/3.28485).
- [106] S. K. Shrivastava and V. J. Modi. Satellite attitude dynamics and control in the presence of environmental torques - a brief survey. *Journal of Guidance, Control, and Dynamics*, 6(6):461–471, 1983. doi:[10.2514/3.8526](https://doi.org/10.2514/3.8526).
- [107] L. B. M. Sagnières and I. Sharf. Stochastic Modeling of Hypervelocity Impacts on Attitude Propagation of Space Debris. In *Proceedings of the 26th AAS/AIAA Spaceflight Mechanics Meeting*, AAS 16-462, Napa, California, 2016.
- [108] M. Pätzold, M. K. Bird, and P. Endenhofer. The Change of Giotto’s Dynamical State During the P/Grigg-Skjellerup Flyby Caused by Dust Particle Impacts. *Journal of Geophysical Research*, 98(A12):20911–20920, 1993. doi:[10.1029/93JA02534](https://doi.org/10.1029/93JA02534).
- [109] R. Ernst. Momentum Transfer to Orbiting Satellites by Micrometeoroid Impacts. Technical report, European Space Agency / European Space Research and Technology Centre, 2007.
- [110] N. Parkhomenko, V. Shargorodsky, V. Vasiliev, and V. Yurasov. **Accident in orbit**. In *Proceedings of the 18th International Workshop on Laser Ranging*, 13-Po03, Fujiyoshida, Japan, 2013.
- [111] J. B. White. Meteoric Effects on Attitude Control of Space Vehicles. *American Rocket Society Journal*, 32(1):75–78, 1962. doi:[10.2514/8.5951](https://doi.org/10.2514/8.5951).
- [112] S. P. Morgan and E. Y. Yu. Meteoric Disturbances of Gravitationally Oriented Satellites. *Journal of Spacecraft and Rockets*, 2(6):857–862, 1965. doi:[10.2514/3.28304](https://doi.org/10.2514/3.28304).
- [113] D. Risquez, F. van Leeuwen, and A. G. A. Brown. Dynamical attitude model for Gaia. *Experimental Astronomy*, 34:669–703, 2012. doi:[10.1007/s10686-012-9310-5](https://doi.org/10.1007/s10686-012-9310-5).
- [114] E. Platen and N. Bruti-Liberati. *Numerical Solution of Stochastic Differential Equations with Jumps in Finance*. Springer-Verlag Berlin Heidelberg, 2010. doi:[10.1007/978-3-642-13694-8](https://doi.org/10.1007/978-3-642-13694-8).

- [115] Y. L. Xu, M. Horstman, P. H. Krisko, J.-C. Liou, M. Matney, E. G. Stansbery, C. L. Stokely, and D. Whitlock. Modeling of LEO orbital debris populations for ORDEM2008. *Advances in Space Research*, 43:769–782, 2009. doi:[doi:10.1016/j.asr.2008.11.023](https://doi.org/10.1016/j.asr.2008.11.023).
- [116] H. Klinkrad. *Space Debris: Models and Risk Analysis*. Springer-Praxis, Chichester, UK, 2006. doi:[10.1007/3-540-37674-7](https://doi.org/10.1007/3-540-37674-7).
- [117] B. P. Denardo. Measurements of momentum transfer from plastic projectiles to massive aluminum targets at speeds up to 25,600 feet per second. Technical Report NASA-TN-D-1210, National Aeronautics and Space Administration, 1962.
- [118] C. R. Nysmith and B. P. Denardo. Experimental investigation of the momentum transfer associated with impact into thin aluminum targets. Technical Report NASA-TN-D-5492, National Aeronautics and Space Administration, 1969.
- [119] K. A. Holsapple and K. R. Housen. Momentum transfer in asteroid impacts. I. Theory and scaling. *Icarus*, 221(2):875–887, 2012. doi:[10.1016/j.icarus.2012.09.022](https://doi.org/10.1016/j.icarus.2012.09.022).
- [120] J. D. Walker and S. Chocron. Momentum enhancement in hypervelocity impacts. *International Journal of Impact Engineering*, 38(6):A1–A7, 2011. doi:[10.1016/j.ijimpeng.2010.10.026](https://doi.org/10.1016/j.ijimpeng.2010.10.026).
- [121] B. Bastida Virgili, S. Lemmens, and H. Krag. Investigation on Envisat attitude motion. In *e.Deorbit Workshop*, Noordwijk, The Netherlands, 2014.
- [122] L. B. M. Sagnières and I. Sharf. Long-term rotational motion analysis and comparison to observations of the inoperative Envisat. *Journal of Guidance, Control, and Dynamics*, 42(2):364–376, 2019. doi:[10.2514/1.G003647](https://doi.org/10.2514/1.G003647).
- [123] T. Lips, R. Kanzler, A. Breslau, P. Karrang, J. Silha, T. Schildknecht, D. Kucharski, G. Kirchner, J. Rosebrock, D. Cerutti-Maori, and H. Krag. Debris attitude motion measurements and modeling - observation vs. simulation. In *Proceedings of the 2017 Advanced Maui Optical and Space Surveillance Technologies Conference*, Maui, Hawaii, 2017.
- [124] S. Lemmens, H. Krag, J. Rosebrock, and I. Carnelli. Radar Mappings of Attitude Analysis of Objects in Orbit. In *Proceedings of the 6th European Conference on Space Debris*, Darmstadt, Germany, 2013. ESA Space Debris Office.

- [125] L. Cerri, A. Couhert, and P. Ferrage. **DORIS satellites models implemented in POE processing.** Technical Report SALP-NT-BORD-OP-16137-CN, International DORIS Service, 2018.
- [126] L. Shakun, N. Koshkin, E. Korobeynikova, S. Melikiants, and S. Strakhova. **Monitoring of the inoperative Envisat satellite's behaviour.** *Odessa Astronomical Publications*, 26(2):282–284, 2013.
- [127] H.-Y. Lin and C.-Y. Zhao. An estimation of Envisat's rotational state accounting for the precession of its rotational axis caused by gravity-gradient torque. *Advances in Space Research*, 61(1):182–188, 2018. doi:[10.1016/j.asr.2017.10.014](https://doi.org/10.1016/j.asr.2017.10.014).
- [128] J.-N. Pittet, J. Šilha, and T Schildknecht. Spin motion determination of the Envisat satellite through laser ranging measurements from a single pass measured by a single station. *Advances in Space Research*, 61(4):1121–1131, 2018. doi:[10.1016/j.asr.2017.11.035](https://doi.org/10.1016/j.asr.2017.11.035).
- [129] C. Le Fèvre, V. Morand, M. Delpech, C. Gazzino, and Y. Henriquel. Integration of Coupled Orbit and Attitude Dynamics and Impact on Orbital Evolution of Space Debris. In *Proceedings of the 25th AAS/AIAA Spaceflight Mechanics Meeting*, AAS 15-335, Vail, Colorado, 2015.
- [130] L.-L. Fu, E. J. Christensen, C. A. Yamarone Jr., M. Lefebvre, Y. Ménard, M. Dorrrer, and P. Escudier. TOPEX/POSEIDON mission overview. *Journal of Geophysical Research: Oceans*, 99(C12):24369–24381, 1994. doi:[10.1029/94JC01761](https://doi.org/10.1029/94JC01761).
- [131] C. Jekeli. The determination of gravitational potential differences from satellite-to-satellite tracking. *Celestial Mechanics and Dynamical Astronomy*, 75(2):85–101, 1999. doi:[10.1023/A:1008313405488](https://doi.org/10.1023/A:1008313405488).
- [132] D. Kucharski, G. Kirchner, J. C. Bennett, M. K. Jah, and J. G. Webb. High-definition Photometry - New tool for space debris characterization. In *Proceedings of the 21st International Workshop on Laser Ranging*, Canberra, Australia, 2018.
- [133] D. E. Gault. Displaced mass, depth, diameter, and effects of oblique trajectories for impact craters formed in dense crystalline rocks. *The Moon*, 6:32–44, 1973. doi:[10.1007/BF02630651](https://doi.org/10.1007/BF02630651).